Radiation sensitive optical fibres for radiation detection and dosimetry

by

Carly A. Whittaker

A thesis submitted in fulfillment of the degree of Doctor of Philosophy

in the
Faculty of Sciences
School of Physical Sciences
University of Adelaide, Australia

February 2018

Abstract

Optical fibre-based alpha and beta particle sensing devices have been investigated for the purpose of detecting low levels of Uranium-238 and its decay products in liquids for mineral processing applications. Both sensors operate using the mechanism of scintillation produced within scintillating polymer optical fibres. The prototype devices which have been created are capable of performing direct, real-time, semi-continuous measurements of alpha and beta particle emitting radionuclides within solutions or suspensions, which is not possible with current measurement techniques. This work aims to help improve current processing techniques for the production of high quality copper concentrates from ore by monitoring the quantities and distributions of non-target minerals throughout various mineral processing stages.

Using the fibre fabrication facilities at IPAS, optical fibres have been drawn in-house from the commercial bulk scintillators EJ204 and EJ262 from ELJEN Technologies. Fibres with outer diameters of 160 µm were fabricated for alpha particle detection, and through refinement of the fabrication conditions, a transmission loss of 14 dB/m at 440 nm (EJ204) was achieved, down from > 30 dB/m in an earlier trial. 1 mm diameter canes were fabricated for beta particle detection, with transmission losses of 5 dB/m at 450 nm (EJ204), comparable to similar commercial fibre varieties.

In-house fabricated fibres were tested alongside commercially available scintillating optical fibres in radiation sensing experiments, where their response to X-rays, alpha and beta particles were evaluated. Optical fibres have been tested under laboratory-simulated environmental conditions analogous to those encountered during mineral processing, where commercial fibres with outer claddings displayed the best performance.

Prototype devices have been created and tested in real-world mineral processing solutions. Both alpha and beta particle sensors have demonstrated detection limits below the 1 Bq/ml per isotope of ^{238}U target level. The work which has been presented shows the concept of using scintillating polymer fibres for low level radionuclide detection in liquids has been proven, and successful prototype alpha and beta particle sensors have been developed.

Acknowledgements

I would like to express my sincere gratitude to my supervisors: Nigel Spooner, Heike Ebendorff-Heidepriem and David Ottaway for their time, ideas and patience throughout my PhD. I have been extremely fortunate to have supervisors who cared so much about my work. Without your ongoing support and encouragement this would not have been possible.

I wish to thank Bob Chivell, Alastair Dowler, and Evan Johnson for their technical support. Your skilled assistance with fibre drawing and component fabrication has proved invaluable for this work.

For their financial support, I would like to thank the Australian Research Council Australian Copper-Uranium Transformation Research Hub, and the South Australian node of the Australian National Fabrication Facility for usage of fabrication facilities.

To my family, thank you for your constant support and encouragement in all my pursuits, and for the good laughs. Mum and dad: thank you for producing such a great human being (me), for always being proud of me, believing in me and working hard to provide me with every opportunity in life. Your dedication and self-discipline have been a huge inspiration to me.

Despite my eccentricities, and absenteeism over the course of this PhD, I feel very fortunate to have such a fantastic group of friends who I would like to thank for their support and friendship. Thanks to the environmental luminescence group, especially Chris (extra points there for all the help and insight you provided with this project), Jillian, Ruth and Katherine for making this experience more than bearable (perhaps even fun) and for politely turning the other way whenever I cried at my desk. And Danielle, your kind words, great ideas, snacks, pink gifts and all round pleasantness is always appreciated.

To Nic, thank you for all your advice and support throughout this process. You managed to cheer me up every time I was an inconsolable mess, and helped me see the bigger picture when I was struggling to see anything positive at all. Thank you for all the fun and happiness you bring into my life, my world is a better place with you in it.

Declaration

I, Carly Whittaker, declare that this thesis titled 'Alpha and beta radiation sensing using scintillating polymer optical fibres' and the work presented in it are my own.

I certify that this work contains no material which has been accepted for the award of any other degree or diploma in my name in any university or other tertiary institution and, to the best of my knowledge and belief, contains no material previously published or written by another person, except where due reference has been made in the text. In addition, I certify that no part of this work will, in the future, be used in a submission in my name for any other degree or diploma in any university or other tertiary institution without the prior approval of the University of Adelaide and where applicable, any partner institution responsible for the joint award of this degree.

I give permission for the digital version of my thesis to be made available on the web, via the University's digital research repository, the Library Search and also through web search engines, unless permission has been granted by the University to restrict access for a period of time.

Signed ____________________________

Date ____________________________

Contents

Abstract

Acknowledgements

Declaration

Chapter 1

Introduction

1.1 Introduction to radiation dosimetry

Following the discovery of X-rays in 1895, Becquerel discovered three new types of radiation, later classified as alpha, beta and gamma radiation, thereby opening an entirely new field of study dedicated to radiation and radioactive substances. The first major developments in nuclear research commenced after the neutron was discovered in 1932, starting with the creation of a self-sustaining fission reactor in 1942. Most early atomic research that followed was focused on the development of weapons for the second world war, until the Atomic Energy Act of 1954 was passed, allowing the licensing of private companies to use nuclear materials and build nuclear power plants. The technology associated with the production of energetic radiation has since undergone massive advancements, and is extensively used today in research, industry and medical treatments. This widespread use of high energy, man-made radiation quickly made apparent its dangers and detrimental health effects, prompting the development of the field of radiation dosimetry.

Radiation dosimetry, which involves the detection and quantification of ionising radiation, was originally focused on limiting the exposure of workers in radiation intensive environments by determining the integrated dose they receive. The applicability of this field has grown in several areas including medical diagnostics and radiation therapy. In these applications, the radiation dose delivered to patients must be carefully planned and monitored to increase therapeutic efficacy and minimise toxicity [66, 4, 14]. Other areas in which dosimetry plays a central role are environmental monitoring [86], industry [34, 39], and space research [7].

1.2 Project motivation and scope

1.2.1 Mining application

Iron Oxide Copper Gold Uranium (IOCG-U) ores in Australia are among the most complex mineral systems worldwide and include deposits at Olympic Dam, Prominent Hill, and Carrapateena. Extraction of valuable metals such as copper and gold poses a technological challenge, and improvements in current techniques would allow greater mining efficiencies, lower costs and less energy inputs. To do this, an in-depth understanding of the distribution of small quantities of contaminant minerals, including uranium-238 daughters, throughout various mineral processing stages is required. This knowledge is critical in order to efficiently and reliably extract marketable products with low radioactivity for global export and trade.

The process for treating the ore and extracting copper involves a number of stages such as underground mining, ore grinding, flotation and acid leaching, where radionuclide distributions and quantities differ substantially. Current techniques used to measure radionuclide quantities are time consuming (turn around times of $\approx$ weeks), and require samples to be sent off-site for analysis. The goal of this work is to develop optical fibre based sensors to directly detect uranium and its decay products on site, and in real-time during the liquid processing stages. These real-time sensors can be used to improve the current understanding of the distribution and movement of radionuclides through various processing stages, which will help develop better processing techniques for production of high quality copper concentrates. In order to detect the presence of Uranium and its daughter radionuclides, two optical fibre-based sensors are proposed:

- **Alpha particle sensor:** Small diameter (250 µm) plastic scintillating fibres in a bundled configuration will be used as a liquid dip sensor to directly detect alpha particles emitted by radionuclides in the uranium-238 decay chain.
- **Beta particle sensor:** A second fibre bundle optimised for detection of beta particles emitted throughout the uranium-238 decay chain is proposed. The sensor is created using 1 mm thick plastic scintillating fibres to enhance beta particle energy deposition within the fibre volume.

Both optical fibre-based sensors are capable of performing continuous, real-time measurements within liquids (either solutions or fine suspensions), and are designed to achieve a targeted detection limit of at least 1 Bq/ml per isotope of ^{238}U (8 alpha events, and 6 beta events per ml in secular equilibrium, discussed below)

Uranium-238 decay chain

Uranium is a naturally occurring heavy metal and is widespread throughout the earths crust. The most common isotope of uranium is uranium-238, making up more than 99% in weight of natural uranium, and is one of the contaminant radionuclides in IOCG-U ore. Uranium-238 decays by alpha particle emission and gives rise to a decay series illustrated in Figure 1.1.

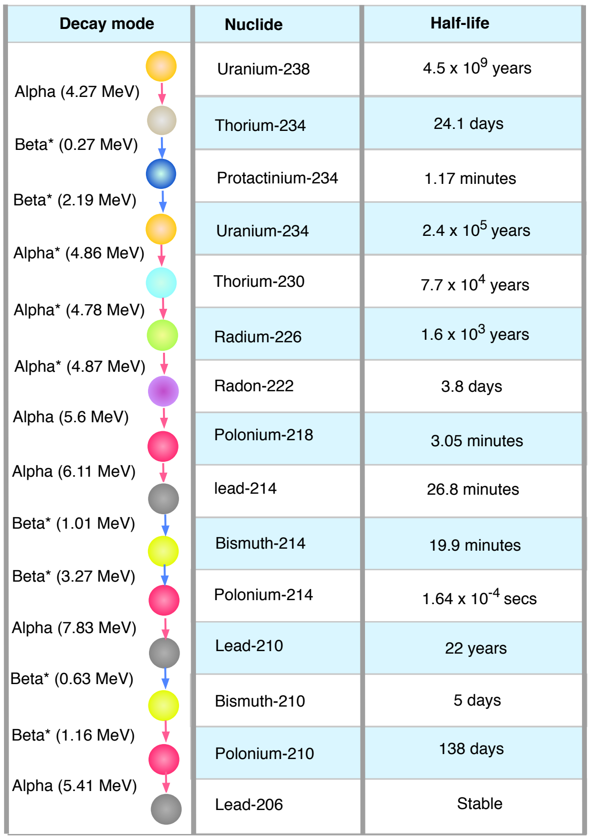

Decay mode	Nuclide	Half-life
Alpha (4.27 MeV)	Uranium-238	4.5 x 10^9 years
Beta* (0.27 MeV)	Thorium-234	24.1 days
Beta* (2.19 MeV)	Protactinium-234	1.17 minutes
Alpha* (4.86 MeV)	Uranium-234	2.4 x 10^5 years
Alpha* (4.78 MeV)	Thorium-230	7.7 x 10^4 years
Alpha* (4.87 MeV)	Radium-226	1.6 x 10^3 years
Alpha (5.6 MeV)	Radon-222	3.8 days
Alpha (6.11 MeV)	Polonium-218	3.05 minutes
Beta* (1.01 MeV)	lead-214	26.8 minutes
Beta* (3.27 MeV)	Bismuth-214	19.9 minutes
Alpha (7.83 MeV)	Polonium-214	1.64 x 10^{-4} secs
Beta* (0.63 MeV)	Lead-210	22 years
Beta* (1.16 MeV)	Bismuth-210	5 days
Alpha (5.41 MeV)	Polonium-210	138 days
	Lead-206	Stable

Figure 1.1: Decay of ^{238}U. * Denotes accompanying gamma emission

When a system reaches secular equilibrium the mass of each isotope in the decay chain is static, so the mass gained from decay of the parent isotopes will occur at the same rate as the mass lost by decay to the daughter isotopes. In the uranium-238 chain, the longest half life is that of uranium-238, hence the activity of the sample is limited by this half life.

When a uranium-238 sample is in secular equilibrium, for each alpha decay from uranium-238 there will be 7 further alpha decays, and 6 beta decays from the daughter isotopes ending in the production of lead-206. For a sample in secular equilibrium containing 1 Bq/unit mass of uranium-238, the total alpha and beta activities of the sample will therefore be 8 and 6 Bq/unit mass. During mineral processing, the state of secular equilibrium is disturbed due to the mobilisation of certain radionuclides through the various processing stages, and as a result the actual alpha and beta activities will be less than achieved in secular equilibrium.

Radionuclide analysis techniques

Current techniques used to determine the presence and concentrations of radioisotopes in mineral processing solutions are:

- **Gamma ray spectroscopy:** A high resolution germanium detector is used to identify and quantify a range of radionuclides and determine their count rates. The detection and data processing system is used to generate and display a pulse height spectrum showing the characteristic gamma ray peaks emitted from a radioactive sample. The corresponding energies and intensities of these peaks unambiguously determine the presence of a radioisotope. Very long acquisition times are required for radionuclides present at low concentrations in the sample.
- **Neutron Activation Analysis (NAA):** This technique is able to measure the concentrations of uranium, thorium and potassium isotopes within ore at the ppm level, regardless of the physical or chemical form of the sample. The measurement involves irradiating a sample with neutrons to produce specific radionuclides which then decay by emitting characteristic gamma rays. The presence and concentration of specific radionuclides are informed by data analysis of the gamma ray energy spectrum.
- **Inductively Coupled Plasma Mass Spectrometry (ICPMS) with Optical Excitation Spectroscopy (OES):** This is a type of mass spectrometry which is capable of detecting very low concentrations (down to parts per quadrillion) of metals and several non-metals. Samples are digested or dissolved in acid and ionised with inductively coupled argon plasma. The constituent elements and their concentrations are determined by analysing the characteristic optical radiation emitted by the ions with an Optical Emission Spectrometer.
- **Alpha and beta spectrometry:** This technique is used to identify and quantify radionuclides based on the alpha or beta particles emitted by the radionuclides as they decay. Samples require often lengthy chemical separation procedures to isolate the radionuclides of interest (to reduce interference effects) and the energy spectra are analysed using high precision detectors, electronics and specialised software.

Although these techniques are able to accurately measure the type and amounts of trace contaminant radionuclides, they often require lengthy, destructive preparation prior to measurements (i.e radiochemical separation for alpha/beta spectrometry). The samples must be collected at the site and taken away for analysis meaning there is a significant turn around time. The proposed sensing devices aim to develop a method capable of performing in-situ measurements of alpha and beta particle concentrations in real-time in liquids, eliminating the need to perform lengthy sample collection, preparation and analysis off-site. These sensors could help identify the radionuclide quantities, distributions and changes over time to help gain an understanding of how the various metals and radionuclides in the IOCG-U system behave during the extraction process in an effort to improve current techniques.

1.2.2 Medical application

The use of plastic scintillating fibres has been studied extensively for dosimetry in MV beams for irradiations with electrons or photons, however the scope of published research for dosimetry in low-energy photon beams is limited in comparison. Low energy photon dosimetry is a major challenge for radiology, superficial therapy and brachytherapy, for which plastic scintillation detectors may be well suited for as a dosimetry tool [64]. There has been a growing interest in this field in recent years [21, 43], however, to date there is no comprehensive study assessing the response of the range of commercially available plastic scintillators under this regime.

A considerable part of this thesis is concerned with evaluating the properties of plastic scintillators when exposed to alpha and beta radiation. Given the extensive range of plastic scintillators on-hand, the lack of published work regarding their response to low energy photons, and the fact the proposed devices will be placed in a radiation field containing energetic photons, it was required to characterise the scintillators under photon irradiation to create a more comprehensive understanding of their properties..

1.3 Radiation detection and measurement

Detection and measurement of radiation uses the ionisation and/or excitation of atoms that are produced when it is incident on a material. The types of instruments designed to detect radiation are numerous and differ in their physical state, chemistry, associated instrumentation and electronic circuitry. The efficiency with which a radiation detector will perform depends on a host of factors including the instrumentation characteristics, the properties of the radiation detected, and the measurement sample properties which make the detector choice strongly application dependent. Radiation detectors can be broadly categorised into three groups; dosimeters; track visualisation instruments; and counters.

1.3.1 Dosimeters

These devices accumulate dose over time, thus measure the integral effect of many radiations as opposed to recording individual events. Active dosimeters in this category, such as the ionisation chamber, are capable of measuring both integrated and instantaneous dose, while passive dosimeters such as photographic film, thermoluminescent dosimeters (TLD's) and optically stimulated luminescence (OSL) dosimeters generally require removal of the device from the radiation field to read out the accumulated dose. The direct readout functionality of ionisation chambers has given them widespread usage as radiation survey meters where they are able to check equipment, facilities and personnel for radioactive contamination as well as measure any ambient radiation levels to directly assess any exposure hazards. Although passive dosimeters are not suitable for measuring instantaneous dose rates, they have proven highly successful and convenient for measuring the radiation dose accumulated over time, making them well suited for use as personal dosimeters. Radiation workers, or anyone working in an occupation where they may be exposed to ionising radiation, are required to wear personal dosimeters to ensure their occupational exposure is accurately measured and recorded.

1.3.2 Track visualisation devices

These devices exploit the damage imparted to a material by radiation in order to visualise and record the trajectories of individual ionising particles over a period of time. The most well known track visualisation detectors are photographic emulsion plates, cloud chambers, bubble chambers and solid state track detectors. The operational principle of this detector class is based upon counting the number and geometry of the tracks produced by radiation within the sensitive detection volume. The number of tracks produced gives a measure of the fluence of the radiation field, the track length is used as a measure of the particle range or energy, and the track density can be used to identify different particle types based on their linear energy transfer. The ability to distinguish between different radiation types, and the possibility of obtaining a comprehensive spatial pattern of a radiation field makes these detectors extremely useful for cosmic ray research [17], and in nuclear physics where, owing to these detectors, nuclear decays, reactions and novel particles have been discovered [12]. A major drawback associated with this technique lies in the retrieval of data from the detectors. Manual counting procedures, usually with a microscope, are often required if detailed track information or a high degree of counting precision is needed, making readout a labor and time intensive process.

1.3.3 Counting devices

Radiation counting instruments detect individual ionising particles, and use electronic circuitry to generate an electronic pulse. Radiation counters operate in one of two ways. They detect the primary and/or secondary ions formed when radiation interacts with the detector medium (i.e gas proportional counters, Geiger-Muller counters, liquid and solid ionisation chambers) or by detecting photons produced by ionising radiation in the detector material (i.e scintillation and Čerenkov counters). Scintillation counters are by far the most versatile counting instruments, and are of most relevance to this thesis. They operate by detecting the photons produced when ionising radiation is incident on a scintillating material and encompass a range of instruments that will be discussed shortly. Scintillation counters can operate as ratemeters, spectrometers, particle discriminators or timing devices and are suitable for measurements of a vast array of radiation types and energies.

1.3.4 Scintillation counting devices

When ionising radiation interacts with certain materials it will excite or ionise a large number of atoms or molecules. Return of the atom or molecule to the ground state will sometimes result in the emission of photons with wavelengths in the visible (or near-visible) region of the electromagnetic spectrum. The scientific name for this phenomenon is radioluminescence (RL), but it is more commonly called scintillation. A variety of materials will produce scintillation in response to ionising radiation, however the amount of light produced is generally low. A few materials, called scintillators, are able to efficiently convert the energy deposited by radiation into UV and visible photons much more efficiently. Detection of ionising radiation by observing scintillation light produced in zinc sulfide was one of the first radiation detection and counting techniques. Scintillation flashes were counted by eye using a microscope, a technique that imposed considerable strain and fatigue among observers but provided a simple method of counting individual alpha particles. This method of scintillation counting has come a long way since the invention of photomultiplier tubes and other highly efficient radiation detectors, and remains one of the most useful methods available for radiation detection.

The steps involved for radiation detection with scintillation counters are:

- Radiation interacts with the scintillation material.
- Energy transfer from radiation to the bound states of the material.
- Relaxation of excited states to the ground level causing photon emission

- Photon collection by a photodetector
- Generation of an electronic signal by associated electronics.

Given the relevance of each of the processes listed above to the work performed throughout this thesis, a more detailed discussion of each point is required, starting with the interactions of alpha, beta and gamma radiation with matter (See Section 1.4). Scintillating materials broadly fall into two categories: organic and inorganic scintillators. The properties, applications and physical mechanisms of light production are very different between organic and inorganic materials, so it is important to discriminate between the two. A description of each scintillator class is provided in 1.5, with particular attention paid to plastic scintillators because they are the focus of this research. Finally, the advantages and disadvantages of some commonly used photodetectors are reviewed in Section 1.7, along with a description of the photodetector and detection electronics used for scintillation measurements for experiments performed as part of this thesis.

1.4 Interactions of radiation with matter

The design and operation of any radiation detector relies on knowledge of the processes which occur when radiation interacts with the detector material. Depending on the detector material and the characteristics of the radiation, there are differences in the fundamental mechanisms by which radiation is able to interact and deposit energy. The primary focus of this research is based on the detection of alpha and beta particles, which lose energy primarily via direct ionisation and excitation of atoms as they travel through a medium. Photons are indirectly ionising particles, usually they transfer their energy to the nucleus of an atom, which then ejects a secondary electron that produces ionisation within a detector medium. Differences in these energy deposition mechanisms mean charged particles can deposit energy continuously as they pass through a medium, whereas a photon can travel much larger distances before depositing any energy and may not interact with the detector at all. An understanding of the differences in energy deposition mechanisms and characteristics between radiation types is essential, as it forms the basis for which devices are tailored for their detection.

1.4.1 Alpha particle interactions with matter

Energy loss mechanism

Heavy charged particles, including alpha particles interact with matter via columbic forces with atomic electrons. Energy transfer to the medium occurs primarily through ionisation, where the energy transfer to an atomic electron is sufficient to remove it from the atom, or by excitation, where the energy transfer leaves an atomic electron in an excited, higher energy state. Conservation of energy and momentum require there is a maximum amount of energy an alpha particle can transfer to an electron in any given collision: $E_{max} = 4Em_e/m$ [58], where m_e is the electron mass, m is the mass of an alpha particle (or any heavy charged particle), and E is the initial kinetic energy of the alpha particle. Therefore, for a 5 MeV alpha particle, around 28 keV or 0.06% of the initial kinetic energy can be transferred. Consequently, the alpha particles deflection following a collision will be negligible. Given the kinetic energy loss per collision is such a small fraction of the alpha particle kinetic energy, many interactions with atomic electrons occur before an alpha particle is stopped within the material. The result is a straight path through the material with many ionised and excited atoms along the track.

Stopping power

The stopping power, also referred to as the linear energy transfer (LET) of the particle, represents the linear rate of energy loss of a charged particle as it traverses a medium. It is defined by the differential of the energy loss, dE, divided by the corresponding differential path length, dx:

$$S = -\frac{dE}{dx} \tag{1.1}$$

The stopping power of a non-relativistic charged particle varies inversely with its velocity squared, so as the particle is slowed down in a medium, its rate of energy deposition increases. The Bethe formula (Equation 1.2) is a classical expression which describes the mean energy loss per unit distance for heavy charged particles traversing matter.

$$-\frac{dE}{dx} = \frac{4\pi z^2 e^4}{m_o \nu^2} nZ \left[\ln \frac{2m_0 \nu^2}{I(1-(\nu^2/c^2))} - \frac{\nu^2}{c^2} \right] \tag{1.2}$$

Where:

z = charge of the energetic particle
ν = velocity of energetic particle
Z = atomic number of the target material
n = number of electrons per unit volume in the medium
e = electron charge
m_0 = rest mass of electron
c = speed of light in vacuum
I = mean excitation energy of the medium

The Bethe formula shows that particles with higher charges will have the greatest specific energy losses as $-\frac{dE}{dx} \propto z$. Hence alpha particles will lose energy at a greater rate than a proton of the same velocity. If we consider an alpha particle, with a 2^+ electronic charge, the Bethe formula predicts at higher energies, the stopping power will increase roughly as 1/E for the majority of the particles track. At lower energies, when $\frac{v}{c} \rightarrow 0$, the logarithmic term in Equation 1.2 decreases, and the factor in front of the brackets increases, causing a peak in the stopping power. This peak is known as the Bragg peak, and at this location the rate of energy loss is maximum. Towards the end of the alpha particle track, the positively charged particle will slow down to a point where it is able to pick up electrons from the absorber material, thus its charge is reduced to zero and the curve falls off. A schematic of the stopping power of a 5.5 MeV alpha particle in air is shown in Figure 1.2.

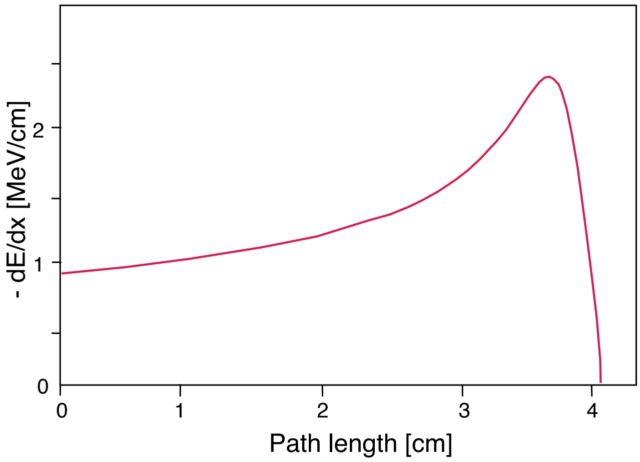

Figure 1.2: Stopping power along an alpha particle (5.5 MeV) track in air, derived from Equation 1.2

Range

The range, R(E), of a heavy charged particle with kinetic energy, T, is related to its stopping power via the expression:

$$R(T) = \int_0^T \left(-\frac{dE}{dx} \right)^{-1} dE \tag{1.3}$$

Equation 1.3 is based on the continuous-slowing-down approximation (csda), where it is assumed a charged particle loses energy continuously along its path, and energy loss fluctuations in collisions are ignored. For practical purposes, R(T) will be referred to from this point onwards as R_{csda}, which represents the average path length of a charged particle as it comes to rest. A list of R_{csda} for alpha particles is provided for a range of absorber materials in the NIST ASTAR database [60], and for the most relevant materials in Appendix A. Alpha particles have very short ranges, considerably less than a photon or electron of a similar energy as a consequence of their high linear energy transfer. Penetration depths for a 5.5 MeV alpha particle range from 4.1 cm in air, to 40 µm in polystyrene and even less in ore depending on its composition.

1.4.2 Beta particle interactions with matter

Energy loss mechanism

Beta particles or electrons, like alpha particles, deposit energy by ionising and exciting atoms within a material. In addition, beta particles can radiate x-rays by bremsstrahlung when undergoing acceleration due to proximity to an atomic nucleus (and to a lesser extent in the vicinity of an atomic electron). In contrast to heavier charged particles, a large fraction of the beta particle energy is lost in a single collision as its mass is equal to that of the electrons it interacts with. Additionally, for a given energy, beta particles travel much faster than alpha particles so there is less time for the coulomb force to act on the particle. Hence, beta particles will lose energy at a lower rate, with abrupt deviations in direction often occurring after each collision. These large-angle deflections along a beta particle track cause a transverse spread in energy deposition as the particle propagates forward, until roughly the last 1 keV, where energy deposition is in the forward direction. No Bragg peak is observed for electrons in a given material, as the multiple path deflections completely smear out this feature.

Stopping power

The stopping power expression for beta particles is composed of a collisional and a radiative component. For fast electrons, the collisional component (Equation 1.4) describes the specific energy loss due to ionisations and excitation, and is described by the expression [58]:

$$-\left(\frac{dE}{dx}\right)_c = \frac{2\pi e^4}{m_0 v^2} nZ \left(\ln\frac{m_0 v^2 E}{2I^2(1-\beta^2)} - (\ln 2)(2\sqrt{1-\beta^2} - 1 + \beta^2) + (1-\beta^2) + \frac{1}{8}\left(1-\sqrt{1-\beta^2}\right)^2 \right) \tag{1.4}$$

The terms in the above expression are the same as those in Equation 1.2, with $\beta = v/c$.

The radiative component of the stopping power describes the linear specific energy loss from bremsstrahlung, and is given by:

$$-\left(\frac{\mathrm{dE}}{\mathrm{dx}}\right)_{\mathrm{r}} = \frac{\mathrm{nEZ(Z+1)e^4}}{137\mathrm{m}_0^2\mathrm{c}^4}\left(4\ln\frac{2\mathrm{E}}{\mathrm{m}_0\mathrm{c}^2} - \frac{4}{3}\right) \tag{1.5}$$

From Equation 1.5, it is apparent from the E and Z^2 factors that radiative losses are most important at high electron energies, and in large atomic number materials. Experiments performed throughout this thesis use beta particles with a maximum energy of 2.3 MeV, within low effective atomic number materials (polystyrene and PMMA). The bremsstrahlung yield is thus negligible, and collisional stopping power will be the dominant source of specific energy loss. In relation to alpha particles, the presence of the m_0 factor in the denominator of the multiplicative term outside the brackets means the bremsstrahlung yield will be insignificant for this radiation type.

Range

The range of a beta particle is also defined using the total stopping power, and can be easily found for a range of initial particle energies and absorber materials on the NIST ESTAR database [61], and in Appenix A. Due to the erratic nature of electron trajectories, the stopping power values used to describe their energy loss when they penetrate a material will exhibit large deviations about the mean values. Consequently, the electron range will also generally exhibit large deviations from the mean. The CSDA (Continuous Slowing Down Approximation) electron range describes the path length of an average electron in a material before it stops completely, and for the purposes of this research is considered sufficient in estimating the maximum penetration depth. For an equivalent energy, the ranges of electrons in a given material is typically hundreds of times larger than that of heavy charged particles due to their lower specific energy loss.

1.4.3 Photon interactions with matter

Energy loss mechanisms

Photons, being electrically neutral do not interact with matter and lose energy steadily as they penetrate a material as charged particles do. Interactions of photons with matter occur through the following processes:

- **Photoelectric absorption**: A photon is absorbed by an atom and is completely destroyed. Following this interaction, a photoelectron is emitted from one of the bound shells of the atom with energy $E_{e^-} = h\nu - E_b$, where E_b is the binding energy of the photoelectron. The vacancy in the shell of the ionised atom is replaced by either an outer shell electron or a free electron in the medium, releasing characteristic X-rays in the process.

- **Incoherent (Compton) scattering**: A photon interacts with an initially stationary electron in the absorber medium. The photon is scattered from its original direction, and a fraction of its energy is transferred to the electron.

- **Coherent (Rayleigh) scattering**: As with incoherent scattering, a photon interacts with an electron in the absorber atom, however the photon retains its energy following the scattering event and the atom is neither excited nor ionised. This generally happens at lower energies.

- **Pair production**: Provided the photon energy exceeds twice the rest mass energy of an electron (1.02 MeV), the photon can be converted into an electron-positron pair in the field of an atomic nucleus. Pair production can also occur in the field of an atomic electron, however with much lower probability and with a higher threshold energy (2.04 MeV). When pair production occurs near an atomic nucleus, the photon energy is converted into the mass of the electron-positron pair, plus the kinetic energies of each (the recoil energy of the nucleus is negligible).

Attenuation in matter

The penetration distance of a photon is statistically governed by the interaction probability per unit distance travelled (via the processes listed above), which depends on both the interaction medium and the photon energy. Photon absorption within a uniform material is exponential, with the intensity remaining after penetrating a given material of thickness, x, represented by:

$$I = I_0 e^{-\mu x} \tag{1.6}$$

The linear attenuation coefficient, μ, denotes the interaction probability for a given photon energy and absorber material and has dimensions of inverse length. I_0 and I represent the initial and final photon intensities, and according to Equation 1.6, the transmitted photon intensity is proportional to the initial intensity. By increasing x, the probability of photon removal via any interaction process (photoelectric, scattering etc) increases, as there is a corresponding increase of absorber atoms available for interaction. The neutral charge and zero rest mass of a photon means it is extremely penetrating in comparison with alpha and beta particles.

1.4.4 Radiation sources

The experimental work presented throughout this thesis was performed with a variety of radiation sources. For reference, a brief summary describing the characteristics of each source is presented here.

Alpha particle sources

Americium-241 sealed alpha particle sources were used to evaluate the scintillation response and properties of a range of plastic scintillators in bulk and fibre form. The sealed sources consist of Americium dioxide (AmO_2) mixed uniformly within a gold foil and mounted in stainless steel holder. The Americium atoms are confined to a circular zone, 1.2 cm diameter from which the alpha particles are delivered. ^{241}Am decays predominantly via alpha decay with a low energy, 60 keV gamma ray byproduct. The alpha particle decay energies (and branching ratios) from ^{241}Am are 5.486 MeV (85%), 5.443 MeV (13%), and 5.388 MeV (2%), however the alpha particles emanating from the sealed source will have a lower energy due to attenuation within the thin gold foil covering the active face.

The ^{241}Am sources used for experiments are shown in Table 1.1. Current activities are calculated using the equation $A = A_0 e^{-0.693t/T_{\frac{1}{2}}}$, where A is the current source activity, A_0 is the source activity at the time of manufacture, t is the time elapsed since the source was manufactured, and $T_{\frac{1}{2}}$ is the half life of ^{241}Am (432.2 years).

Source no.	**Year of manufacture**	**Activity when manufactured**	**Current Activity**
1	1978	18 MBq	17 Mbq
2	1978	30 kBq	28 kBq

Table 1.1: ^{241}Am alpha particle sources used for experiments

Beta particle sources

Characterisation of bulk and fibre plastic scintillators was also performed using a range of sealed Strontium-90 beta sources. The active source face is a 1.2 cm diameter alloy of the radioisotope ^{90}Sr and silver which is mounted in a stainless steel holder. Strontium-90 decays with a half life of 28.8 years via β^- decay into yttrium-90, with a decay energy of 546 keV. Yttrium-90 subsequently decays to the stable isotope zirconium-90 with a half life of 64 hours and emission of a 2.28 MeV β^- particle (99.99 %) and a 1.7 MeV photon (0.01%). A list of the ^{90}Sr/^{90}Y sources used are given in Table 1.2.

Source no.	**Year of manufacture**	**Activity when manufactured (MBq)**	**Current Activity (MBq)**
1	1976	0.7	0.28
2	1976	19	6.9
3	1976	778	290.1
4	1985	1480	685.3

Table 1.2: ^{90}Sr beta particle sources used for experiments

Superficial X-ray source

The majority of experiments performed in this thesis used alpha and beta radiation sources, however, a small subset of work has been dedicated to evaluating the response of the scintillating fibres to low energy X-rays. A superficial X-ray (SXR) unit, (Gulmay D3150, Gulmay Medical LTD., UK) was used for this purpose, and was operated with peak voltages between 30 and 150 kV$_p$ and a range of additional filtrations which determine the beam energy spectra. X-ray beams produced by the SXR contain characteristic X-rays and photons produced via bremsstrahlung, hence the beam is heterogeneous in energy. Commonly the photon effective energy is used when describing the energy of X-ray beams, and is defined as the energy of a heterogeneous beam having the same half value layer (HVL) as a homogeneous beam [57]. A list of the relevant beam properties used are given in Table 1.3, with more details discussed in Chapter 7.

Peak Voltage (kVp)	HVL (mm Al)	Effective energy (keV)
30	0.2	14
40	0.5	19
50	1.0	24
80	2.0	29
100	3.0	35
120	4.0	39
120	5.0	43
140	8.0	55
150	0.5 mm Cu	61

Table 1.3: Beam properties of SXR unit

1.4.5 Radiation safety

The experiments performed as part of this thesis involve the use of both sealed and unsealed radiation sources. Safety precautions specific to the radiation type and source were carefully considered for each experiment, a brief discussion of which are provided below.

Sealed sources

- ^{241}Am **sealed sources:** The alpha particles, and low energy gamma rays emitted from the sealed sources pose minimal external risk. Most alpha particles are easily blocked by the dead layer of cells on the skin surface, hence the biggest risk associated with this radiation type is internal. Care is required when handing the sources to ensure the americium alloy is not touched or damaged in order to minimise the risk of ingestion or inhalation.
- ^{90}Sr/^{90}Y **sealed sources:** The beta particles emitted by these sources are more penetrating than alpha particles, and are able to travel up to several mm in tissue. As such, these sources pose a hazard to skin and eyes in addition to being an internal hazard, so are handled with caution. Shielding from beta particles using 1 cm thick Perspex sheets and plastic safety glasses were used where necessary.

  The beta particles from the ^{90}Sr/^{90}Y sources produce bremsstrahlung radiation (X-rays), where the X-ray energy is related to the mean atomic number of the material, Z. High Z materials like lead produce more energetic X-rays than low Z materials like aluminium, for example. Most experiments designed using beta particles used low atomic number materials, and radiation source holders were constructed using aluminium to ensure any bremsstrahlung radiation produced is of low energy. Lead shielding was also used where appropriate to absorb any stray X-rays.

Unsealed sources

- **Potassium chloride (KCl)**: Contains low concentrations of the radioisotope ^{40}K, the majority of emissions from which are beta particles (which are easily shielded by the glass beakers used to contain potassium chloride solutions) and a small fraction of 1.46 MeV gamma rays (which are not considered hazardous at such low concentrations in KCl). Potassium chloride is only toxic if ingested (or injected intravenously) in large quantities, so it is considered safe to handle. The lethal dose (LD_{50}) of orally ingested potassium chloride is roughly 2.5 g/kg, or 150g for a 60 kg adult. Gloves were used when handing potassium chloride, but no other special precautions were necessary.
- **Polonium-210:** Is an alpha particle emitter and is considered extremely dangerous if ingested, inhaled or absorbed. The lethal dose, LD_{50}, for ^{210}Po is less than 1 µg. All polonium solutions were prepared in a fumehood to prevent the risk of inhalation. Fresh surgical gloves were worn at all times when handling the radionuclide, and potentially contaminated labware, has been placed in a sealed labeled waste bag. Experiments have been carefully designed using the minimum amount of equipment and the workspace was kept tidy to avoid accidents and minimise the risk of contamination. All solutions were labeled with the isotope name and activity, and radioactive waste was placed in a designated sealed and labeled waste container.

Experiments performed using the superficial X-ray unit did not require many special precautions. All personnel were in a seperete, shielded room away from the X-ray unit while it was operation.

Further attempts have been made to minimise external exposure with sealed and unsealed sources by:

- Using the source with the smallest practical activity.
- When not in use, sealed sources have been stored in lead holders, and unsealed sources in sealed containers which have been placed securely in a radiation storage room.
- Sealed radiation sources were handled pointing away, and as far as practical from all parts of the body. If it was necessary to remove the source holder, sources were handled using tweezers.
- A personal dosimeter was worn to monitor radiation dose.
- A portable dose rate meter was used regularly to check for any possible radioactive contamination of the working area.

1.5 Scintillation materials

Scintillators are materials which convert energy from radiation into visible or near visible photons. Broadly speaking, scintillators can be divided into two categories: inorganic and organic, with different mechanisms responsible for light production in each. In inorganics, whether the material is crystalline or a glass, scintillation is an effect associated with the band structure of the material, and can be intrinsic (i.e associated with electron-hole recombination) or extrinsic (i.e associated with impurities/defects) in nature.

In organic scintillators (crystals, plastics and liquids), the scintillation light produced is simply fluorescence resulting from the excitation of a single aromatic molecule. In organic crystals, scintillation is an intrinsic effect associated with excitation of the organic molecules of the solid. Plastic and liquid scintillators contain fluorescent organic molecules (fluors) dissolved in a solid polymer matrix or fluid solvent, where each fluor molecule acts as a scintillation centre. Regardless of how light is produced, a good scintillator should ideally possess the following characteristics:

- **High light production efficiency:** The scintillator should convert the kinetic energy of the incident radiation into detectable photons with a high efficiency.
- **Linear energy response:** The light yield of the scintillator should be proportional to the energy deposited by the radiation.
- **High optical quality:** The material should be of good optical quality and transparency (i.e have low absorption) at wavelengths where its scintillation emissions lie to ensure effective light collection.
- **Short decay time:** Short decay times are preferable so signal pulses can be generated quickly and resolved for high counting rate applications.
- **Emission wavelength:** The scintillation emission should lie at a wavelength where it can be efficiently matched to a photodetector and relevant optics.

In reality, no material will meet all these criteria and the scintillator choice for a given application involves a compromise between these and other factors. For example, inorganic scintillators generally have higher light yields than organic scintillators however, decay times are usually much slower.

1.5.1 Inorganic scintillators

inorganic crystals

The scintillation mechanism in inorganic materials depends on the electronic band structure as determined by the crystal lattice of the material. Energy absorption can promote an electron from its normal position in the lower valence band, where it leaves behind a hole, to the upper conduction band of the material. A scintillation photon can then be produced upon return of the electron to the valence band via a radiative transfer. In a pure crystal, this process is very inefficient and typical band gaps are such that photons produced typically lie in the ultraviolet band where optical losses are high. Addition of impurities, called activators, to the inorganic scintillator modifies the material by creating special sites, known as luminescence or recombination centres, in the lattice band gap where electrons can de-excite back to the valence band. Visible photons can be produced during a transition from a recombination centre because the energy from this site to the valence band is lower than the band gap.

The large atomic numbers and high densities of certain inorganic crystals mean they have high stopping powers for low penetrating radiation types such as X and gamma radiation. Hence, inorganic scintillators can be well suited for medical imaging and precision calorimetry in high-energy physics. For example, the inorganic crystals bismuth germanate, and gadolinium oxyorthosilicate have high interaction cross sections for 511 keV gamma rays, making them useful in detecting gamma rays produced by positron annihilation in intravenous tracers used in position emission tomography [92]. The radiation damage resistance, high density and fast response times of certain inorganic scintillators have been exploited for use in high-energy physics experiments [50, 92]. In particular, lead tungstate has been used as a detector element for experiments on the large hadron collider [74].

Alpha and beta particles have shorter ranges than X and gamma radiation in inorganic scintillators, so smaller crystal dimensions are required for their detection. Cerium activated yttrium aluminum garnet, and yttrium aluminum perovskite are fast, chemically and mechanically stable scintillators commonly employed for electron microscopy and counting. These materials have much lower production costs than typical semiconductor detectors and can be assembled in large area arrays to monitor alpha particle activities in radioactive aerosols [87, 88]. Different applications obviously have different demands for scintillator characteristics, however the bulk of applications relating to inorganic scintillators require the basic properties of fast response (<100 ns), high light yield (25,000 photons/MeV), high density and atomic number (hence large absorption coefficient).

Glass scintillators

Although crystalline scintillators are the most commonly used inorganic scintillators, scintillating glasses are also widely used. Glass scintillators, being thermally, mechanically and chemically robust materials, are well suited for operating under harsh environmental conditions, and are most typically terbium or cerium activated lithium silicates and boron silicates. Lithium and boron both lave high neutron cross sections, so are often used for the detection of thermal (slow) neutrons [11, 93]. The main drawback associated with glass scintillators is their low light yield, generally attributed to the inefficient energy transfer between the irregular lattice structure of the glass and the luminescent centre (dopant).

1.5.2 Organic scintillators

Organic materials produce scintillation from molecular energy level transitions, and as such, can occur when the material is in a solid, liquid or vapour state. One of the biggest advantages of using organic scintillators is in the ease at which they can be customised into virtually any geometry, allowing them to be specifically tailored to a given application. The majority of practical organic scintillators contain molecules whose symmetrical properties give rise to what is known as a π electron structure. This electronic structure leads to three types of photon emissions within the material: prompt fluorescence, phosphorescence and delayed fluorescence (see Figure 1.4) . These processes are briefly summarised below with more details given in Section 1.5.3

Fluorescence: This process involves the prompt emission of photons following a transition from the first excited state of a molecule back to the ground state.

Phosphorescence involves a transition to a metastable state of a molecule, where photon emission occurs following a transition back to the ground state. Phosphorescent photons will have longer decay times and wavelengths than fluorescent photons.

Delayed fluorescence involves a transition to a metastable state of a molecule then back to the first excited state following an external excitation (i.e thermal energy). Molecules then decay back to the ground state like normal fluorescence, emitting photons with the same wavelength but longer decay times.

Scintillators are often characterised in terms of the prompt fluorescence light they produce, which should represent the majority of fluorescent emissions. The typical singlet (spin 0) energy states which give rise to prompt fluorescence are shown in Figure 1.3.

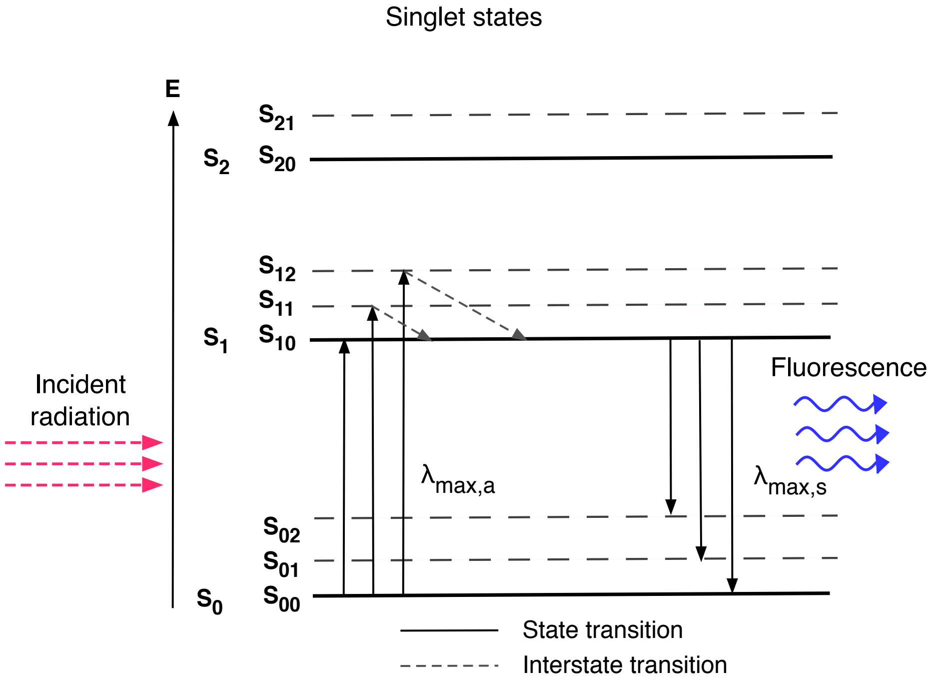

Figure 1.3: Energy level diagram of an organic molecule with π electron structure.

- The S_0 singlet state represents the ground state of the molecule, and is further subdivided into a series of vibrational states, S_{00}, S_{01}, S_{02} etc. Typical spacing between vibrational levels is 0.15 eV, much higher than average thermal energies (0.025 eV) so the majority of molecules at room temperature will lie in the S_{00} state.

- S_1 and S_2 are the first and second excited states of the molecule. Higher energy singlet states exist and transitions to these are only possible if the energy of the incident radiation is high enough. Typically, the energy spacing between S_0 and S_1 is 3-4 eV, with spacing between higher energy levels somewhat less.

- Excitation from the ground level to any vibrational levels of the S_1 (shown in Figure 1.3) or S_2 levels occurs when kinetic energy from radiation incident on the material is absorbed. Any transitions to singlet states S_2 and above are rapidly de-excited back to the S_1 state via radiationless internal conversion. In addition, instability within the system forces interstate transitions from different S_1 vibrational levels to the S_{10} level through radiationless transitions. These transitions are all prompt, and are completed within nanoseconds.

- Scintillation photons are emitted when transitions occur between the S_{10} and any vibrational levels of the ground state (shown as the downward pointing arrows). These photons usually lie in the UV to blue region of the visible spectrum.

- Finally, with the exception of the transition from S_{10} to S_{00}, all transitions have a lower energy than the minimum required for excitation, consequently there is very little overlap between the absorption and emission spectra and hence minimal self-absorption of the scintillation light.

Organic scintillators are available in a variety of forms, the most widely used being plastic, liquid and crystalline scintillators. These materials can be classified according to their composition as unitary, binary or tertiary systems. Unitary systems are pure organic crystals (e.g., anthracene and stillbene), binary systems consist of a scintillating material (fluor) dissolved in an aromatic solvent (e.g. a solvent or polymer base), and ternary systems are composed of two fluors dissolved in a solvent. In ternary systems or wavelength shifting formulations, the light emitted by the primary fluor is absorbed by the secondary fluor and reemitted at a longer wavelength to better match the sensitivity range of a photodetector.

Unlike inorganic scintillators, organic scintillators are composed of low atomic number constituents and as such are less useful for gamma ray spectroscopy without the addition of high Z elements. The majority of applications for these materials are thus based on measurements of alpha and beta particles, fast neutrons and X-rays. Organic crystals such as anthracene and stillbene are very efficient scintillators, with anthracene having the highest light output of all organics. These crystals are fragile, expensive and are difficult to use because of their anisotropic response, so are no longer in widespread use and consequently will not be further discussed.

Liquid scintillators

Liquid scintillators are produced by dissolving an organic scintillator in a solvent, and can be either binary or ternary formulated. As they are typically less expensive than other scintillators, liquid scintillators are often useful when large volume detectors are required such as for neutrino detection [94, 95]. Liquid scintillators are more resistant to radiation damage than plastic and crystalline scintillators [99] because their lack of solid structure limits damage when exposed to intense radiation, however, their transmission properties readily deteriorate in the presence of water and oxygen, so are often sold commercially in sealed glass containers that must be handled with caution.

Liquid scintillators are also widely used for counting radioactive material which can be dissolved within the scintillator solution. In this case, counting efficiencies can reach 100%, as all radiation emitted from the material can immediately pass through and interact with the scintillator. This approach is especially useful for measuring low energy beta particles [19] (particularly from tritium and ^{14}C), as problems associated with other measurement techniques including those relating to attenuation and backscatter of beta particles by detector windows are avoided. Liquid scintillation analysis has also been applied for counting low level alpha particle sources, where the uniform counting geometry and high efficiency of this method offer advantages over semiconductor diode detectors [84].

Plastic scintillators

These are the most widely used class of organic scintillators, possessing several attractive qualities including chemical stability, optical homogeneity and the ability to be formed into virtually any shape or size. Plastic scintillators are created by polymerising a solution containing an organic scintillator in an appropriate solvent, most commonly styrene and vinyltoluene. Many types of plastic scintillator are used for the measurement of low penetrating radiation including low energy X-rays and particulate radiation. They are also becoming increasingly popular for detecting neutrons via neutron induced reactions in the plastic media.

Plastic scintillators are most frequently used as rectangular sheets, with areas ranging anywhere from a few mm^2 to several m^2, with a wide range of applications from beam counters [56] to sampling calorimeters [85]. Although plastic scintillators have low scintillation efficiencies and light yields (hence low energy resolution) for gamma ray detection in comparison to inorganic scintillators, they are ideally suited for high count rate applications where timing properties are crucial and large surface areas are required [16]. Plastic scintillators can also be fabricated as optical fibres, which allows a fraction of the scintillation light to be transmitted over large distances via total internal reflection. These fibres can be used singularly or in arrays and bundles allowing charged particle tracking for certain applications with good spatial resolution [78]. A more detailed discussion on scintillating optical fibres will be given in Section 1.7.

The work presented in this thesis is primarily based on the use of optical fibres fabricated from plastic scintillator, as such discussion from this point forward will be focused on this class of scintillator.

1.5.3 The nature of luminescence produced in plastic scintillators

Scintillation in organic materials is an inherent molecular property arising from the electronic structure of aromatic and conjugated organic molecules following excitation by radiation, as discussed in section 1.5.2. For simple organic molecules, the scintillation emission contains three components: fluorescence, phosphorescence and delayed fluorescence.

Fluorescence

Fluorescence, also referred to as the fast scintillation component, is emitted following a transition from the S_{10} singlet state to any vibrational level of the S_0 state as described in Section 1.5.2. The intensity of the emitted fluorescence is characterised by a fast rise time (≈1 ns) which decays exponentially with time, t, according to the relation

$$I = I_0 e^{(-t/\tau)} \tag{1.7}$$

Where I and I_0 represent the intensities at time t, and t=0, and τ is the decay time of the fluorescence, which is usually on the order of a few nanoseconds for the majority of plastic scintillators. Commercial suppliers, and most published literature, quote rise and decay times for this fast scintillation component without taking into account slower components corresponding to phosphorescence and delayed fluorescence. However, the prompt fluorescence represents the majority of the light yield of the scintillator so this description is adequate for most applications.

Phosphorescence and delayed fluorescence

In addition to singlet (spin 0) states, long-lived triplet (spin 1) states are also present in certain organic molecules, and give rise to the phosphorescent and delayed fluorescent components of the plastic scintillator emissions. Following the absorption of kinetic energy from incoming radiation, a molecule may be excited to the lowest vibrational level of the S_1 state (either directly or after a series of radiationless transitions from higher levels). Instead of decaying to the S_0 ground level and emitting prompt fluorescence, the molecule can undergo a transition to the triplet state T_1 via an intersystem crossing (refer to figure 1.4) and de-excite back down to S_0, emitting phosphorescent photons. The long-lived T_1 state has a radiative lifetime which can range from a fraction of a millisecond to several seconds, and therefore, the emitted phosphorescence will also have a long decay time. As the T_1 state lies below the S_1 state, the phosphorescence will have a longer wavelength than the fluorescence spectrum.

While in the T_1 state, molecules may acquire thermal energy and undergo an intersystem transition back to S_1 then decay through normal fluorescence. This process represents delayed fluorescence, and the emission spectrum is identical to that of the normal fluorescence, however the decay period is increased to ≈ µs or longer depending on the S_1 - T_1 energy gap, the T_1 lifetime etc. A good scintillator should convert as much of the incident radiation energy as possible to prompt fluorescence while minimising contributions from phosphorescence and delayed fluorescence. The prompt

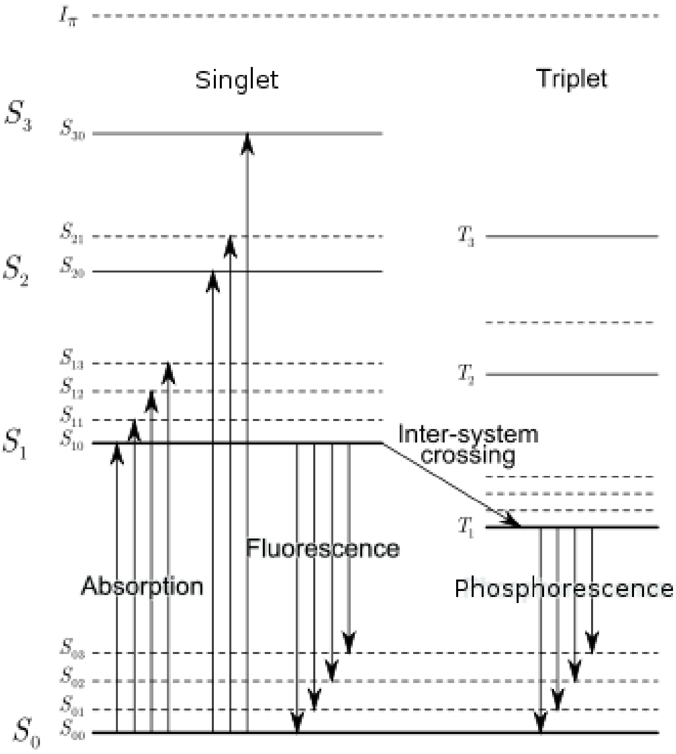

Figure 1.4: Energy level diagram [91] of an organic molecule with π electron structure showing fluorescence transitions and the inter-system crossing leading to phosphorescence emission. Delayed fluorescence occurs following an inter-system crossing back to S1 from T1 which then proceeds as normal fluorescence.

fluorescent component can be isolated and removed from the delayed emissions using pulse height analysis with a photomultiplier tube and appropriate settings of the time constants of the detection electronics. More detail will be provided on this later.

1.6 Optical fibre dosimeters

Optical fibres enable a unique platform for radiation dosimetry, and offer many advantages over conventional detection methods. Notably, information regarding the radiation dose is transmitted optically, as opposed to electrically, and as such, optical fibres are immune to electromagnetic interference that can be a serious issue for electronic dosimeters. The ability for remote radiation monitoring is an additional advantage, as the sensor can be placed a large distance from the readout electronics allowing deployment in harsh environments (i.e. near a nuclear reactor). Finally, their small size and light weight make optical fibres ideally suited for applications in medical dosimetry.

Optical fibre dosimeters are classified as either; intrinsic sensors, where radiation sensing takes place within the fibre itself, and extrinsic sensors, where sensing does not take place within the fibre, but the fibre is used to transmit light from the active material to the detection system. Either class of sensor has its own advantages and disadvantages. Intrinsic systems permit distributed measurements, and accordingly can interact and detect radiation within large regions of an influencing environment. Increased system sensitivity is realised by increasing the fibre length exposed to radiation, however shielding from unwanted signal perturbations can be difficult. Spatially resolved measurements are also made possible using optical time domain reflectometry [82, 47] and time of flight techniques [79]. The ability to measure integrated doses over large areas as well as at fixed positions gives intrinsic fibre sensors unique potential for dosimetry in particle accelerators [42], nuclear waste repositories and storage facilities [28]. Whereas intrinsic sensors have mostly been reported for industrial applications and radioactive environment monitoring, extrinsic fibre sensors have been used extensively for medical applications.

Extrinsic sensors typically consist of a small dosimeter chip (usually a crystal or scintillating material) coupled to a passive optical fibre which serves to guide the optical signal to a detector and where necessary (i.e with OSL dosimeters), to carry optical stimulation to the dosimeter chip. The small detector volume produces negligible perturbation of an external radiation field, leading to high spatial resolutions for point dose evaluations. These features, plus the capability for real-time measurements have lead to widespread use of extrinsic sensors for monitoring patient dose in-vivo, during radiotherapy. The limitations of extrinsic sensors lie in their lack of sensing volume, inability to perform distributive measurements, complications related to sensor-waveguide coupling, and stem effects in some cases.

Regardless of the sensor configuration, the operational principle is similar - ionising radiation encounters a sensitive region of the fibre and induces some change in the materials properties, which is measured to determine the dose. Further classification of optical fibre dosimeters can be made based on their working principles, the most common of which are shown in Figure 1.5.

1.6.1 Luminescence-Based sensors

Radioluminescence dosimeters

Radioluminescence (RL) dosimeters, otherwise known as scintillation dosimeters, operate by detecting the photons produced in a material following exposure to ionising radiation. Their real-time, remote readout capability is especially useful in high radiation level areas where instantaneous dose information is required, such as for radiation protection purposes, monitoring long term nuclear storage, industrial process controls and in medicine.

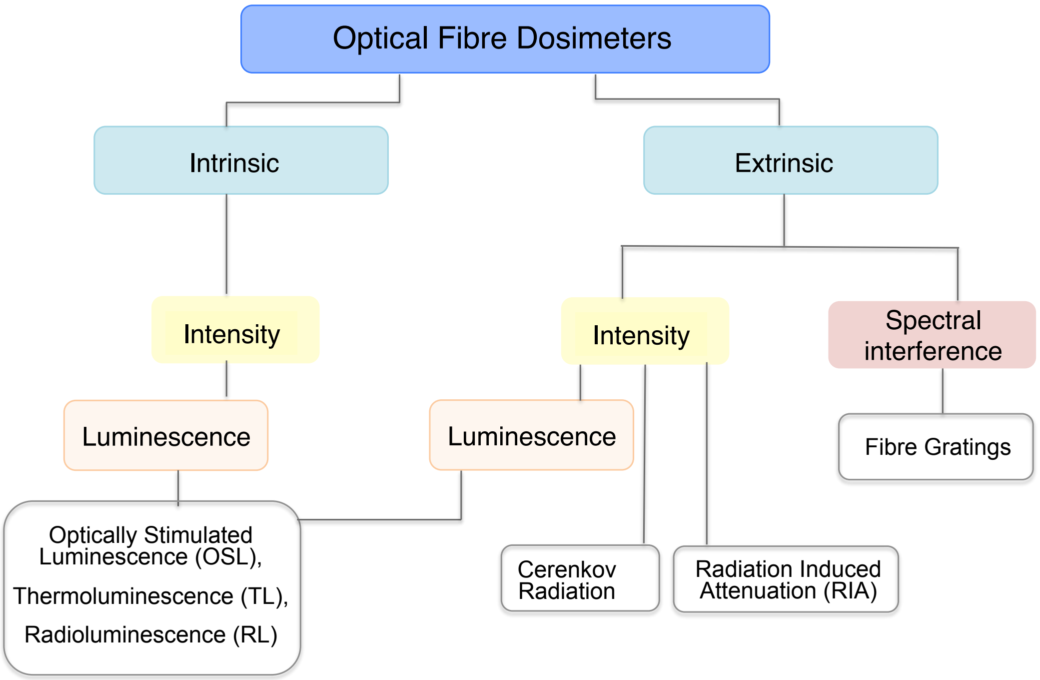

Figure 1.5: Classification of optical fibre based dosimeters

Extrinsic plastic scintillating fibre dosimeters, consisting of a plastic scintillator tip coupled to an optical fibre, are arguably one of the most widely investigated scintillation dosimeters. Plastic scintillators are advantageous for use in radiotherapy dosimetry, owing to their sensitivity, tissue equivalence, dose and energy linearity (for MV photon and electron beams) and real-time response [5, 67]. One of the biggest disadvantages of plastic scintillating dosimeters is their susceptibility to background Čerenkov light, and as such, a significant amount of research has been dedicated to its removal. A number of methods have been successfully implemented for Čerenkov removal including temporal discrimination [18], chromatic removal [33], and the use of a dual, undoped reference fibre [4, 10].

Intrinsic fibre dosimeters fabricated from scintillating plastics and glasses are often fused into bundles or large diameter plates for use in X-ray imaging [49], particle tracking [20] and neutron imaging [80]. The loss of spatial resolution, which would be observed in a bulk scintillator of equivalent dimensions, is avoided as the scintillation signal is confined to the fibre it was produced in.

Thermoluminescence dosimeters

Thermoluminescence (TL) occurs when populations of metastably trapped electrons and holes within defect or impurity sites in certain crystalline materials forms following exposure to ionising radiation. At a later time the material is heated, which allows trapped electrons to escape to the conduction band, in which they diffuse until they encounter a trapped hole and recombine, transitioning back to the ground state via a radiative process. Thermoluminescent dosimeters thus act as a storage device which is capable of retaining dose information until its temperature is raised above a threshold level.

Significant drawbacks to this technique lie in the inability to provide real-time measurements, dose rate information and the requirement to stimulate the material with heat (as opposed to optical stimulation) in order to produce a signal after irradiation. A typical thermoluminescent dosimeter is around 5 mm x 2 mm in area, making it suitable for use in narrow spaces and in-vivo measurements. Fibre-based thermoluminescent sensors have not been studied extensively in the past because of their shortcomings, however they have recently been the focus of much attention and development for potential use in radiotherapy [69, 40, 6]. Specifically, Ge-doped silica materials have been shown to demonstrate good re-usability following thermal annealing, minimal post-irradiation fading, excellent sensitivity and linear response to electrons and x-rays between doses of 1 Gy up to 2 kGy [14].

Optically Stimulated Luminescence

Optically stimulated luminescence (OSL) techniques, like thermoluminescence relies on releasing stored energy within certain materials following exposure to ionising radiation. Unlike thermoluminescence, the material is stimulated optically (instead of thermally) to give off luminescence, a process that makes signal readout significantly faster and more efficient. OSL dosimeters can be re-read multiple times, as only a fraction of the photons are released when optically stimulated, a capability which reduces uncertainty in dose readings. A clear advantage of pairing optical fibre technology with OSL materials is the ability to perform remote sensing. This is realised as the fibre acts to transmit both the optical stimulation (usually a laser beam), and the luminescence signal, eliminating the need to take the dosimeter away for processing.

The most widely used OSL crystal is carbon-doped aluminium oxide ($Al_2O_3 : C$), which is typically coupled onto the end of a commercial silica fibre. Because of its high sensitivity and other favourable characteristics, it is used for low-dose monitoring in personal dosimetry and medical fields [26, 76]. $Al_2O_3 : C$ based extrinsic dosimeters have also provided simultaneous RL/OSL measurements [66], where the RL signal provides real time dose and dose rate information and verification of the post-irradiation OSL dose. Quasi real-time OSL analysis has been demonstrated using single-crystal europium-doped potassium bromide ($KBr : Eu$) coupled to an optical fibre [35]. A pulsed laser beam was used to periodically stimulate the KBr:Eu crystal, and collect the luminescence signal during the laser off period, however the luminescence was found to demonstrate a temperature dependence and post-irradiation fading.

Recently SiO_2 [27] and fluoride phosphate glass [55] have been investigated as an intrinsic OSL sensors for dose ranges between 7-177 Gy and 0.16-2 Gy respectively. These sensors do not provide a tissue equivalent dose as their absorbing and scattering properties are too dissimilar from biological tissue, hence these dosimeters are best suited to industrial and process control applications, where remote distributed sensing is required.

1.6.2 Other optical fibre-based dosimeters

Radiation Induced Attenuation (RIA)

Radiation induced attenuation, or photodarkening, occurs when ionising radiation interacts with dopants, impurities, or defects in a material structure to produce colour centres which absorb light and decrease the transmission of an optical fibre. This photodarkening effect can be used as a sensing mechanism for optical fibre-based dosimeters by monitoring the transmission of the fibre, which can be correlated to radiation dose [37, 3]. Determination of absorbed dose using this technique is complicated by the fact the darkening effect is not permanent and tends to decrease with time, approaching a steady state value post irradiation. Silica fibres, reported as being the least sensitive to radiation are usually doped with ions such as aluminium, germanium, lead or phosphorus to assist with colour centre formation and thus increase their sensitivity [48]. In particular, phosphorus doped fibres, due to their superior temperature stability, sensitivity and linear response at certain wavelengths, have been identified as a promising candidate for integration within a variety of radiative environments including particle accelerators [42] and space programs [2].

Čerenkov dosimeters

Čerenkov radiation is produced when charged particles exceed the speed of light in a material. This luminescence effect is typically regarded as a noise signal in optical fibre dosimetry as its intensity depends on the incident angles and energies of the charged particles, and the irradiated fibre length [52].

The plastic scintillating fibre dosimeters used extensively in radiotherapy suffer from a non-proportionality between absorbed dose and scintillation output for densely ionising particles as they are thought to produce a quenching effect via damage to the scintillator molecules. It is known that this quenching effect, causing a decrease in scintillation output, becomes more pronounced with high LET radiation and subsequently limits their use for heavy charged particle dosimetry. A Čerenkov dosimeter, consisting of a non-scintillating polymer optical fibre (PMMA) has been proposed to overcome these drawbacks, and has proved effective as a dosimeter in proton therapy [54]. Čerenkov radiation is not generated by scintillator molecules, so there is no ionisation quenching effect to account for, and the measured light intensity can be related to the particle flux interacting with the fibre. The same technique has been applied for photon dosimetry [96] and thermal neutron detection [53] by pairing a non-scintillating polymer fibre with a gadolinium (Gd) converter material.

Fibre Bragg Grating (FBG) dosimeters

Fibre Bragg Grating dosimeters operate by monitoring the shift of the Bragg wavelength caused by external perturbations such as temperature, strain and ionising radiation. The majority of published work has focused on the development of radiation resistant FBG's for measuring temperature and strain in nuclear environments [29, 30]. FBG's written in Ge-doped silica fibres have proven effective for use in high dose applications up to 2 kGy [59], however these sensors have limited applicability in industrial environments as measurements were heavily affected by operating temperature fluctuations and set-up instabilities. Fibre Bragg Grating cavity reflectors have also shown promise for monitoring low radiation doses (2 Gy), but are currently of limited use as the interrogation system does not allow for real time measurements [65].

1.7 Detection of scintillation photons

Despite the large light production efficiencies of common plastic scintillator formulations ($\approx$ 8000 photons per MeV deposited electron energy), the number of photons captured and transmitted to the photodetector is typically only a few to tens of photons after the average energy deposition in the fibre volume, the capture fraction and fibre attenuation is taken into account. Regardless of the weak light output from scintillating fibres, it is possible to construct an efficient radiation sensor by using a highly sensitive photodetector in conjunction with appropriate detection electronics. In addition to sensitivity at a given wavelength, a variety of disparate factors need to be considered when selecting an appropriate photodetector, including the active area, time response, detector cost and the minimum acceptable signal-to-noise ratio.

1.7.1 Photodetectors

Most notably, scintillation photons are detected using either photomultiplier tubes or photodiodes. The excellent low-light level response, low-noise and fast rise-time of photomultiplier tubes make them the most widely used detectors for scintillation counting. Bialkali photomultiplier tubes are typically sensitive in the wavelength range between 200 to 600 nm, which is where the majority of organic scintillator emissions lie, however the drawbacks of these detectors lie in their lack of portability and ruggedness. A solid state alternative to the photomultiplier tube are the silicon based avalanche photodiodes (APD), which unlike the photomultiplier tube are compact, rugged, have lower power consumption and offer an extended wavelength response with quantum efficiencies reaching 90 % in the visible. Another recent technological innovation has been the development of a Geiger mode avalanche photodetector (also called a silicon PM, SiPM) which is able to detect single photons like a photomultiplier tube, but with much greater energy resolution. A comparison of an Electron Tubes (ET) 9829B photomultiplier tube, a Thorlabs 120A2 silicon avalanche photodiode (both which were on-hand for experiments) and a Hamamatsu 513360-6075PE Silicon photomultiplier is presented in Table 1.4.

	PMT	**APD**	**SiPM**
QE(%)			
400 nm (blue)	28	50	43
500 nm (green)	15	70	48
Gain	10^6	50*	4×10^6
Threshold sensitivity	1 p.e	≈ 10 p.e	1 p.e
Noise	300 cps	not listed in cps	2000 kcps
Active diameter	46 mm	1 mm	6 mm
Operating voltage	800-1200 V	± 12 V	± 3 V

Table 1.4: Comparison of specifications for a ET 9829B photomultiplier tube, a Thorlabs UV enhanced 120A2 silicon avalanche photodetector (APD), and a Hamamatsu 513360-6075PE SiPM. p.e = photoelectron
* = Gain at 650 nm.

Despite the attractive properties of APD's and SiPM's, bialkali photomulitplier tubes offer significantly larger active detection areas which will be compatible for coupling to the fibre bundles used in the later stages of this project. The low noise and high internal gain of the ET9829B PMT provides excellent signal-to-noise ratios which offset its low quantum efficiency, and as a result this detector has been chosen for use in all fibre based scintillation experiments presented in this thesis.

1.7.2 Signal processing and detection electronics

With respect to radiation detection and measurement, the two most important characteristics of the detector output are its amplitude and timing information. Certain applications like particle tracking require precise pulse timing information, whereas in energy spectroscopy the amplitude of the detector pulse is required to gather information about the energy of the radiation. In this case, the amplitude of the detector signal is of importance as it permits the isolation of specific energy radiation events from background noise. In order to extract the amplitude information from the detector signal, a few analogue and digital processing steps are first required.

In response to scintillation photons arriving at the active detector face (photocathode) of the photomultiplier tube, a current pulse will be produced at its anode with a total charge that is proportional to the energy deposited by the radiation in the scintillator. This current pulse typically has a very short duration and low amplitude, which makes direct measurements of each parameter difficult and error prone. For spectroscopic applications such as scintillation counting, the detector signal is fed to a charge-sensitive preamplifier where it is converted into a voltage signal. Subsequently, this signal is processed and analysed with a shaping amplifier and multichannel analyser (MCA) as shown in Figure 1.6. The function of each signal processing stage is summarised below.

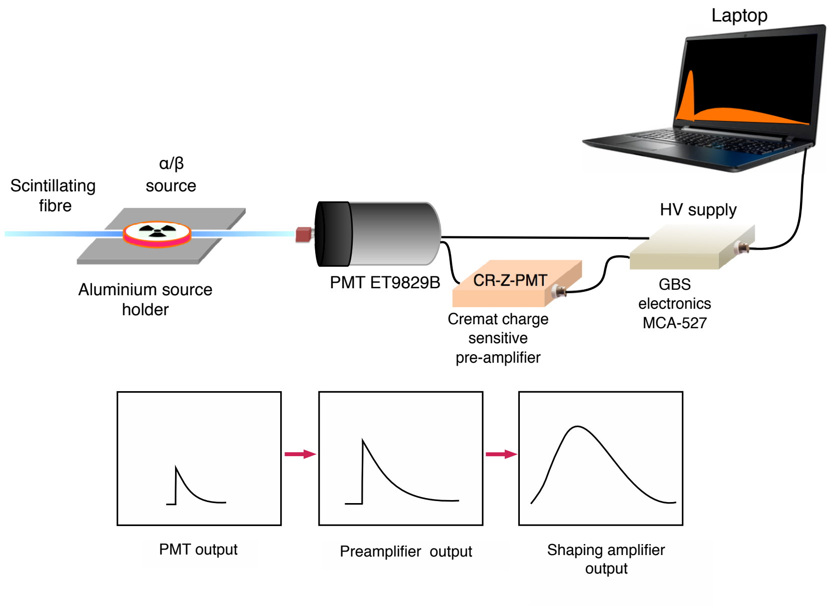

Figure 1.6: Setup used for fibre scintillation detection. Photons produced within the scintillating fibre are detected with a photomultiplier tube which outputs a current pulse. The pulse is fed to a charge sensitive pre-amplifier where it is converted to a voltage pulse, then amplified and widened making it suitable for subsequent electronic processing. The shaping amplifier further amplifies the voltage pulse and shapes it to improve energy resolution and reduce pulse pile up. The pulse height is then digitized and sorted using the MCA.

Preamplification stage: The current pulse from the PMT is fed to a charge-sensitive preamplifier where it is amplified and widened, making it suitable for processing by the subsequent electronic circuitry. The output signal is a voltage pulse whose height is proportional to the total charge, hence energy deposited in the scintillator.

Shaping amplifier: The primary purpose of the shaping amplifier is to amplify the pulse from the preamplifier to facilitate pulse amplitude measurements by the MCA. In addition to being amplified, high and low pass filters are applied to shape the pulse in order to improve energy resolution and prevent overlap between successive pulses (pulse pile-up).

Multi-channel analyser (MCA): As the output pulse height is proportional to the energy deposited by the radiation in the scintillator, it is implied that the energy distribution of the radiation can be determined by counting the different pulse amplitudes. The multi channel analyser takes the output signal from the shaping amplifier, digitises the pulse height, then places it as a count in a corresponding energy bin. The spectrum of pulse heights can then be displayed and analysed on a computer screen, further details of which are provided in Chapter 4. For this work, a GBS electronics MCA-528 was used which contained the shaping amplifier and battery powered high voltage supply for the photomultiplier tube. Given the portable nature of the high voltage supply, the experimental setup for optical fibre radiation measurements is easily transportable for field measurements.

1.8 Summary

The research presented in this thesis aims to produce two prototype intrinsic optical-fibre based sensing devices to prove the concept of detecting low levels of radionuclides in liquids using the mechanism of scintillation within the fibres. The intrinsic configuration of these devices allow large volumes of radionuclide containing liquids to be rapidly sampled at sufficient sensitivity to detect down to levels of 1 Bq/ml of ^{238}U. The proposed detection method offers many advantages over existing techniques, as the sensor can be placed directly in the processing liquids enabling direct, in-situ measurements and eliminating the need for lengthy off-site analysis. The production of scintillation light is prompt (ns), and readout can be performed with a simple, portable detection system allowing measurements to be performed in real time on a continuous basis at the optimum locations within the mineral processing plant or medical environment.

The chapters presented in this thesis outline the work that has been undertaken to help achieve the project goals. In Chapter 2, a variety of plastic scintillators have been characterised in order to determine the most favourable formulation based on its radiation response and optical and material properties. A blue-emitting plastic scintillator, EJ204, was deemed to be the most promising candidate and was selected for fibre drawing trials. Chapter 3 presents the work performed to fabricate optical fibres from plastic scintillators. Fibres were fabricated with an outer diameter of 160 µm to facilitate alpha particle detection, and 1 mm fibres for beta particle and X-ray detection. The fibres fabricated in-house, and a range of commercial scintillating fibres are characterised in terms of their alpha and beta radiation response characteristics and optical properties in Chapter 4. An outer cladding was shown to give the optical fibres superior optical properties and proved essential for use under the proposed environmental conditions. This limited the fibre types available for incorporation into sensor devices to commercial fibre varieties, as a method to consistently fabricate optical fibres in-house with the required cladding thicknesses had not yet been established.

In Chapter 5, the performance of the scintillating fibres are tested under environmental conditions analogous to those which will be encountered during mineral processing. Minimal degradation of the fibres are observed at elevated temperatures within acidic solutions, indicating the suitability of these materials for long term, continuous operation. Prototype devices for alpha and beta particle detection were constructed and tested in radionuclide containing solutions in Chapter 5. Device improvements were made and detection limits below 1 Bq/ml of the relevant isotopes were achieved, however polonium-210 contamination was found to produce elevated background readings in the alpha sensing device.

An investigation into the adsorption behaviour of polonium-210 was conducted in Chapter 6. A range of fibre coatings to prevent contamination were explored and proved ineffective, however the ^{210}Po accumulation rate on the alpha sensor was found to quickly stabilise in solution. Periodic removal of the alpha sensor from mineral processing solutions to measure background contamination levels was explored as a possible measurement technique and would allow the sensor to be operated near-continuously. Final alpha and beta sensing fibre bundles were created and tested in mixed radionuclide solutions. The beta sensing device was able to accurately measure the concentration of beta emitting radionuclides in a mineral processing solution, however substandard commercial optical fibres in the alpha sensing device has limited its ability to accurately measure the concentration of alpha emitters in solution.

Finally, the 1 mm fibres which had been fabricated in-house have been coupled to non-scintillating waveguides in an extrinsic configuration in order to test their response to low energy X-rays (see Chapter 7) for medical applications of this thesis. Of all the scintillators tested, EJ204 was found to have the lowest energy dependence, making it most suitable for radiation dosimetry in the tested energy range.

Chapter 2

Material and optical characterisation of plastic scintillators

The selection of a material for low level radiation detection is largely concerned with the sensitivity to the radiation types of interest, and hence is the first material property investigated before further characterisation and testing is performed. A small selection of potentially appropriate materials including doped glasses and plastics were tested by looking at their scintillation response to alpha and beta radiation, the results are presented in Section 2.1, where a plastic scintillator (EJ204) displayed the best performance. Following initial sample screening, a range of optical and material characteristics of a variety of plastic scintillators are evaluated in order to identify the most appropriate candidate for the project goals and fibre fabrication as outlined in Chapter 3.

2.1 Initial sample survey

An initial survey was performed to find materials with appropriate scintillation response to alpha and beta radiation and that could be drawn into optical fibres at a later stage. The materials tested included:

- Tb^{3+} and Mn^{2+} doped fluoride phosphate glass
- PET plastic drink bottles [70]
- EJ204 plastic scintillator from ELJEN technologies

Samples were placed in the chamber of a Princeton Instruments SpectraPro 2300i spectrofluorimeter, and irradiated using a 290 MBq $^{90}Sr/^{90}Y$ beta source, and a 17 MBq Am^{241} alpha particle source. The scintillation light produced was collected and focused onto a fibre using a fused silica lens which guides it into a thermoelectrically cooled (1024 × 256 pixel) CCD coupled monochromator. The emission spectra for each sample wsd collected over the full sensitive detector range (200 - 1000 nm) using 60 s integration times. The PET plastic and Mn^{2+} doped fluoride phosphate glass showed no detectable scintillation, and Tb^{3+} doped fluoride phosphate produced detectable scintillation emissions under beta, but not alpha irradiation. The best performing material was the ELJEN plastic scintillator, which produced clearly detectable scintillation emissions, with good signal-to-noise ratios under both alpha and beta particle irradiation so it was selected for further testing.

2.2 Plastic scintillator varieties

The plastic scintillator EJ204 appears the most promising for purposes of this project of the materials tested in 2.1. In addition to its high light output in response to both alpha and beta radiation, the material has a fast response time, can be extruded and drawn into fibres at low temperatures [44]. The fibres produced were much more flexible than glass fibres, and a cheaper alternative than doped glasses in terms of material and processing costs. Several varieties of plastic scintillators are commercially available in a range of shapes, sizes, and formulations suited for different applications. Plastic scintillator formulations differ mainly in:

- **Scintillation efficiency**: Defined as the number of photons produced in the material per MeV energy deposited by a minimum ionising particle.
- **Decay time**: Defined as the time taken for a scintillation light pulse to decay to 1/e of its maximum height, and is usually on the order of 2-20 ns. Decay times stated by the manufacturer are usually characterised by the fast scintillation

component. Although this represents the majority of the scintillation emission, there is also a slow component with decay times of up to 100's of µs. Short decay times are required for high counting rate and timing applications.

- **Attenuation length**: The length of material over which the scintillation light is attenuated to 1/e of its original value. The intensity of the scintillation light is reduced as it propagates through the material due to several effects, which will be discussed later. The cumulative effects of these processes are quoted as a single value, L_{att}. Long attenuation lengths are desirable, especially if extended lengths of scintillating materials are to be used.
- **Peak emission wavelength**: Defined as the wavelength corresponding to the peak intensity of the scintillation emission spectrum, and is of importance for choosing an appropriate photodetector.
- **Wavelength shifting formulations**: Wavelength shifting plastics usually have absorption bands in the blue region of the visible spectrum where most scintillators have prominent emissions, so are able to absorb this scintillation light and re-emit at a longer wavelength to better match the spectrum with the sensitive wavelength regions of certain detectors. The probability that one wavelength shifted photon will be emitted per absorbed photon is represented by the quantum efficiency, QE, of the material. High QE's are required for preservation of information carried by the original scintillation photons.

The vast differences in scintillator formulations alone provide motivation for testing a larger range of materials than just the EJ204, so several more plastic scintillators (Table 2.1) were sourced from ELJEN Technologies and Saint-Gobain. Polystyrene based bulk plastic in the form of 1 and 3 cm diameter cylindrical rods from ELJEN Technologies were obtained in a high and low molecular weight formulation to extrude and draw customised optical fibres in-house, as the range of fibres available commercially are more limited in size and scintillator type. Some scintillating polymer fibres are available from Saint-Gobain, and these have also been sourced and used for comparison with the in-house drawn fibres.

The properties listed in Table 2.1 for the ELJEN plastics relate to the standard polyvinyltoluene (PVT) based scintillators. The scintillators sourced for this project are all polystyrene based due to its more consistent fibre drawing properties [44], higher softening point and increased hardness in comparison to PVT [13]. According to the manufacturer, the bulk optical properties of polystyrene and PVT are very similar, however polystyrene based materials have approximately a 15% lower scintillation efficiency [46]. Values listed for the scintillation efficiency, γ, below have been corrected (i.e multiplied by 0.85) to account for this, however the exact scintillation efficiencies have not been measured.

Scintillator	**Manufacturer**	**OD (µm)**	L_{att}**(m)**	$\boldsymbol{\gamma}$	$\boldsymbol{\lambda}_{peak}$ **(nm)**	τ **(ns)**
BCF 10 (F)	Saint-Gobain	1000	2.2	8000	432	2.7
BCF 12 (F)	Saint-Gobain	250, 1000	2.7	8000	435	3.2
BCF 20 (F)	Saint-Gobain	250, 1000	> 3.5	8000	492	2.7
BCF 60 (F)	Saint-Gobain	1000	7,100	3.5	530	7
BCF 91a* (F)	Saint-Gobain	1000	N/A	3.5	494	12
BCF 92* (F)	Saint-Gobain	1000	N/A	3.5	492	2.7
EJ 204 (B)	ELJEN	3 cm, 1 cm	1.6	8,840	409	1.8
EJ 240 (B)	ELJEN	1 cm	2.4	5,355	435	230
EJ 260 (B)	ELJEN	1 cm	3.5	7,820	490	9.2
EJ 262 (B)	ELJEN	1 cm	2.5	7,395	481	2.1
EJ280* (B)	ELJEN	1 cm	3.5	N/A	490	9.2
EJ284* (B)	ELJEN	1 cm	N/A	N/A	608	14

Table 2.1: (B)=Bulk plastic, (F)=Fibre, **OD**: Outer diameter of fibre or bulk cylinder, $\boldsymbol{\lambda}_{peak}$=Wavelength corresponding to the scintillation emission maximum as specified by the manufacturer, $\mathbf{L_{att}}$=Attenuation length, defined as the length of fibre where the signal amplitude is attenuated to $\frac{1}{e}$ of its original value (manufacturer specified), $\boldsymbol{\gamma}$=Manufacturer specified scintillation efficiency, defined as the number of photons produced within the material per MeV of deposited energy by a minimum ionising particle, $\boldsymbol{\tau}$ = Manufacturer specified scintillator decay time. N/A = not specified by manufacturer.

Light production efficiency is arguably one of the most important properties of a plastic scintillator when designing a radiation sensor. It places restrictions on the maximum useable fibre length, the detection efficiency, minimum detectable radionuclide activities, and hence the overall effectiveness of the device. However, the light production efficiency alone does not determine how effectively a radiation sensor will perform under any given circumstance: the optical attenuation characteristics and the matching of scintillation emission to an appropriate photodetector must also all be considered when selecting an appropriate material. In the sections that follow, a range of characterisation experiments are performed using each plastic scintillator variant to determine which formulation has the most desirable characteristics overall. In section 2.3, selected optical and material properties of the scintillators are investigated.

2.3 Preliminary optical and material characterisation

The emission and absorption spectrum of a plastic scintillator are critical properties to characterise as they will impact upon the choice of photodetector and determine the degree of transparency of the material to its own fluorescence emission. The transparency of the material will influence the maximum practical length of optical fibre for incorporation within the radiation sensor and requires minimal overlap between the emission and absorption regions, both of which are characterised and presented in section 2.3.

2.3.1 Bulk plastic emission and absorption spectra

The emission spectrum of a plastic scintillator is of importance when choosing an appropriate readout device. The quantum efficiency (QE) of a detector is usually highly wavelength dependent so the emission peak of the scintillator should be closely matched to the wavelength corresponding to the maximum detector QE. Further, to ensure efficient light transmission over extended fibre lengths it is desirable to choose a scintillator with minimal overlap between its absorption and emission bands as this causes self-absorption and a decrease in intensity of the generated fluorescence as it propagates through the material. Emission and in some instances, absorption data of the scintillators are offered by the manufacturers, however they are specified over a limited wavelength range and can be affected by inconsistencies in product formulation. Measurements were performed to obtain emission and absorption spectra for each scintillator over an extended wavelength range to look for any major discrepancies with manufacturers data.

Absorption measurements were performed using a Agilent Cary 5000 UV-Vis-NIR spectrophotometer in transmission mode, however measurements could only be performed on samples of bulk plastic as the input beam within the sample chamber is unable to be focused into a fibre core. Emission spectra were obtained as in Section 2.1 with a Princeton Instruments 2300i spectrofluorimeter using a 7 MBq ^{90}Sr/^{90}Y beta source, and for wavelength shifting plastics and 250 µm diameter fibres, a 290 MBq ^{90}Sr/^{90}Y source was required to improve signal-to-noise ratios. Slight variations in the setup were required depending on whether the scintillator was in fibre or bulk form so results are presented separately. Emission and absorption measurements were performed using polished 3 mm thick slices cut from low molecular weight varieties of each bulk cylinder, with the results shown in Figure 2.2. Absorption data was found to match that provided by the supplier (where supplied).

The major emission peak locations for each scintillator vary at most by a few nm from the manufacturer specified values - an effect caused by attenuation. Shorter wavelength emission components are attenuated more rapidly in the material than longer wavelengths causing an apparent shift in the peak location towards longer wavelengths with increasing plastic thickness/fibre length. Such an emission shift would be observed by taking a measurement with thicker sample of material than used by the manufacturer. Based on the emission and absorption spectra, EJ204 appears most promising for further study, it has the highest light yield of all scintillators, minimal overlap between the absorption and emissions bands, with emissions lying within the sensitive region of a bialkali photomultiplier tube (Fig 2.1).

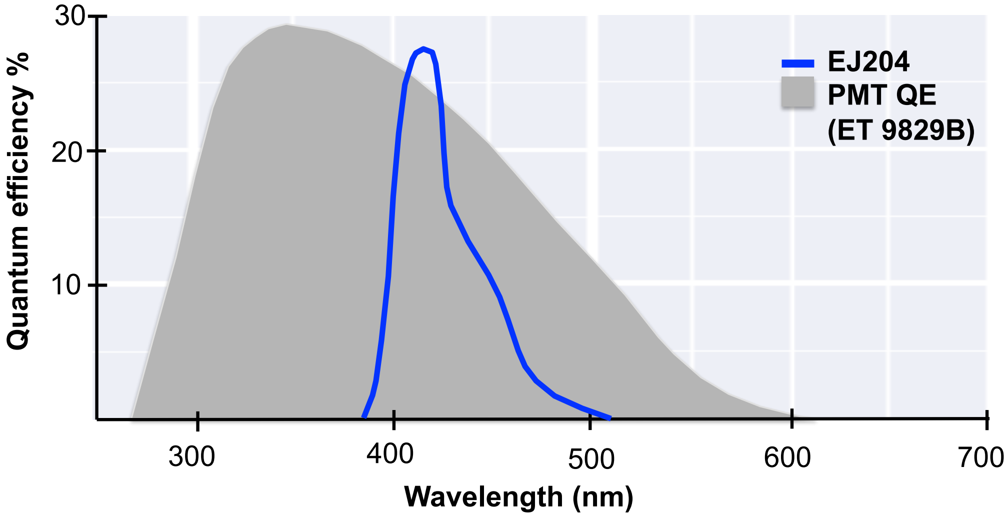

Figure 2.1: Quantum efficiency curve for ET 9829B PMT shown with emission spectrum of EJ204

2.3.2 Optical fibre emission spectra

Whether in bulk or fibre form, the emission spectrum for a given scintillator formulation will be the same apart from any absorption effects, as will be discussed in detail in Chapter 4. Fibre emission spectra were collected by irradiating the mid-point along a 10 cm long fibre sample with a ^{90}Sr/^{90}Y beta source. One end of each fibre was blackened to eliminate back-reflections and the emission was collected from the opposite end by coupling the polished fibre output to the collection lens within the sample chamber of the spectrophotometer. No differences in emission spectra were observed between bare and cladded fibre varieties, or between 1 mm and 250 µm OD fibres indicating the fibre geometry has no detectable effect on the emission characteristics. Emission spectra are presented in Figure 2.3 for the 1 mm cladded fibre varieties. Comparison of emission peaks to manufacturer provided data are in good agreement, displaying 5 nm variations at most. Both BCF10 and BCF12 appear good candidates for comparison with fibres

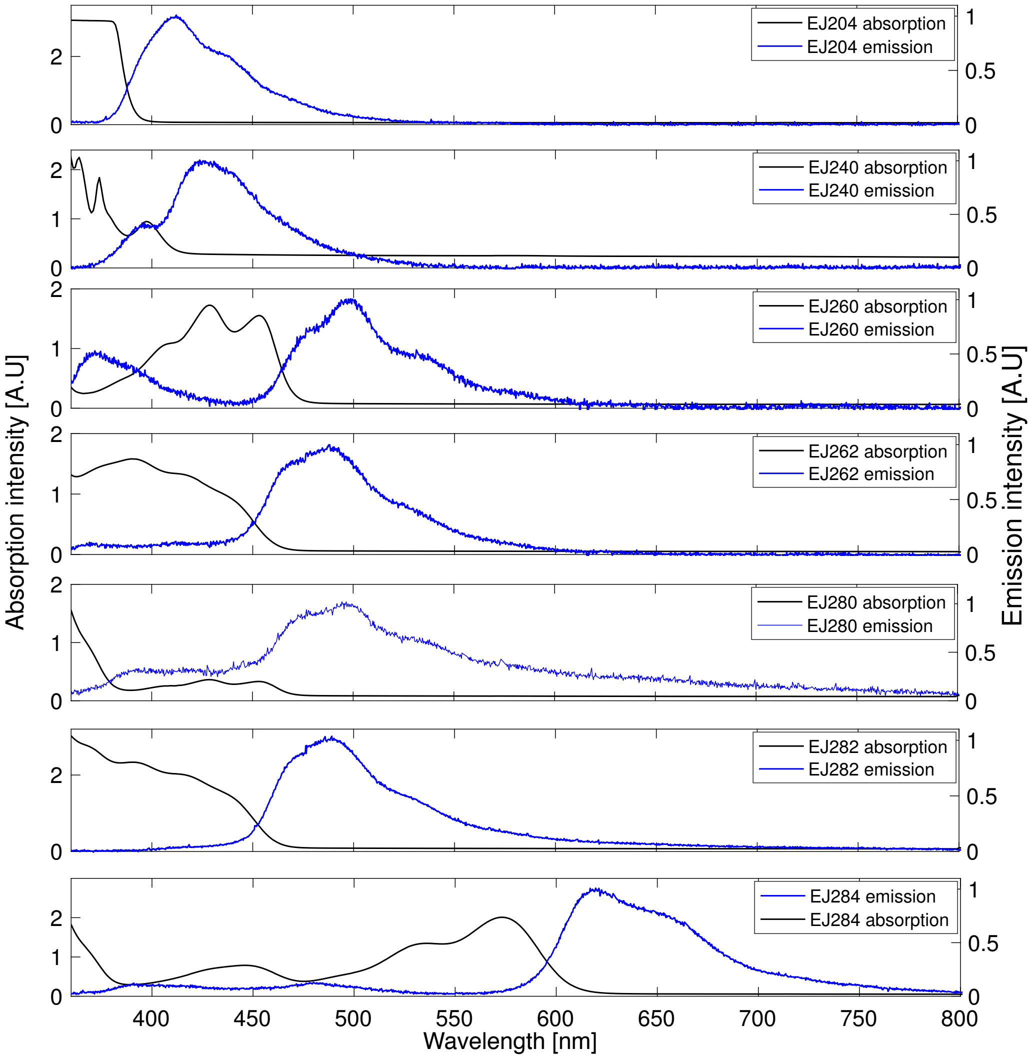

Figure 2.2: Emission spectra (excited by ^{90}Sr/^{90}Y beta radiation) and absorption spectra (measured using a spectrophotometer) of bulk, low molecular weight ELJEN plastic scintillators

which were drawn from EJ204 as they possess similar emission characteristics and scintillation efficiencies.

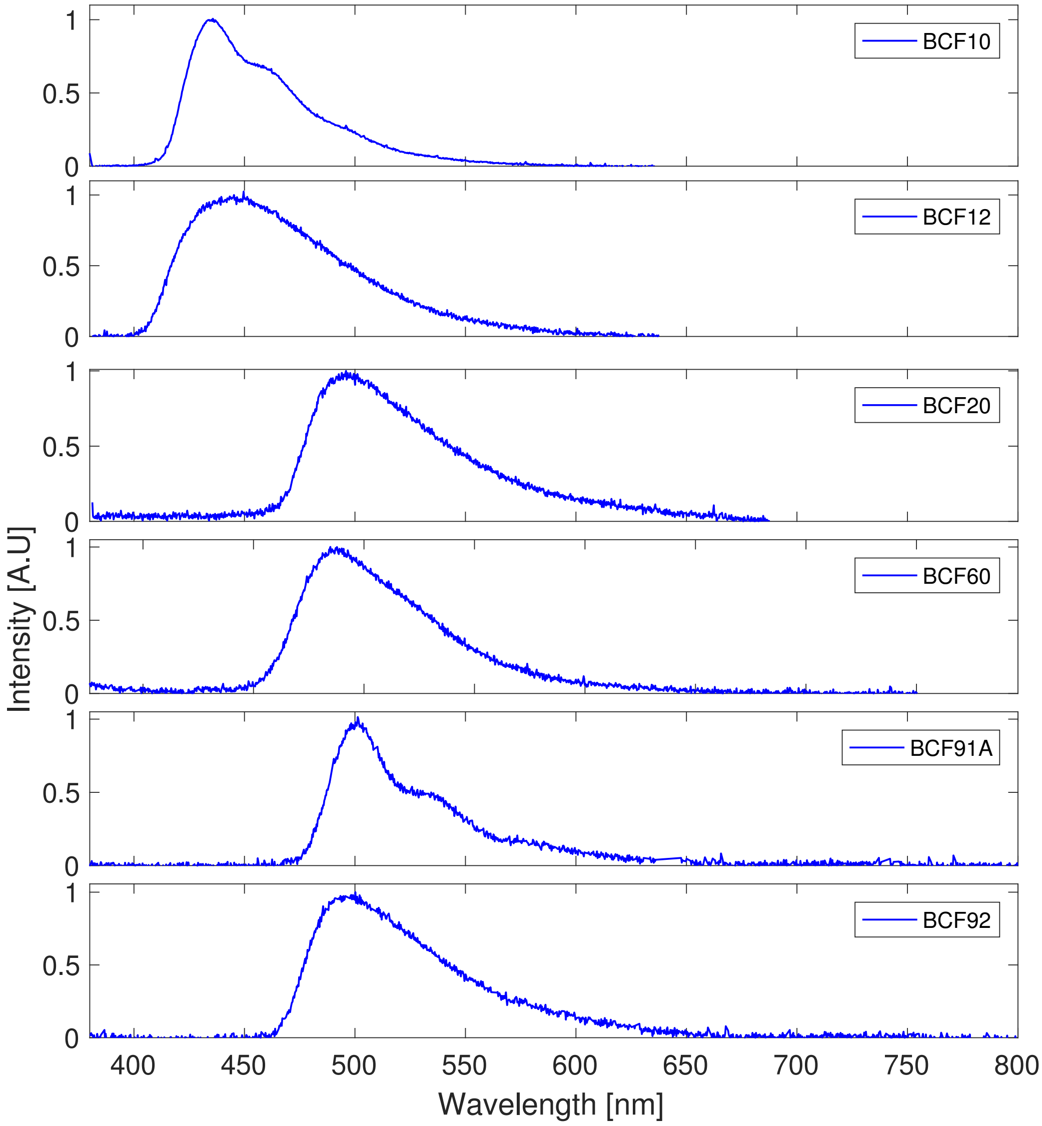

Figure 2.3: Emission spectra of Saint-Gobain scintillating fibres.

2.3.3 Polymer molecular weight effects

The molecular weight of a polymer is a representation of the length of individual polymer chains in the material and is an important parameter related to many physical properties including mechanical strength, flexibility, temperature resistance, and deformation ability. Given the molecular weight of each polymer chain, $\mathrm{M}_i(i = 1 \rightarrow \mathrm{x})$, and the total number of polymer chains, $\sum_{i=1}^{\mathrm{x}} \mathrm{N}_i$, the total molecular weight will be $\sum_{i=1}^{\mathrm{x}} \mathrm{N}_i\mathrm{M}_i$. A common way to define the molecular weight of a polymer is using the number average molecular weight, $\mathrm{M_n}$, which represents the statistical average molecular weight of all polymer chains, and is defined by:

$$\mathbf{M_n} = \frac{\sum_{i=1}^{x} \mathrm{N}_i \mathrm{M}_i}{\sum_{i=1}^{x} \mathrm{N}_i}$$

High and low molecular weight samples of each bulk plastic scintillator with dimensions 12 mm dia × 125 mm length were obtained for extrusion and fibre drawing trials to determine which formulation produces optical fibres with superior optical and mechanical properties. Prior to fibre drawing trials, the effect of the polymers molecular weight on the emission/absorption spectra and the glass transition temperatures are investigated. The molecular weights of the plastics are not precisely known, but the manufacturer reported only LMW polymerisations of PVT to average around 350,000 units and the HMW polymerisations to average around 450,000 units, with a similar distribution expected for polystyrene [45].

Effect of molecular weight on emission and absorption spectra

To determine if molecular weight has any effect on the absorption and emission spectra of the scintillators, measurements as described in 2.3.1 were repeated using the high molecular weight scintillator formulations. No differences were observed in the intensities or spectral shape of the absorption and emission spectra between different molecular weight formulations of the same scintillator, with the exceptions of EJ260 and EJ280 (Fig. 2.4). For these two scintillator formulations, the high molecular weight variety showed a larger emission intensity with an increase in peak photon counts of 25% and 10% observed for EJ260 and EJ280 respectively, compared to the equivalent low molecular weight scintillator. An increase in peak absorption intensity of 39% (430 nm) is observed in the low molecular weight EJ260, and a 11% decrease in peak absorption intensity for the low molecular weight EJ280 at 430 nm.

The measured absorption and emission intensities are sensitive to numerous factors relating to sample preparation and reproducibility of the experimental setup. The sample thickness, surface finish, and particularly for absorption measurements, the degree to which both sample surfaces are flat and parallel can all have an effect on the measurements. It is feasible that these differences and changes in the sample placement within the measurement chambers caused the discrepancies observed between the different molecular weight samples.

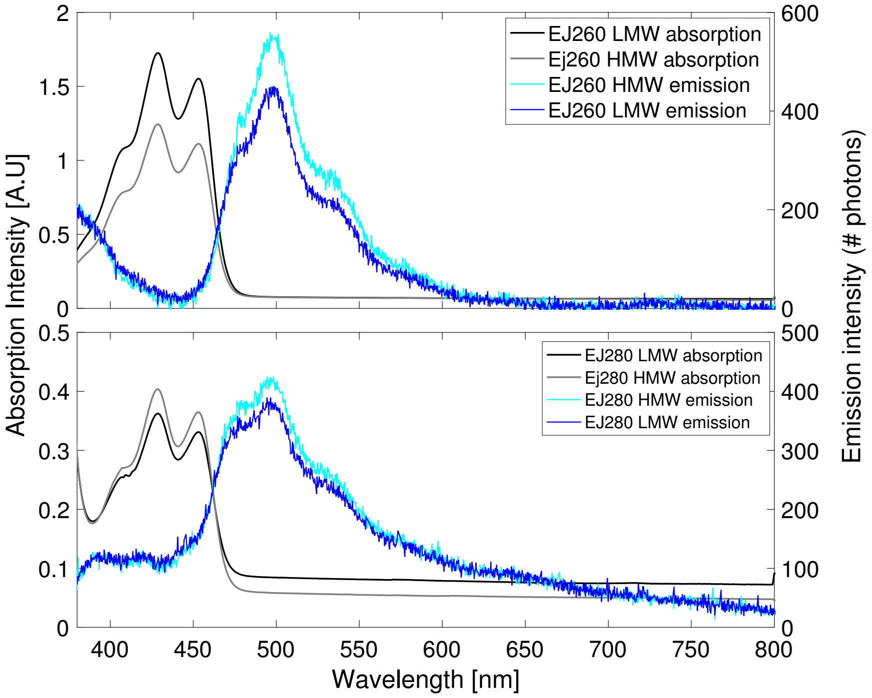

Figure 2.4: Emission and absorption spectra of high and low molecular weight EJ260 (top) and EJ280 (bottom)

Effect of molecular weight on the glass transition temperature

The glass transition temperature, T_g, of a polymer is a threshold temperature related to long-range molecular movement of the plastic. At temperatures below T_g, the polymer is rigid and glassy, and above T_g the polymer becomes soft and rubbery. This change in the properties of a polymer does not occur distinctly, but over a range of temperatures, so for polymers, T_g usually represents the centre of this transition region. Knowledge of the glass transition temperature for a particular polymer is especially useful in determining the processing temperature of the material for extrusion and fibre drawing, and is of major importance in characterising an upper operating temperature limit for the sensing device.

T_g was measured for the high and low molecular weight samples of EJ204 using a PerkinElmer STA8000 Simultaneous Thermal Analyser (STA), that can measure heat flow and weight loss simultaneously. The heat flow data allows determination of T_g, while the weight loss data gives an indication of the amount of gas and moisture trapped within the plastic which is released during heating. A small sample of each plastic was heated from 30 to 290° at a rate of 10°C per minute. Figure 2.5 (a) shows an STA measurement of the low molecular weight polymer, the small bump around 85°C on the heat flow curve is due to the glass transition. T_g can be determined using the software with the half C_p extrapolated point method (Fig 2.5 (b)). This method defines T_g as the temperature where the heat capacity, C_p, is midway between the extrapolated linear portions of the heat flow curves either side of the transition region. The glass transition temperature of the high molecular weight plastic (T_g=90.7°C) was found to be higher than that of the low molecular weight plastic (T_g=86.4°C). Both plastics also showed similar weight loss profiles, with less than a 4% change upon heating to 290°C, a result which is of significance for fibre fabrication. The minimal weight change of the plastic upon heating suggests the polymers do not contain significant amounts of trapped moisture/gas which could lead to defect formation (i.e bubbles within the material) during extrusion and fibre drawing.

Generally, T_g increases with molecular weight, up to a limiting temperature and can be understood in terms of molecular mobility. A larger molecule or polymer chain is less mobile than a shorter one, and a greater temperature is required to give the molecule energy in order for it to move in a rubbery state.

2.3.4 Summary of material and optical characterisation results

The absorption and emission spectra of a range of scintillating optical fibres and bulk plastic scintillators have been characterised. Based on these results, the bulk scintillator EJ204 was selected for further testing as it displayed minimal overlap of its absorption and emission regions, with emissions well suited for detection with a bialkali photomultiplier tube. Of the optical fibres tested, BCF10 and BCF12 display similar properties to EJ204 and hence will be used later for a comparison of the radiation response, optical properties and overall performance with fibres drawn from EJ204.

The glass transition temperature was found to be 4°C larger for high molecular weight polymer formulations. T_g establishes an upper operational temperature limit, this suggests high molecular weight polymers may be more temperature resistant which is of importance if the material is to be used in high temperature environments.

2.4 PMT operation - Analogue vs. Digital mode

The photomultiplier tube has several attractive properties which make it well suited for scintillation detection. A photomultiplier tube can be operated in digital (photon counting) or analogue (current) mode depending on the nature of the input light and the characteristics of the detector and processing electronics. In the earlier stages of this project, work was performed using a photomultiplier tube in digital mode with an ORTEC photon counting card. This mode of detector operation had serious limitations, as

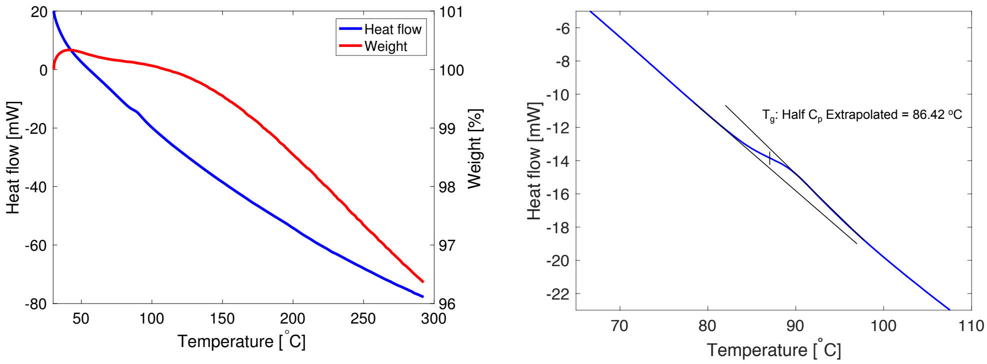

(a) (b)

Figure 2.5: (a) Temperature dependent heat flow and weight change for LMW polymer, (b) Zoom in of plot (a) showing calculation of T_g

will be discussed in this section shortly, and the photomultiplier tube was subsequently operated in analogue mode with the electronic circuitry described in Section 1.7.2.

The difference between digital and analogue mode operation of a photomultiplier tube can be understood as follows: photons striking the photocathode of the photomultiplier tube will liberate photoelectrons, which are multiplied by secondary electron emission as they accelerate through the dynode structure, and the current is collected at the anode for processing.

- In **digital mode** at low light levels, the anode signal is in the form of discrete pulses, which are transferred to an amplifier and discriminator where they can be separated from noise pulses. The majority of the noise pulses are generated in the dynode chain after the photocathode, they are usually low amplitude and easily distinguished from signal pulses, enabling high precision measurements.
- In **analogue mode**, the DC component of the anode pulses are used regardless of their source, whether signal or noise. The amplitude of the current produced depends on the number of anode pulses within the timing resolution of the detector, and any noise pulses generated at the photocathode or down the dynode chain. This means the noise is added directly to the signal and is harder to remove, so signal-to-noise ratios are poorer than those achievable using digital mode.

Digital mode offers many advantages over analogue mode operation: signal-to-noise levels are improved and the stability of the photon counting system is enhanced as it is resistant to variations in supply voltage and tube gain which can significantly affect analogue measurements. However, when photon intensities and count rates are high, analogue mode operation is preferred over photon counting, as is generally the case with scintillation counting. To illustrate the limitations of digital mode photomultiplier tube operation with scintillation counting, consider the following experiment designed to count the number of photons produced by interaction of an alpha particle with the plastic scintillator.

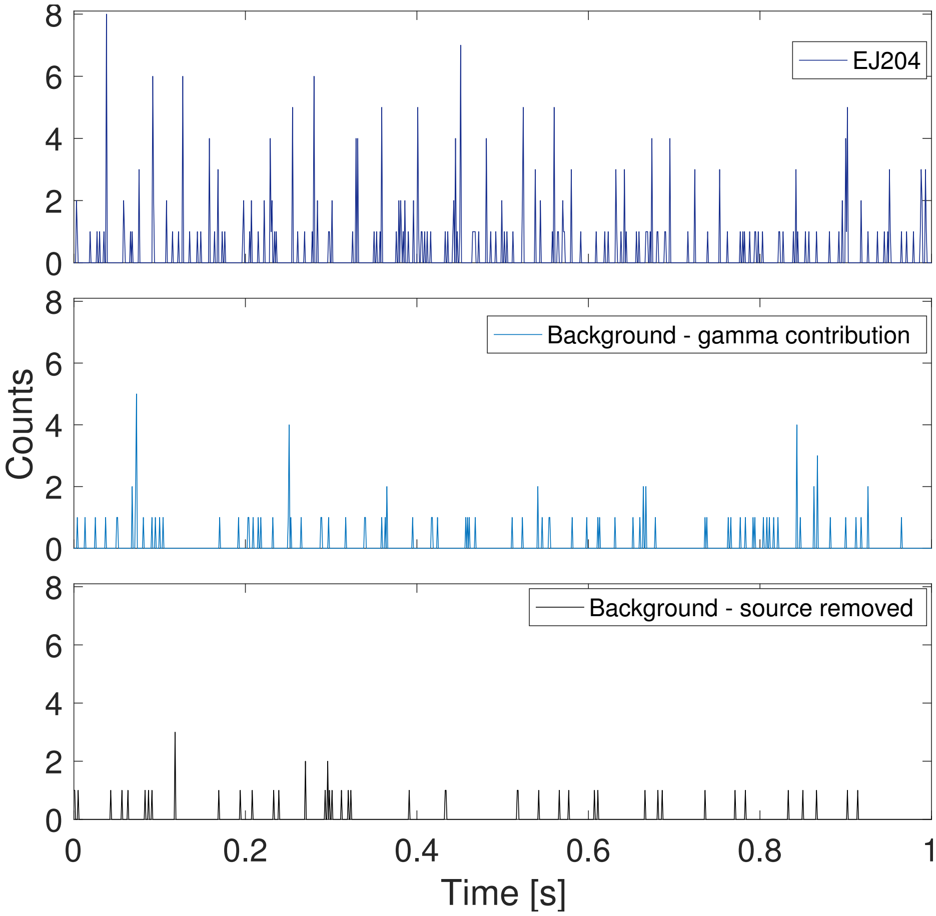

Figure 2.6: Digital mode PMT operation showing photon counts as a function of time observed for: EJ204 plastic scintillator exposed to an ^{241}Am source (top), 60 keV gamma contribution from ^{241}Am (middle), and background counts measured with radiation source removed from setup (bottom)

A 28 kBq ^{241}Am alpha particle source was placed beneath a 3 mm slice of EJ204 plastic scintillator and the photons produced within the material are collected with a photomultiplier tube connected to an ORTEC photon counting card. A 2 mm thick sheet of lead with a 2.8 mm pinhole in its centre is used to reduce the number of alpha particles interacting with the scintillator such that 1 alpha particle is emitted within the pinhole area every 1.3 ms. The bin time was set to 1 ms, so it is likely at least one scintillation event will be detected per bin.

Upon interaction with the plastic scintillator, an alpha particle will produce a pulse of light containing a large number of photons within a very short timeframe (typically a few nanoseconds). Taking into account the drop in scintillation efficiency of alpha particles relative to electrons, a 4 MeV alpha particle is expected to produce just above

1000 photons in a single event once the detector QE ($\approx$ 28% at 400 nm) is accounted for. Now consider the number of photons produced within the scintillator EJ204 using the ^{241}Am source as detected with the photomultiplier tube is shown as a function of time in Fig 2.6 (top).

Recall, ^{241}Am releases a 60 keV gamma ray in addition to alpha particles. A piece of paper was placed between the lead pinhole and scintillator to block any alpha particles and allow the gamma rays to pass freely and interact with the scintillator. The photons detected as a function of time are shown in Fig 2.6 (middle). Note the gamma ray scintillation signal shows a similar distribution to the background (Fig 2.6 (bottom)) when the radiation source was removed from the setup, in that the majority of events detected (87%) consist of a single photon in any given time bin. The low photon numbers produced in a single gamma ray interaction event are to be expected because of the weakly ionising nature of the radiation. The feature which sets apart the alpha interactions in the plastic from the gamma interactions and background noise is the increase in detected photon numbers per event, most notably an increase in events with amplitudes of 3 photons and above. The maximum number of photons detected in a single event is only 8 photons, much less than expected.

Digital mode operation of the photomultiplier tube is best suited for situations where light intensities are low, and photons are well separated in time. The nature of the scintillation light produced with the majority of plastic scintillators, including EJ204 is such that a large number of photons are produced within a few nanoseconds by the exciting radiation. The individual anode pulses at the detector output from each scintillation photon are spaced too closely in time for the system electronics to distinguish between them so they are counted as a single pulse. Consequently, the count rate response of the photomultiplier tube is no longer linear with respect to intensity ("pulse pile-up"), which explains why so few photons are observed per event. These results also suggest that the effective production of photons is much lower than expected. Analogue mode operation of the photomultiplier tube overcomes the issue of pulse pile-up by outputting a current at the anode which is proportional to the incident photon numbers.

Effect of scintillator decay time

To determine if the decay time of the scintillator has any effect on the observed count rate measured using the photomultiplier tube in photon counting mode, a sample of EJ240 was irradiated in place of EJ204. Given that EJ240 has a decay time 2 orders of magnitude larger than that of EJ204, the photons produced by a radiation event in the scintillator are emitted from the material over a much longer period in time.

The photomultiplier tube anode signal will then consist of pulses with increased time spacing compared to the faster scintillator, and if sufficiently spaced in time to be separately resolved by the detector, a dramatic increase in event amplitude would be expected. Using the same experimental conditions as described in section 2.4, EJ240 was irradiated with a 28 kBq ^{241}Am source, and the scintillation collected with a photomultiplier tube in photon counting mode. The frequency of event amplitudes from 1 to 9 photons in each time bin were counted and compared with EJ204.

:

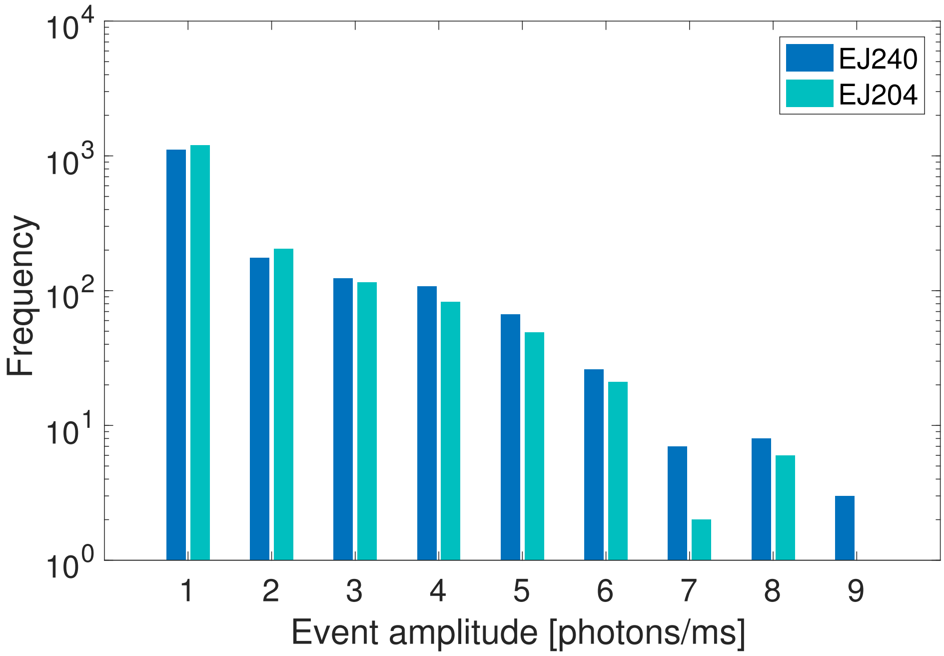

Figure 2.7: Frequency of event amplitudes for 10 s irradiations of EJ204 and EJ240 with ^{241}Am

Using a total measurement time of 10 s, the number of photons detected in each time bin following irradiation of EJ204 and EJ240 with a 28 kBq ^{241}Am alpha source is shown in Figure 2.7. There is a marginal increase in event frequency for those events most likely caused by alpha particle interactions (amplitude 3 and above) when the long decay time scintillator, EJ240 is used. This slight improvement in detection is not enough to warrant using the photomultiplier tube in digital mode in conjunction with the slower scintillator, hence experiments from this point onward were performed using analogue mode operation of the detector.

2.5 Effect of radiation type on scintillator properties

Experiments conducted throughout this thesis are primarily concerned with the response of plastic scintillators to alpha and beta radiation, therefore it is important to determine the effect of both radiation type on the optical properties of the material.

The tests on the bulk scintillator in this chapter are organised as follows: In section 2.5.1, the effect of alpha and beta radiation on the scintillator emission spectrum is investigated, then the difference in scintillation efficiency of the material between the two radiation types is explored in section 2.5.2. Later, in Chapter 4, the response of the scintillating fibres, both commercial and in-house drawn varieties are characterised using the ^{241}Am and ^{90}Sr/^{90}Y sources, followed by testing of prototype devices in liquids containing alpha and beta emitting radionuclides.

2.5.1 Effect of radiation type on emission spectra

The characteristic luminescence wavelength spectrum of a plastic scintillator caused by interactions with ionising radiation is an inherent molecular property governed by the electronic structure of the scintillator molecules, hence is independent of the type of radiation producing it. This is in contrast to a materials scintillation efficiency, where the amount of light produced by an ionising particle depends on both the type of particle and its energy, as will be discussed in 2.5.2.

To confirm the emission spectrum of a plastic scintillator is not radiation type dependent, the low molecular weight EJ204 sample was irradiated with a 17 MBq ^{241}Am alpha source using the same method as was performed using beta irradiation in 2.3.1. Apart from the signal-to-noise ratio differences, the normalised emission spectra (Fig 2.8) produced by alpha and beta radiation show no major differences, as expected.

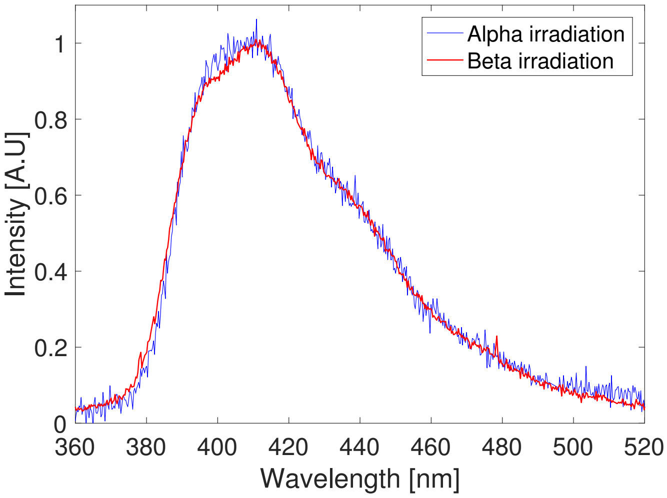

Figure 2.8: Alpha and beta radiation induced emission spectra of EJ204

2.5.2 The alpha-to-beta ratio

The majority of the kinetic energy from an ionising particle absorbed by a plastic scintillator is dissipated non-radiatively as heat (lattice vibrations) with only a small fraction (≈ 4 %) converted to fluorescence [9]. Further to this, the fraction of energy converted to fluorescence is particle type and energy dependent, with heavier charged particles such as α particles and protons producing less light compared to an equivalent energy electron. To explain how a plastic scintillator responds to charged particles, Birks [58] suggests higher ionisation densities along a particle track causes quenching (absorption) of scintillation light from damaged molecules and a subsequent lowering of the scintillation efficiency. Assuming the ionisation density of a particle, $\frac{\mathrm{dE}}{\mathrm{dx}}$, is directly proportional to the density of damaged molecules along its path, the concentration of damage centres along a path length x, can be represented by $\mathrm{B}\frac{\mathrm{dE}}{\mathrm{dx}}$, where B is a proportionality constant. The response of an organic scintillator can then be described in terms of the fluorescent energy per unit path length, $\frac{\mathrm{dL}}{\mathrm{dx}}$ via Birks formula:

$$\frac{\mathbf{dL}}{\mathbf{dx}} = \frac{\left(\mathrm{S}\frac{\mathrm{dE}}{\mathrm{dx}}\right)}{1 + \left(\mathrm{kB}\frac{\mathrm{dE}}{\mathrm{dx}}\right)} \tag{2.1}$$

Where S is the absolute scintillation efficiency of the material (in # photons/MeV electron), and k is a parameter describing the fraction of damage centres leading to quenching of the scintillation light. For a fast electron (E > 125 MeV), $\frac{\mathrm{dE}}{\mathrm{dx}}$ is small, and the individual excitations produced within the scintillator are spaced far enough along the path of the particle that interactions between them are considered negligible. In the absence of quenching effects, Equation 2.2 is reduced to:

$$\frac{\mathbf{dL}}{\mathbf{dx}} = \mathrm{S}\frac{\mathrm{dE}}{\mathrm{dx}} \tag{2.2}$$

and the light yield is proportional to energy loss. When ionisation densities are large enough that quenching effects are non-negligible as is the case when the exciting particle is an alpha particle or slow electron, the fluorescent energy per unit path length is always less than that of an electron by a factor of $\left[1 + \left(\mathrm{kB}\frac{\mathrm{dE}}{\mathrm{dx}}\right)\right]$.

The **alpha-to-beta ratio**, α/β, is a parameter widely used to describe the difference in light output per unit energy between alpha and beta particles in an organic scintillator. A beta particle will always produce a greater fraction of scintillation light than for an equal energy alpha particle, so α/β is always less than 1.

Measurement of the alpha-to-beta ratio in plastic scintillator

Fig 2.9 shows the experimental setup used for measurement of the alpha-to-beta ratio. A 1.3 cm thick sample of EJ204 was cut from the 3 cm diameter bulk cylinder and the ends polished. The scintillator thickness is enough to completely stop the 2.3 MeV electrons from a ^{90}Sr/^{90}Y beta source (R_{max}= 1.18 cm) and much more than required to stop the alpha particles from an ^{241}Am source. The plastic scintillator is placed in the centre of an integrating sphere on top of the radiation source.

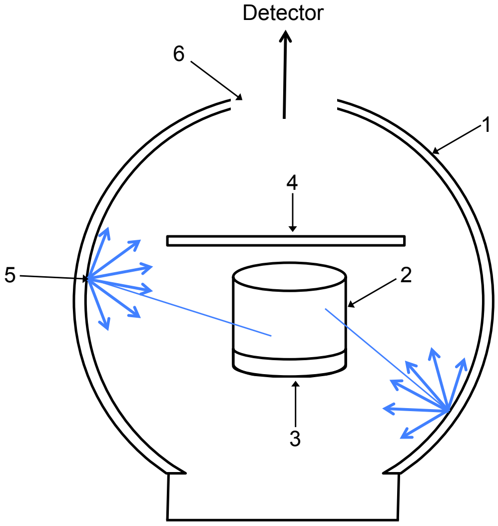

Figure 2.9: Experimental setup for measurement of α/β.
1.Integrating sphere **2.**Plastic scintillator **3.**Collimated radiation source **4.**Baffle **5.**Scattered scintillation light **6.**Emission port

The fluorescence produced in the scintillator by alpha particles will be concentrated in a shallow surface layer near the radiation source because of its short interaction length. Whereas fluorescence produced by the beta particles will be distributed in a much larger volume throughout the plastic. Use of an integrating sphere in this arrangement is necessary to collect and scatter as much light as possible from the plastic towards the emission port regardless of the position it is produced within the scintillator. The scattered light is collected with a photomultiplier tube fixed on the emission port, with the direct path blocked. This ensures only uniformly distributed scattered light is detected, since the path between the scintillator and emission port is blocked by a baffle to ensure no light directly from the scintillator reaches the photomultiplier tube. To prevent oblique electrons from the beta source exiting the plastic before their full energy is absorbed, both radiation sources are collimated using a 1.5 mm pinhole in an aluminium and lead layered sheet. The aluminium component is used to minimise high energy bremsstrahlung produced by the beta source, and the total collimator thickness is sufficient to completely absorb all beta particles not exiting the pinhole.

Measurement of α/β involves use of a pulse height spectrum to gather information regarding the number of photons produced by alpha and beta particles of a given energy. A detailed description of pulse height analysis is given in Chapter 4. For now, it is sufficient to know that the x-axis of the pulse height spectrum depends on the energy of the primary radiation event, and hence the number of photons produced within the scintillator, and the y-axis is proportional to the number of events detected. A high energy radiation interaction producing many photons within the scintillator will show as an event located at a high channel number of the pulse height spectrum, and a low energy event causing emission of a single photon will show as a low channel number event. The channel number can then be calibrated for a particular type of radiation such that the number of detected photons will be related to the energy of the radiation event causing the photon emission in the scintillator. For this measurement, the channel number is calibrated using beta radiation from a ^{90}Sr/^{90}Y beta source, then by finding the channel number where the scintillation peak produced by mono-energetic alpha particles lies on the pulse height spectrum, the α/β ratio can be calculated as follows:

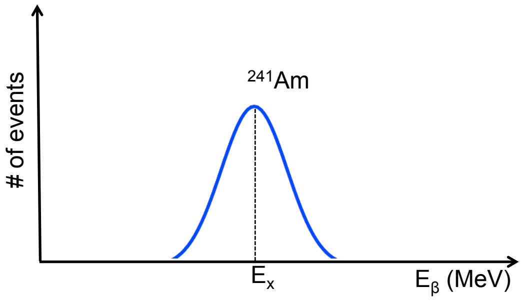

Figure 2.10: Schematic of pulse height spectrum used for calculation of α/β

Firstly the x-axis (channel number) of the pulse height spectrum is calibrated using beta radiation. The channel number will then correspond to the number of photons detected by irradiating a scintillator with a beta particle of energy E_β. Now, suppose the fluorescence collected by irradiating a plastic scintillator with 5.5 MeV alpha particles from ^{241}Am results in a pulse height spectrum as illustrated in Fig 2.10. The peak produced by the alpha particles is located at E_x such that $E_x = E_\beta(x)$, so a 5.5 MeV alpha particle will produce the same number of photons as a beta particle with energy $E_\beta(x)$. The alpha particle energy, E_α, and the beta particle energy at channel number x, $E_\beta(x)$ can be measured, and the alpha-to-beta ratio can be calculated using:

$$\frac{\alpha}{\beta} = \frac{E_\beta(x)}{E_\alpha} \tag{2.3}$$

Before measuring α/β, the alpha particle energy, E_α, must be measured and the channel number of the pulse height spectrum calibrated in terms of the beta particle energy, $E_\beta(x)$. This will be explored in the following sections.

Alpha particle energy measurement

The nominal energy of ^{241}Am alpha particles is 5.49 MeV, however the sealed source used in this experiment has a thin gold coating of unknown thickness causing attenuation and energy loss of the emerging radiation. In calculating α/β, E_α must be known accurately so a surface barrier detector was used to determine the energy of the alpha particles emitted from the 28 kBq ^{241}Am source.

By placing the source in the surface barrier detector, and varying the source to detector distance, d, the alpha particle energy can be deduced using the pulse height spectrum. The position of the alpha peak on a pulse height spectrum shifts towards lower channel numbers as the alpha particles rapidly lose energy in air when the source-detector distance is increased (Fig 2.11(a)). By recording the channel number of the peak position for each source-detector distance until it can no longer be resolved from detector noise, the maximum range of the alpha particles were obtained. Extrapolation to the zero energy point (channel number=0) in Figure 2.11(b) yields the maximum range in air for the alpha particles, $R_{\alpha,\text{air}}$.

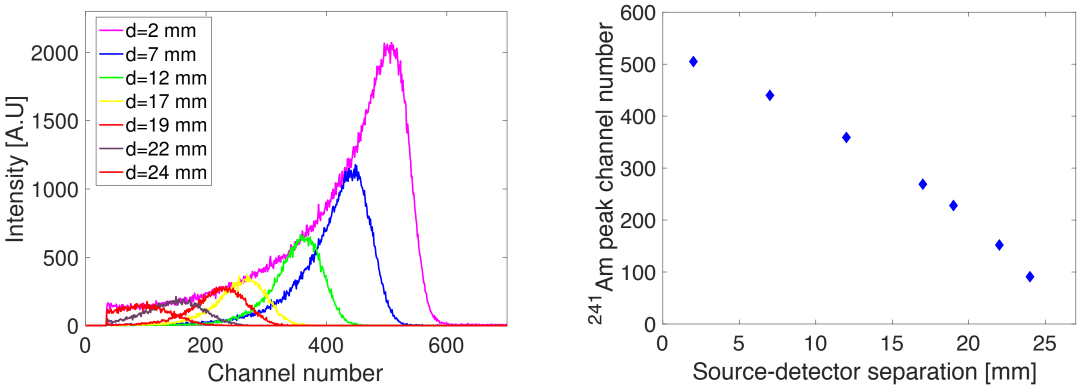

(a) (b)

Figure 2.11: (a): Pulse height spectrum for various source-detector distances, (b): Peak position as a function of source-detector distance

For $R_{\alpha,\text{air}} = 26$ mm, the alpha particle energy is obtained from the ASTAR database [60] using the kinetic energy and range data for dry air near sea level, in this case E_α= 4.02 MeV.

Calibration of a pulse height spectrum using beta radiation

Measurement of the alpha to beta ratio using the method described in 2.5.2 requires the x-axis of the pulse height spectrum be calibrated using beta radiation. Using the set-up shown in Figure 2.9, a 280 kBq ^{90}Sr/^{90}Y source is placed underneath the plastic scintillator, the pulse height spectrum recorded and repeated using a 1.6, 4 and 4.5 mm aluminium absorber between the collimated source and the plastic scintillator. Eight hour integration times were required to achieve good signal-to-noise ratios as observed count rates were low. By recording the approximate channel number where the high energy beta tail in the pulse height spectrum intersects with the x-axis, and given the maximum energy of beta particle emerging from a given thickness of an absorber, $E_{max,t}$, is known, these data points can be used to construct a calibration curve to convert the channel number to beta particle energy. $E_{max,t}$ can be calculated using the total stopping power in aluminium, S, as follows:

$$E_{max,t} = E_{max,t=0} - (S \times \rho_{Al} \times t) \tag{2.4}$$

Where t is the absorber thickness in cm, the absorber density ρ_{Al}= 2.7 g/cm^3, and the term in brackets represents the energy lost by the beta particle upon passing through the aluminium sheet. For a 2.27 MeV electron in aluminium, S=1.53 MeV cm^2/g [61]. Relevant values of $E_{max,t}$ are listed below in Table 2.2.

t[mm]	**E_{max}**(MeV)
0	2.27
1.6	1.61
4	0.62
4.5	0.42

Table 2.2: Maximum beta particle energy for various thicknesses of aluminium absorbers

Included in the energy calibration (see Figure 2.12) is a zero energy point which corresponds to the electronic noise of the detection system. The electronic noise (called the pedestal), observed as a low energy peak in the pulse height spectrum corresponds to zero induced photoelectrons at the PMT photocathode (hence zero energy). Recording the channel number of the noise peak under the same gain conditions the experiment was performed under gives the zero energy data point. For each aluminium absorber, the channel number corresponding to the maximum beta particle energy was recorded and a linear trendline fitted to the points using a least squares regression (Figure 2.12) to give a relationship between energy and channel number,

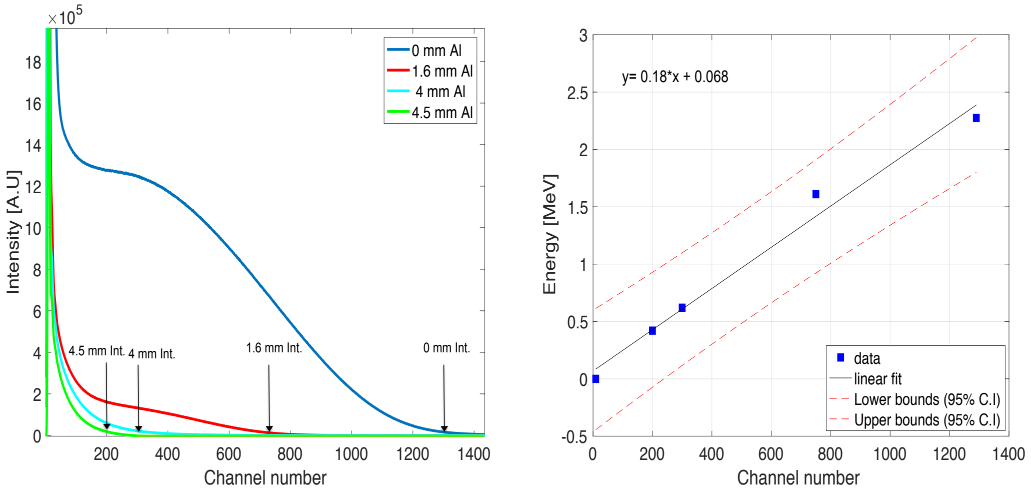

(a) (b)

Figure 2.12: (a): Beta particle pulse height spectrum for EJ204 with varied thickness Al absorbers (b): Observed E_{max} as a function of channel number with linear fit and 95% C.I bounds

E_β(MeV) = (0.0018 × channel number) + 0.067. The standard error on the slope and y intercept of this line is σ_m= 0.0014, and σ_b=0.093 respectively, and the standard error on E_β is 0.14 MeV.

Results

The thickness of the collimator used in this experiment is 3 mm so there will be a slight drop in the energy of the alpha particles before they reach the plastic. Using the stopping power of a 4.02 MeV alpha particle in dry air, S=886.5 MeV cm^2/g with ρ_{air} $=1.225 \times 10^{-3}$ g/cm^3, the energy of the alpha particle after travelling 3 mm is 3.69 MeV (calculated using equation 2.4). A 28 kBq ^{241}Am source is placed in the integrating sphere according to the arrangement shown in Figure 2.9 and the pulse height spectrum is collected over a period of 30 minutes and presented on the energy scale calibrated in 2.5.2 (see Figure 2.13). The integration time was much shorter than used for the beta particle irradiations, as count rates were high, giving good signal-to-noise ratios in the region of interest.

Background noise and the 60 keV gamma emission from the ^{241}Am source give rise to the single electron peak (SEP) located near E_β=0.1 MeV. To confirm the spectral peak near E_β=0.35 is caused by alpha particles, a piece of paper was placed between the source and collimator to check the alpha peak disappears and the SEP remains. The alpha peak position lies at E_β=0.356 ± 0.14 MeV, which corresponds to $\frac{\alpha}{\beta} = \frac{0.356 \pm 0.14}{3.69} = \mathbf{0.096 \pm 0.04}$. Hence the alpha particles will produce roughly 1/10th the amount of light as an equivalent energy beta particle, which is on par with what

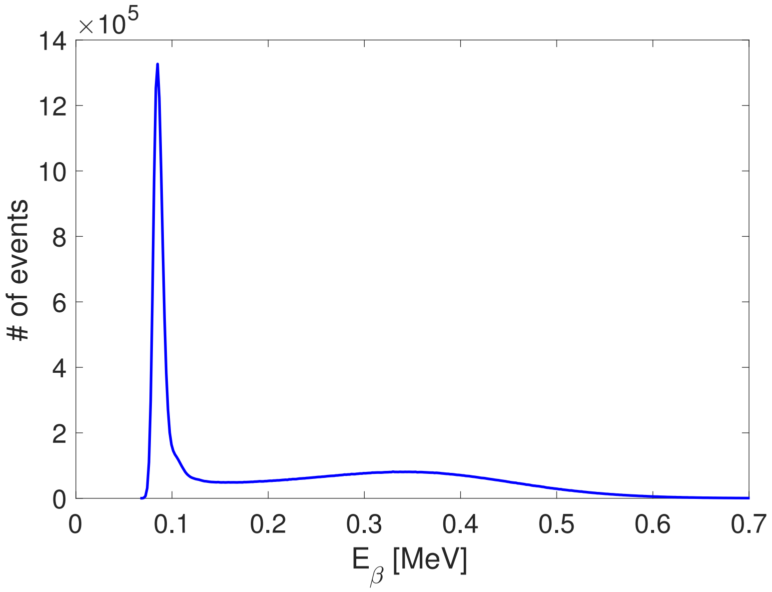

Figure 2.13: Pulse height spectrum using alpha particle source within integrating sphere setup

is reported in literature [9]. This value is only applicable for the energy ranges used in this measurement as the value of α/β is energy dependent.

2.6 Summary

An initial characterisation has been performed on a range of plastic scintillators in bulk and fibre form to screen for varieties with the most favourable optical and physical properties for further testing and ultimately incorporation into a radiation-sensing device. The scintillators emission and absorption properties have been studied to (a) determine which scintillators will be most transparent to their fluorescence emissions and (b) match the emission spectra to an appropriate photodetector. The blue emitting EJ204 was deemed most appropriate at this stage for further characterisation and fibre fabrication trials based on the material having an emission spectrum in the high QE region of a bialkali photomultiplier tube, minimal overlap of its absorption and emission bands and a high light production efficiency. T_g was measured for high and low molecular weight samples of EJ204, and based on these values, upper operational temperatures were established with the high molecular weight variant possessing a greater temperature resistance. Minimal weight changes were observed upon heating the plastics, which is important if high quality fibres are to be fabricated from these materials.

The operational mode of the photomultiplier tube was investigated for detection of scintillation photons produced within two plastic scintillator variants, EJ204 and EJ240. Photon counting mode of the detector was found to be unsuitable, as the photons produced in the material during a radiation event are spaced too closely in time for the detector and associated electronics to resolve, leading to a non-linear response of the detector with respect to photon intensity. The scintillator decay time did not improve the ability of the detection system to resolve individual photons. Analogue mode operation of the photomultiplier tube will hence be used from this point onwards, as it overcomes pulse pile-up by outputting a signal that is proportional to the photon intensity regardless of their time spacing (provided count rates are not excessive).

Finally, alpha and beta radiation sources were used to show the emission spectrum of a scintillator is independent of the type of exciting radiation, and the relative difference in the number of photons produced by each radiation type has been measured. Alpha particles were found to produce 0.096 ± 0.04 times the amount of light in a plastic scintillator as an equivalent energy beta particle.

Chapter 3

Fabrication and characterisation of polymer optical fibres

3.1 Introduction

This chapter describes the work that was performed to fabricate optical fibres from scintillating polystyrene. The bulk of the work presented revolves around the fabrication of bare fibre geometries from high and low molecular weight variants of the ELJEN scintillator EJ204 and EJ262 whose material properties were characterised in Chapter 2. Fabrication of fibres with outer diameters of 160 µm for alpha particle detection are the initial focus of this work, however work performed fabricating 1 mm diameter fibres (”canes”) is discussed briefly as these were required at a later stage in the project, and are more suitable for detection of beta particles.

A two step fabrication process was used where a preform was created via the extrusion technique, some background on this fabrication technique is given in Section 3.2, followed by experimental results. Section 3.3 onwards covers the fibre drawing trials and characterisation. Improvements to the quality of the 160 µm fibres were made during the fabrication process, and the loss within the 1 mm canes was found to be comparable to similar commercially available fibres. The outcomes are summarised in the concluding remarks in Section 3.7.

3.1.1 Scintillator choice

Initial tests were focused on extruding and drawing EJ204 into optical fibres from a 3 cm diameter billet of material. EJ262 was drawn directly into fibre from a 1 cm diameter billet, hence skipping the extrusion step. The radiation sensitivity and loss of the fibres drawn from EJ204 and EJ262 are compared in Chapter 4 to determine if the extrusion process has a significant impact on the fibre quality. No significant differences in radiation response or optical properties were found between high and low molecular weight based scintillators of any formulation as described in the preceding chapter. Both high and low molecular weight plastic types were used in fabrication trials to determine if either formulation offered any advantages in terms of process control during the drawing process or in the quality of the final product. Each ELJEN sample was drawn into a 1 mm cane at a later stage in the project to test the response of each material to X-rays, so some relevant fabrication and loss results are presented, however, the focus of this chapter remains primarily on trials performed using the EJ204 scintillator.

3.1.2 Geometry

The differences in energy deposition per unit track length between alpha and beta radiation means the sensitivity of an optical fibre will be strongly influenced by the size and structure of its core. The limited range of alpha particles in plastic (≈ 40 µm in polystyrene for a 5.5 MeV α) means a sensor designed to maximise the scintillator surface area would best facilitate their detection. A large diameter fibre increases the surface area of the scintillator, however, the alpha particles will only deposit energy and produce photons in a thin surface layer - hence the majority of the fibre material only contributes increased background levels from more penetrating radiation types. A more efficient, cost-effective approach to increase the surface area of the scintillator is to use a large number of small diameter fibres in a bundle configuration, choosing a fibre diameter close to the α particle penetration distance.

The initial goal of this research project was focused on alpha particle detection, hence fabrication trials were targeted on producing fibres tailored for their detection. Fibres were chosen to have a bare geometry with no outer cladding (air or the environment surrounding the core acts as a cladding). This eliminates energy loss in the cladding and maximises the energy available for light production in the scintillator. A target diameter of 160 µm was chosen to compromise the trade-off between sensitivity and robustness.

The research direction expanded to include an investigation of fibres suitable for beta particle detection. These particles deposit their energy over a larger distance ($\approx$ several mm in polymer), hence the fabrication of thicker fibres, having a 1 mm outer diameter is also presented. A 1 mm fibre diameter was chosen to compromise between signal production and background reduction.

3.1.3 Temperature dependent behaviour of polymers

The mechanical properties of polymers are influenced by their temperature, which governs their behaviour during extrusion and fibre drawing. Solid polymers are viscoelastic materials, meaning they show a combination of elastic and viscous behaviour. The degree of viscosity or elasticity is strongly dependent upon the polymer temperature, deformation rate, degree of cross-linking (covalent bonds between polymer chains) and molecular mass. The elastic modulus is a measure of the stiffness of an elastic material, and is a function of temperature as shown in Figure 3.1.

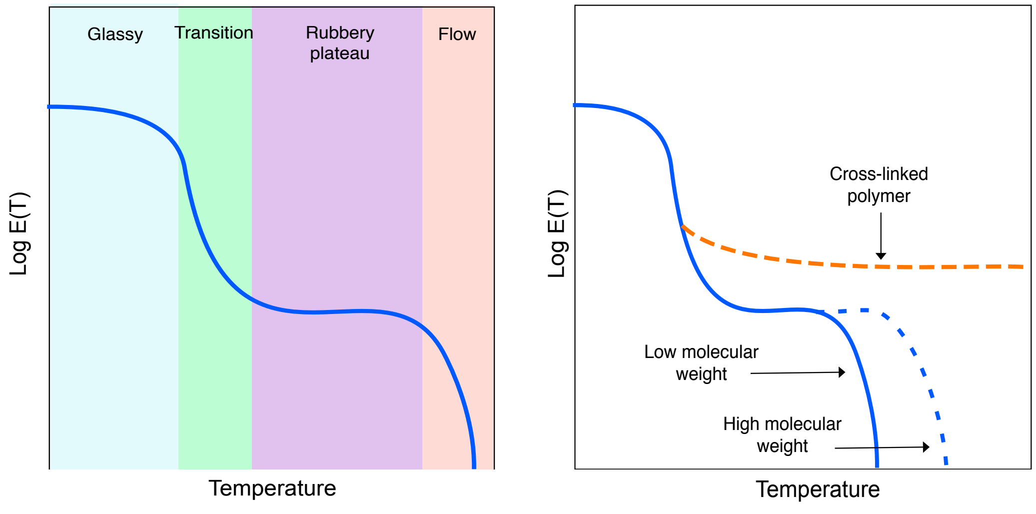

(a) (b)

Figure 3.1: Schematics showing (a) Polymer plastic elastic modulus - temperature curve showing different regions of viscoelastic behaviour (b) Changes to polymer elastic modulus - temperature curve for different molecular weight variations and cross-linking. Image adapted from [90].

For an amorphous polymer like polystyrene, four regions of viscoelastic behaviour are usually observed [73, 83] (see Figure 3.1(a)).

1. **Glassy region**: This region, which exists at low temperatures, is characterised by a high value of the temperature dependent elastic modulus, E(T). In this state, short range motion of polymer side chains is possible but overall there is limited molecular motion so the polymer behaves as a rigid solid, and is considered ‘undeformable’.

2. **Transition region**: This region shows a sharp drop in E(T) as temperature increases beyond the glassy state, and is characterised by a single temperature, T_g. Chain motion occurs on a scale of roughly ten monomer units, and overall molecular motion is still rather limited.

3. **Rubbery plateau region**: In this region, the temperature is such that substantial segments of polymer chains have sufficient energy to move about freely. Entanglement between individual chains prevents large scale translational motion, making the polymer elastic and temporarily deformable.
4. **Flow region**: In this region the polymer is mainly viscous, and chain motion is so large that entanglement does not prevent translational motion. Molecules can easily flow past each other and the material behaves like a liquid and can permanently deform.

In order to permanently deform the shape of a polymer, such as is done during extrusion or fibre drawing, the polymer temperature must be raised so it enters the flow regime.

Effect of molecular weight and cross-linking

The molecular weight of the polymer will have an effect on its viscoelastic behaviour and can be understood with the aid of Figure 3.1(b). Molecular weight in polymers relates to the length of individual chains: the higher the molecular weight, the longer the average chain length. In the glassy and transition regions, molecular motion is mostly confined to the chain ends, which are negligible in size compared to the overall chain length, regardless of molecular weight and consequently, no real difference is observed in the elastic modulus-temperature behaviour in these regions. The behavioural differences between polymers of varying molecular weight becomes noticeable at higher temperatures when the material enters the viscous flow regime. On average, longer polymer chains will suffer a greater degree of entanglement than shorter chains, making them more elastic and resistant to flow, thus will require higher temperatures to overcome this elasticity and enter the viscous flow regime. Additionally, polymers with a high degree of cross-linking are unable to flow regardless of applied temperature, and subsequently cannot be extruded or drawn into fibres.

Viscosity

The majority of polymers above $\mathrm{T_g}$ are non-Newtonian liquids which means their viscosity depends on factors other than the rate of shear strain (velocity gradient) and subsequently, the polymer viscosity will decrease as the shear rate increases. One possible explanation for this behaviour is that the application of shear causes alignment of polymer chains allowing them to flow more easily and reducing the viscosity [38]. This phenomenon, called shear thinning can be described using a power law formulated by

Ostwald and Waels:

$$\tau = \eta \times \dot{\gamma} \tag{3.1}$$

$$\eta = \mathrm{m} \times \dot{\gamma}^{(\mathrm{n}-1)} \tag{3.2}$$

Where η is the shear viscosity, τ is the shear stress, $\dot{\gamma}$ is the shear rate, n is a constant known as the power law index, and m is called the consistency index. For Newtonian liquids, n=1 (hence the viscosity is equal to m) and for non-Newtonian liquids n is less than 1. The index m includes the temperature dependent viscosity which is described by the Arrhenius equation [38]:

$$\eta = \eta_0 \times \exp\left(\frac{\mathrm{E}}{\mathrm{RT}}\right) \tag{3.3}$$

Where η_0 is a characteristic polymer constant, E is the activation energy, R is the universal gas constant and T is the absolute temperature. Thus, the polymer temperature will have a profound effect on its viscosity, with increased polymer temperature related to decreased viscosity. Other factors like molecular weight ($\eta \propto \mathrm{MW}^{3.5}$), cross-linking, processing additives and pressure will all affect the viscosity and so different polymers will respond differently to similar temperature changes. The effects of the polymer processing temperature will thus have a large impact on the extrusion and fibre drawing results, as will be discussed in Section 3.2.

3.2 Extrusion

The fabrication process employed here for the production of polymer optical fibres is divided into two categories, an extrusion process, which involves creating a preform, and a drawing process where the preform is heated and drawn down into optical fibre. Several methods can be employed for creation of a preform, including extrusion [24, 23], injection moulding [77], reactive extrusion [8], and casting [98]. The extrusion process was chosen due to its simplicity. Preforms can be fabricated in a single, automated step allowing the creation of complex structures if required. A schematic of the extrusion procedure is shown in Figure 3.2. A 3 cm diameter polymer billet is heated to a fixed temperature above $\mathrm{T_g}$ until it just softens, and is then forced at fixed speed through a stainless steel die with a computer controlled ram. The exit structure of the die determines the final geometry of the preform.

Prior to extrusion, the polymer billets and extrusion apparatus require preparation to ensure optimal results. Foreign particles in the fibre can cause scattering losses,

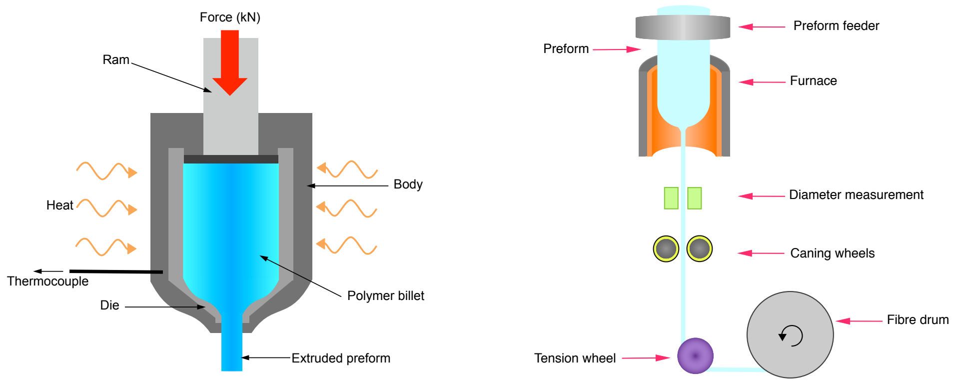

(a) (b)

Figure 3.2: Schematics showing (a) the extrusion process and (b) the fibre drawing process

so to prevent foreign particles contaminating the preform (and ultimately the fibre), the billets are thoroughly cleaned to remove any traces of grease and dust from their surface. Cleaning was performed by rinsing the polymer billet with distilled water and a mild detergent and then placing it in a beaker containing isopropyl alcohol in an ultrasonic bath for 15 minutes. The same process was used to clean the die and sleeve.

The quality of the extruded preform will depend on how carefully the extrusion processing parameters are managed, a brief description of each is given below:

The extrusion temperature determines the polymer viscosity and how soft it will be as it is pushed through the die. Even a few degrees difference in temperature is enough to significantly change the preform quality. The ideal extrusion temperature is bounded by an upper limit, where the polymer will either begin to flow under its own weight or thermally degrade, and a lower limit, where die swell (when the preform diameter is larger than the die exit diameter) distorts the preform structure. Die swell is less problematic for preforms without an inner structure, as is the case here. However, when the extrusion temperature is set too low, the force required to push the polymer through the die is so large the preform surface can become damaged. Although die swell cannot be completely avoided, severe surface roughness and distortion of the preform structure can be avoided as will be discussed. The extrusion temperature will vary depending on the molecular weight of the polymer but is generally between 120 and 160°C for the polystyrene varieties used in this work.

The ram speed determines the speed at which the polymer is pushed through the die, and is typically between 0.05 to 0.2 mm/min for the trials performed here. This speed remains fixed throughout the extrusion by varying the extrusion force, which is controlled by an electronic feedback loop. High extrusion speeds can cause unacceptable die swell and poor preform surface quality. These can be greatly improved by slowing down the ram speed, but the process becomes impractical time-wise, so a balance between efficiency and preform quality needs to be established.

The extrusion force, or ram force, is a dynamic variable dependent on the billet temperature and ram speed. The extrusion force determines the extent of preform die swell, and as the force is dependant on extrusion speed and temperature, alteration of either of these parameters can be used to control the die swell during extrusion. A constant extrusion speed will ensure the preform has constant dimensions along its length. The extrusion force is continually adjusted via an electronic feedback loop to ensure the ram speed remains fixed. To help understand this concept consider the relationship between force, F, speed, v_0, and temperature, T, for an isothermal extrusion at fixed speed which can be derived using equations 3.1, 3.2 and 3.3 and other parameters related to die geometry and flow rate [24].

$$\mathrm{F} = \mathrm{K} \times \exp(\mathrm{E}/\mathrm{RT}) \times \mathrm{v}_0^n \tag{3.4}$$

The exponential term is proportional to the polymer viscosity (see equation 3.3), K is a constant containing parameters related to billet and die geometry, and the index n is the same power law index as in equation 3.2. According to Equation 3.4, it is apparent that decreasing the extrusion temperature or increasing the ram speed has the effect of increasing the extrusion force, in practice this was shown to cause die swell and a rough preform surface. On the other hand, low extrusion forces caused by increasing the extrusion temperature or decreasing the ram speed was found to produce preform tapering and bubbles within the material caused by thermal degradation of the polymer.

A typical force profile for extruded high molecular weight polystyrene is shown in Figure 3.3. Once the polymer is soft enough to flow and has filled the die, it is forced out the die exit and enters a steady state regime where the force remains relatively unchanged with time. Towards the end of the extrusion, as the remainder of the polymer is forced through the die, the force was found to increase rapidly. The majority of the preform is extruded under the steady-state force regime, so the effects of extrusion temperature and ram speed on the average force in this region will be explored in the following sections.

In summary, the success of the extrusion, as determined by the quality of the preform is highly dependent on correctly specifying the extrusion temperature and ram speed. Knowing which values to set for these parameters is non-trivial and requires some knowledge of the material properties. Annealing tests and several extrusion trials were performed to better understand the best extrusion parameters.

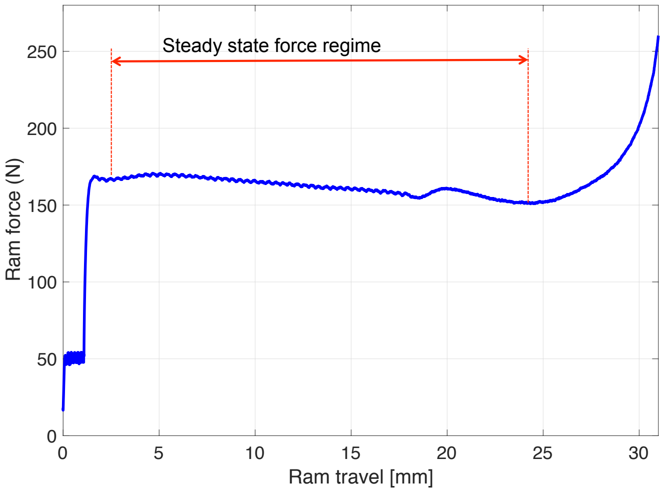

Figure 3.3: Extrusion force profile for HMW polystyrene

3.2.1 Atmosphere

Oxidation of polystyrene can cause the material to develop a yellow colouring, resulting in decreased transmission in the blue region of the visible spectrum where a significant fraction of the scintillation emission lies for most plastics used here. To prevent oxidation of the material, a nitrogen atmosphere was used for all extrusion, fibre drawing, and annealing processes, and also acts to ensure progressive cooling of the preform and fibre during fabrication.

3.2.2 Annealing tests

Prior to extrusion, annealing tests were performed using high and low molecular weight EJ204 to determine if any trapped moisture or gas was contained in the polymer, and to provide an estimate for the extrusion temperature.

Polymer deformation testing

The deformation temperature of the polymer will be above the glass transition temperature of the material, and serve as an approximate extrusion temperature. Recall T_g was measured in Chapter 2.3.3, and found to be 86.4°C and 90.7°C for low and high molecular weight polymers respectively. The deformation temperature was measured using 2 mm thick slices of polymer, which were angled upright in a brass holder and placed within a furnace. The polymers were heated incrementally until they were observed to distort under their own weight. Figure 3.4 shows the results of the first deformation test where high and low molecular weight polymers (arranged from right to left) were placed in the brass holder and heated to 135°C. In this example, the low molecular weight polymer has deformed too much, while the high molecular weight polymer has not deformed at all.

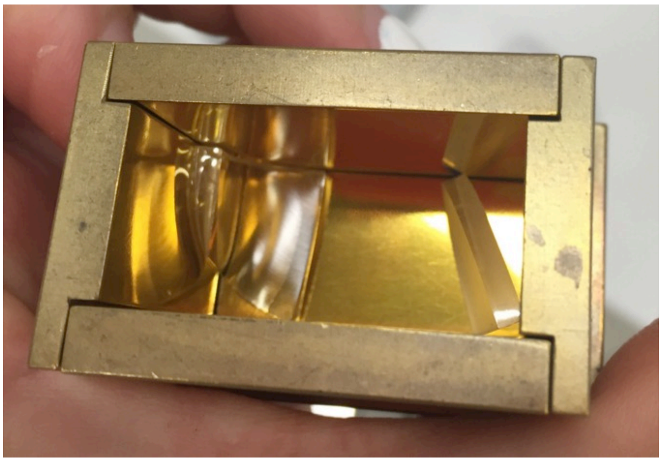

Figure 3.4: Polymer slices in brass holder for deformation testing.

Ideally, the deformation temperature should be such that the polymer becomes viscous enough to 'just' slump under its own weight. Figure 3.5 shows the results of more annealing tests where the low molecular weight polymer was annealed at temperatures 120°C and 123°C. At 120°C very slight deformation can be observed, while the amount of deformation observed at 123°C looks ideal as a starting point for extrusion trials. The same degrees of deformation was observed in high molecular weight polymers at 143°C and 150°C.

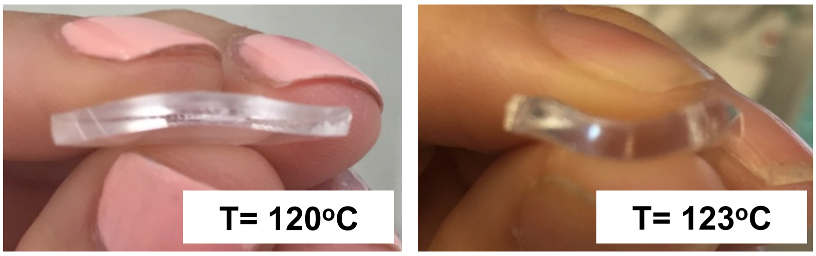

Figure 3.5: Deformation of low molecular weight polymer after annealing at 120°C (left) and 123°C (right)

Outgassing tests

Upon heating, moisture and gases trapped within the polymer can lead to the formation of defects like blistering and bubbles within the material, which can cause unwanted scattering loss and fibre breakage. Annealing the polymer prior to each fabrication stage involves heating and cooling the material at a controlled rate to remove any internal stress and promote outgassing to reduce the likelihood of defects forming at elevated temperatures. Annealing to promote outgassing should be performed below T_g so the plastic doesn't deform, or begin to decompose. Based on the deformation testing results, an annealing temperature of 95°C was chosen for high and low molecular weight polymers as it is around T_g and well below the deformation points. Annealing of high and low molecular weight EJ204 was performed in a nitrogen atmosphere, and the samples were heated at a controlled rate of 1°C/min to the set temperature, and left to dwell for 72 hours before slowly returning to room temperature.

To determine if either molecular weight formulation or a pre-annealing step makes a difference in the quantity of gas emitted during heating, STA analysis was performed on annealed and un-annealed polymer samples. A PerkinElmer STA6000 was used to heat each sample and monitor the weight changes over time, using two heating programs as discussed below.

High temperature STA analysis

To determine if annealing has any impact on the weight loss of the polymer during heating, STA analysis was performed to monitor the weights of annealed and un-annealed samples in the temperature range of 30°C to 290°C at a rate of 10°C/min.

The weight change of each sample is shown as a function of temperature in Fig 3.6. The annealed low molecular weight sample appears to experience an increase in weight between 30 and 100°C. This behaviour could potentially be a result of moisture incorporation within the STA atmosphere (the chamber is not gas-tight) which is removed with time at higher temperatures, or by changes in the background level. Given a single measurement took over three hours to complete, a background measurement was made at the start of the day and applied to all sample data taken on that same day. Further to this, at $\approx$ 150°C - a likely extrusion temperature, the weight loss of all samples is less than 0.03%. Based on these observations, annealing at 95°C does not appear to have an impact on the weight loss of the samples in the studied temperature range, which indicates the polymers do not readily absorb moisture from the air or contain any solvents. The heating process used for this analysis was useful in determining the temperature at which the polymer weight begins drop significantly ($\approx$ 160-170°C). This

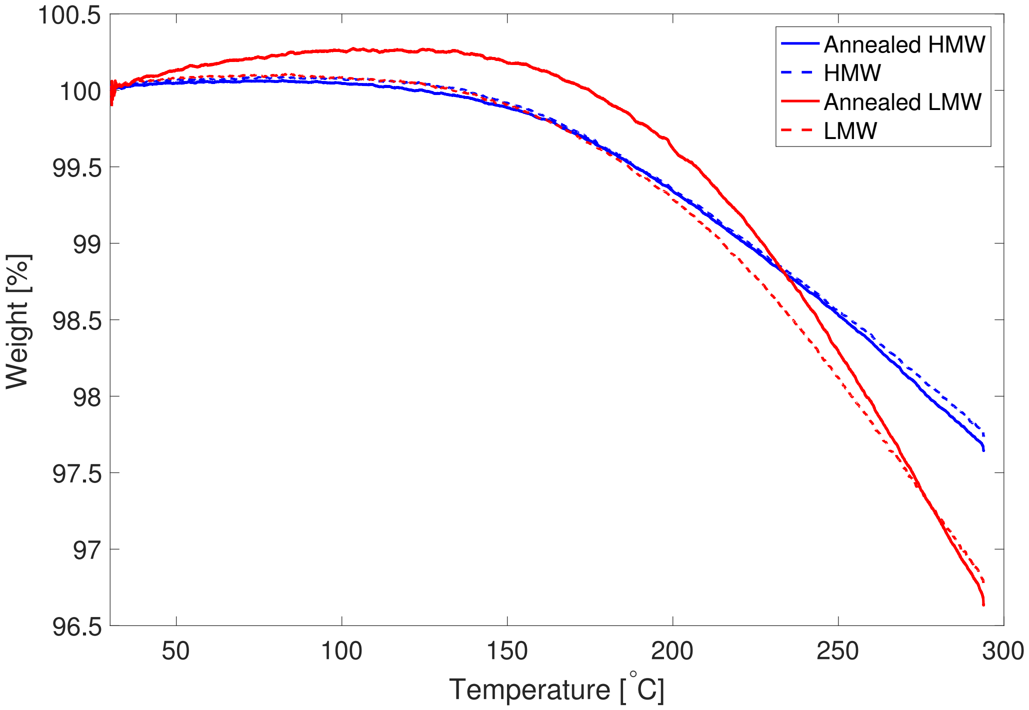

Figure 3.6: Weight losses of annealed and un-annealed polymer samples during heating

is likely a result of depolymerisation, where the polymer chains are broken down into smaller units, some of which are instantly vaporised and can form defects within the material. Extrusion should thus be performed at a temperature below this limit.

Isothermal STA testing

To achieve a better understanding of the quantity of evolved gasses likely to be expelled during extrusion, STA analysis is performed using an extended isothermal heating program at 150°C for 3 hours (similar to what would be encountered during extrusion). Samples annealed at 95° for 72 hours and un-annealed samples were tested. All samples initially show a decrease in weight as expected (Fig. 3.7), followed by a weight increase after 20 minutes for unknown reasons. This may be attributed to the lack of reproducibility and accuracy of the instrument when measuring changes in such small weight fractions. In all cases, whether the polymers are subject to a pre-annealing treatment or not, the weight change of the material during prolonged heating is so small that outgassing is unlikely to cause any issues during extrusion.

3.2.3 Low molecular weight polymer extrusions

Initial extrusion trials were performed using un-annealed, low molecular weight polystyrene, and a stainless steel die with an exit diameter of 1 cm. An extrusion temperature of

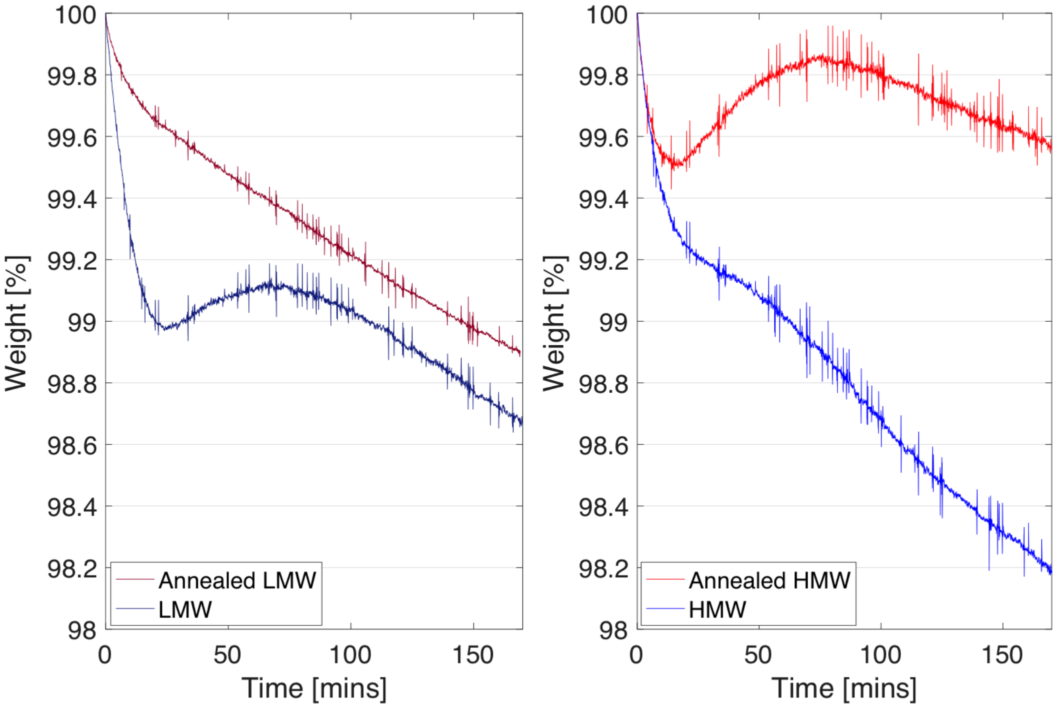

Figure 3.7: Weight losses of annealed and un-annealed polymer samples during heating

123°C was chosen (3°C higher than the upper annealing limit as determined in section 3.2.2) with extrusion speeds ranging from 0.05 to 0.1 mm/min. A summary of the extrusion parameters for each trial are shown in Table 3.1.

The preform from trial LMW3 displays a somewhat matt surface finish and a larger die swell than the LMW1 preform (Figure 3.8). For the same extrusion speed and temperature as trials LMW1/2, a higher force, and corresponding increase in surface roughness and die swell was observed for the LMW3 trial. Upon speaking with the manufacturer, it was disclosed that the polymers from batch 2 had a higher molecular weight distribution than those in batch 1 because the polymerisation conditions could not be exactly reproduced. This increase in molecular weight means the polymer viscosity would be higher for an equivalent extrusion temperature (as $\eta \propto MW^{3.5}$), and correspond to a larger extrusion force (Equation 3.4) as was observed.

For all subsequent low molecular weight extrusions, the temperature was raised a further 12-15 °C to lower the polymer viscosity and extrusion force. Preforms from these trials looked similar in appearance to LMW1 so are not shown. An improvement in surface quality and die swell did appear to be correlated with a lower extrusion force which was achieved with higher temperatures and lower ram speeds as predicted. In the interest of time, no further extrusion tests were conducted to further investigate this relationship, as the preform quality appears suitable and consistent enough for fibre drawing trials.

Trial no.	**Polymer batch**	**Temperature (°C)**	**Speed (mm/min)**	**$\mathrm{F}_{\mathrm{ave}}$ (N)**
LMW1	1	123	0.1	165
LMW2	1	123	0.1	115
LMW3	2	123	0.1	570
LMW4	2	135	0.05	140
LMW5	2	135	0.05	155
LMW6	2	138	0.05	150

Table 3.1: Parameters for LMW extrusion trials. Extrusion temperature and speed were set parameters, and $\mathrm{F}_{\mathrm{ave}}$ is the average extrusion force measured over the steady state force region.

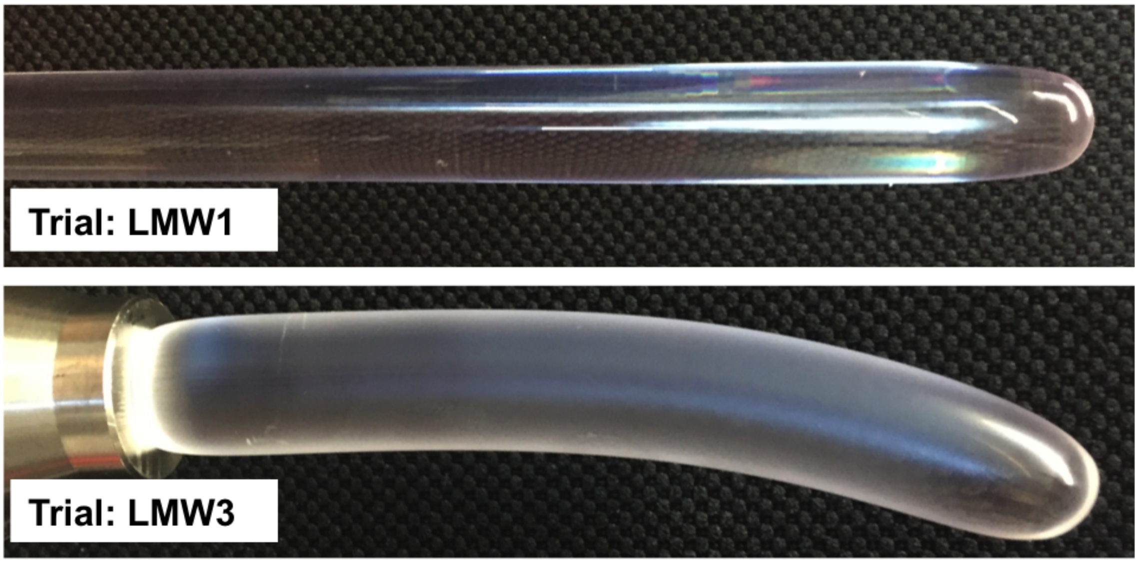

Figure 3.8: Extruded LMW preforms from trial LMW1 (top) and LMW3 (bottom)

3.2.4 High molecular weight polymer extrusions

A summary of the extrusion parameters for the high molecular weight polymer trials are shown in Table 3.2. Initially, an extrusion temperature of 150°C was chosen based on results from the annealing trial performed in Section 3.2.2. The preform from trial HMW1 had a very rough "sharkskin" appearance with minimal die swell (Figure 3.9). An average extrusion force of 180 N was recorded, larger than observed for the successful low molecular weight extrusion trials. The sharkskin present on the preforms appears as a series of transverse ridges along the preform length and is believed to result from instabilities in the flow behaviour of the polymer as it is forced through the die. Polymer close to the die wall moves at a much slower rate than the extrudate being forced out at constant speed, which causes the outer polymer layer to stretch and tear [68].

For the second trial, HMW2, the extrusion temperature was set 5°C higher than that in HMW1 in an effort to lower the extrusion force. The temperature increase alone was not sufficient to lower the force significantly, so the extrusion speed was reduced to 0.05 mm/min from a starting value of 0.1 mm/min at the beginning of the trial. Although efforts to reduce the force were successful (80 N compared to 180 N in HMW1 trial), there was not a significant improvement in the preform surface quality as hoped. Although it is unknown how the preform surface quality correlates with fibre quality, the preforms do not appear suitable for use in drawing trials at this stage. To investigate the effects of speed and temperature on preform quality, two trials were performed by independently varying each of these parameters.

Trial no.	**Temperature (°C)**	**Speed (mm/min)**	**F_{ave}(N)**
HMW1	150	0.1	180
HMW2	155	0.1, 0.05	160,80
HMW3	159,163,167,171,175	0.1	170, 110, 80, 60
HMW4	160	0.01,0.025,0.05,0.1,0.2	140
HMW5	160	0.05	82
HMW6	165	0.05	150

Table 3.2: Parameters used for HMW extrusion trials.

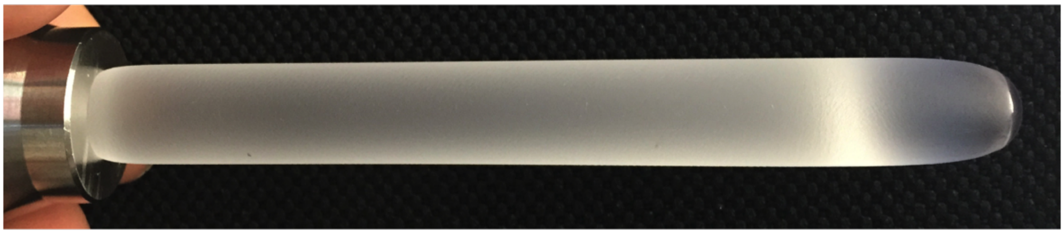

Figure 3.9: Extruded HMW preform from trial HMW1 showing 'sharkskin' surface

Temperature varied extrusion trial

To determine the effect the extrusion temperature has on the preform quality, the temperature was adjusted by 4°C increments between 159°C and 175°C for a fixed time period during the course of the extrusion while maintaining a constant speed (Trial:HMW3). The extruded preform and corresponding force profile are shown in Figures 3.10 and 3.11. Increasing the extrusion temperature from 159°C, the surface finish of the preform improves but the sharkskin appearance remains. Die swell decreases with increased temperature, however above approximately 167°C, the polymer viscosity becomes so low the preform at the die exit becomes stretched under its own weight and tapers. The tapering of the preform is not likely to have a large impact on the quality of the optical fibre once drawn, however small bubbles observed towards the end of the preform will translate to increased scattering losses and potential breakage of the fibre during the drawing process.

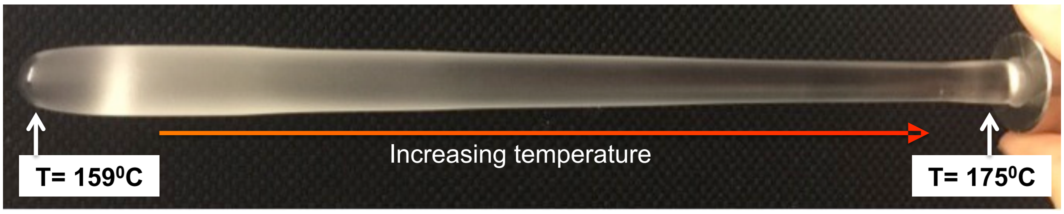

Figure 3.10: Preform from temperature varied extrusion trial HMW3

Increasing the extrusion temperature has the effect of lowering the extrusion force resulting in a subsequent decrease in die swell and improvement of surface quality. The optimum extrusion temperature range is between 163 and 171°C, as die swell and surface quality are reasonable and no defects caused by depolymerisation are observed.

Speed varied extrusion trial

For the extrusion trial HMW4, a constant temperature of 160°C was maintained for the extrusion, and variable ram speeds of 0.01, 0.025, 0.05, 0.1, 0.2 mm/min were used. The preform and force profiles are shown in Figures 3.12 and 3.13. Decreased

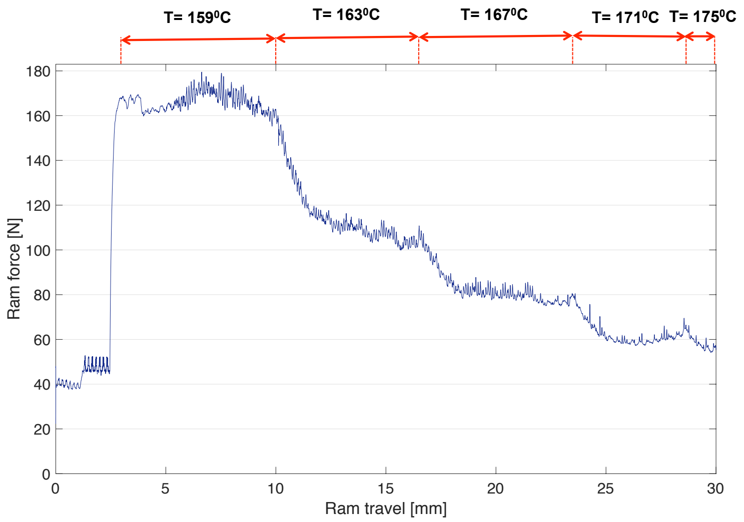

Figure 3.11: Force profiles from temperature varied extrusion test

extrusion speeds correlate with lower extrusion forces. Consistent with the temperature controlled extrusion trials, this decrease in extrusion force translates to smaller die swells and improved surface quality. At the slowest extrusion speed, the sharkskin surface is still present, and the die swell is almost completely absent, however extrusion at 0.01 mm/min is rather impractical, taking 50 hours to completely extrude a 30 mm long billet. The preform outer diameters were measured at points where die swell was largest and found to be 15.8, 14.9, 12.5, 11.5, and 10.8 mm at sections corresponding to extrusion speeds of 0.2, 0.1, 0.05, 0.025 and 0.01 mm/min.

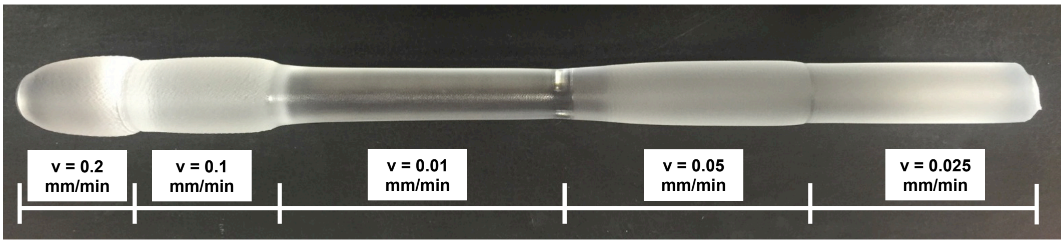

Figure 3.12: Preform from speed varied extrusion trial HMW4

An increase in temperature, and decrease in ram speed were found to improve the preform surface quality. Hence, subsequent extrusion trials were performed using a speed of 0.05 mm/min and a temperature of 160-165°C to compromise between surface quality and extrusion time.

3.2.5 Preform annealing

The high pressures and temperatures used in extrusion resulted in preforms with residual internal stress, as is seen using crossed polarisers in Figure 3.14. Failure to remove this internal stress can lead to distortion of the fibre structure during drawing which

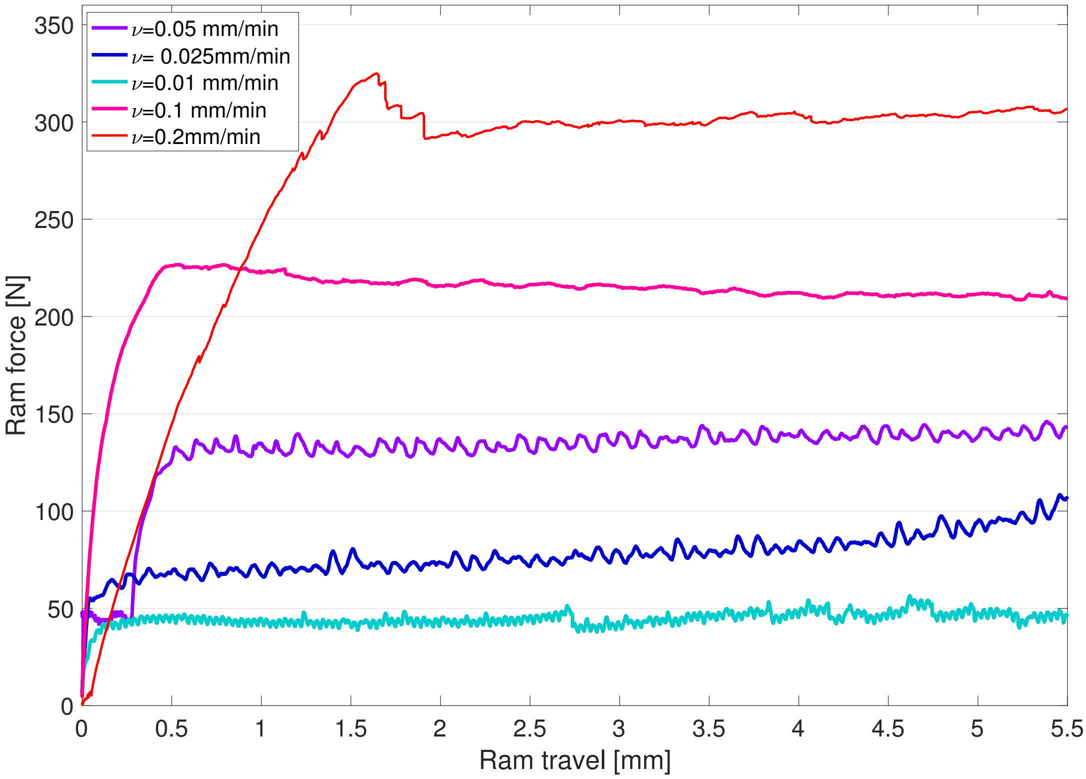

Figure 3.13: Force profiles for speed varied extrusion test

can increase transmission losses. To remove the residual stress, low molecular weight preforms were annealed at 85°C, and high molecular weight preforms at 120°C for 24 hours.

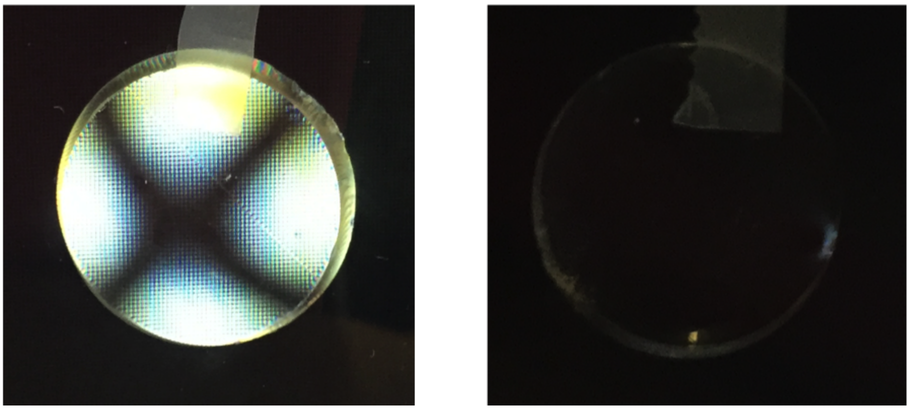

Figure 3.14: extruded LMW preform slice viewed through cross polarisers before annealing (left) and after annealing (right)

3.2.6 Summary of extrusion results

Six extrusion trials were performed for high and low molecular weight EJ204 polymers. With the exception of one trial, all low molecular weight preforms were extruded reproducibly, had good surface quality, minimal die swell and were free of any visible defects, making them suitable for fibre drawing. In contrast, high molecular weight polymers displayed a rough 'sharkskin' surface, but otherwise were defect free with minimal die swell. An improvement in surface quality, and decrease in die swell correlates with a lower extrusion force which was achieved by increasing the extrusion temperature or decreasing the ram speed. For equal extrusion forces, the low molecular weight polymers had superior surface finish to the high molecular weight polymers.

The extrusion speed is limited by poor surface quality at high speeds and very long extrusion times at lower speeds, whereas temperatures are restricted by depolymerisation defects at high temperatures and surface quality at low temperatures. It is unknown if the sharkskin surface on the high molecular weight polymers will negatively impact the fibre quality, if so, slow extrusion speeds may be a necessity.

3.3 Fibre drawing

The final stage in the fabrication process involves heating and drawing down the extruded preform to produce the optical fibre with desired final diameter using a fibre drawing tower (see Figures 3.2(b) and 3.15). The optical fibres are drawn directly from preforms in a single step. The low production temperatures used with this method ensure the polymers are minimally degraded.

Figure 3.15: Fibre drawing tower

Fibre drawing begins with clamping and heating the extruded preform above its glass transition temperature (T_g) with an induction heated furnace. The drop in viscosity of the polymer caused by heating allows the material to taper and fall under its own weight. The descending end of the fibre is attached to the drum at the bottom of the draw tower, which is then set to rotate at a fixed speed. Control of the fibre diameter is achieved by adjusting the feed and draw rates for a given preform diameter. The preform feed rate is the speed with which the preform is fed into the hot zone of furnace, and the fibre draw speed is the speed with which the fibre is pulled out of the hot zone and spooled onto the rotating drum. Under steady-state conditions there exists a relationship between the preform feed rate, ν_{feed}, the fibre draw speed, ν_{draw}, and the preform and fibre diameters D and d:

$$\frac{D^2}{d^2} = \frac{\nu_{\text{draw}}}{\nu_{\text{feed}}} \tag{3.5}$$

Usually to achieve a certain diameter, the feed rate is fixed and the draw speed is changed until the desired outer diameter is obtained. Increasing the feed rate will move the preform faster into the hot zone of the furnace allowing it to soften more quickly, which usually requires an increase in draw speed to maintain the fibre diameter. The outer diameter and tension of the fibre are monitored as it is drawn, which allows the operator to adjust various parameters until the desired diameter and operating stability is achieved. Following fibre fabrication, the transmission losses of the fibres were measured as a means of comparing their optical quality during each drawing trial.

3.3.1 Quality of fabricated fibres

The fibre drawing process is inherently sensitive to any fluctuations in the processing parameters, similar to the extrusion process. The geometry and temperature of the furnace, drawing speed and the feed speed will have a direct impact on the physical and optical properties of the drawn fibres, hence fibre draws were performed by a technician with considerable experience in operating the draw tower. A quick summary of the main factors affecting fibre quality are presented below.

Material quality

Ultimately, the optical quality of the drawn fibers will be limited by the bulk loss of the polymer. Any impurities, dopant aggregates, or volatile solvents remaining from the polymerization process will cause scattering losses in the fibres, hence why selection of a high quality bulk material is crucial.

The polymer must be compatible with the drawing process; this has a lot to do with the molecular weight and degree of cross-linking within the polymer. For example, the molecular weight needs to be sufficiently low with no cross linking between chains, otherwise they have difficulty moving past one another and the material becomes too rubbery to draw upon heating, even at temperatures high enough to cause depolymerisation. In contrast, if the molecular weight is too low, the material will form a liquid upon drawing and break apart into drops due to the low surface tension if the temperature is not chosen correctly. Ideally, the molecular weight should permit the material to flow smoothly upon heating without turning into a liquid. The type of polymerisation method has an effect on fibre quality, for instance, one method called unassisted free radical polymerisation typically produces polystyrene chains with unsaturated ends making the chain prone to depolymerisation during heating causing the formation of bubbles.

Preform feed rate and drawing speed

Variations in the core diameter of the fibre can lead to increased surface scattering losses, hence the preform feed rate and drum speed should be monitored and adjusted to stabilise the outer diameter as much as possible.

Temperature

The drawing temperature was established by slowly heating the preform in the drawing tower until a section softened and dropped under its own weight to form a taper. Furnace temperatures ranged from 300 to 400°C (actual preform temperatures are lower) depending on the molecular weight of the polymer. Due to the molecular weight dependance of the polymers viscosity, higher temperatures were required for high molecular weight polymers to achieve a viscosity low enough to drop under the influence of gravity. Low molecular weight polymers were typically drawn at 350°C while high molecular weight variants were drawn at 400 °C.

The high molecular weight polymers proved problematic to draw at first, as the elastic nature of the material caused large tensions and subsequent breakage of the fibres on several occasions. The elastic modulus of the polymer must have been high enough that it still had a significant elastic component (caused by polymer chain entanglement) despite the temperature being sufficient to be in the viscous flow regime. This caused the polymer to resist deformation and spring back like a rubber band. A 10°C increase in furnace temperature was sufficient to reduce the elastic component of the polymer flow, resulting a decrease in fibre tension, and stabilised drawing conditions.

Process monitoring and control are crucial when drawing a preform into fibre. An appropriate furnace temperature is set, then the speed and feed rates are adjusted until the required diameter is achieved and remains stable.

3.4 End-face termination of polymer optical fibres

A method to effectively cleave the end-faces of the fibres needed to be established, since a high quality end-face termination is needed for accurate, low loss coupling of light into the fibre core for characterisation and sensing measurements, and for accurate reproducible connectorising and coupling to other optical components. Glass fibres are easily cleaved with the crack cleaving method. In this method, a controlled micro crack is induced and propagated across the fibre surface to produce a near perfect optical end face. This method works well for hard, brittle materials but not for polymers as their rubbery nature makes crack propagation complex and messy. Best results for cleaving polymers are usually achieved by the hot blade method [62, 1]. In this technique, a heated razor blade is used to cut the fibre at a slow controlled speed. UV laser cleaving has also demonstrated excellent results for cleaving polymer optical fibres [15], however the hot blade method was trialled for this work due to the availability of components and simplicity of the method.

3.4.1 Hot blade cleaving

A standard V-sharpened razor blade was used to cut the fibres transversally. To prevent movement during cleaving which could potentially distort the end-face, the fibres were taped to a glass microscope slide. The blade was heated on a hotplate to a temperatures of 100°C and 150°C and the fibre cut by hand using different speeds. Results are shown in Figure 3.16.

Overall, cleaving the fibre with a sharpened razor blade produced very poor results, with surfaces distorted and often angled. It was difficult to accurately reproduce the cutting speed and angle when cutting the fibres by hand, so the cleaves were highly variable, with no improvement in surface quality evident when the blade is heated to either 100°C or 150°C. At 150°C, the fibre surface was melted in parts suggesting the blade temperature may be too high and the cutting speed not optimal. At 150°C, faster cutting appears to produce a marginal improvement in surface quality, however cleaves of this quality would still produce significant scattering resulting in poor coupling efficiencies.

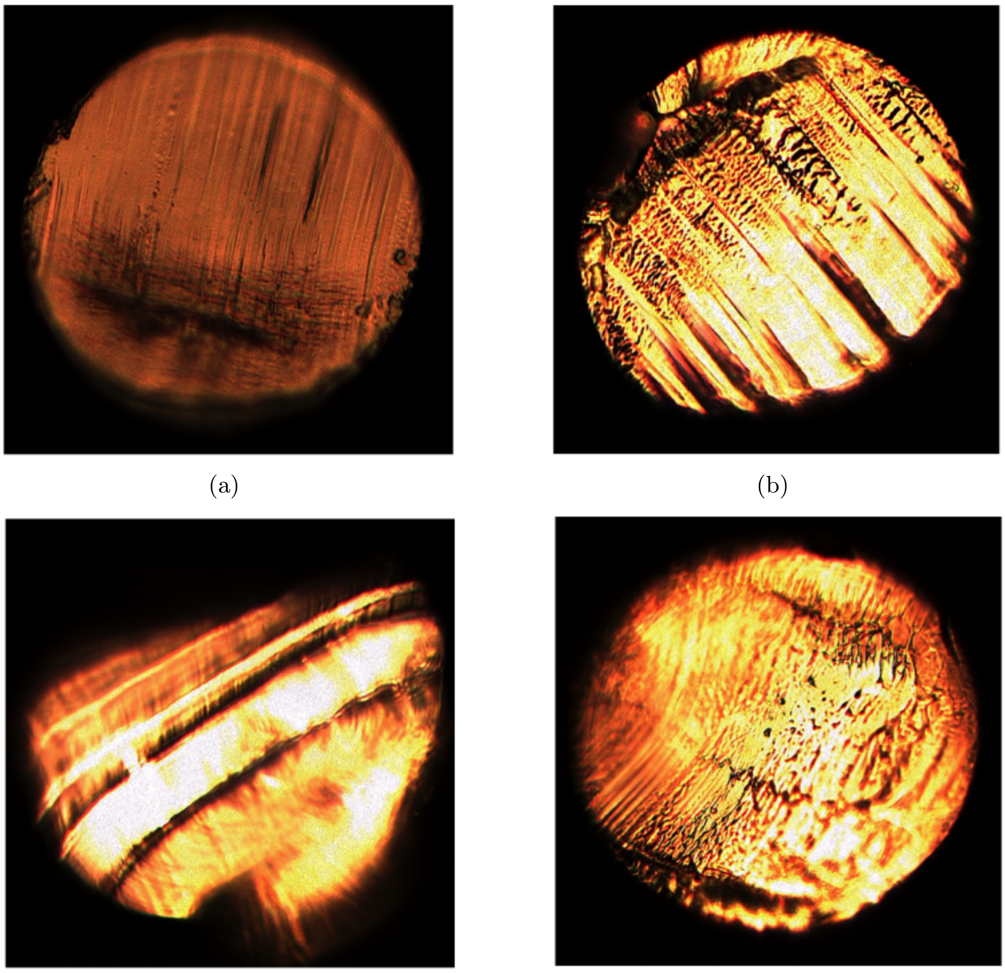

(a) (b)

(c) (d)

Figure 3.16: Microscope images of fibre cleaves using a razor blade, where: (a) The blade is not heated before cutting and cut at a slow speed (b) The blade is heated to a temperature of 100°C and cut at a slow speed (c) The blade is heated to 150°C and cut at a slow speed (d) The blade is heated to 150°C and cut at a faster speed

3.4.2 Fibre polishing - 160 µm diameter fibres

The various cleaving procedures all produced a poor surface quality, so it reasons to polish the ends of the ends of the fibres after cleaving to produce an optical quality surface. Improvements in the end-face quality of the optical fibres were made using a REV2 fibre polisher from Krell technologies. The fibres are first cut using a room temperature sharpened razor blade. They are then inserted through a bare fibre adaptor exposing a small fraction of the fibre tip. Too much exposed material can lead to breakage and bending of the fibre within the ferrule. The diameters of some fibres were quite variable along their length in comparison to the quoted tolerance of the ferrule bore size (-0, +10 µm [71]), and often difficult to fit. A range of ferrules were purchased with inner hole diameters between 150 to 180 µm in an attempt to ensure a good fit for a range of fibre diameters and limit movement and subsequent damage of the fibre during polishing. The polishing was performed in two stages for 15 s each, the first step using a 3 µm grain size silicon carbide (SiC) polishing pad, and finally using a 0.3 µm alumina polishing pad with a light water spray. Microscope images taken before and after are shown for the low molecular weight 160 µm drawn fibre in Figure 3.17.

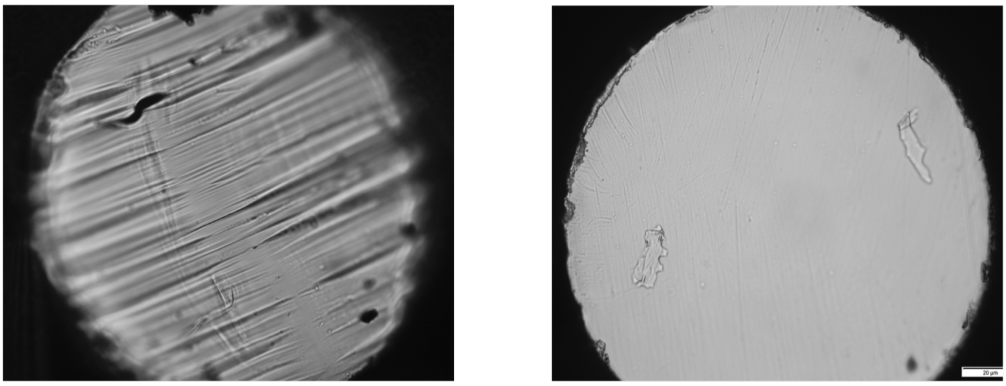

(a)

(b)

Figure 3.17: Microscope images of fibre tip (a) Fibre cleaved with room temperature razor blade prior to polishing (b) Fibre polished for 15 s each with 3 µm SiC and 0.3 µm alumina polishing pads

Polishing the fibres using the process described offers a reproducible improvement in the surface quality of their end-faces. Occasionally the fibre surface would not be completely flat which is most likely due to excessive movement of the fibre during the procedure, hence inspection of the fibre tip prior to use was necessary. After acquiring microscope images, a Bruker Contour GT-K optical profiler was used to measure the size of the surface variations on the polished fibre tip, however the surface roughness of the unpolished fibres was too large to accurately obtain images for measurements. An example of an optical surface profile image for a low molecular weight fibre is shown in Figure 3.18. Measurements were taken using several fibres, and the values of the average surface roughness R_a acquired, with the majority of fibres displaying average surface variations less than 40 nm.

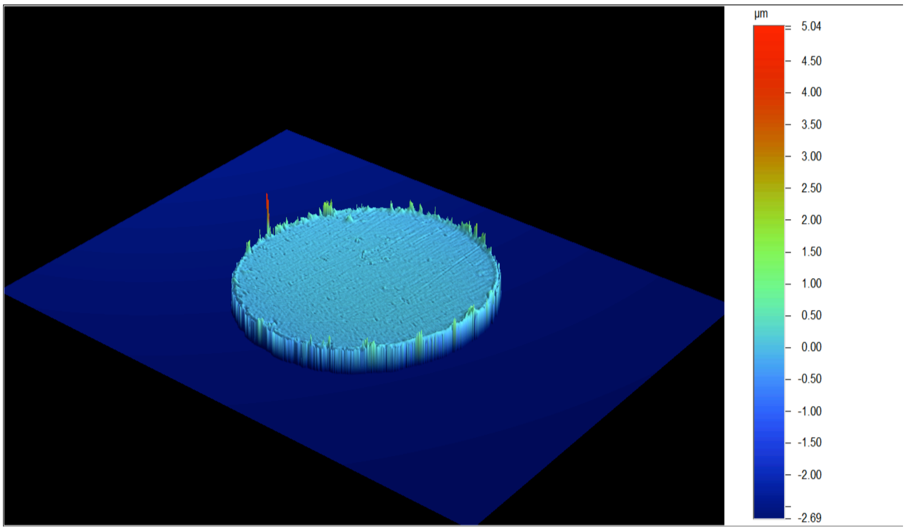

Figure 3.18: Surface profile image of LMW fibre tip. R_a=22 nm

3.4.3 Fibre polishing - 1000 µm diameter fibres

The number of polishing stages, film type (grain size and material), and total polishing time varies depending on the outer diameter of the fibre. For small diameter fibres, 250 µm and less, the polishing procedure outlined above produced a good quality fibre end-face, suitable for the purposes of optical measurements and coupling. Adjustments to the polishing procedure in terms of the polishing time and grain size of the polishing film were required for the 1 mm diameter fibres used throughout this work.

Significant distortion to the fibre structure and damage to the outer cladding (where applicable) on the commercial fibres occurred when the 1 mm fibres were cut with a room temperature razor. Heating the razor prevented any distortion to the fibre, and kept the cladding intact most of the time (see Figure 3.19(a)). Following hot blade cleaving, four polishing steps were required, first using a 30 µm SiC film for 30 s (Figure 3.19(b)), following this 9 µm and 3 µm SiC and 0.3 µm films were used for 15 seconds each (Figure 3.19(c)). The end face quality as shown in Figure 3.19(c) is typical. Several air bubbles can be observed in the fibre core and are most likely introduced during fabrication. Small scratches are evident on the fibre surface following the final polishing stage and no noticeable improvement was made by altering the polishing time or using a finer grained polishing film. These scratches however, are only shallow and were not found to have a noticeable effect on the coupling efficiency for subsequent characterisation measurements.

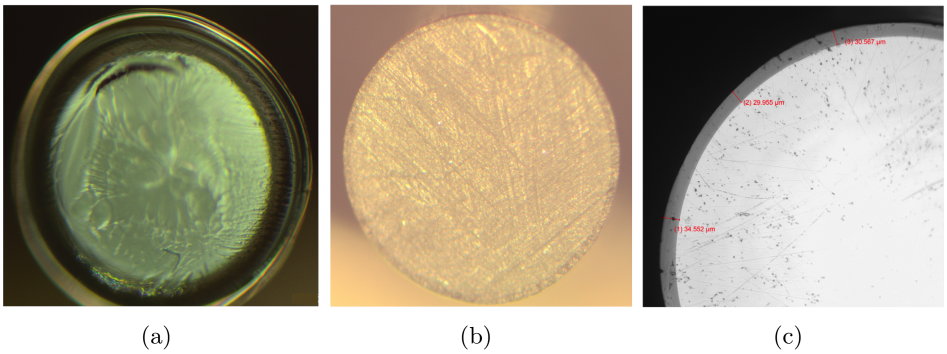

(a) (b) (c)

Figure 3.19: Microscope images of 1 mm OD fibre tip (a) Fibre cleaved with heated razor blade (b) Fibre polished for 30 s with 30 µm SiC (c) Section of fibre after final polishing stage

3.4.4 Summary of fibre cleaving results

Optical fibre cleaving using a hot blade alone was not able to produce end-faces of sufficient quality for optical measurements, coupling and connectorising with other optical components. The addition of a polishing procedure following hot blade cleaving is capable of producing high quality fibre cross sections without distorting the fibre geometry or destroying the outer cladding where present. The process was found to work for fibres of different diameter and takes less than two minutes from start to finish. The automated nature of the procedure ensures good fibre end face quality which is consistent and easy to achieve.

3.5 Characterisation of polymer optical fibres

The majority of fabrication trials focused on drawing 160 µm diameter fibres from the blue scintillator EJ204. The green scintillator EJ262 was also fabricated into a 160 µm diameter fibre to determine the effect of the scintillator emission wavelength on the fibre loss. A summary of the parameters for each fibre drawing trial is shown in Table 3.3, with the values shown being those that resulted in the most stable drawing conditions at the nominated outer diameter. In an effort to improve fibre quality, different parameters were altered for each drawing trial. An increase in feed speed following the first trial resulted in greater control of the fibre outer diameter. Increases in drawing temperature were required for low molecular weight trials following Poly11 due to the higher softening points of these polymers from billet formulation inconsistencies as discussed in Section 3.2.3. A temperature increase was also required to overcome large fibre tensions in high molecular weight trials, which caused the fibre to snap on a few occasions. Drawing and annealing conditions for poly15 and poly17 were unchanged to determine the reproducibility of the fibre quality. Not all drawing and extrusion variables could be tested individually due to expense and time. Initial drawing trials produced fibres with 12.5% variation in outer diameter, which was reduced to 3.1% in later trials. For reference, Saint-Gobain fabricated fibre varieties specify diameter tolerances on fibres as 3%.

The process used for drawing 1 mm diameter fibres, or canes, differed slightly from the 160 µm fibre draws. Canes were drawn directly using 1 cm bulk plastic rods from the supplier, which eliminated the need for an extrusion and pre-annealing step. To assist with the initial drop of the preform during caning, a 50 g weight was attached to the end of the preform, which was then quickly replaced by a 20 g weight to slow the rate at which the cane dropped. Once the cane had descended to an appropriate level, the operator was able to pull the cane out the preform and lightly apply tractor wheels (see Figure 3.2(b)) to control the drawing speed, and hence outer diameter. Feed speeds were increased to 3 mm/min, and draw speeds were decreased to 0.3 m/min from previous trials to stabilise drawing conditions. Diameter variations for all trials were 2.5 % (±0.025 mm), comparable commercial fibre tolerances. A comparison of fibres drawn in-house will also be compared to commercial varieties.

Trial	**Preform**	**Preform annealing**	**Material**	**OD(μm)**	**ΔD**	**T (°C)**	ν_d	ν_f
poly11	LMW1	85°C for 24 h	EJ204	160	$> \pm$ 20 μm	300	16	1.4
poly12	HMW1	120°C for 24 h	EJ204	160	$> \pm$ 20 μm	390	5.1	1.2
poly13	HMW2	120°C for 24 h	EJ204	160	±5 μm	400	9.6	2
poly14	HMW6	Preform polished and annealed at 120°C for 24h	EJ204	160	±4 μm	400	10.2	2
poly15	LMW4	85°C for 6 days	EJ204	160	±5 μm	350	8.9	2
poly16	N/A	Not annealed	EJ262	160	±5 μm	350	9.1	2
poly17	LMW6	85°C for 6 days	EJ204	160	±5 μm	350	9.0	2
poly18	N/A	Not annealed	EJ262	1000	±25 μm	355	0.3	3
poly19	N/A	Not annealed	EJ204	1000	±25 μm	355	0.3	3
poly20	N/A	Not annealed	EJ240	1000	±25 μm	355	0.3	3
poly21	N/A	Not annealed	EJ260	1000	±25 μm	355	0.3	3

Table 3.3: Parameters used for fibre drawing trials.
Preform = Preform name from which fibre was drawn from, OD = Nominal outer diameter, ΔD = Variation in outer diameter
T = Drawing temperature, ν_d = Draw speed in m/min, ν_f = Feed speed in mm/min, N/A = Not applicable, fibre drawn directly from 1 cm OD low molecular weight polymer billet

3.5.1 Loss measurement techniques

Following fabrication, fibres from each trial were characterised in terms of their loss. The transmission loss of the fibre is the reduction in transmitted light intensity as a function of distance travelled in the fibre core. This parameter is especially important when considering weak optical signals or long fibre lengths, as the loss determines how well the scintillation light will be transmitted to the detection system. The losses of the 160 µm diameter fibres were measured using a standard cut-back technique [41] by coupling a white light source into one end of the fibre and measuring the output power with an Optical Spectrum Analyser (OSA) over a series of cutbacks from its initial length.

The SIF (Side Induced Fluorescence) technique [22, 36] was also used to measure the loss and confirm results obtained with the cutback method. This technique induces scintillation within the fibre using a UV diode, and measures the output power as a function of distance by translating the UV source horizontally along the length of the fibre. The sources of loss in polymer fibres and the techniques for measuring transmission loss are discussed in more detail in Chapter 4.

The loss of 1 mm diameter fibres were characterised using the SIF technique only, as limited lengths were fabricated (only a short length could be fabricated from a 1 cm diameter billet), making it difficult to perform a cutback measurement. The non-destructive nature of the SIF procedure also ensured the fibres weren't destroyed and could be used for other experiments. The losses of selected 1 mm and 160 µm diameter fibres drawn in-house are presented to show the effects that selected fibre properties and drawing parameters have on the fibre attenuation.

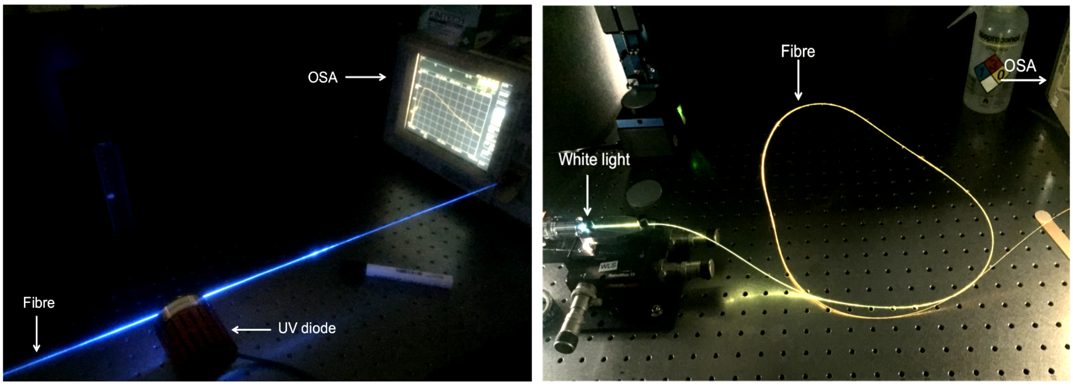

(a) (b)

Figure 3.20: Photographs showing the setup used for loss measurements using (a) The SIF technique (b) The white light cutback technique

3.5.2 160 µm fibre losses

The losses of the 160 µm in-house fabricated fibres are shown in Figure 3.21. The sharp attenuation edge observed at shorter wavelengths is attributed to the combined effects of Rayleigh scattering and self-absorption caused the by overlap of the emission and absorption bands of the scintillator (See Chapter 5 for more detail). The light in this shorter wavelength spectral region is rapidly absorbed as it travels through the fibre core, and the amount reaching the detector is so small that the loss cannot accurately be determined. The fibres fabricated from EJ204 (poly11, 13, 14, 15 and 17) have an emission peak at 409 nm, with losses displayed from 440 nm as signal-to-noise decreases rapidly below this wavelength. Likewise, poly16, which was fabricated using EJ262 with emission peak at 481 nm has loss displayed from 490 nm onwards. The attenuation peaks at 607 and 715 nm are a result of absorption by the carbon hydrogen (C-H) bonds in the polymer. The molecules absorb photons at characteristic frequencies and convert them to vibrational energy (heat).

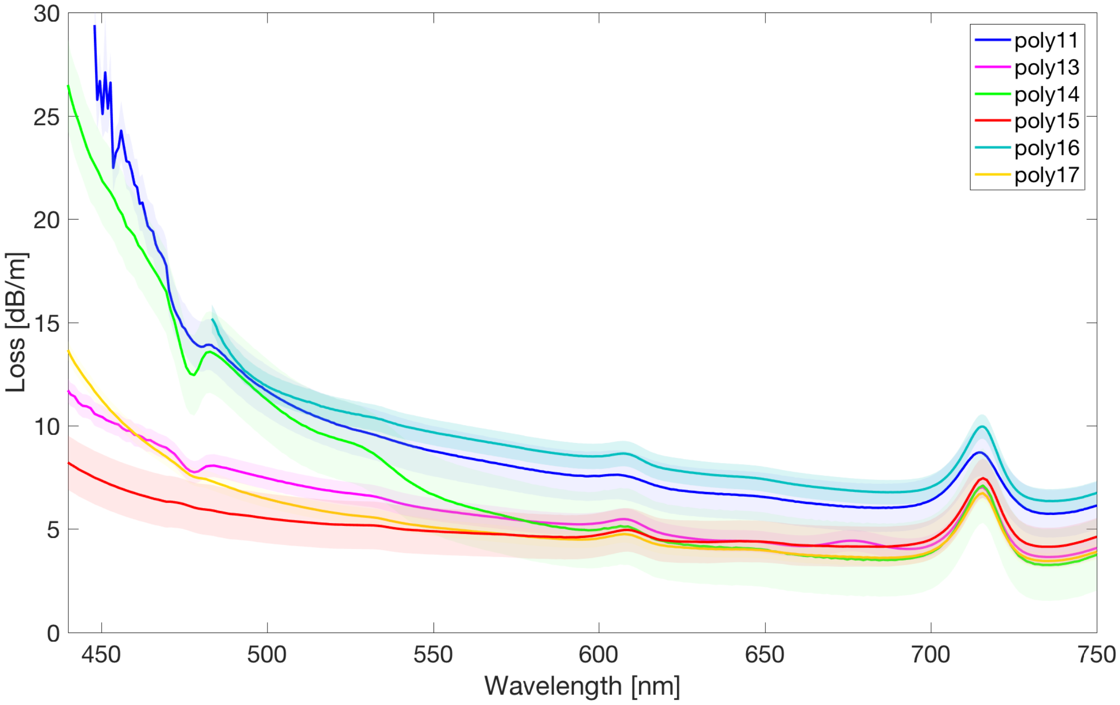

Figure 3.21: Loss of 160 µm drawn fibres measured using the cutback technique. Rayleigh scattering and self absorption cause the attenuation edge below ≈ 500 nm. Peaks at 607 nm and 715 nm are C-H vibrational absorption losses

The loss of fibres poly11 and 16 do not converge at longer wavelengths with the other fibre varieties. Both these fibres were fabricated from different polymer batches than poly 13, 14, 15 and 17 so the elevated background loss may be a result of variations in the bulk material loss of the polymer (caused by impurities, solvents remaining in the material etc), which will determine the limiting loss of the fibre. In all cases, fibre losses are rather high ranging from of 8-30 dB/m at shorter wavelengths near the materials emission peaks, then decreasing to ≈ 3-7 dB/m at 750 nm.

3.5.3 Loss of 1 mm diameter fibres

The 1 mm canes listed in Table 3.3 were drawn for x-ray characterisation measurements presented in Chapter 6. All canes were drawn from low molecular weight polymers, using the same drawing parameters so unsurprisingly, they have very similar measured losses. Here, the loss of the canes drawn from EJ262 and EJ204 are characterised using the SIF technique and presented for comparison with the 160 µm fibres drawn from the same material to determine how the core diameter of the fibre affects the transmission loss (Figure 3.22(a)) and (Figure 3.22(b)).

For consistency, the 160 µm diameter fibre loss using the SIF technique is presented. Note that loss values for 160 µm fibres may differ slightly from those shown in Figure 3.21 due to measurement errors associated with using the two different techniques. The measurement noise is higher for the 160 µm fibres, and is caused by a combination of factors. Firstly, less light is generated within their core as a result of the smaller scintillator volume interacting with the UV radiation, secondly, the higher loss of these fibres means less signal reaches the detector in comparison to the 1 mm fibres.

Based on the images shown in Figure 3.22, it appears the increase in core diameter results in an overall decrease in attenuation. A possible explanation is that when the core diameter decreases, there will be a greater fraction of the propagating modes extending outside the core and interacting with the surface of the fibre, hence scattering effects caused by surface irregularities or contaminants on the fibre surface will be enhanced. The 160 µm diameter fibres drawn from EJ204 appear to have higher Rayleigh scattering losses than the 1 mm variety, but the same is not true for the fibres drawn from EJ262. Rayleigh scattering is dominant at shorter wavelengths so will have a larger impact on the loss of the blue emitting scintillator EJ204, than the longer wavelength green emitter, EJ262. The attenuation curve of the 160 µm diameter EJ262 fibre lies at an elevated level above the 1 mm variety instead of converging at longer wavelengths, and may be due to batch-to-batch variation in the bulk material loss of the polymer.

3.5.4 Impact of drawing conditions on fibre loss

The limited number of drawing trials makes it difficult to relate the effect of a particular parameter to the loss, however the following observations were noticed:

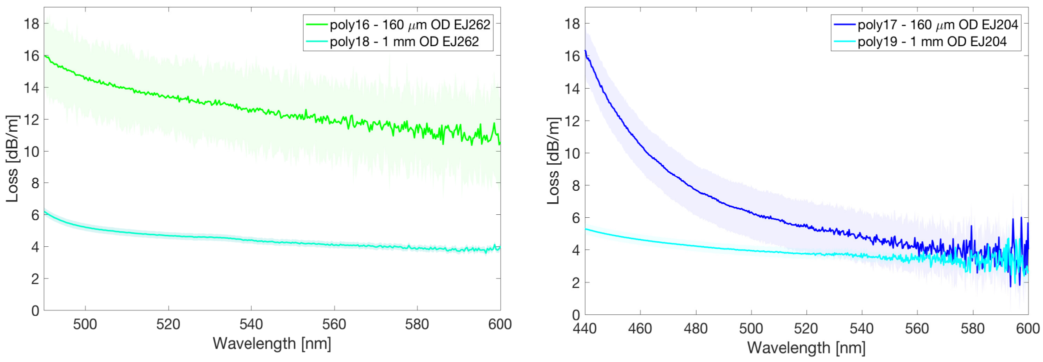

(a) (b)

Figure 3.22: Fibre loss comparison measured using the SIF technique for (a) 1 mm and 160 µm OD EJ262 LMW polymers (b)1 mm and 160 µm OD EJ204 LMW polymers

Diameter stability

During initial drawing trials the temperature, draw and feed speeds were adjusted in order to establish which values are required to achieve stability at the nominal diameter. Diameter variations for poly11 were measured to be $> \pm 20$ µm, which is reflected in the high attenuation of this fibre. High fibre tension during drawing in trial poly12 caused the fibre to break on two occasions; the fibre drawn was of very poor quality and was discarded, and no loss measurement was performed. An increase in drawing temperature, feed and draw speeds for future high moecular weight polymer drawing trials were sufficient to achieve good diameter stability with variations of $\approx \pm 5$ µm. Overall, small diameter fluctuations appeared to be correlated with lower measured losses.

Preform surface quality

The molecular weight of the polymer has an impact on the surface quality of the extruded preform, with low molecular weight polymer preforms displaying superior surface finishes than high molecular weight polymers for similar extrusion forces (see Section 3.2.4). Surprisingly, the loss results suggest the preform quality does not have a large impact on the fibre quality. The fibre from trial Poly13 was drawn from a high molecular weight preform with a rough surface texture as shown in Figure 3.9. Its attenuation is similar to fibres drawn from low molecular weight preforms (poly15, poly17) whose surface quality was distinctly improved. The most likely explanation for this is that the rough surface on the high molecular weight preforms are fire polished or smoothed from the high temperatures in the furnace during drawing, so have little effect on the fibre loss.

The high molecular weight preform used for the drawing trial poly14 was hand polished using water, various grade SiC polishing sheets, then colloidal silica until the surface quality resembled the low molecular weight preforms. The fibre drawn from this preform had considerable losses below the 550 nm region. It is likely the outer layer of the polymer was damaged during this procedure which contributed to the large losses observed.

Preform annealing conditions

All extruded preforms were annealed prior to drawing to remove the internal stress, however, annealing was not required when fibres were drawn directly from 1 cm outer diameter rods as purchased from the supplier, as no stress pattern was evident. The annealing conditions were varied with low molecular weight preforms, initially performed at 85°C for 24 h (poly11) and for subsequent trials the preform was annealed at the same temperature but for 6 days. In all cases, the stress pattern was removed and a decrease in fibre attenuation across the entire measurement range is observed when preforms were annealed over a 6-day period. This is not likely attributed to the change in annealing conditions, but in the refinement of the drawing conditions.

Molecular weight

High and low molecular weight optical fibres with similar diameter stability (LMW trials poly15, 17 vs. HMW trial poly13) show similar values of fibre loss. This indicates the molecular weight of the polymer does not appear to have a large impact on fibre quality. More drawing trials are needed to make any solid conclusions.

3.5.5 Comparison of in-house fabricated and commercial fibres

1 mm canes

The loss of the 1 mm canes drawn from EJ204 and EJ262 are compared with commercial varieties of the same dimensions with a similar scintillator formulation to determine if the fabrication process used could produce fibres of comparable quality. Presented in Figure 3.23 are the losses as measured using the SIF technique for the following fibres:

- **(a) EJ204 and BCF12** Both fibres are polystyrene based with outer diameters of 1 mm and no outer cladding. The scintillator formulations are not the same, but similar enough for a meaningful comparison to be made. Peak emission wavelengths vary slightly (409 nm for EJ204 compared to 432 for BCF12), as do manufacturer specified attenuation lengths (1.6 m for EJ204, and 2.2 m for the clad variety of BCF12 - unclad variations will have a lower attenuation length).

- **(b) EJ262 and BCF20** Again, both fibres polystyrene are based with no outer cladding and 1 mm diameters. Manufacturer specified emission peak and attenuation lengths are 481 nm and 2.5 m respectively for EJ262 and 492 nm and > 3.5 m for BCF20 (cladded variety)). Reported diameter variations for Saint-Gobain fibres are specified as 2 % of fibre outer diameter, similar to in-house drawn fibres with a 2.5 % diameter variation.

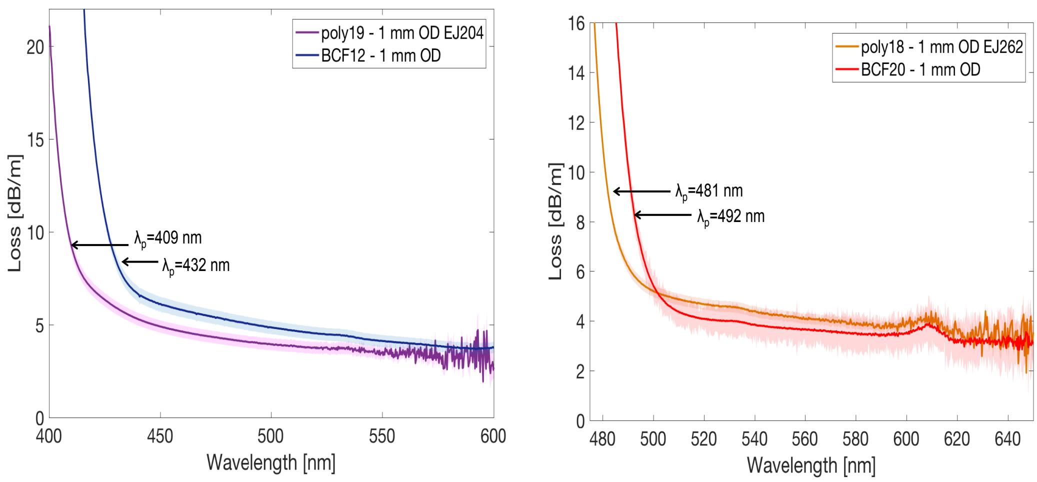

(a) (b)

Figure 3.23: Fibre loss comparison measured using the SIF technique for (a) 1 mm OD unclad poly19 (EJ204) and BCF12 fibres (b)1 mm OD unclad poly18 (EJ262) and BCF20 fibres

The loss of the in-house drawn fibres and the similar commercial varieties are approximately equal (within error) at longer wavelengths away from the emission peaks. The higher losses of the drawn fibres at the emission peak wavelengths may be due to their locations, as the in-house fabricated fibre emission peaks lie at shorter wavelengths where Rayleigh scattering is more pronounced.

160 µm diameter fibres

Commercial fibres with a similar diameter to the 160 µm in-house fabricated fibres without a cladding were not on-hand, however a comparison is made between 250 µm diameter clad fibres BCF12/20, and poly16/17. (see Figure 3.24).

The wavelength range over which attenuation values are displayed is limited by noise at shorter wavelengths, especially for fibres with higher losses. Consequently, for the 160 µm diameter fibres, the losses near the emission peak wavelengths could not be accurately measured so are not displayed. Diameter variations of the fibres fabricated in-house are approximately 3.2 %, larger than that specified for the commercial fibres (2%). Poly17 has a higher attenuation than BCF12 at shorter wavelengths, which is

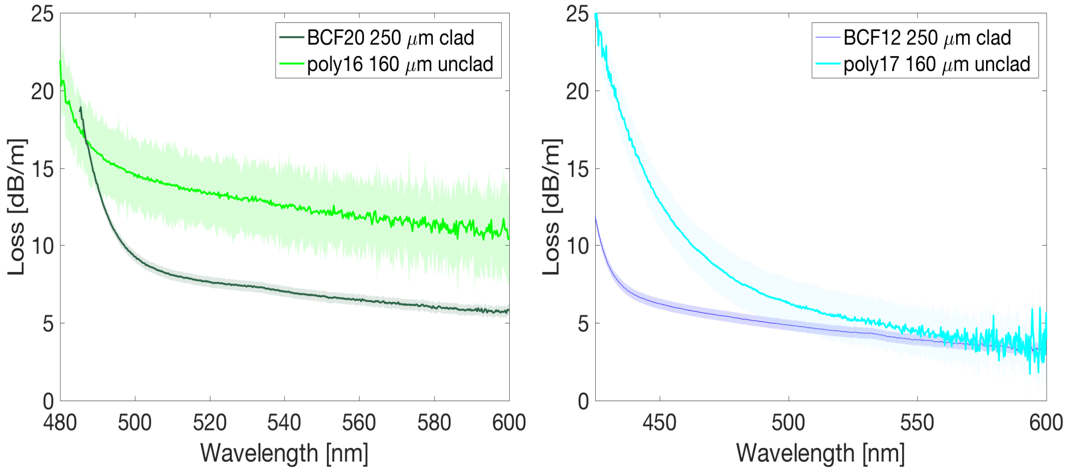

(a) (b)

Figure 3.24: Fibre loss comparison measured using the SIF technique for (a) 160 µm OD unclad poly16 (EJ262) and 250 µm OD clad BCF20 fibres (b)160 µm OD unclad poly17 (EJ204) and 250 µm OD clad BCF12 fibres

not surprising, given these fibres lack an outer cladding and a smaller diameter, both of which would contribute to increased surface scattering losses. The losses begin to approach the same value at longer wavelengths where surface or interface scattering effects will be low.

Poly 16 has a higher overall loss across the measurement range. In addition to higher surface scattering losses, the bulk loss of the polymer may be a cause of this increased loss.

3.6 Summary of fibre quality

The preceding sections document the fabrication of optical fibres from scintillating polymers, either directly from a 1 cm billet, or using a two step process where a preform is extruded from a 3 cm billet then drawn into fibre. Initial fabrication trials focused on drawing fibres down to an outer diameter of 160 µm, and losses upwards of 25 dB/m were reported at 440 nm with diameter fluctuations larger than 20 µm (12.5 %) recorded. Refinement of the drawing conditions by altering the drawing temperature, feed and draw speeds assisted with diameter stability, with average variations of ≈5 µm (3.2 %) recorded, with the loss at 440 nm brought down below 14 dB/m. Further attempts to reduce the attenuation by polishing high molecular weight preforms, or alter the annealing conditions were unsuccessful. No obvious difference in fibre quality was observed overall between high and low molecular weight polymers.

1 mm canes were drawn from low molecular weight polymers with outer diameter fluctuations (2.5 %) comparable to commercial fibres purchased (3%). The loss of 1

mm diameter fibres were found to be lower than 160 µm fibres drawn from the same material. 1 mm canes were found to have the similar losses to the commercial varieties tested, indicating the in-house drawing process can produce optical fibres of comparable qaulity.

3.7 Conclusions

Optical fibres with outer diameters of 160 µm and 1 mm have been fabricated using bulk polystyrene based scintillators, EJ204 and EJ262 from ELJEN Technologies, using a two step fabrication method. Bulk cylindrical billets were first extruded then drawn down to the required dimensions using a vertical drawing tower. The quality of extruded preforms were found to vary with molecular weight, extrusion speed and temperature the effects of all these parameters have been explored and discussed. Hot blade cleaving and automated polishing were investigated as cleaving techniques to produce optical quality end-faces of the fibres. Best results were obtained using an automated polisher, with average surface variations less than 40 nm observed in the 160 µm fibres. The transmission losses of fabricated fibres were characterised using white light cut-back, and SIF techniques. The quality of the 160 µm diameter fibres were improved by refinement of fibre drawing conditions, although their transmission losses were still rather high. The 1 mm canes were found to have much lower attenuation than 160 µm diamter fibres, and are comparable in quality to commercially available fibres. This indicates the high loss of the smaller diameter fibres is a result of scattering losses caused by greater interaction of the guided modes with the fibre surface and is not caused by a sub-standard fabrication process. The losses of commercially available fibres will be discussed in the following chapter.

No significant difference was observed in the optical properties of fibres fabricated from high and low molecular weight polymers. Both materials displayed nearly identical emission and absorption characteristics (as was shown in Chapter 2), so at this stage there does not appear to be any benefits choosing one formulation over the other. Characterisation of the fibres presented here in terms of their response to alpha and beta radiation will be presented in Chapter 4.

Chapter 4

Radiation and optical characterisation of polymer optical fibres

4.1 Introduction

There are several parameters which need to be considered when selecting an optical fibre for radiation measurements. Primarily, we are concerned with the sensitivity of the material to alpha and beta radiation, so the scintillating dopants within the material must produce enough photons in response to these radiation types, all the while maintaining low attenuation losses to enable the photons to reach the detection system. Performance and reliability of the dosimeter under specific environmental conditions must also be taken into consideration, and this will be investigated and discussed later.

During exposure to radiation, the amount of light detected from a scintillating fibre can be approximated using the expression:

$$\mathbf{N_{pe}} \propto \mathbf{S} \times \mathbf{CT} \times \mathbf{QE} \tag{4.1}$$

Where:

- $\mathbf{N_{pe}}$ is the mean number of photoelectrons detected, and is proportional to the light yield (number of detected radiation events) of the scintillator.

- **S** is a term that combines the scintillation efficiency of the material in terms of the number of photons produced per unit energy, and the total energy deposited in the fibre element.

- **CT** is the collection and transfer function, which depends on several factors including the trapping efficiency of the fibre, the attenuation of the scintillation light as it travels along the fibre, and coupling efficiencies between the fibre and photo sensor.
- **QE** is the quantum efficiency of the photo sensor at the wavelength region of interest.

Optimisation of these factors often involves application-specific trade-offs. For example, the light yield may be compromised so that the fibre can function under harsh environmental conditions. In this chapter, the scintillation response of a number of commercial optical fibres, and the highest quality 160 µm diameter in-house fabricated blue and green scintillating fibres (poly16, 17) are tested when exposed to β particles (from ^{90}Sr/^{90}Y) and α particles (from ^{241}Am). The spectrally dependant attenuation properties of the fibres are also considered as a means to illustrate how each term in Equation 4.1 affect the amount of light detected from a scintillating fibre and ultimately determine its suitability as a radiation detection element.

4.2 Experimental Program

4.2.1 Materials

Eight different types of plastic scintillating fibre were used in this investigation, six of which were sourced from a commercial supplier (Saint-Gobain), and the remaining two were fabricated in house using bulk plastic scintillator sourced from ELJEN technologies. All of the fibres have a round polystyrene based core, and in some instances, a poly(methyl-methacrylate) (PMMA) optical cladding. A list of the relevant fibre properties is shown in Table 4.1.

Name	**Manufacturer**	**Φ(µm)**	**Clad.(µm)**	**λ_{peak}(nm)**	L_{att}**(m)**	**γ**	**$\Delta\lambda_{peak}$ (nm)**
BCF10	St. Gobain	1000	30	432 (432)	2.2	8000	10
BCF 12	St. Gobain	1000	30	435 (435)	2.7	8000	12
		1000	0				16
		250	7.5				16
BCF 20	St. Gobain	1000	30	492 (496)	> 3.5	8000	10
		1000	0				15
		250	7.5				14
BCF 60	St. Gobain	1000	30	530 (530)	3.5	7100	1
BCF 91A (WLS)	St. Gobain	1000	30	494 (498)	> 3.5	N/A	10
BCF 92 (WLS)	St. Gobain	1000	30	492 (492)	> 3.5	N/A	14
BCF 98	St. Gobain	1000	30	N/A	N/A	N/A	N/A
		1000	0				N/A
.		250	7.5				N/A
poly 16	ELJEN	160	0	(486)	N/A	7400	14
poly 17	ELJEN	160	0	(432)	N/A	7400	49

Table 4.1: List of fibre varieties.

Φ=Outer diameter, **Clad.**=Cladding thickness, λ_{peak}=Wavelength corresponding to the scintillation emission maximum as specified by the manufacturer. Values shown in brackets were measured using an optical spectrum analyser, L_{att}=Attenuation length, defined as the length of fibre where the signal amplitude is attenuated to $\frac{1}{e}$ of its original value, and is specified by the manufacturer, γ=Scintillation efficiency, defined as the number of photons produced within the material per MeV of deposited energy by a minimum ionising particle, $\Delta\lambda_{peak}$= Measured shift of the emission peak in nm for a 150 cm length of fibre. N/A = Not applicable.

The scintillators used here are classified as either binary or ternary systems (Figure 4.1), depending on whether they have one or two fluors added to the base polymer. Following exposure to ionising radiation, energy is dissipated in the polystyrene matrix, a fraction of which is converted to fluorescence lying predominantly in the UV region of the electromagnetic spectrum. This fluorescence is rapidly attenuated and not well matched to the characteristics of common detectors like photomultiplier tubes. In a binary system, a fluor whose absorption band overlaps the polystyrene emission is incorporated within the base polymer to absorb the primary light emission and re-emit it at blue/green wavelengths where it can be efficiently detected. If a second fluor is added to the base polymer, it becomes a ternary system, otherwise known as a wavelength shifter. The second fluor in this formulation has its absorption band overlapping the emission band of typical blue scintillators, so are often used to absorb and shift the wavelength of the light emitted by binary systems to even longer wavelengths to match certain detectors. Green scintillators have their absorption and emission bands shifted towards longer wavelengths than blue scintillators, as such, their emissions lie in a wavelength region where Rayleigh scattering is less pronounced, allowing longer distributed sensing lengths.

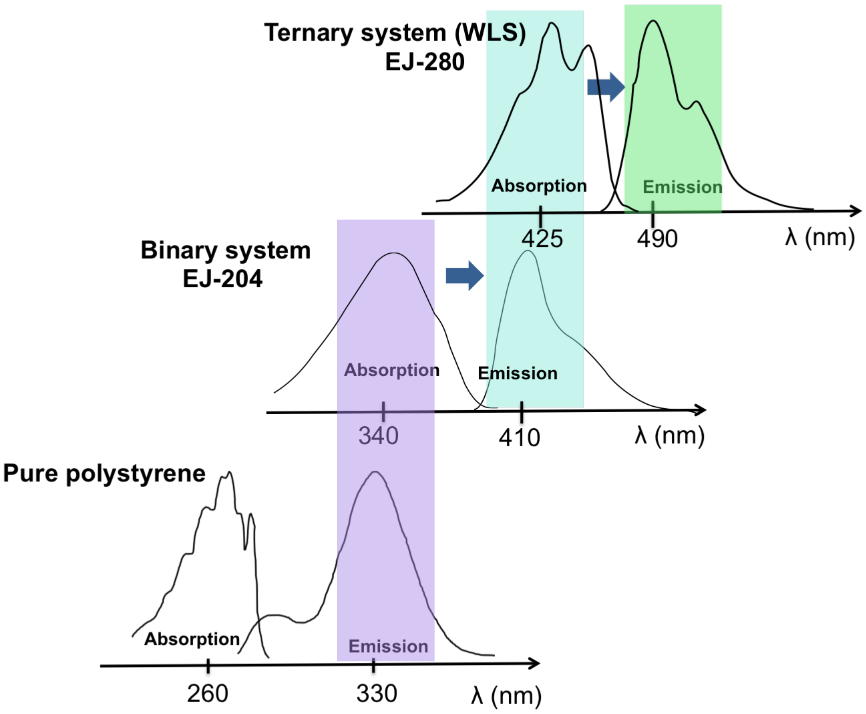

Figure 4.1: Emission and absorption band overlap between pure polystyrene, binary (EJ204) and ternary (EJ280) formulated scintillators

4.2.2 Sources of loss in polymer optical fibre

The transmission loss of scintillation light that travels along the fibre is a critical parameter when choosing a fibre suitable for radiation detection. Many processes contribute to light attenuation in optical fibres, the cumulative effects of which can be summed up within a single value, α, the attenuation coefficient.

$$\alpha = -\frac{10}{L}\log\left(\frac{P_0}{P_1}\right) \tag{4.2}$$

Where P_o, P_1 are the output and input optical powers respectively, L is the fibre length, and α is given in units of dB/unit distance. Within optical fibres, the loss mechanisms can be categorised as intrinsic or extrinsic, and scattering losses can be classed as either surface (S) or volume (V) scattering (Fig 4.2). Volume scattering is caused by imperfections within the volume of the fibre, and depends strongly on the size of the imperfections, whereas surface scattering is caused by imperfections or irregularities on the fibre core surface. The origins of intrinsic and extrinsic losses are:

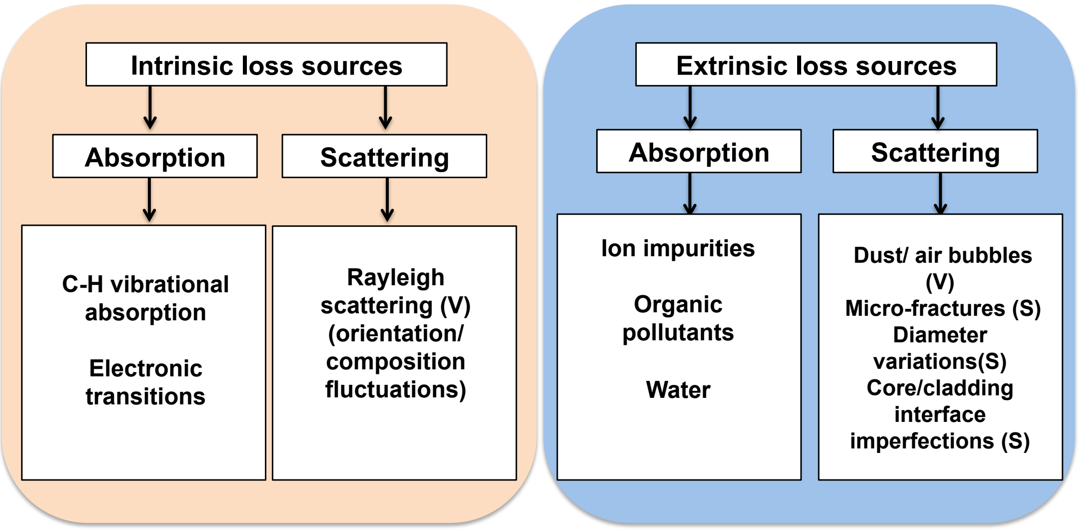

Figure 4.2: Sources of loss in polymer optical fibres. (V) = volume scattering effect, (S)=surface scattering effect

Extrinsic loss sources: This category of loss sources arises from imperfections and impurities present in the fibre core that are often introduced during and after (i.e fractures/scratches) the fabrication process. Some examples are:

- **Impurity absorption losses:** Absorption of light by impurities such as transition metal ions and water absorbed by the polymer matrix all lead to transmission losses in the fibre.

- **Scattering by physical imperfections:** Imperfections introduced during the drawing process such as:
  - Variations in the core diameter of the fibre will lead to surface scattering losses which are wavelength independent.
  - The introduction of dust and air bubbles during fabrication will lead to a wavelength dependant scattering loss which depends on the size of the imperfection.

Intrinsic (internal) loss sources: These arise from the material composition of the polymer and can cause large absorption losses in the visible and near IR wavelengths. In POF, the intrinsic sources of loss are:

- **Molecular vibrational absorption losses:** The organic molecules which make up the polymer absorb photons in the IR spectral region at characteristic frequencies and their harmonics, converting them into vibrational energy (heat). In particular, vibrational absorption from the carbon hydrogen bonds (C-H) in the polymer cause large losses in the near IR regions.

- **Electronic absorption losses:** Polystyrene, along with other polymers experience very strong absorption in the UV region of the spectrum due to electronic transitions between energy levels of the material bonds. In polystyrene, the π to π^* transitions within the bonds in the benzene rings account for the UV absorption edge.

- **Rayleigh Scattering:** Fluctuations in density, molecular orientation and composition of the polymer all lead to scattering of the light propagating within the fibre. This loss mechanism is a volume scattering one, and is inversely proportional to the fourth power of the wavelength ($L_R \propto 1/\lambda^4$), the implication of which is increased scattering losses at shorter wavelengths.

In plastic scintillators, self-absorption can be a significant source of light attenuation. Overlap of the emission and absorption bands of the material can lead to re-absorption of the short wavelength components of the emission spectrum followed by re-emission over the entire spectrum. This can result in large losses near the emission peak, λ_{peak}. The stokes shift of a scintillator is defined as the difference in wavelength between the peak of the absorption and emission wavelengths, $\Delta\lambda_{stokes} = \lambda_{peak,em}$ - $\lambda_{peak,abs}$. Higher stokes shifts generally result in less re-absorption of the scintillation due to the smaller overlap in area of the absorption and emission bands (Figure 4.3)

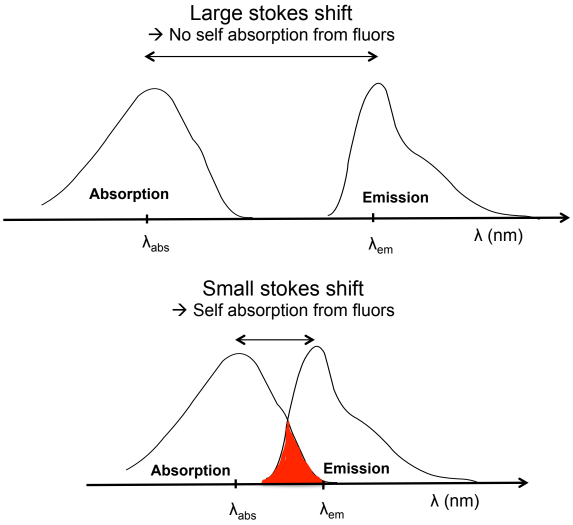

Figure 4.3: Schematic of self-absorption by scintillator emission/absorption band overlap

In addition to the loss sources described above, environmental factors can also have a large effect on fibre losses, because micro-fractures and other imperfections can be introduced or worsened. Ageing of the scintillator or exposure to radiation can cause colour centre formation within the material, further increasing attenuation. To illustrate the various sources of loss in a polystyrene based POF (poly17) refer to the schematic in Figure 4.4.

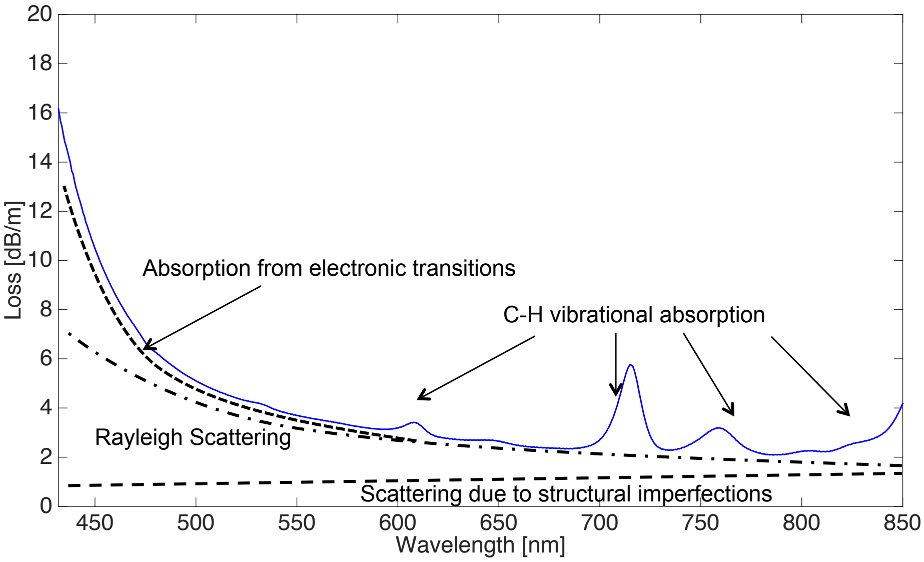

Figure 4.4: Schematic loss spectrum of poly17 showing various loss factors

4.3 Transmission loss measurements

4.3.1 Techniques for loss measurements

Attenuation length measurement

The attenuation length is defined as the length of fibre where the signal intensity is attenuated to $\frac{1}{e}$ of its original value. For the commercial fibres used in this study, the attenuation length is measured using a 3 m long piece of fibre which is excited at fixed points along its length by a ^{90}Sr/^{90}Y β source. The readout end of the fibre is polished and butt-coupled to a bialkali photomultiplier tube operating in analogue mode. The total signal collected is digitised and recorded at each irradiation point, and the attenuation length derived from a least squares analysis of these points. Using this method, L_{att} is calculated by collecting the total optical signal across the entire scintillation wavelength range for each data point, and gives no spectral information, so was not measured here. Wavelength specific attenuation was measured using the cut-back and Side Induced Fluorescence techniques (SIF). For the commercial fibres, attenuation lengths are specified for the 1 mm clad fibre varieties only, and are given in Table 4.1. Measured values of fibre attenuation are presented in Section 4.3.2.

White light cut-back technique

A common technique used to measure the wavelength dependant attenuation of an optical fibre is the cut-back method [41]. A stable broadband light source, in this case, a halogen globe, is coupled to the input end of the fibre and the wavelength dependent power, $P_0(\lambda)$, is measured at the output end of the fibre, length L, using an optical spectrum analyser (OSA). A length of fibre is cut, and the power, $P_1(\lambda)$ measured. Several of these measurements are performed, over a length of roughly 2 m, and the attenuation coefficient is calculated by fitting the data to Equation 4.1. The attenuation coefficient can vary with position along the fibre length so the cut-back method can be useful as it provides the total average attenuation. Fresnel reflections are eliminated, and any dependance of the attenuation on the launch conditions is removed as the input remains fixed. However, this method can also be disadvantageous as we lose information as to where the source of loss is along the fibre.

Any effects on the core light emission and subsequent power transmission caused by differences in fibre end-face quality were averaged out by carefully polishing the fibre end face flat several times to produce a new end-face at each measurement length. To ensure only light from the fibre core is measured, the modes propagating within the fibre cladding were removed by applying a graphite based paint, DAG, at each end of the fibre, near the collection and launch points.

UV induced scintillation loss measurements

An alternative technique for measuring the attenuation coefficient is using the SIF [22, 36], shown in Figure 4.5. This is primarily used to characterise the loss mechanisms in fluorescing waveguide structures, and has the advantage of being a non-destructive procedure. To perform the measurement, a monochromatic light source whose wavelength lies within the absorption band of the fluor illuminates the optical fibre from the side. The fluorescence produced within the core is guided by the fibre and recorded using an OSA at its end. To determine the fluorescence intensity variation as a function of fibre length, the illumination point on the fibre is varied by translating the source horizontally at fixed points along the fibre, and the attenuation coefficient is calculated by fitting the data to equation 4.1, as with the cut-back method.

For these measurements, a UV diode was used to induce scintillation within the fibres, as the radioactive sources on hand were too weak to produce enough light to be measured with the OSA. A 365 nm UV diode was used, because this was a common absorption wavelength for all scintillators in this study. The setup between these measurements and those using the cut-back technique were kept as similar as possible in order to compare results, and confirm the wavelength dependent attenuation values are similar. To reduce positioning effects and maximise the amount of light collected from the fibre end, an FC fibre adaptor was used to couple the fibre output to the OSA. The fibre was kept straight throughout the experiment to reduce bending losses and ensure the vertical illumination point on the fibre was kept constant. Consequently, the maximum fibre length that could be used for the SIF measurements was 150 cm, as this was the longest length of fibre that could lie straight across the optical table.

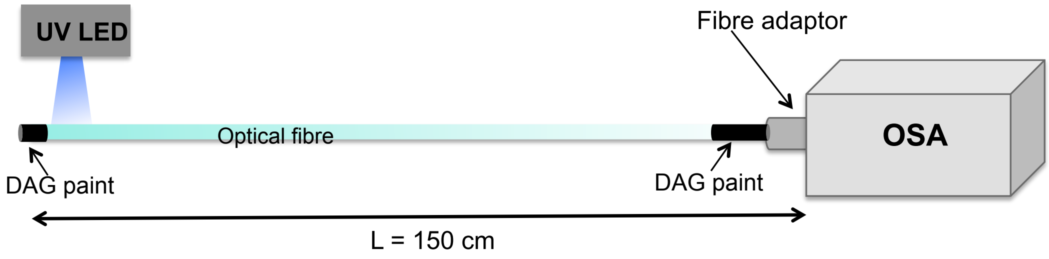

Figure 4.5: Schematic SIF setup

4.3.2 Results

For each fibre, the transmission loss was measured using the cut-back technique, and the SIF technique described above. Both measurements show good agreement of the attenuation values (Figure 4.5), and are within measurement error. From this point onwards, the measurements using the cut-back technique will be used to summarise findings as they generally had lower measurement errors.

A few trends were observed in the attenuation values of the fibres and will be discussed below.

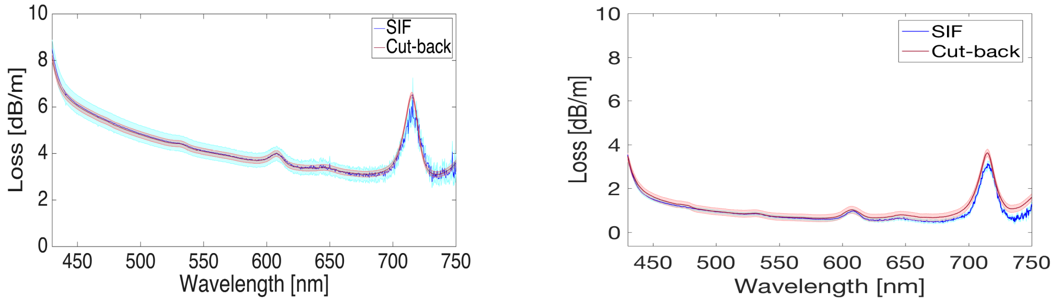

(a) BCF12 1 mm (b) BCF12 1 mm clad

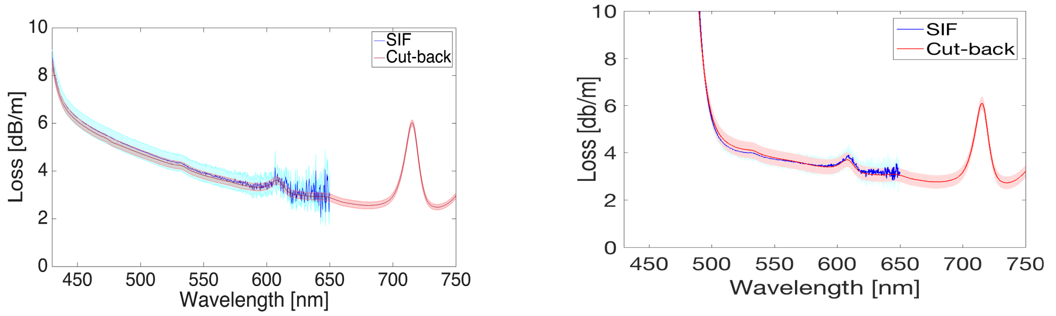

(c) BCF12 250 µm clad (d) BCF20 1 mm

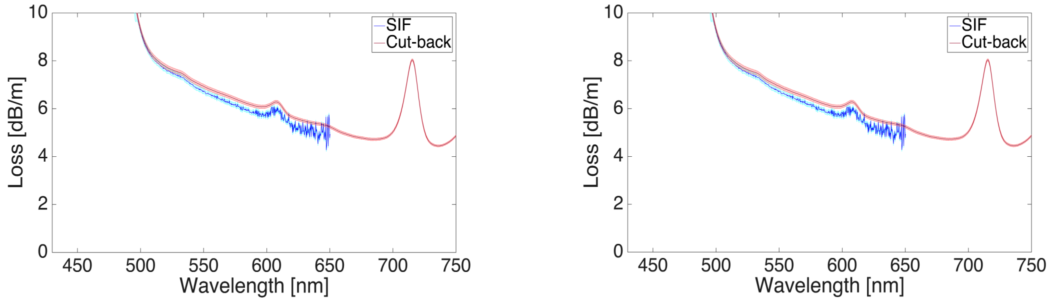

(e) BCF20 1 mm clad (f) BCF20 250 µm clad

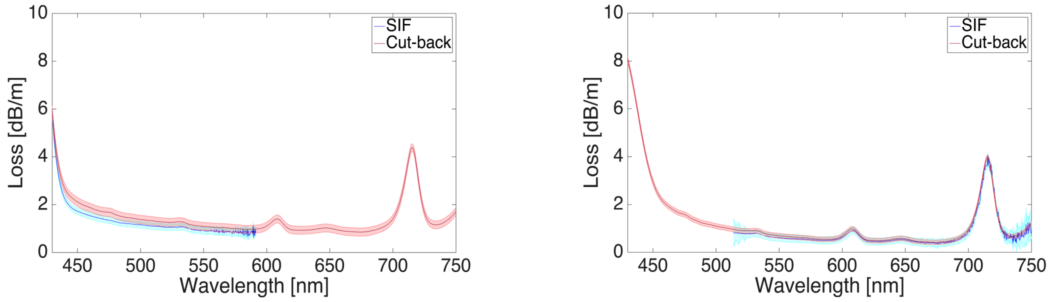

(g) BCF10 1 mm clad (h) BCF60 1 mm clad

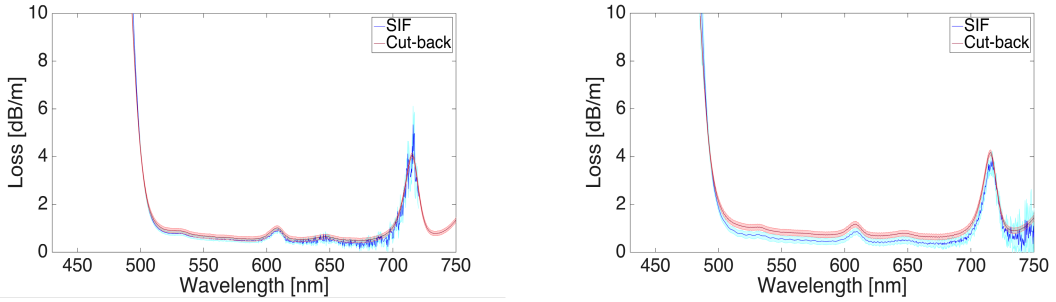

(i) BCF91A 1 mm clad (j) BCF92 1 mm clad

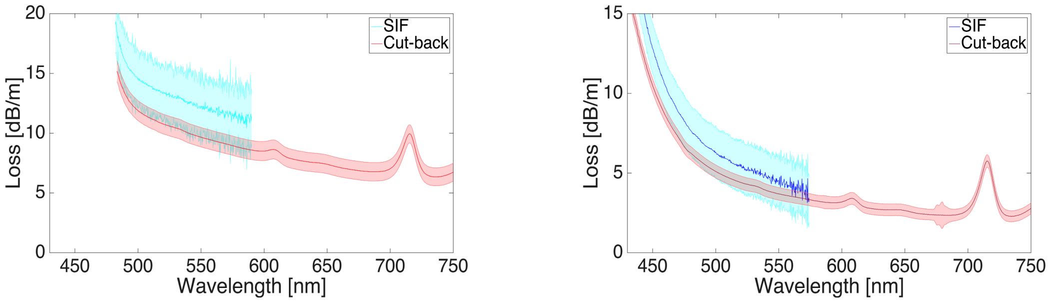

(k) poly16 160 µm

(l) poly17 160 µm

Figure 4.5: Comparison of loss measurement methods

Effect of scintillation wavelength on attenuation

The fibres used for this comparison are all of the 1 mm diameter variety with a 30 µm outer cladding, from which, a few results are shown for illustrative purposes. The following trends can be observed:

Consider a comparison between the undoped polystyrene fibre, BCF98, and the scintillator, BCF12 (see Figure 4.6). Generally, the scintillators will experience a rapid increase in attenuation at wavelengths near λ_{peak}, which can mostly be attributed to self-absorption and Rayleigh scattering (especially for the blue scintillators). The important thing to note, is the undoped fibre does not possess the sharp attenuation edge below 500 nm associated with self absorption, and the major loss source of this fibre below 500 nm would be Rayleigh scattering with no self absorption contribution. For unknown reasons, the doped BCF12 fibre appears to have an enhanced background loss, which could be related to the a difference in the optical quality of the bulk polymer, making it generally less transparent across the entire measurement range. The attenuation peaks at 607 and 715 nm are present in all the polystyrene based fibres tested, and are an intrinsic loss source caused by absorption of the carbon hydrogen bonds (C-H) in the polymer as described in Section 4.2.2.

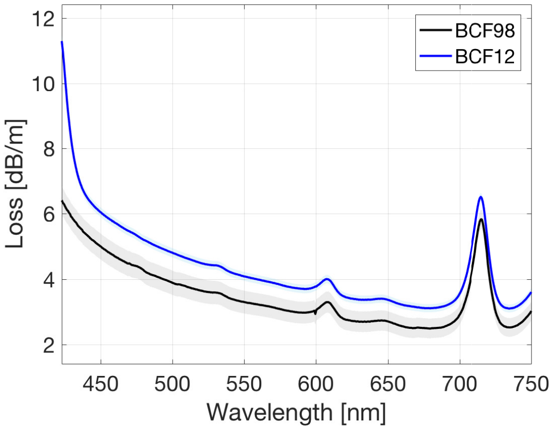

Figure 4.6: White light loss of 1 mm uncladded BCF12 and BCF 98

The blue and green scintillating fibres have different attenuation characteristics resulting from the location of the absorption and emission bands of their fluors, as was discussed in Chapter 1. The green scintillators will emit in a more transparent region of the material where Rayleigh scattering is less pronounced. Hence, these scintillators possess longer attenuation lengths than the blue varieties, consistent with the attenuation measurements performed here. The green scintillators BCF20 and BCF60 display lower losses near their emission regions (wavelengths above ≈ 500 nm) than the blue scintillators BCF10 and BCF12 (see Figure 4.7). The wavelength shifting formulations BCF91A and BCF92 show similar losses in this region. Below 500 nm, the loss of the blue scintillators are lower than observed for the green scintillators and the wavelength shifting fibres.

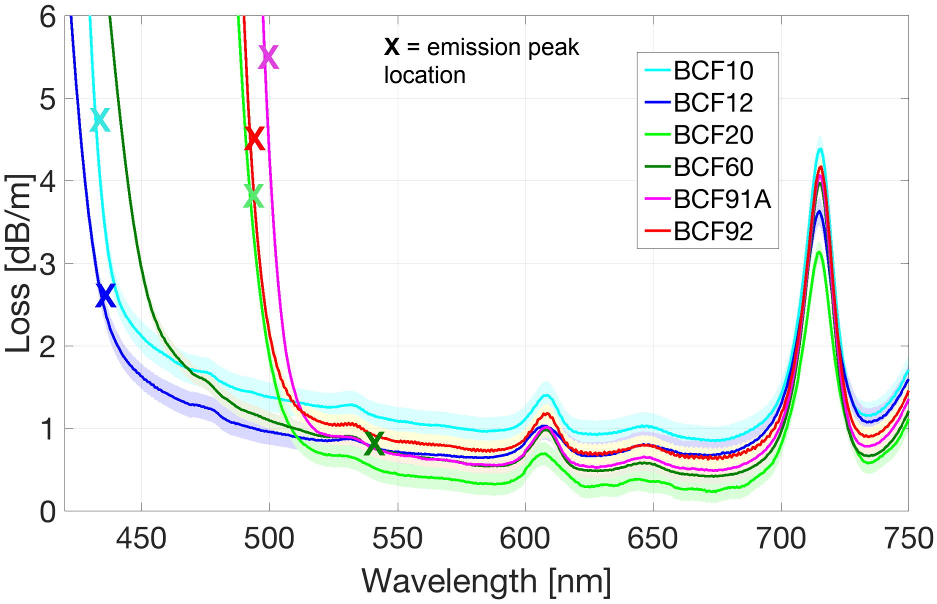

Figure 4.7: white light cut-back loss of all 1 mm cladded fibres

All the fibres tested except BCF60 displayed the attenuation edge attributed to Rayleigh scattering and self absorption near λ_{peak}. According to the manufacturers specification, this scintillator variety is formulated using 3HF, a wavelength shifter with a large stokes shift, meaning the absorption and emission bands are very well separated (Figure 4.3). More specifically, the absorption band is below ≈ 370 nm and emission begins around 480 nm. The attenuation edge associated with this fibre is not present near λ_{peak} as with all other fibres tested, but instead coincides with the location of the longer wavelength components of the absorption band of the fluor.

Effect of optical cladding on attenuation

The majority of the fibres used in this investigation have a polymer cladding layer which acts as a protective coating around the fibre core. In contrast, unclad fibres do not have a protective coating, and the fibre core is exposed to the surrounding environment (usually air). Fibre transmission is dependent on the degree of surface finish, making it very susceptible to light loss via surface scattering effects from any damage or imperfections present on the core surface, and from the surrounding environment. Generally, the surface quality of the fibre core has less of a pronounced effect on the transmission when an outer cladding is present (provided there is no contamination between the polymer/polymer interface), and in addition, the fibre will also be more robust against physical damage and environmental effects.

To demonstrate the effect the outer cladding has on the attenuation characteristics of the fibres, consider BCF12 and BCF 20, shown in Figure 4.8 (a) and (b) respectively. In each configuration, the two scintillators differ only by the presence of an outer cladding. The cladded fibres display lower attenuation values over the entire wavelength range, and could mostly be attributed to a reduction in surface scattering losses. Imperfections between the core/cladding interface would still contribute to loss, however this effect would be minor compared to losses caused by imperfections at the polymer/air interface of unclad fibres. Nevertheless, addition of an outer cladding around the fibre core dramatically decreases the fibre attenuation.

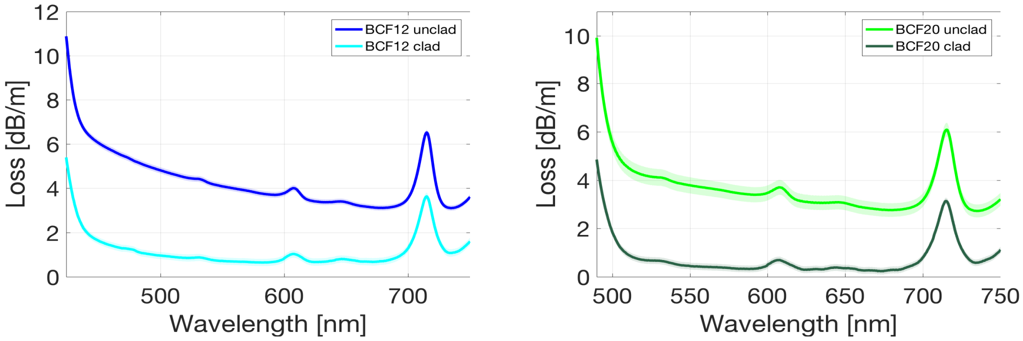

(a) (b)

Figure 4.8: Loss effects of clad vs. unclad 1 mm fibres

Effect of core diameter on attenuation loss

To illustrate the effect of core diameter on the fibre core attenuation, it is important to compare fibres that only differ by their core diameter. For the case of the 1 mm fibres, the core diameters of the clad and unclad varieties are essentially equivalent for most purposes, but given the cladding was found to have a significant effect on attenuation only fibres with or without claddings whose outer diameters differ will be considered. The fibres used for this comparison will be:

- BCF12 with outer diameters of 250 μm and 1000 μm, both with outer cladding (see Figure 4.9(a)). The cladding thicknesses are specified as 3% of the outer diameter by the manufacturer, but we will assume here this small difference in cladding thickness between the two fibres has a negligible effect on the attenuation properties when compared with the differences in core diameter.

- BCF20 with outer diameters 250 µm and 1000 µm, with outer claddings (See Figure 4.9(b)).
- BCF 12, 1000 µm outer diameter, and poly 17 with an outer diameter of 160 µm, both with no outer cladding. These fibres have similar emission wavelengths and differ mostly by their core diameter so will also be included in this comparison (see Figure 4.9(c)).
- BCF 20, 1000 µm outer diameter and poly 16 with a 160 µm outer diameter, both without outer cladding. Again, these fibres were chosen for their similar properties and differing core sizes (see Figure 4.9(d)).

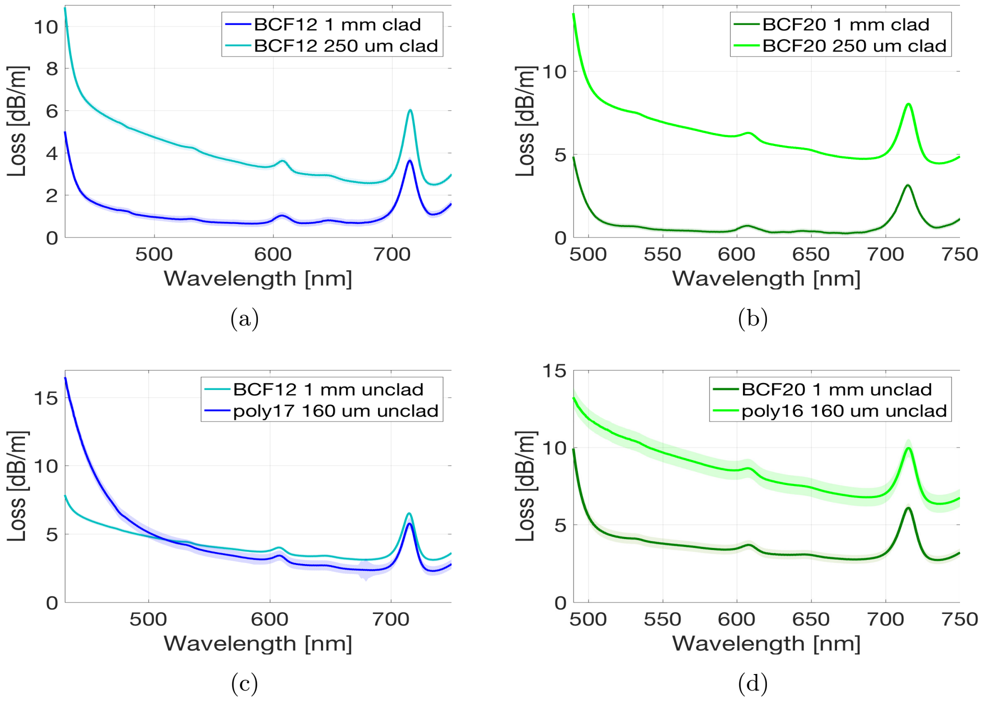

(a) (b)

(c) (d)

Figure 4.9: Fibre core diameter effect on fibre losses

Based on the graphs shown in Figure 4.9, it appears the increase of the core diameter causes an attenuation decrease as expected. There will be a larger component of the propagating modes interacting with the surface of the fibre as the core diameter decreases, so surface scattering effects are expected to increase. The result is an overall increase in fibre attenuation, which is more pronounced in the shorter wavelength regions with decreasing core diameters. BCF12 and poly17 are not consistent with this trend at wavelengths above ≈ 500 nm, as the loss of poly17 becomes smaller than that of BCF12, again this may be due to differences in the attenuation of the bulk material.

Loss effect on fibre emission spectra

The SIF technique measures the fibre loss by recording the intensity of the scintillation emissions from the fibre as a function of irradiation distance. In addition to the fibre loss, this measurement technique provides an insight as to how the emission spectrum changes as a function of the fibre length. Using the setup in Figure 4.5, the fibre emission spectrum was recorded when the fibre was irradiated at 10, 25, 30, 45, 60, 75, 90, 105, 120, 135 and 150 cm from the detector.

A red shifting of the scintillation emission was observed as the irradiation distance from the detector was increased, a phenomenon that is believed to result from fluorescence self-absorption. When the fibre is illuminated at points further from the OSA, the path length of the generated photons is increased which results in a higher frequency of interactions with the fluor molecules in the polymer. Consequently, there are more opportunities for the shorter wavelength components of the scintillation to be re-absorbed causing an effective red-shifting of the scintillation. A small fraction of the re-absorbed light will be re-emitted across the entire scintillation spectrum and captured, however this is not expected to alter the emission spectrum significantly.

The peak emission shifts for each fibre type are listed in Table 4.1. Despite the differences in scattering losses between different fibres, no real trend is evident which indicates scattering loss does not contribute significantly to the emission shift. The majority of fibres display a peak shift, Δ_{peak}, between 9-18 nm (with the exception of poly 17 where Δ_{peak}=39 nm). The emission spectrum of Poly17 (Figure 4.10) looks somewhat distorted, with no change observed after repeated measurements. One possible cause is the preferential attenuation of the higher energy spectral components by the coupling adaptor, as such, it would be hard to draw any conclusions based on this spectrum.

Evidence for the self-absorption induced emission shift is illustrated nicely when we compare BCF60 (Figure 4.11), with a comparable fibre, say BCF 20. Both are green scintillators, with the same dimensions and optical claddings, however BCF60 does not suffer any noticeable self-absorption effects due to the large stokes shift between its absorption and emission bands. There is a gradual decrease in measured intensity more evenly across the whole spectrum in the BCF60 fibre as the path length of the scintillation light increases, producing an overall peak emission shift of 1 nm (Figure 4.11(a)). In contrast, the intensity of the lower wavelength scintillation components are attenuated much more rapidly in the BCF20 fibre and there is an emission peak shift of 10 nm (Figure 4.11(b)). Although the red-shifting behaviour of the scintillation emission is not overly dramatic, it should be considered when designing a sensor and choosing an appropriate photodetector, as long fibre lengths can shift the emission

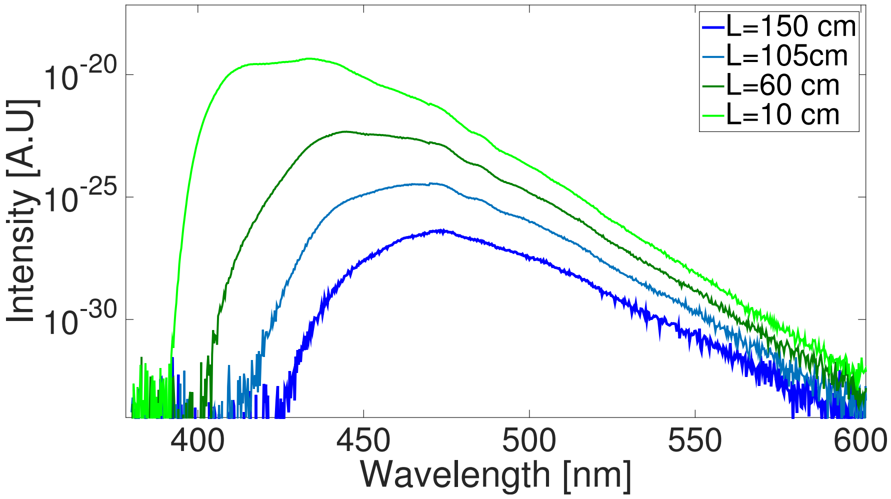

Figure 4.10: Scintillation emission of poly 17 as a function of fibre length between 10 and 150 cm

spectrum away from the desired quantum efficiency region of the photodetector.

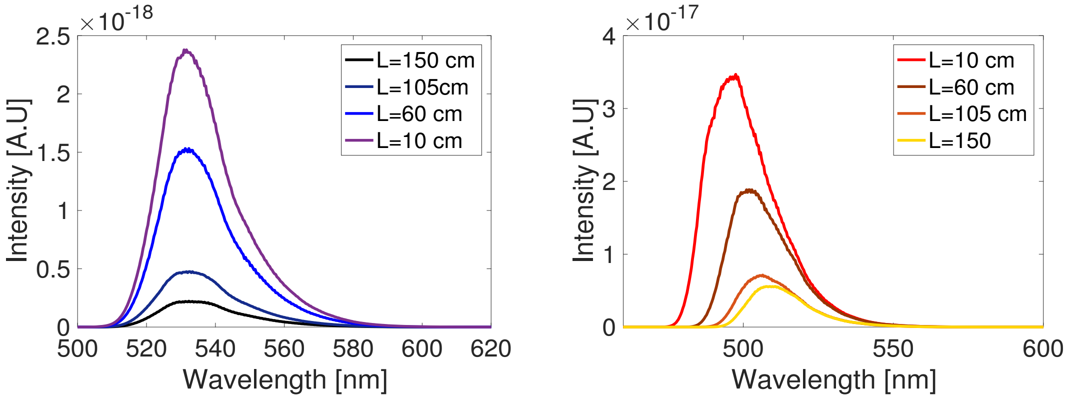

(a) BCF 60 1 mm clad (b) BCF 20 1 mm clad

Figure 4.11: Scintillation emission spectra variation as a function of fibre length between 10 and 150 cm

4.3.3 Summary of optical attenuation measurements

The fibre attenuation was found to vary considerably depending on the core diameter, scintillator composition and optical cladding. The most dramatic impact on the fibre attenuation is realised when an outer cladding is present, and as will be shown in Chapter 5, the outer cladding is essential in preventing signal loss under the proposed environmental conditions.

4.4 Alpha and beta particle irradiation measurements

The light yield of the scintillating material is arguably the most important material property when considering device design for practical applications. Once all the various efficiency factors are taken into account, including coupling losses, fibre attenuation, trapping efficiency etc, it is likely that only a couple to 10's of photons are reaching the detector from a single ionising particle interaction. Hence, the total amount of light produced within a fibre and collected is critical for the final device design, so in this section the fibres listed in Table 4.1 are investigated to determine their response and behaviour under α and β irradiation.

To measure the response of the scintillating fibres to α and β radiations, a length of fibre is placed on the test setup (see Figure 4.12). The fibre is held reproducibly in place relative to the source using a grooved holder machined from aluminium, which was chosen because its low atomic number minimises high energy bremsstrahlung contributions to the signal. The source is translated along the fibre a distance, z, between 10 to 160 cm to vary the distance between the excitation point and fibre end. To ensure comparisons between fibre measurements are accurate and reproducible, a number of precautions were taken. The readout ends of the fibres have been polished flat and held in place relative to the detector face using a fibre adaptor to improve the coupling efficiency, and minimise positioning errors. To avoid any back-reflections at the plastic-air interface, the non-readout ends of the fibres were roughened and blackened by applying DAG paint. The same paint was also applied to a small section around the outside of the clad fibres near the detection end to strip away any cladding modes in the same way as with the loss measurements. This ensures the light collected from the fibre contains only contributions from the scintillating core.

The scintillation light was read out with an ET 9829B photomultiplier tube, and data collected for 100 s at each irradiation point along the fibre. The dark counts were subtracted to give the total light yield (number of events detected). The error bounds shown were taken by moving the fibre tip ±0.5 mm from the normal position within the adaptor and recording the light yield deviation. The maximum variation was $\pm$ 3%, which was combined with the counting error, $\sqrt{n}$. The activities of the ^{90}Sr/^{90}Y β source and the ^{241}Am α source are 280 kBq, and 28 kBq respectively. For comparison purposes, the total light yield measured using the β source was divided by a factor of $\frac{A_\alpha}{A_\beta} = 10$ to correct for differences in source activities.

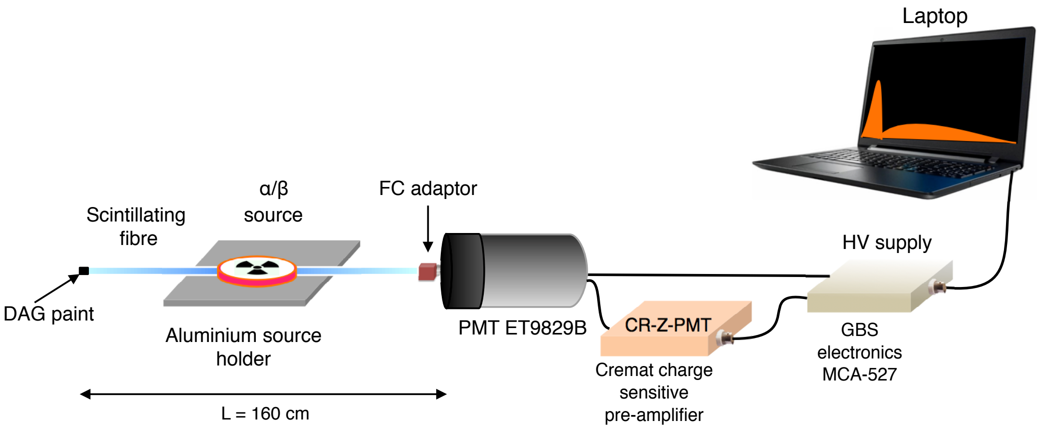

Figure 4.12: Setup for irradiation measurements

Alpha particle penetration depths

The alpha particles emanating from the surface of the 28 kBq source have an average energy of 4 MeV. Their ranges in PMMA and polystyrene can be calculated using the expression:

$$\mathrm{R} = \mathrm{R}_{\mathrm{csda}} \div \rho_{\mathrm{material}} \tag{4.3}$$

Where $\mathrm{R}_{\mathrm{csda}}$ gives the average value in $\frac{\mathrm{g}}{\mathrm{cm}^2}$ of the alpha particle penetration depth

as it comes to rest, ρ is the density of the material the alpha particle is incident upon ($\frac{\mathrm{g}}{\mathrm{cm}^3}$), and R gives the penetration depth in cm. The values for $\mathrm{R}_{\mathrm{csda}}$ are taken from the NIST ASTAR database [60]. Using Equation 4.3, the penetration depths of the alpha particles are calculated and presented below in Table 4.2.

Material	**Density**$(\mathrm{g/cm^3})$	$\mathbf{R_{csda}}(\mathrm{g/cm^2})$	**R (µm)**
PMMA	1.18	2.734e-3	23.17
PS	1.03	2.634e-3	25.57

Table 4.2: Alpha particle ranges in PMMA and PS

Because the penetration depth is limited, the alpha particles are expected to deposit all their energy in a very thin layer at the surface of the material. The scintillation signal produced within the optical fibre is expected to scale with the surface area of the optical fibre, so the light yield will be proportional to the radius. Additionally, due to the limited penetration depth, the alpha particles are not expected to penetrate the 30 µm outer cladding of the 1 mm fibres, but should be able to pass the 7.5 µm cladding on the 250 µm cladded fibres to interact with the core.

Beta particle penetration depths

The beta particles from the ^{90}Sr/^{90}Y have a more complex energy distribution than the ^{241}Am alpha particles. The long lived ^{90}Sr ($t_{1/2}$=29.1 y) component of the beta source decays to a short lived daughter, ^{90}Y ($t_{1/2}$=64.1 h), with the two components existing in equilibrium. The energy spectrum is thus the sum of the spectra of its components with $\overline{E}_{Sr}$=196 keV and $\overline{E}_{Y}$=933 keV. Due to the continuous energy spectrum, the penetration depths of the beta particles within the plastics will vary considerably depending on their energy. The ranges for a few different beta particle energies are calculated using Equation 4.3 and shown in Table 4.3. Only the ranges in polystyrene are considered as the small density difference between PMMA and PS will have a negligible effect on the range.

$\mathbf{E}_\beta$	$\mathbf{R_{CSDA}}$**(g/cm^2)**	**R(mm)**
200	4.578e-2	0.44
500	2.059e-1	1.99
2000	1.008	9.79

Table 4.3: beta particle ranges in polystyrene.

Beta particles will travel on the order of two magnitudes further in the scintillator than an alpha particle of equivalent energy, however they deposit much less energy per unit path length. The cladding thickness is insignificant in comparison to the calculated ranges and consequently will not inhibit energy deposition in the fibre core by the beta particles.

4.4.1 Detector choice

For these measurements, a bialkali photomultiplier tube (PMT) was chosen for detection of the scintillation light produced within the fibres due to its fast response time, high detection efficiency around 400 nm, and large detection area (50 mm diameter photocathode). The photomultiplier tube is operated in analogue mode with a charge sensitive pre-amplifier, and multichannel analyser as described in Chapter 1.

The number of photons produced within the scintillator depends on the energy deposited in the material by the primary radiation event. A large energy deposition within the scintillator can cause the emission of several tens of photons within a few nanoseconds (depending on the decay time of the scintillator), and a small energy event may only result in the production of 1 photon within the same time frame. The output DC pulse produced by the photomultiplier tube will have an amplitude dependent on the number of photons generated by a single event - an event consisting of several tens of photons will produce a larger amplitude pulse than an event containing a few photons (refer to Figure 4.13). The multichannel analyser will bin large amplitude events at higher channel numbers than low amplitude events, hence the channel number shown on a pulse height spectrum is proportional to the energy of the primary radiation event causing the scintillation pulse. The y-axis represents the total number of events (intensity) detected of a given voltage output.

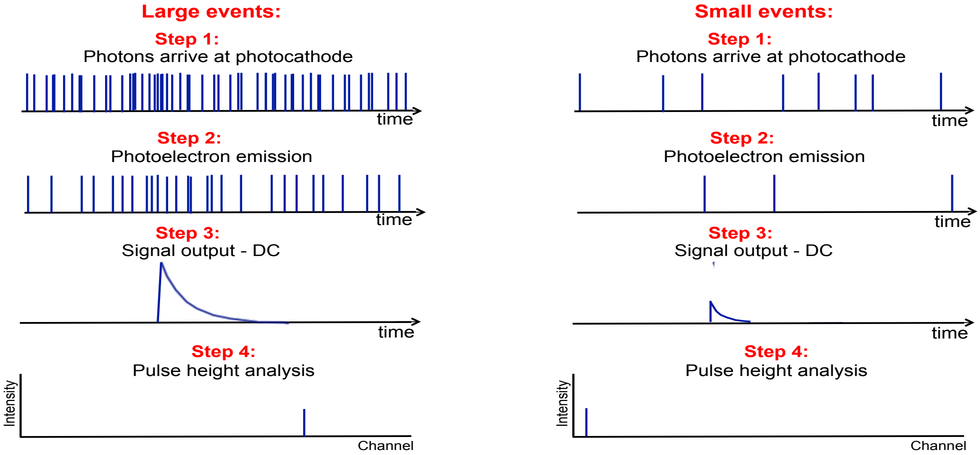

Figure 4.13: PMT analogue mode operation

In addition to the fast (≈ 3-12 ns) scintillation component produced in plastic scintillators, there will also be phosphorescent and delayed fluorescent emissions produced whose decay times are of the order of µs or longer (see Chapter 1.5.2 for more details). The fast fluorescence represents the majority of the signal for most organic scintillators, and as such, the time constants of the detector circuitry were set up to be very short to measure this emission component. These time constants are much shorter than the typical decay times of the phosphorescence and delayed fluorescence and consequently, each photon associated with these components is usually resolved on an individual basis. These 'slow' decaying photons will correspond to the generation of a single photoelectron which cannot be distinguished from thermal noise. It is worth noting the slow components of the scintillation depends on the nature of the ionising particle and can be used for pulse shape discrimination, however for applications involving high counting rates the phosphorescence is undesirable.

Pulse Height Analysis

A typical scintillation pulse height spectrum using a scintillating fibre and a ^{90}Sr/^{90}Y β source is shown in Figure 4.14. The narrow, large intensity peak located around channel 70 is called the single electron peak (SEP), and corresponds to events which cause the emission of a single photoelectron, including thermal photoelectrons. When performing the light yield measurements, the high voltage was kept constant but the coarse gain was chosen to ensure all the high energy events were recorded for each type of fibre. Coarse gain does not affect the total number of events detected (this was verified), it just shifts each event proportionally to a lower channel number.

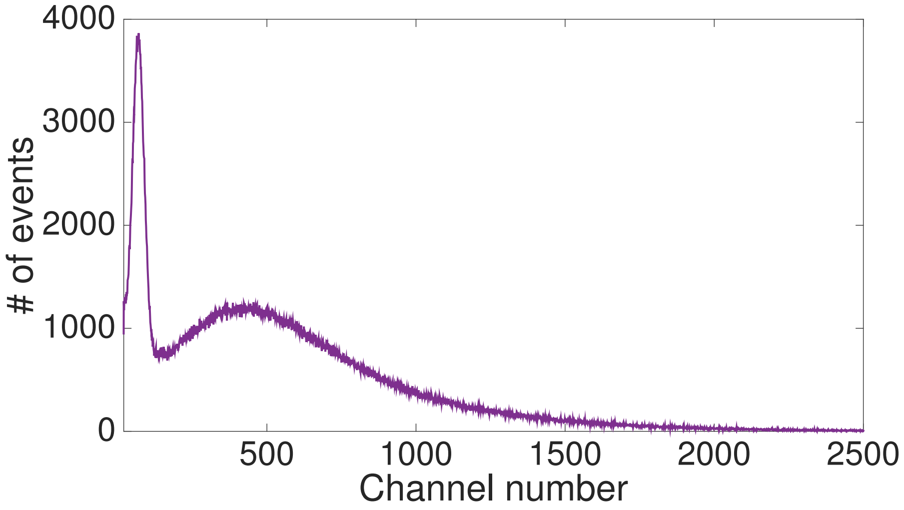

Figure 4.14: Scintillating fibre pulse height spectrum using beta irradiation

4.4.2 Alpha particle irradiation results

The ^{241}Am source used for these experiments produces a 60 keV gamma photon in addition to alpha particles. To ensure the signal collected from the fibre is purely alpha particle induced, a background measurement was performed at each irradiation point by placing a thin aluminium foil between the source and the optical fibre. The foil will completely block the α particles, and allow relatively free passage of the 60 keV gamma photon. The gamma signal is then subtracted from the total signal. A few trends in the detected light yield were observed between fibre types, however, due to the lack of fibre variations of a particular type these trends are difficult to quantify. The findings are discussed below.

Total light yields for alpha irradiation

The highest light yield using alpha particle irradiation was measured with the 1 mm diameter uncladded BCF12 fibres. The large surface area of the fibre, high detection efficiency of the scintillation light and the lack of outer cladding all contribute to the large signal detected using this fibre type. These effects will be discussed in greater detail in Section 4.5. The light yield as a function of irradiation distance for each fibre is shown relative to that of the 1 mm unclad BCF 12 fibre in Figure 4.15.

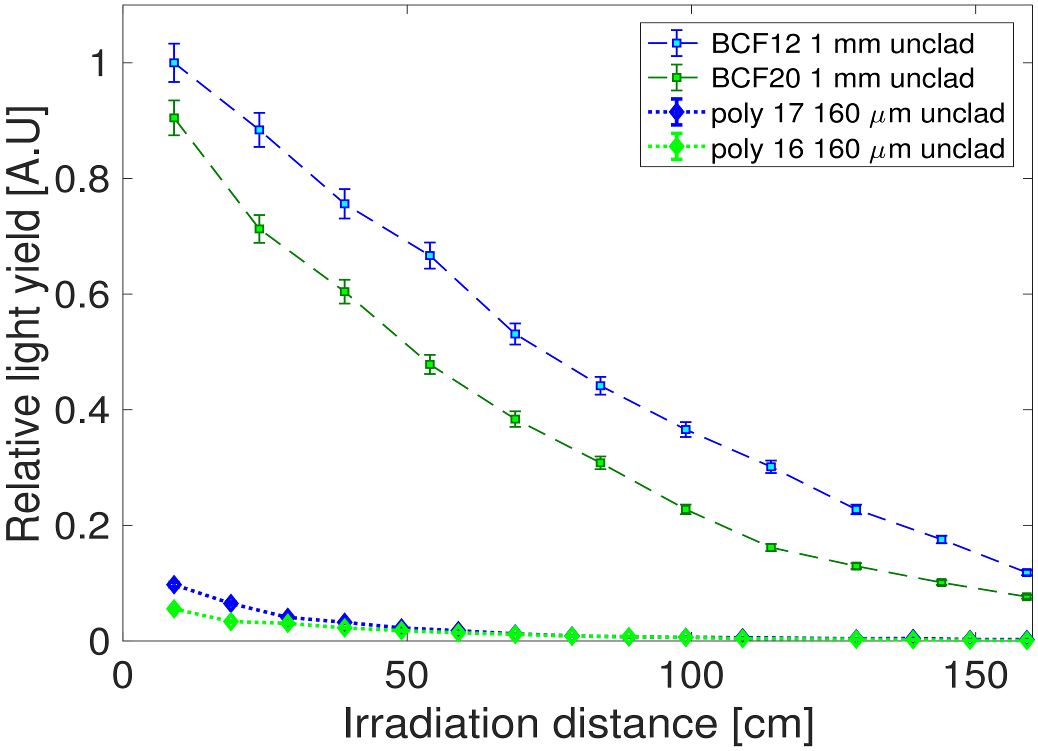

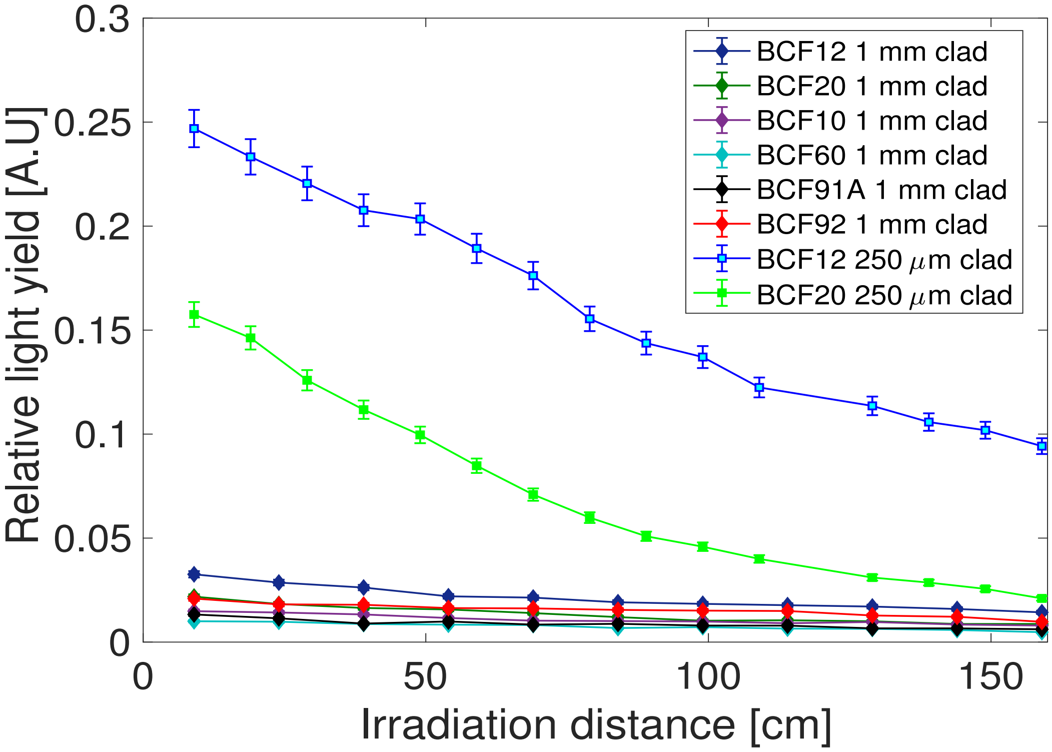

Figure 4.15: Relative light yields for alpha irradiated fibres without outer claddings (top) and with outer claddings (bottom)

The 1 mm clad fibres produce the lowest light yields. This is expected as the 30 µm cladding on these fibres is too thick to allow the 4 MeV alpha particles to penetrate and reach the fibre core. Despite the cladding thickness exceeding the alpha particle range, a small amount of light is still detected above background levels and could be attributed to fluorescence produced in the cladding material. The 250 µm fibres display good light yields despite having an outer cladding, as it is thin enough (7.5 µm thick) to allow the alpha particles to penetrate the fibre core. Signal losses across the fibre length are proportionally lower when an outer cladding is present and can be attributed to the decreased transmission losses of these fibres. Fibres drawn in-house show a larger response than the 1 mm clad fibres, however the scintillation signal decays quite rapidly with distance which limits their useable length.

4.4.3 Beta particle irradiation results

These measurements were performed in the same way as the alpha particle measurements, except the background measurement was taken with the ^{90}Sr/^{90}Y source removed so that it was not in contact with the optical fibre. The photomultiplier tube was surrounded by lead blocks to protect it from stray x-rays and secondary electrons.

Total light yields for beta irradiation

The cladded 1 mm thick BCF12 fibre produced the highest light yield across the whole measurement range (10 to 160 cm) in response to beta radiation, and the response of all fibres (shown in Figure 4.16) have been normalised relative to this. BCF10 shows roughly the same light yield as a function of distance as the 1 mm cladded BCF12, both fibres have very similar emission wavelengths and the same photon production efficiency, however BCF12 has a longer quoted attenuation length which is not noticeable here. Similarly, BCF 20 has only a slightly higher light yield than BCF 60 for the 1 mm clad varieties across the entire fibre length, consistent with BCF 60 having a lower scintillation efficiency. The wavelength shifting fibres have the lowest light yields of the 1 mm diameter fibre varieties. Further decreases in light yield are observed with 250 µm and 160 µm fibres.

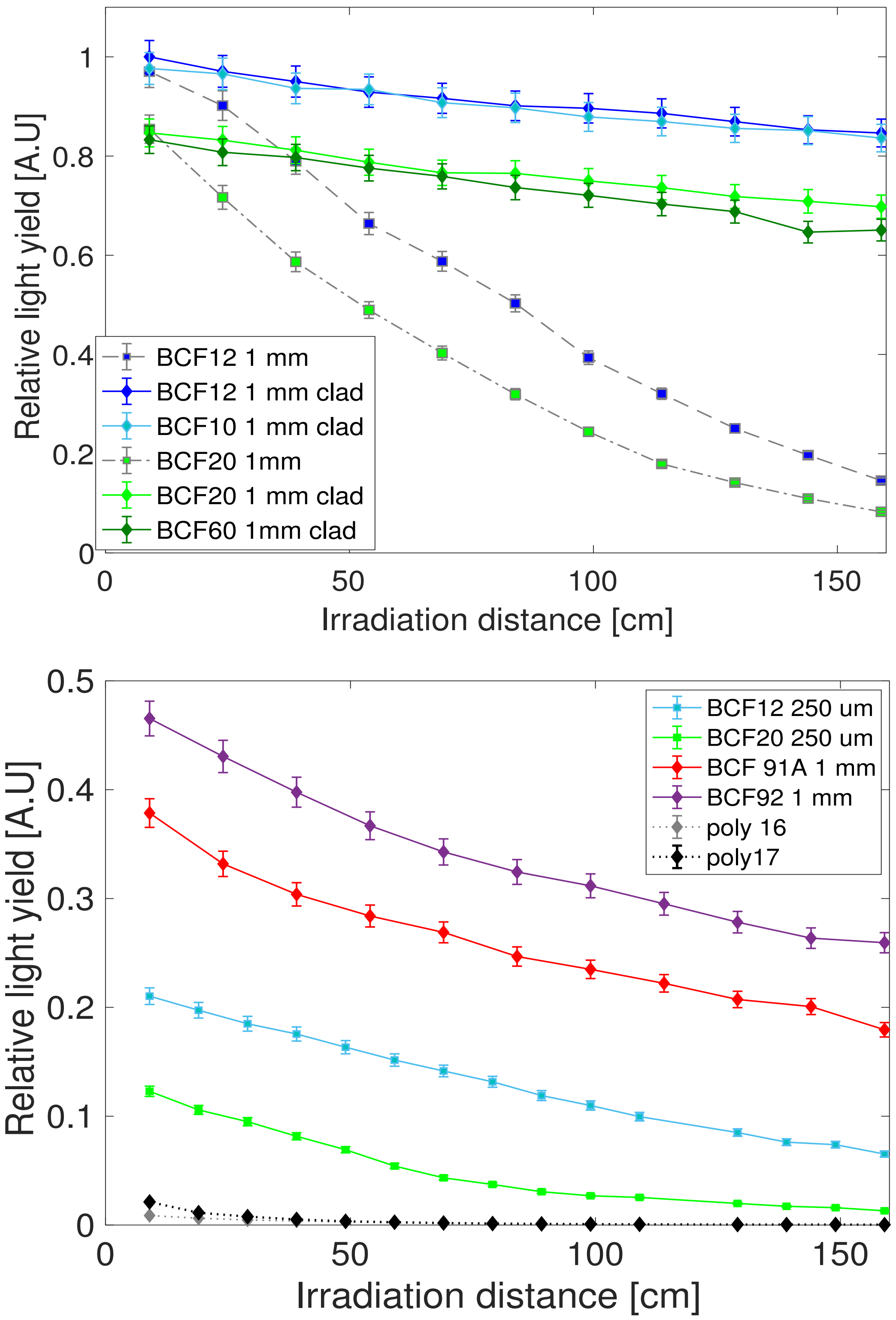

Figure 4.16: Relative light yields for beta irradiated fibres

4.5 Discussion of factors affecting fibre light yields

Light yield dependence on emission wavelength

When comparing blue and green scintillators of the same configuration (see Figures 4.16 and 4.15), the light yield is always larger for the blue varieties regardless of irradiation source, as a result of the wavelength dependent sensitivity of the photomultiplier tube. The detection quantum efficiency varies with the wavelength of incident light, ranging from a maximum of almost 30 % at 350 nm and dropping sharply thereafter at larger wavelengths. At 550 nm, the QE is only 5%, so the detector response across the whole emission spectrum of the scintillator must be taken into account. Figure 4.17 shows the wavelength dependant quantum efficiency of the photomultiplier tube overlaid with the emission spectra of the blue and green scintillators BCF12 and BCF 20. The spectral response of the blue scintillator is higher which accounts for the observed increase in light yield.

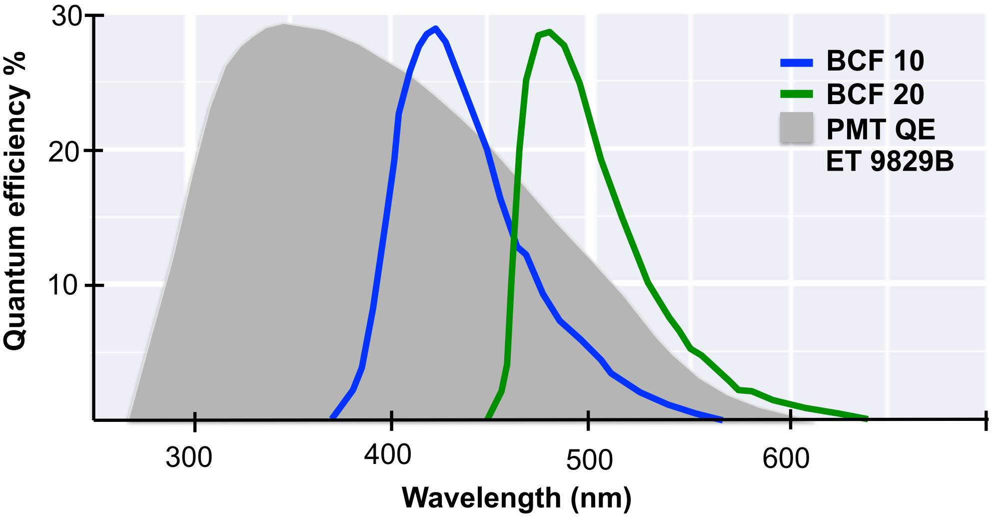

Figure 4.17: PMT quantum efficiency curve shown with BCF 12/20 emission spectra

An increase in detector quantum efficiency for blue scintillators means that more photoelectrons are produced at the photocathode per radiation event. This can be observed in the pulse height spectra (see Figure 4.18), where the blue emitting fibres display a larger proportion of events binned at higher channel numbers (where the channel number is proportional to the number of photoelectrons produced). The number of photoelectrons detected per event relates to how efficiently a single alpha or beta particle event can be detected, as the probability of detecting a signal whose average value is $< n >$ photoelectrons with a photomultiplier tube is given by 1 - $e^{-<n>}$. Hence a blue scintillating fibre would appear the better option when paired with a bialkali photomultiplier tube.

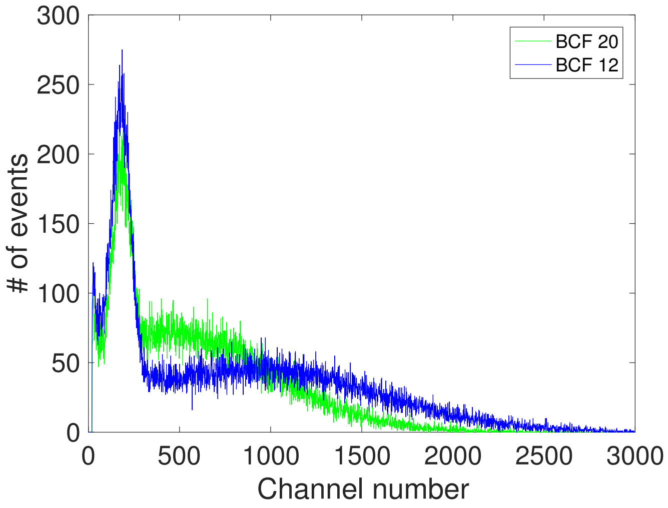

Figure 4.18: Pulse height comparisons for alpha irradiated BCF 12/20 1 mm variety with no outer cladding

Effect of outer cladding on light yield

The addition of an outer cladding around the fibre core affects several properties of the fibre which contribute to the final detectable light yield, including the light trapping efficiency, attenuation, susceptibility to environmental effects and the alpha particle penetration depth into the fibre core.

- **Trapping efficiency**: The trapping efficiency (or fluorescence collection efficiency), ε_{m}, of an optical fibre can be derived using a meridional approximation, and is given by:

  $$\varepsilon_{\mathrm{m}} = \frac{1}{2}(1 - \cos\vartheta_{\mathrm{c}}) \tag{4.4}$$

  Where ϑ_{c} is given by:

  $$\vartheta_{\mathrm{c}} = \sin^{-1}\left(\frac{\mathrm{n_{clad}}}{\mathrm{n_{core}}}\right) \tag{4.5}$$

  A core cladding combination for a polystyrene core ($\mathrm{n_{core}}$=1.6) surrounded by air ($\mathrm{n_{clad}}$=1) gives a trapping efficiency of 18.75%, however this value is significantly decreased to 3.44% when a PMMA cladding ($\mathrm{n_{PMMA}} = 1.49$) is used. According to the trapping efficiency, it is predicted 5.45 x more light is trapped in the fibre core when no cladding is present. In reality this is not the case as the predicted increase in light yield does not take into account light losses from coupling and environmental effects, as will be discussed shortly.

- **Attenuation losses:** The addition of an outer cladding on the fibre leads to a decrease in the attenuation of the guided photons within the core (see Section

4.3.2). Figure 4.19 shows the light yield as a function of distance for the 1 mm BCF12 fibre, both bare and cladded under beta irradiation (alpha particles were unable to produce enough signal in the core of the 1 mm cladded fibres for a meaningful comparison). At 9 cm from the detector, where attenuation differences between fibre types will not be significant, the light yield measured using each fibre is roughly the same. When no outer cladding is present, the signal decays rapidly as the fibre length is increased as would be expected from the higher transmission loss of this fibre.

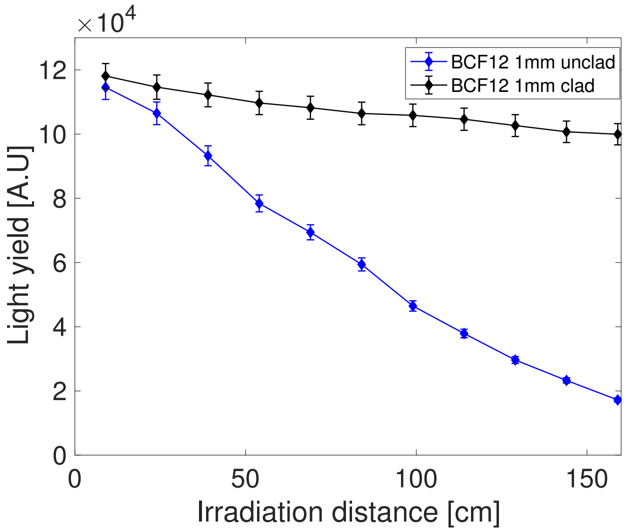

Figure 4.19: Cladding effect on light yield for beta irradiated 1 mm BCF12 fibres

The pulse height spectra for these fibres (Figure 4.20) give a little more insight into the attenuation processes occurring. When the fibre length is kept short (L=9 cm), there are significantly more events binned at higher channel numbers, hence more photoelectrons detected per radiation event. With an increase in fibre length, the same number of photons will be produced per radiation event, however a smaller number reach the detector because of attenuation losses, which is more pronounced in the unclad fibres. This is consistent with the greater proportion of low channel number events, and a decrease in overall detected events at L=160 cm. When no cladding is present on the fibre, the majority of scintillation events detected at 160 cm are indistinguishable from noise, which is problematic for background subtraction techniques which will be used with the sensors developed in this project. This obviously places constraints on fibre type and useable lengths for an efficient radiation sensor. In Figure 4.20, the gain settings of the photomultiplier tube when acquiring spectrum (a) and (b) were not the same, which is why the spectrum in (b) is spread out across a greater number of channels.

The alpha particles will only travel roughly 25 µm in the polymer coating (Table

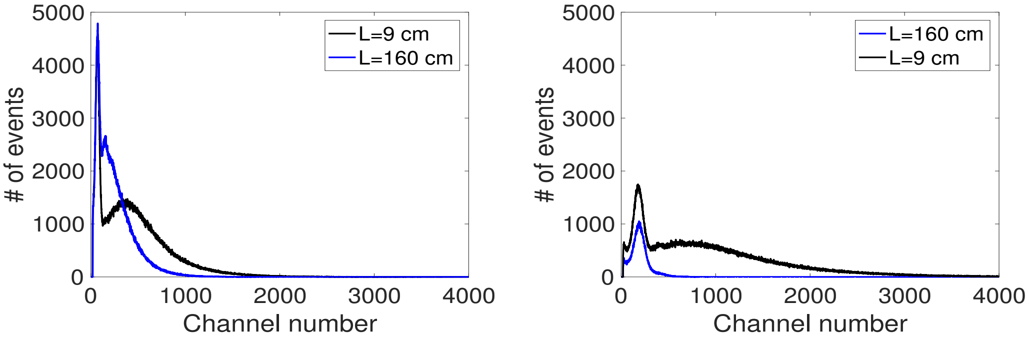

(a) BCF12 1 mm clad (b) BCF12 1 mm unclad

Figure 4.20: Pulse height spectra of beta particle irradiated BCF12 1mm clad fibre (a) and unclad fibre (b) at L=9,160 cm from PMT. .

4.2) before being stopped, meaning they should not be able to reach the fibre core of the 1 mm fibres to produce any fluorescent signal. The pulse height spectra show the signal is barely distinguishable from noise because the detected events lie in the single electron peak region (see Figure 4.21(a)), hence these fibres are not suitable for alpha particle detection. Alpha particles are able to effectively penetrate the 7.5 µm thick fibre cladding in the 250 µm diameter fibres (Figure 4.21(b)), as made apparent by the higher signal levels and the number of high channel number events observed. The cladding also ensures the scintillation light is not significantly degraded before reaching the detector when using longer fibre lengths.

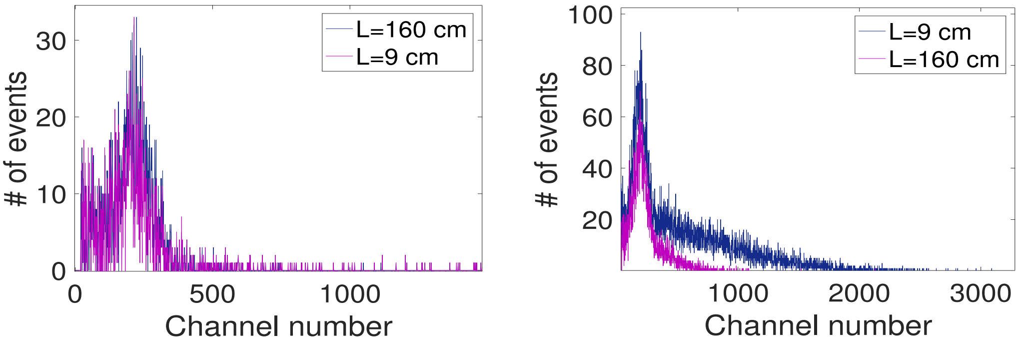

(a) BCF12 1 mm clad (b) BCF12 250 µm clad

Figure 4.21: Pulse height spectra of alpha irradiated BCF12 1mm clad fibre (a) and unclad fibre (b) at L=9, 160 cm from PMT

- **Coupling losses:** Significant signal losses were observed with the unclad fibres as a result of the fibre adaptor used to couple the optical fibre to the photomultiplier tube. From the trapping efficiencies alone, an overall increase in the number of photons detected by a factor of 5.5 x is predicted when no outer cladding is present, however when comparing the clad and unclad 1 mm diameter fibres (with β irradiation), the light yields were roughly the same. To determine the effect the coupling adaptor has on the light yield of the optical fibre, the 1 mm unclad BCF12 fibre was irradiated using an α source and in one instance the fibre was loosely positioned near the photocathode with no adaptor, then secondly the adaptor was used for coupling (Figure 4.22).

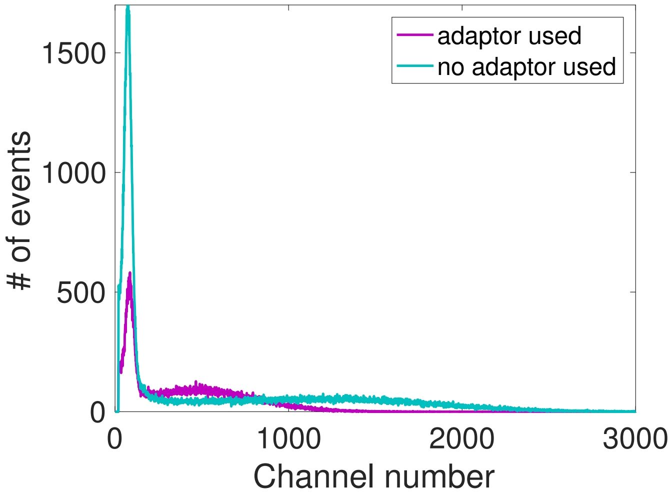

Figure 4.22: Effect of coupling adaptor on BCF12 light yield

A 93.5 % increase in overall detected events, and a spectral shift towards higher channel numbers is apparent when no adaptor is used. Given high energy events contain more than one photon, the total number of photons could be determined if the pulse height spectrum was calibrated in terms of photoelectron numbers, which has not been perfomed here. One way to overcome the coupling losses encountered when using the unclad fibres would be to use a fibre adaptor made from a lower refractive index material like PMMA. This has not been investigated, as the clad fibres seem to offer superior performance at this stage of the project.

Wavelength shifting fibres

The response of the wavelength shifting fibres to beta particles will be discussed here as the alpha particles were unable to penetrate the cladding of these fibres and produce good signal-to-noise ratios. The wavelength shifting fibres BCF91A and BCF92 displayed significantly lower light yields (37.9% and 46.5 % less than BCF12 respectively) than other 1 mm cladded fibres when irradiated with beta particles (Figure 4.16). Further to this, the pulse height spectra (Figure 4.23) show the detected events are mostly composed of single photoelectrons, making them unsuitable for our application. The decreased signals are believed to be a result of the low efficiency at which these wavelength shifting fibres are able to convert deposited radiation energy into photons. In contrast to the majority of scintillators used here which are binary scintillators, the wavelength shifters are ternary formulated, meaning there is an additional energy transfer process occurring (hence a drop in photon conversion efficiency) following irradiation before the scintillation light is produced.

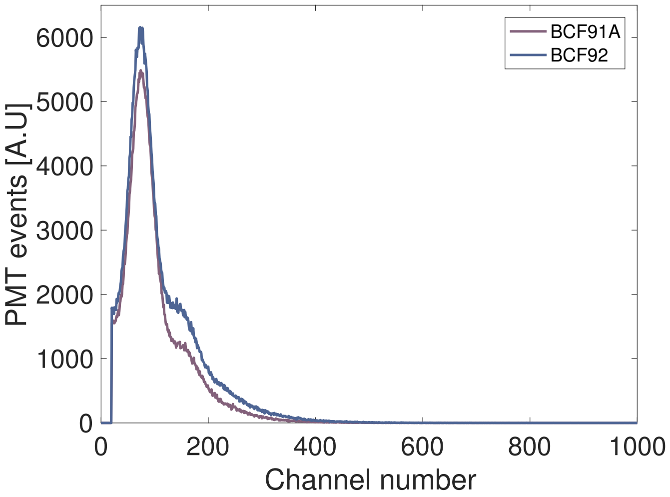

Figure 4.23: Pulse height spectra of WLS fibres under beta irradiation

4.6 Effect of fibre outer diameter on light yield

These experiments were performed to show the light yield produced from alpha particles incident on scintillating optical fibres scale with a shallow surface area type effect, and the beta particle induced light yield depends on the total volume of exposed scintillator, not the surface area. A fibre bundle was made using 39, 160 µm blue scintillating optical fibres with no outer cladding (poly17), the end faces were polished and the fibres laid slide by side on a teflon sheet. A 1 mm thick length of BCF12 with no outer cladding was polished and mounted in the same way as the 160 µm fibres. The combined total fibre volume exposed to the radiation sources is similar between the fibre bundle and the 1 mm cane, but they differ in that the surface area of the fibre bundle is much larger.

4.6.1 Surface area and volume ratios

The mean energy of the alpha particles from the 28 kBq ^{241}Am source is 4 MeV, giving them a 25.6 µm range in polystyrene. However some alpha particles were found to be able to penetrate more than 30 µm in PMMA, consistent with a slightly broad energy spectrum as was also observed with surface barrier detector measurements. The uncertainties in the energy spectrum of the alpha particles are not known, so an average penetration depth of 25 µm ± 5 µm in polystyrene is considered.

Due to the limited penetration depth of alpha particles, their scintillation light yield is expected to depend on the exposed surface area of the fibre as opposed to the fibre volume. Instead of comparing the surface areas of the two fibre types used here, the ratio of the shallow volume in the upper hemisphere of the fibre between 39, 160 µm fibres, and a 1 mm optical fibre (see Fig 4.24) will be compared. This calculation will provide an estimate for the expected increase in signal caused by increasing the "surface area" of a fibre bundle while maintaining a constant volume.

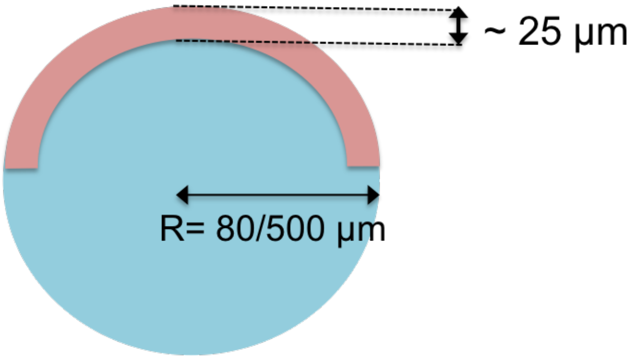

Figure 4.24: Cross section of fibre showing surface volume (red) used in calculations

The total volume ratio, V_r, between the 160 µm fibre bundle, V_{bundle}, and the 1 mm cane, V_{cane} for a given length of fibre is calculated below taking into account uncertainties in the fibre diameter. The drawn fibres, have a measured diameter and uncertainty of $r_{80\mu m}$= 80 µm ± 5 µm. The uncertainty in the radius of the 1 mm canes is listed in the specification sheet as 2% of the fibre radius, so $r_{500\mu m}$= 500 µm ± 10 µm.

So V_r is calculated as follows:

$$\mathbf{V_r} = \frac{V_{bundle}}{V_{cane}} = \frac{39 \times \pi \times (80)^2 \times L}{\pi \times (500)^2 \times L}$$

$$= \frac{39(6.4 \times 10^3)}{(2.5 \times 10^5)} \tag{4.6}$$

$$\mathbf{V_r} = 0.998.$$

The maximum and minimum bounds on V_r can be calculated numerically by taking into account the variation in fibre diameters, and gives $0.84 < V_r < 1.17$.

The ratio of the shallow irradiated volumes, $V_{r,surf}$ between the bundle, $V_{bundle,surf}$ and the cane $V_{cane,surf}$ is as follows:

$$\mathbf{V_{r,surf}} = \frac{\mathrm{V_{r,surf}}}{\mathrm{V_{cane,surf}}} = \frac{0.5 \times 39 \times \pi \times ((80)^2 - (55)^2) \times \mathrm{L}}{0.5 \times \pi \times ((500)^2 - (475)^2) \times \mathrm{L}}$$

$$= \frac{39 \times (3.38 \times 10^3)}{(2.4 \times 10^4)} \tag{4.7}$$

$$\mathbf{V_{r,surf}} = 5.4$$

The bounds on this value need to take into account a variation in alpha particle range of 5 µm in the plastic as well as diameter variations. Numerically, the maximum and minimum bounds are calculated to be $4.71 < \mathrm{V_{r,surf}} < 6.08$.

The $\mathrm{V_{r,surf}}$ calculation only relates to alpha particles. Beta particles should easily penetrate the entire fibre volume, so the amount of light they produce should not be affected by a change in surface area, only volume, hence by keeping the volume nearly constant there should be no significant change in signal.

4.6.2 Attenuation corrections

The 1 mm cane (BCF12) and the 160 µm fibres (fabricated from EJ204) have different loss characteristics, so the scintillation produced within the fibre will be attenuated to different degrees in the fibre before reaching the detector and this must be corrected for. The attenuation values measured with the SIF technique at the peak emission wavelength of each fibre is used (refer to Figure 4.5). The 1 mm BCF12 fibre has a loss of 7.3 ± 0.4 dB/m at 435 nm, and the 160 µm poly17 fibres have a loss of 24 ± 1.5 dB/m at 425 nm. Using the expression:

$$\frac{\mathrm{I_T}}{\mathrm{I_0}} = \exp^{\frac{-\alpha \mathrm{L}}{10}} \tag{4.8}$$

The loss of light in a given length, L, of fibre can be calculated, where $\mathrm{I_T}$ is the transmitted light intensity, $\mathrm{I_0}$ is the intensity of light at the irradiation point, and α is given in units of dB/[L]. When irradiating the fibre bundle and cane with alpha particles, the source was placed 1 cm from the end of the fibres (to minimise light losses) so the attenuation in this 1 cm length needs to be accounted for. With beta particle irradiations, the source was moved back further from the end of the fibres (5.5 cm) to prevent any scattered electrons from the source reaching the photomultiplier tube and causing increased background levels. The intensity ratios for alpha and beta particle irradiated bundle and cane configurations are calculated using Equation 4.8 and are shown in Table 4.4. To account for attenuation in each fibre configuration, the measured signal is multiplied by the inverse of the intensity ratio to give the corrected signal, $\mathrm{Sig}_{\mathrm{corr}} = \mathrm{Sig}_{\mathrm{meas}} \times \mathrm{I}_0/\mathrm{I}_{\mathrm{T}}$. An additional correction is applied to account for the differences in light yields of the two materials as the poly17 fibres have a 10% higher light production efficiency than the BCF12 fibres.

Configuration	**Source**	**Fibre loss (dB/m)**	**L(m)**	$\mathrm{I_T/I_0}$
Bundle	α	24 ±1.5	0.01	0.976 ± 0.001
	β	24 ±1.5	0.055	0.876 ± 0.003
Cane	α	7.3 ±0.4	0.01	0.993 ± 0.0005
	β	7.3 ±0.4	0.055	0.96 ± 0.003

Table 4.4: Intensity ratios $\mathrm{I_T/I_0}$ with error bounds for irradiated bundle and canes.

4.6.3 Surface area dependance results

Both the fibre bundle and cane were irradiated for 100 s each with alpha and beta radiation, and the total light yield collected with the photomultiplier tube after background subtraction was measured. Measurements were taken five times for each fibre and source configuration and the mean light yield and standard deviations were calculated. The results are corrected to account for attenuation and light yield differences and are presented in Table 4.5. A comparison to the predicted values is shown in Figure 4.25.

Source	$\mathbf{Sig}_{\mathrm{bundle}}$	$\mathbf{Sig}_{\mathrm{cane}}$	$\frac{\mathrm{Sig}_{\mathrm{bundle}}}{\mathrm{Sig}_{\mathrm{cane}}}$(Exp.)	$\frac{\mathrm{Sig}_{\mathrm{bundle}}}{\mathrm{Sig}_{\mathrm{cane}}}$(corr.)
α	830,991 ± 2.2%	185,361 ± 2.1%	4.48 ± 3.04%	4.11 ± 3.24%
β	157,068 ± 2.97%	138,649 ± 2.42 %	1.13 ± 3.83%	1.12 ± 3.85%

Table 4.5: Surface area dependence results
$\mathrm{Sig}_{\mathrm{bundle}}$ = mean light yield recorded using fibre bundle
$\mathrm{Sig}_{\mathrm{cane}}$ = mean light yield recorded using fibre cane
(Exp.) Experimental measurement
(corr.)=Experimental measurement with attenuation correction, and light yield correction

These results suggest the alpha particle induced light yield has a strong dependance on the surface area of exposed scintillator, while beta particle induced light yields remain largely unaffected by this surface area change. The experimental errors shown do not reflect positioning errors as measurements were taken with the fibre outputs fixed

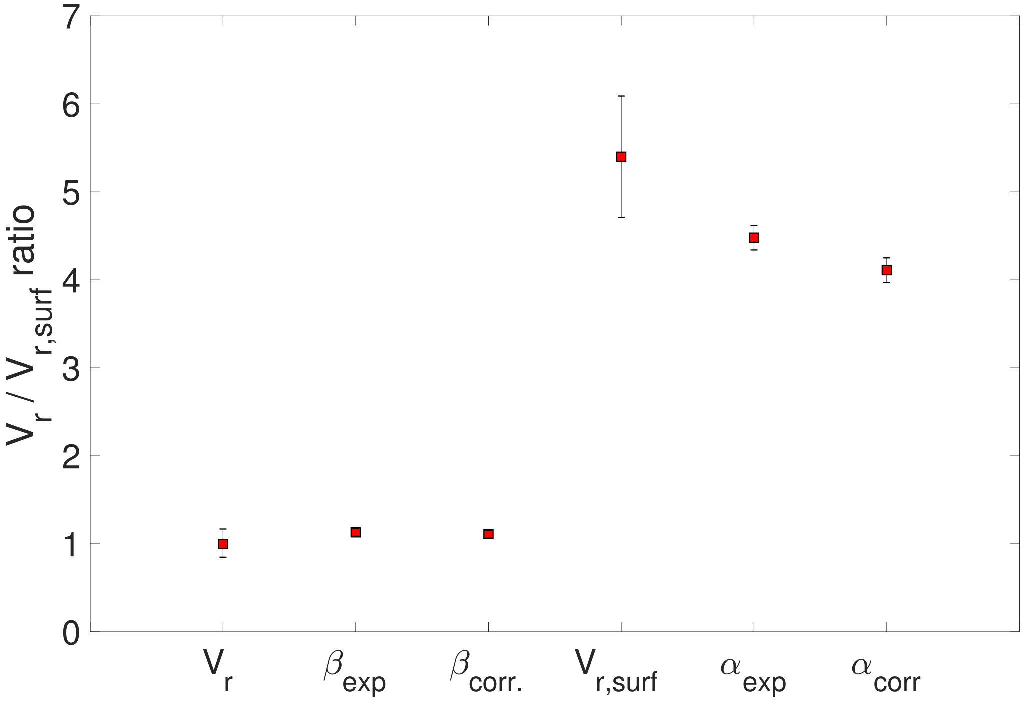

Figure 4.25: 39 fibre bundle to cane signal ratios for alpha and beta irradiation.
β_{exp}, $\beta_{corr.}$ = experimental and corrected light yield ratios Sig_{bundle}/Sig_{cane}(Exp./corr.)
α_{exp}, $\alpha_{corr.}$ = Sig_{bundle}/Sig_{cane}(Exp./Corr.)

relative to the photomultiplier tube, hence why they are small. The experimentally measured light yield ratios α_{exp} and α_{corr} lie just outside the bounds of the predicted value, and this is thought to be a result of the layout of the bundle configuration as it was difficult to seperate each fibre and keep the array size as small as possible. Hence the alpha particles would not be able to interact individually with each fibre as some were overlaid slightly.

4.6.4 Scintillator volume dependence

Six, 160 μm poly17 fibres were mounted and epoxied in an adaptor and coupled to the photomultiplier tube, similarly for a single 1 mm cane. The ratio of the volumes of this fibre bundle, $V_{bundle2}$ to the 1 mm cane V_{cane2} is now:

$$
\begin{aligned}
V2_R = \frac{V_{bundle2}}{V_{cane2}} &= \frac{6 \times \pi \times 80^2 \times L}{\pi \times 500^2 \times L} \qquad (4.9)\\
&= 0.15
\end{aligned}
$$

With bounds (0.13, 0.18). The surface area ratio for this bundle configuration is:

$$\mathrm{V2}_{\mathrm{R,surf}} = \frac{\mathrm{V}_{\mathrm{bundle2,surf}}}{\mathrm{V}_{\mathrm{cane2}}} = \frac{0.5 \times 6 \times \pi \times (80-25)^2 \times \mathrm{L}}{0.5 \times \pi \times (500-475)^2 \times \mathrm{L}} \tag{4.10}$$

$$= 0.83$$

with bounds between (0.72, 0.93) as were determined numerically. Measured and corrected alpha and beta particle light yields for the fibre bundle and cane are given in Table 4.6, and compared to the predicted values in Figure 4.26. Experimental error bounds were used from the previous experiment.

Source	**Sig**$_{\mathrm{bundle2}}$	**Sig**$_{\mathrm{cane2}}$	$\frac{\mathrm{Sig}_{\mathrm{bundle2}}}{\mathrm{Sig}_{\mathrm{cane2}}}$(Exp.)	$\frac{\mathrm{Sig}_{\mathrm{bundle2}}}{\mathrm{Sig}_{\mathrm{cane2}}}$(corr.1)
α	131,913 ± 2.2%	163,224 ±2.1%	0.82 ± 3.04%	0.74 ± 3.24%
β	21,407 ± 2.97%	145,499 ± 2.42	0.15 ± 3.83%	0.14 ± 3.85%

Table 4.6: Volume dependence results
Sig$_{\mathrm{bundle2}}$ = mean light yield recorded using 6 fibre bundle
Sig$_{\mathrm{cane2}}$ = mean light yield recorded using fibre cane
(Exp.) Experimental measurement
(corr.)=Experimental measurement with attenuation correction, and light yield correction

These results show the alpha particles do not have a volume dependant light yield, as expected, whereas the beta particles do. The results agree with the predicted ratios more nicely than with the previous experiment, likely due to the ease at which the 6 fibres can be separated compared to 39. Having clear separation of the fibres for alpha particle irradiation means they can be irradiated in a similar geometry to the fibre cane, at the same time we require the fibres close enough together so they can project light on a similar area of the PMT photocathode (which is position sensitive). Having the fibres mounted in an adaptor also means the PMT to fibre coupling is less variable between the bundle and cane.

4.7 Summary of irradiation results

Given the differences in energy deposition mechanisms between alpha and beta particles, two different sensor designs must be considered for efficient detection of each radiation type. When taking into account signal losses under environmental conditions and the rapid degradation of large energy events via attenuation, fibres with outer cladding are essential for minimising signal degradation and maximising detection efficiency. The outer cladding presents no issue for beta particle detection, but has shown to significantly affect the ability to detect alpha particles. Despite this, the 250 µm

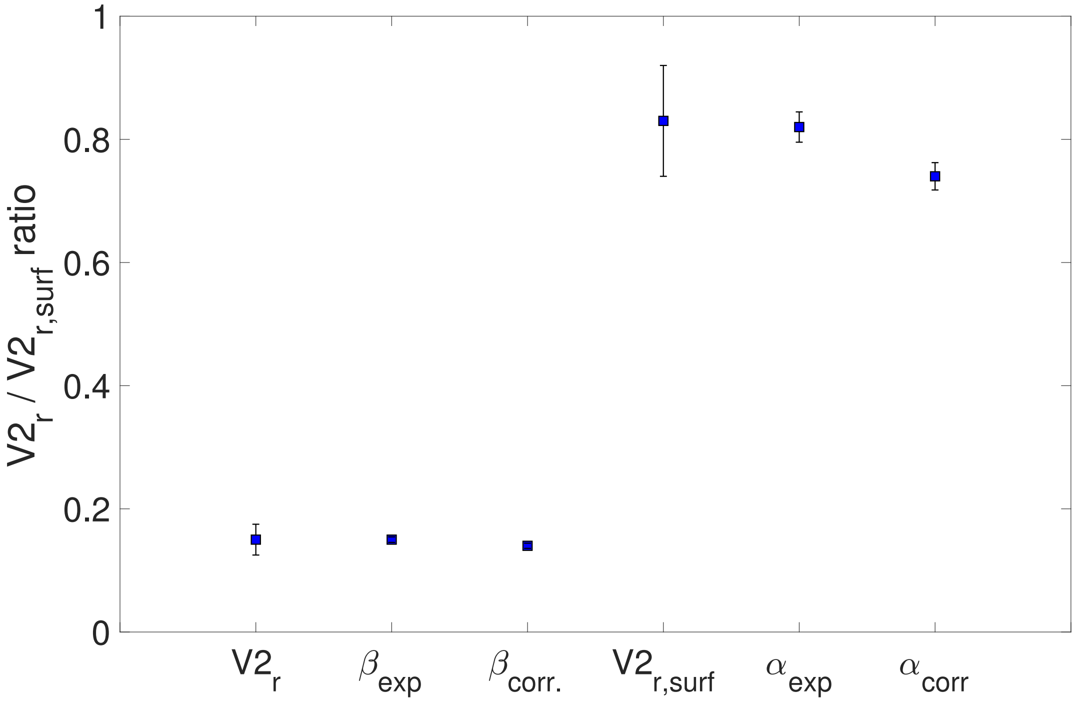

Figure 4.26: 6 fibre bundle to cane signal ratios for alpha and beta particle irradiation

fibres have shown promise for alpha particle detection as the cladding is thin enough to allow significant energy deposition in the fibre core, however improvements should be seen using thinner outer claddings, and maximising the surface area of scintillator exposed to the radiation source by making use of several small diameter fibres in a bundled configuration.

Maximising the scintillator volume relative to the path length of beta particles should also allow improvements in detection efficiency as this would allow maximum conversion of the beta particle energy into scintillation light. In both cases, blue scintillators should be used when using a bialkali photomultiplier tube, and minimising fibre length should also offer improvements in detection efficiency by minimising attenuation losses.

Chapter 5

Environmental testing of fibres and prototype devices

5.1 Introduction

Several of the polymer optical fibres tested appear to be suitable for integration into a radiation-sensing device based on their alpha and beta particle response and optical properties. The experimental results described in this chapter characterise the fibre in the operating conditions similar to that the device will ultimately be subjected to. This chapter is arranged as follows: In Section 5.2.1, the degradation of a test fibre is assessed in an acidic solution, and in an environment analogous to a flotation tank where the fibre is subjected to the combined effects of acidity, abrasion and elevated temperatures (Section 5.2.2). The results indicate the fibres are resistant to degradation under the proposed operating conditions and thus are a promising candidate for radionuclide monitoring in mineral processing liquids. Fibres are then selected for alpha and beta particle detection, and prototype devices are created and calibrated in radioactive test solutions as outlined in Section 5.3.

5.2 Environmental testing of polymer fibres

The proposed device must be capable of directly monitoring low-level concentrations of alpha and beta emitting radionuclides in real time in solutions. The liquids which require monitoring typically have a pH around 1, temperatures of up to 80°C and solid fractions of up to 50% by weight in constant agitation. The capability of polymer fibres to function effectively under these conditions is evaluated by performing two tests, the first assesses any potential long term degradation of the fibre within an acidic solution, the second test introduces elevated temperatures and abrasive particles to an acidic solution to mimic conditions within a flotation tank.

5.2.1 Effect of acidic environment on fibre transmission

To determine the impact of long-term immersion of the optical fibres within a pH 1 acid, an experiment was designed to monitor transmission changes which result from the degradation of the fibre material by the acid. A schematic diagram of the experiment is shown in Figure 5.1. The beam of a 640 nm laser diode is split equally between a 'Reference' and 'Signal' fibre, both coupled to a Thorlabs PDA100A-EC silicon transimpedance amplified photodetectors. These detectors were chosen for a number of reasons; they have a broad sensitive detection region between 320-1100 nm, a large active area (100 mm^2) for ease of coupling, and switchable gain settings to accomodate a range of signal levels from the fibre outputs. The signal fibre was immersed in a pH 1 sulphuric acid solution and the output monitored with PD2 (see Figure 5.1), the reference fibre was not subject to acid immersion and was monitored with PD1. The readings from both photodiode outputs were recorded by a Picoscope 2206B data logger, and a MATLAB code was written to calculate and store the mean values every 60 s. Any structural damage to the 'Signal' fibre such as pitting or erosion causing scattering losses would lead to a drop in the amount of light transmitted and measured with the detector PD1, and would not be apparent in the 'Reference' signal measured by PD2.

The test fibre, poly17, was chosen based on its small outer diameter (160 µm) and lack of outer cladding. The larger surface-to-volume ratio of the fibre in comparison to a larger diameter fibre means the propagating modes within the core interact with a greater proportion of the fibre surface, and as a result, fibre transmission is more susceptible to surface modification of the material. Additionally, the lack of outer cladding means the fibre core is in direct contact with the acidic solution, making any surface defect formation likely to occur on a faster timescale.

The normalised photodiode power measured from the signal, Sig, and reference, Ref,

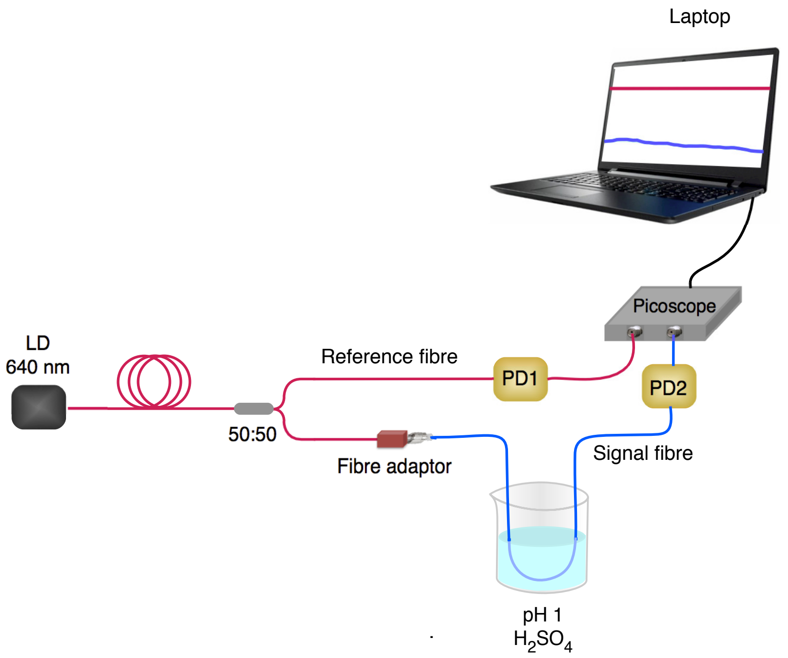

Figure 5.1: Experimental setup for acid degradation testing. A 640 nm laser diode (LD) is split equally between a 'Signal' fibre immersed in a sulphuric acid solution and a 'Reference' fibre in air. The light output from each fibre is measured with photodiodes PD1 and PD2 and the signals collected with a Picoscope data logger.

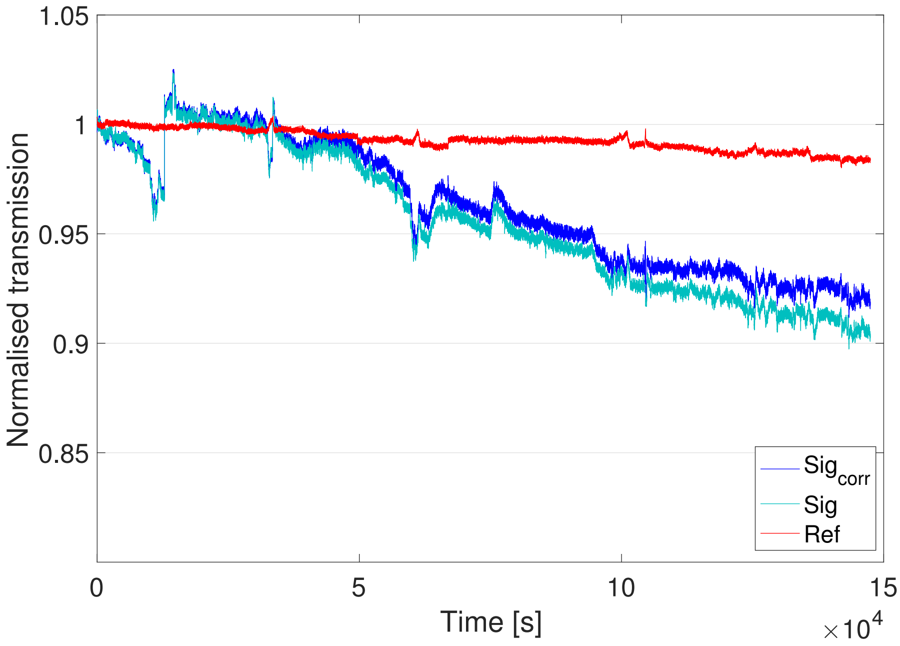

Figure 5.2: Normalised transmission of signal, Sig, and reference, Ref fibre outputs, and the corrected signal (Sig_{corr}) which takes into account fluctuations in the reference signal over time.

fibres are shown in Figure 5.2. Any changes in the output of the photodiode over time is accounted for in the signal measurement by calculating a corrected signal, $\mathrm{Sig}_{\mathrm{corr}}$ using:

$$\mathrm{Sig}_{\mathrm{corr}} = \mathrm{Sig} \times \frac{1}{\mathrm{Ref}} \tag{5.1}$$

Data was collected using a single fibre over a period of 105 days, and show a loss in transmission of 8 % which should be accounted for if the final proposed device is to be used for extended periods of time. Due to the time consuming nature of this experiment it was not practical to conduct several tests for extended periods of time to confirm the initial result, however tests were performed under identical conditions with other fibre samples over shorter time scales (2 weeks) and similar transmission losses were observed. One possible explanation for the cause of the signal loss is that the polymer surface was gradually degraded by the acid, which would cause an increase in scattering loss in the fibre and hence a drop in transmission. The same surface damage would be expected if the bare fibre was replaced with a cladded fibre, however, there would be less overlap of the guided modes with the outer surface, hence the impact of any surface defects on transmission should be significantly reduced but is yet to be confirmed. The laptop which was collecting and saving data had shut down unexpectedly on a few occasions, which caused the discontinuities in Figure 5.2. The results

5.2.2 Effects of elevated temperatures and abrasion on fibre transmission

The fibre tested in Section 5.2.1 showed good resistance to acid over extended timescales. The fibre device must also function efficiently in the presence of abrasive particles and elevated temperatures: the next experiment was designed to test the performance of an optical fibre under these three conditions simultaneously. To accurately simulate the conditions encountered within a flotation tank, samples of dry concentrate containing 150 ppm U_3O_8 and leach liquor containing 450 ppm U_3O_8 were acquired and combined in a proportion typically found in mineral processing (50% w/w) to make a slurry.

Similarly to the experiment performed in Section 5.2.1, the transmission of a 'Signal' and 'Reference' fibre were monitored, but the sulphuric acid solution was replaced with a 200 ml sample of the slurry which was placed on a hotplate stirrer (Fig. 5.3). Initially, tests were performed using a 160 µm diameter bare fibre, however, transmission losses upwards of 70% were observed using this, and all other fibres without an outer cladding following immersion in the slurry. The slurry was very dark and completely opaque, so it is likely light losses are caused by either absorption or the high refractive index of the dark liquid surrounding the fibre core. Although the loss mechanisms for each scenario are different, both would cause an instantaneous transmission loss upon immersion as was observed. This is in contrast to the gradual transmission loss caused by slow corrosion of the fibre surface by the liquid.

The decrease in the signal-to-noise ratio caused by light leakage from the fibre core following immersion in the slurry shows that bare fibres are unsuitable for incorporation into a device and for use in this experiment. To determine if an outer cladding on the fibre prevents instantaneous transmission losses in the slurry, the 640 nm light transmitted through 250 µm (7.5 µm thick cladding) and 1 mm (30 µm thick cladding) diameter cladded fibres was monitored with a photodiode upon transferring the fibre from air to the slurry. No difference in photodiode power was observed, indicating the cladding confines the light to the fibre core so it is unaffected by the surrounding environment. For these reasons a cladded fibre was used for abrasion and temperature testing in the slurry, specifically a 250 µm diameter fibre as it was flexible enough to easily incorporate into a 250 ml flask. The slurry was agitated by stirring at 500 rpm, and heated in 5°C increments up to a maximum temperature of 80°C over a period of 13 days. Care was taken to ensure the fibre was not touching the glass, as this caused the fibre to melt at high temperatures due to the increased glass temperature relative to the liquid.

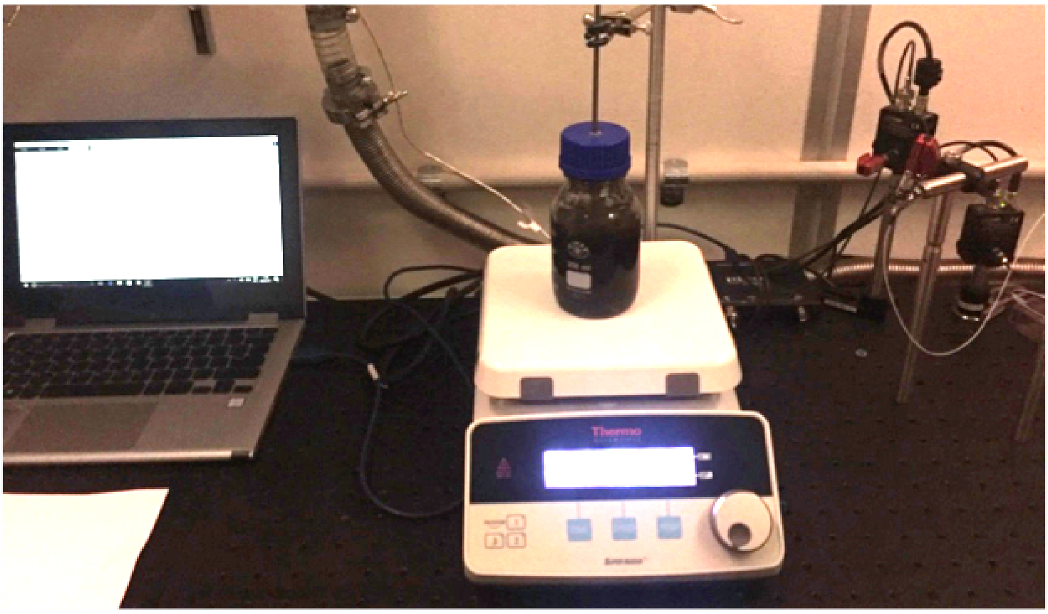

Figure 5.3: Experimental setup to monitor fibre transmission changes in slurry

No significant changes in fibre transmission were observed up to the maximum temperature tested (Figure 5.4), indicating damage to the fibre, if any, is present only on the outer surface of the cladding. If the cladding thickness were significantly decreased or removed in the slurry, the guided light within the core would overlap with the fibre

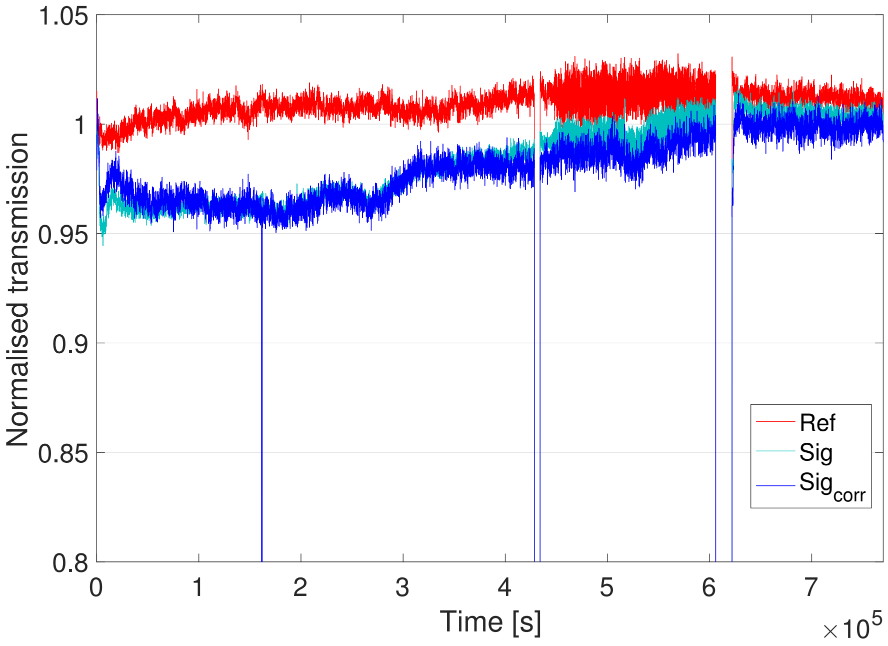

Figure 5.4: Normalised transmission of 'Signal' (Sig), 'Reference' (Ref) and corrected signal ($\mathrm{Sig}_{\mathrm{corr}}$) as a function of time for fibre immersed in slurry. Note LED down time.

surface and be affected by any surface damage and absorption/refractive index losses of the liquid as is the case with bare fibres. The downward spikes in the spectra occur because the laser diode needed to be switched off to perform other light-sensitive experiments. Similar results were observed when a second identical fibre sample was tested. Based on these results, the polymer fibres appear to withstand long-term degradation in acidic environments, and also show resistance to abrasion and temperatures up to 80°C. Constant heating of the slurry over longer time periods has not been investigated.

5.2.3 Summary of environmental testing

Two experiments have been performed to assess how effectively the polymer optical fibres function under environmental conditions similar to those which will be encountered during radionuclide monitoring in mineral processing. Before fibres are incorporated into a radiation sensing device for this application, we must ensure they are able to withstand long-term operation within an acidic environment at elevated temperatures with exposure to abrasive particles. The first experiment monitored the transmission of a bare fibre in a pH 1 sulphuric acid solution over the course of 105 days. An 8 % decrease in transmission was observed, indicating the fibre material is particularly resistant to acid and shows potential for long-term operation in a low pH liquid.

A second experiment was conducted to assess any potential damage to a fibre caused by the combined effects of elevated temperature and abrasion in an acidic environment. A slurry was created to simulate such an environment using dry concentrate and leach liquor samples in a proportion typically encountered in a flotation tank. Bare fibres were deemed unsuitable for testing in slurrys and for incorporation into a device because significant light losses from the fibre core occurred instantaneously upon immersion in the slurry. From this point onwards, only fibres with an outer cladding will be considered as they are protected against signal losses caused by absorption and the high refractive index of the surrounding slurry. No significant damage to a 250 µm fibre was observed after 13 days of operation in the slurry which was agitated and heated to 80°C.

5.3 Prototype device construction and testing

Inclusion of a cladding on the fibre core has been shown to be essential for this application as it prevents light leakage from the fibre core into the slurry. In considering an appropriate fibre for device construction this is taken into account and limits the number of fibres available. Construction, principles of operation, detection limits, and improvements of two prototype devices for measuring alpha and beta emitting radionuclides in solution are discussed in the following sections.

5.3.1 Radiation detection in slurry samples

A test to determine the feasibility of detecting low radionuclide concentrations in solution using fibre bundles was performed using a slurry sample prepared in Section 5.2.2. The ^{238}U activity within the slurry was measured using gamma spectrometry and found to be 5 Bq/ml. If the slurry were in secular equilibrium, the activity of each isotope measured using gamma spectrometry would also have an activity of 5 Bq/ml which is not the case, as the activities of ^{210}Pb, ^{226}Ra and ^{230}Th are 5.2, 4.5, and 3.3 Bq/ml respectively. In secular equilibrium there would be 8 alpha particles and 6 beta particles produced each time a ^{238}U atom decays, however, in this case there would be slightly less alpha and beta decays for each uranium as the equilibrium has been disturbed. Regardless, the total sample activity is much greater than the targeted detection limit of 1 Bq/ml per isotope in the ^{238}U decay chain. Successful detection of radionuclides within the slurry will provide information as to whether significant design improvements are required before proceeding with further experimentation.

Fibre choice for beta sensing

It has been shown in Section 4.6.4 that the beta particle induced light yield of the optical fibres is volume dependent. Larger scintillator volumes exposed to beta particles will result in greater light production within the material but will also cause an increase in the amount of light produced by terrestrial and cosmic ray background. A balance needs to be struck between maximising sensitivity to the radiation type of interest and reducing the contributions from background radiation. The 1 mm OD cladded BCF12 fibres displayed the best beta particle response of all the fibres tested in short and extended fibre lengths (Section 4.4.3). Hence they were chosen for incorporation into the first bundle sensor. Importantly, these fibres do not have enough sensitive volume to produce significant counts from background gamma ray and cosmic radiation.

The 30 µm cladding on the fibres is not thick enough to entirely stop alpha particles penetrating into the fibre core and producing some scintillation, so there will be a small contribution to the signal from alpha particles when used in a uranium containing liquid. Non-standard cladding thicknesses were not available from the fibre manufacturer, however the 1.5 mm OD fibre from the manufacturer would have sufficient cladding thickness (45 µm) to stop any incident alpha particles. Unfortunately this fibre was not available when performing these experiments, so the 1 mm variety was used and serves well for proof of principle of low level beta particle detection in liquids.

Fibre choice for alpha sensing

The fibre chosen for incorporation into an alpha particle sensor differ from those chosen for beta particle sensing in their outer diameter and cladding thickness only. Alpha particles have a much shorter range than beta particles, so the active sensing volume surrounding a single fibre will be much smaller than that for a similar energy beta particle making their detection especially challenging. To further complicate detection, a fraction of the alpha particle path length does not contribute to any detectable signal, as energy is lost in the non-scintillating fibre cladding.

In contrast to beta particles, the amount of light produced by alpha radiation was found to be surface area dependent (see Section 4.6.4), with volume having no observed effect. By utilising a large number of small diameter fibres, the surface area of the scintillator can be maximised, thus increasing the proportion of light produced by alpha particle events and minimising background contributions. The 250 µm clad BCF12 fibre was used for the initial device construction as they demonstrated the best alpha particle response of all the cladded fibres as was shown in Section 4.4.3. Beta particles were found to produce a significant amount of light within these fibres, although the scintillator volume is small they do not suffer significant energy losses in the cladding as alpha particles do. Hence the beta particle signal must be accounted for when using the device in liquids containing both alpha and beta particle emitters.

Fibre bundle designs and considerations

Given the differences in energy deposition mechanisms between alpha and beta particles, two different sensor designs must be considered to optimise detection of each radiation type within the slurry. A prototype of each was constructred, and a brief description of each is given below.

- **Beta particle detection**: A fibre bundle consisting of 20 fibres structured in a 5 × 4 array was created (Fig. 5.5(a)), with the total length of each fibre kept short, at 15 cm (with a 5 cm immersion length) to ensure minimal attenuation of scintillation light produced in the core. The passage of a beta particle through multiple fibres would result in an overestimation of the actual radionuclide activity within the liquid, and this has been avoided by maintaining a 1 cm separation between fibres, greater than the maximum calculated range of the majority of beta particles in the slurry. For reproducible coupling to a PMT the fibres were cemented within an SM05 adaptor and polished. For easy reference, a naming scheme is applied to the fibre bundles, with a full list of details supplied in Appendix B. This beta sensing bundle is named B1.
- **Alpha particle detection**: A fibre bundle (bundle A1) was created using a large number of short fibres to maximise surface area and minimise attenuation losses (Fig. 5.5(b)). 200 fibres of length 15 cm were cemented within an SM05 adaptor and polished. Due to the limited range of the alpha particles, it is not necessary to separate the fibres using a structure, as the slurry will permeate between fibres. Additionally, the short range of the alpha particles means no single event will be detected across multiple fibres.

Experimental results

Each fibre bundle was placed in the slurry and the output coupled to the PMT using a custom SM05 adaptor. Radiation events were counted by integrating across all channels in the pulse height spectrum, with integration times of 90 minutes each used to ensure good signal-to-noise ratios. Recall, the channel number on the horizontal axis represents the pulse height which is proportional to the number of photons produced in the material per event, hence to the energy of the incident radiation, and the vertical axis is the number of events detected in a given channel. Thus high channel numbers correspond to high energy radiation events, and low channels correspond to low en-

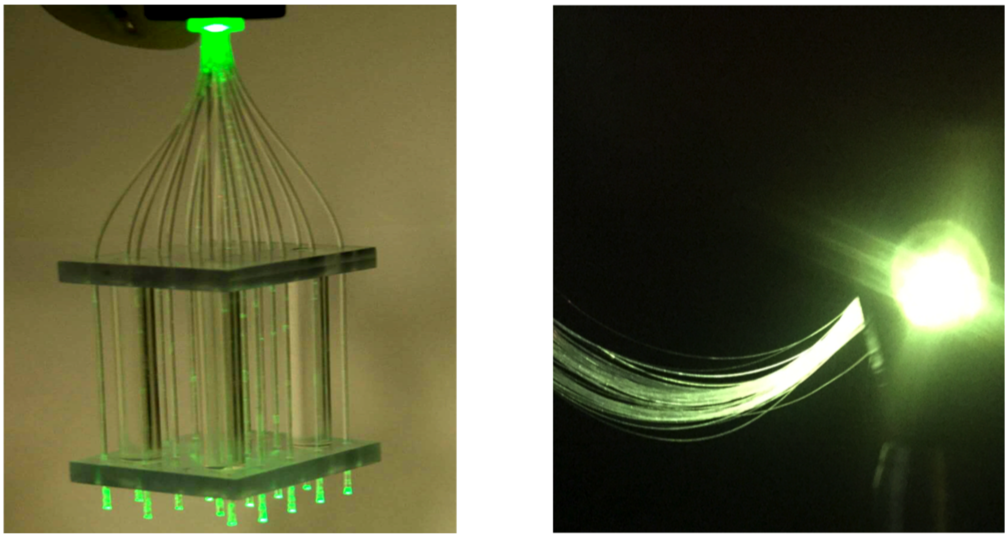

(a) (b)

Figure 5.5: Fibre bundles (illuminated with flashlight) employed for (a) beta sensing (B1), and (b) alpha sensing (A1) in slurry samples.

ergy events. Specifically, the single electron peak (SEP) region corresponds to events which produce a single photoelectron at the PMT photocathode, and includes contributions from thermal noise, and scintillation events caused by high-energy background radiation, and low-energy alpha/beta events.

The pulse height spectra obtained using alpha and beta sensing bundles in the slurry is shown in Figure 5.6. Event count numbers above background noise were observed using both A1 and B1 fibre bundles. A significant high energy component is present in the pulse height spectra which indicates the count number increase results from radiation interactions within the fibre, as background noise contributions lie mostly within the single electron peak located near channel 100. The count increase above background noise indicate both sensor types are able to efficiently detect radionuclides within a liquid containing concentrations of ^{238}U of $\approx$ 5 Bq/ml. At this stage, quantification of alpha and beta emitting radionuclides is not possible as the slurry contains unknown concentrations of each, which are producing combined signals in each bundle. Hence separate solutions containing known concentrations of alpha and beta emitting radionuclides are needed to establish more accurate detection limits for each fibre bundle, and hence these standard solutions are created, as described in Sections 5.3.3 and 5.3.4.

5.3.2 Considerations for radioisotope selection

When selecting a radionuclide for use in a solution with the alpha and beta sensors, the following requirements should be considered:

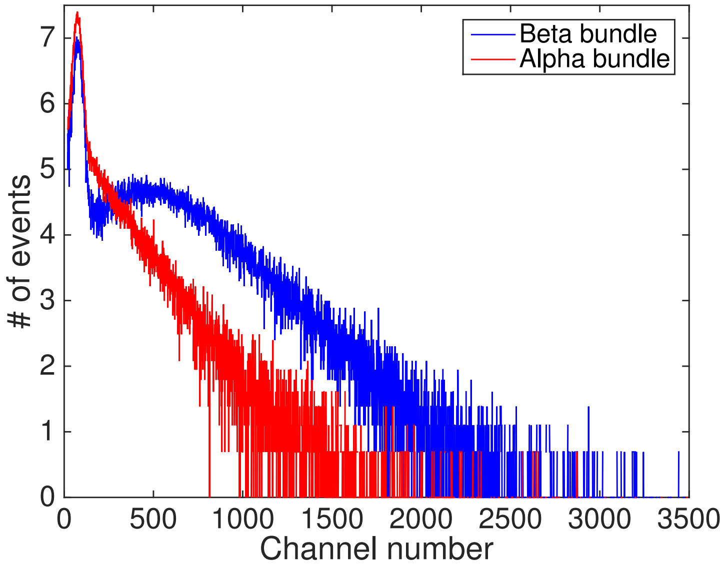

Figure 5.6: Background subtracted pulse height spectra of alpha and beta sensing bundles, A! and B1 in a slurry containing approximately 5 Bq/ml of ^{238}U.

- The radioisotope should have a relatively long half life to ensure sufficient time to perform experiments before the isotope decays to a stable form.
- Ideally, the radioisotope in solution should be a pure beta (or alpha) emitter.
- The compound containing the radioisotope should easily disperse in solution.
- The solution is stable (will not react) under required operating conditions and safe to handle.

5.3.3 Beta particle sensing of Potassium-40 in test solutions

The results in Section 5.3.1 demonstrated that detection of low radionuclide levels in slurry samples is possible using both bundle architectures, however the targeted detection limit for this research project is 1 Bq/ml per isotope of ^{238}U, a factor of approximately five lower than the concentration in the slurry. Experiments performed in this, and the following section aim at quantifying and improving the minimum detectable activity concentrations of alpha and beta emitting radionuclides in solution with each sensing device. In order to quantify detection limits for each radiation type, it is necessary to use separate solutions of alpha and beta emitting radionuclides as it is not possible at this stage to separate alpha and beta components of the signals produced in each fibre bundle device.

For beta particle measurements, potassium chloride (KCl), composed of potassium (of which, 0.012% is the radioisotope ^{40}K) and chloride ions in solution, was selected as it satisfies all the above requirements in Section 5.3.2 (there are a small proportion of gamma emissions, which are accounted for in measurements). In addition KCl is inexpensive, readily available, and easily dissolved in water. A few physical properties of this compound are given below.

Chemical formula	KCl
Specific activity ($\mathbf{A}_\mathrm{s}$)	16.35 Bq/g
Emissions	**β:** 89.28%, E_β= 1.31 MeV **γ:** 10.72%, E_γ= 1.46 MeV
Half life ($\mathbf{K}^{40}$)	1.25×10^9 yr
Density	1.984 g/cm^3
Solubility in water (20°C)	25.4%

Table 5.1: Physical properties of potassium chloride.

To determine the minimum detectable activity of the beta sensing device, several solutions with varying concentrations of ^{40}K are required. Using the fibre bundle in each solution and looking at the radiation events detected above background noise allows not only a minimum detection limit to be established, but also provides a calibration curve enabling a conversion between the number of radiation events detected and the concentration of beta emitters in a given KCl solution.

Ten dilutions were prepared by dissolving a known mass of solid KCl (m_{KCl}) in water and recording the total volume of the solution (V_T). Given the specific activity, A_s, of KCl, the activity concentrations, defined as the activity per ml of solution, A_C (Bq/ml) are calculated using:

$$\mathbf{A_C}[\mathrm{Bq/ml}] = \frac{m_{KCl}}{V_T}\frac{[\mathrm{g}]}{[\mathrm{ml}]} \times A_s\frac{[\mathrm{Bq}]}{[\mathrm{g}]} \tag{5.2}$$

The highest possible activity concentration is determined by the solubility limit of KCl in water at a given temperature. With this in mind, the following solutions were prepared:

Solution no.	$\mathbf{A}_{\mathrm{C}}$[Bq/ml]	$\mathbf{A}_{\mathrm{C}\beta}$[Bq/ml]
1	4.15	3.70
2	3.70	3.30
3	3.20	2.87
4	2.76	2.46
5	2.29	2.04
6	1.80	1.60
7	1.36	1.21
8	0.89	0.71
9	0.43	0.38
10	0.22	0.20

Table 5.2: KCl solutions prepared for experiment with the beta sensor

$A_{C\beta}$ is the contribution to the activity from beta particles, given by the product of the branching ratio of beta decays and the activity concentration, so $A_{C\beta}= 0.8928 \times A_C$. The fibre bundle used in section 5.2.2 was first tested in solution 1, as it has the highest activity concentration, however, no meaningful signal was detected above background noise. Detectable signals above background noise were observed using this fibre bundle in the slurry in Section 5.3.1, however this liquid contained 5 Bq/ml of ^{238}U, a single decay of which, releases eight alpha and six beta particles along the chain. Hence the actual concentrations of individual alpha and beta radionuclides would be much greater than 5 Bq/ml. The inability to detect radionuclides at 3.7 Bq/ml in a KCl solution necessitates the need for improvements to either the experimental setup or the fibre bundle device. Enhancing the coupling between the fibre bundle and detector and reducing background noise by shielding are examples of ways the experimental setup could be optimised, however, improvements to the design of the fibre bundle is likely to have the largest experimental impact. This is investigated in the following sections.

Improvements in sensitivity

Any beta particle emitted within the beta particle range of a liquid, R_β, surrounding each fibre (red shaded region in Fig. 5.7 (a)) has the potential for detection. In an array of fibres, this active volume will depend on the overall geometry of the structure. The fibre separation distance in the beta sensing bundle is less than R_β, so there will be some overlap of active volumes surrounding each fibre, hence a simple approximation of the total active volume is made by considering a rectangular volume surrounding the bundle with dimensions L × W × H as shown in Figure 5.7 (b), where H is the length of fibre immersed in the liquid (5 cm).

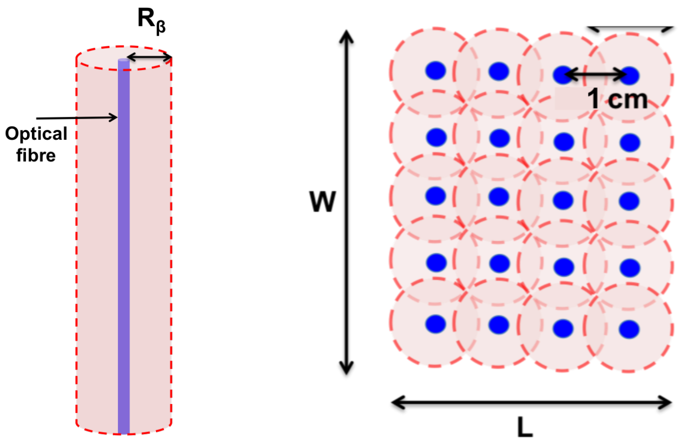

(a) 'Active sensing volume' surrounding optical fibre

(b) Top down view of the geometry of fibre bundle

Figure 5.7: 'Active sensing volume' of a single fibre and fibre bundle

Using L=3.1 cm, W=3.6 cm and H=5 cm gives an active sensing volume of 55.8 ml. This fibre bundle configuration did not have sufficient sensitivity to usefully detect signals above the background noise, so a new bundle, B2, was created with the goal of improving signal-to-noise levels in the KCl solution. By increasing the active sensing volume of the fibre bundle, an increase in the number of beta particle interactions with the fibres should be possible. The improved design of bundle B2 is pictured in Fig 5.8.

Improvements from the previous design (B1) include:

- Number of fibres increased from 20 to 42.
- The height between the top and bottom plates of the structure holding the fibres was increased from 5 to 10 cm. This height is equal to the length of fibre immersed in the sensing solution.
- Spacing between fibres decreased to 0.5 cm to account for maximum range of beta particles in KCl liquid.

These design changes result in an increase to the active sensing volume by a factor of 15.

The changes described above which were implemented in the design of the beta sensor, B2, resulted in significant improvements in the signal-to-noise ratios in KCl solutions from the previous sensor. A fraction of the measurement signal will contain contributions from the gamma rays emitted by ^{40}K which can easily be subtracted by counting pulses above a certain threshold in the pulse height spectra, as described in the following section.

Figure 5.8: Fibre bundle B2 for beta particle detection.

Removal of gamma contributions

By taking advantage of the path length differences between beta particles and gamma rays in KCl, the gamma contribution to the pulse height spectra can be analysed, and subsequently removed. The range of 1.3 MeV beta particles in pyrex is around 3 mm (ESTAR database). Hence by stacking a smaller pyrex beaker within a larger one, and filling the space between with solid KCl, this should allow relatively undisturbed passage of the 1.47 MeV gamma rays into the inner beaker while stopping the beta contribution. With this in mind, the following measurements were performed with the new fibre bundle to show differences and similarities in the pulse height spectra when looking at background noise, gamma processes, and gamma plus beta processes. Measurements were performed for 100 seconds each, and pulse height spectra collected (Figure 5.9) using the following three scenarios:

(i) The innermost beaker is filled with water to act as a blank solution, the fibre bundle is immersed and pulse height spectra collected. This gives information about background processes including cosmic rays, thermal noise etc.

(ii) The space between the inner and outer beaker is filled with solid KCl, and the fibre bundle remains in the innermost beaker in the blank solution. This gives information about background processes and gamma ray contributions from the KCl.

(iii) The fibre bundle is immersed in a new beaker containing KCl solution 1, so beta, gamma, and background processes are all counted

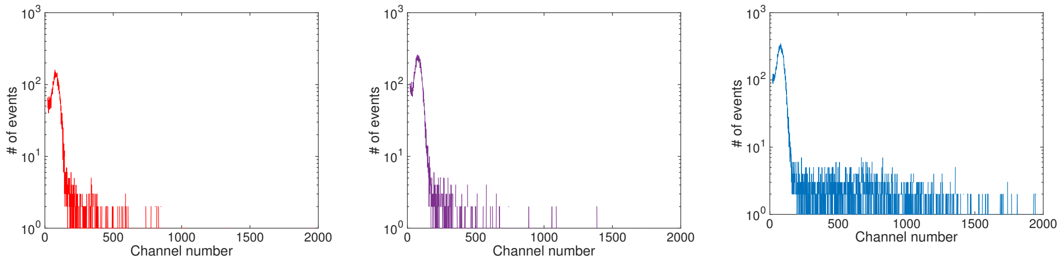

(a) Scenario (i) (b) Scenario (ii) (c) Scenario (iii)

Figure 5.9: Pulse height spectra obtained using fibre bundles showing (a) background events (b) background + gamma ray events from KCl and (c) background + gamma and beta events in KCl solution

Figure 5.9 (a) shows the pulse height spectrum representing scenario (i) where events detected should result only from thermal and electronic noise of the detector and scintillation light produced within the fibre bundle by any terrestrial radiation or cosmic rays. The majority of counts in the pulse height spectrum appear in or close to the SEP region, consistent with the idea the detector is measuring background noise.

In Figure 5.9 (b), background processes as in scenario (i) are measured in addition to gamma ray events from KCl. Due to the sparsely ionising ability of gamma rays, any given interaction with a fibre is not expected to produce much more than a single photoelectron at the detector, so theoretically an increase in counts only near the SEP should be observed. Comparison of Figures 5.9 (a), (b) confirms this hypothesis. A count increase is observed in the lower energy part of the pulse height spectrum near the SEP region, with the counts observed at higher channel numbers (300+) remaining constant within counting error.

Addition of the fibre bundle to a KCl solution (scenario (iii)) changes the radiation field surrounding the fibre bundle to include beta particles from the radioisotope as well as the gamma rays and background noise. An overall increase in counts across the entire spectrum, not just in the SEP region is observed (Figure 5.9 (c)). The distinguishing feature in this pulse height spectrum is the larger numbers of counts in higher channel numbers resulting from beta particle interactions with the fibre bundle.

The measurements above show that scintillation events produced by beta particles in KCl can be distinguished from noise processes and gamma ray events in the pulse height spectrum. To isolate the beta contribution to the signal, a threshold in the channel number is applied to count events which the majority of which would be produced by beta radiation. Based on the spectra in Figure 5.9, the majority of events above channel 300 appear to be caused by beta particles, hence events detected from this channel number onwards are used for analysis of the beta component of the total measurement signal. To show how this works, the measurements (i), (ii), (iii) were repeated five times and counts summed above and below channel 300, with the mean and standard deviations of these measurements presented in Table 5.3 below.

	Count sum (1:300)	**Count sum (301:4295)**
(i) Background	9,719 ± 122	468 ±15
(ii) Background + KCl_{γ}	16,177 ± 145	475 ± 12
(iii) Background + $KCl_{\gamma,\beta}$	20,552 ± 241	2057 ± 28

Table 5.3: Integrated counts above and below channel 300 for scenarios (i),(ii),(iii)

Conclusions drawn from Table 5.3 include:

- The addition of gamma rays to the radiation field results in a significant count increase below channel 300.
- No significant difference in detected count numbers above channel 300 is observed as a result of gamma interactions with the device.
- Beta particle interactions with device cause increased counts across the whole pulse height spectrum.

To summarise: For the high voltage and gain settings used here, integrating the total counts in the region above channel 300 allows removal of the gamma component of KCl emissions detected with the fibre bundle. Signals in this integration region will still contain a small amount of background noise, which needs to be separately measured and subtracted to isolate the beta contribution to the signal.

Minimum detectable activity

To determine the minimum detectable activity of beta particles within a test solution, the fibre bundle was placed in the KCl solutions listed in Table 5.2, starting with the highest concentration. Background data was taken with the fibre bundle in a beaker of distilled water, and this was performed prior to using the bundle in each solution. Background counts above channel 300 remained constant within counting error throughout the experiment, the mean and standard deviation (336 ± 8) was taken and used for subtraction purposes. Four measurements were performed for 100 s in each KCl solution, and counts above channel number 300 were integrated. Results are presented in Table 5.4 with each count sum represented by the mean and standard deviation of the four measurements. Considering the limited number of measurements taken in each solution, counting errors ($\sqrt{n}$) would likely provide a more accurate representation of the count sum errors. For this reason, error bars shown in 5.10 are calculated using counting statistics. The point at which count numbers are no longer distinguishable above background will give an indication of the minimum detectable activity with this particular fibre device.

Solution no.	$A_{C\beta}$ **[Bq/ml]**	**Count sum**	**Background subtracted sum**
1	3.70	2057 ± 28	1721 ± 29
2	3.30	1921 ± 15	1585 ± 17
3	2.87	1710 ± 53	1374 ± 53
4	2.46	1511 ± 21	1175 ± 23
5	2.04	1350 ± 39	1014 ± 40
6	1.60	1130 ± 20	794 ± 21
7	1.21	899 ± 19	563 ± 20
8	0.71	754 ±25	418 ± 27
9	0.38	548 ± 22	213 ± 23
10	0.20	398 ± 13	63 ± 16

Table 5.4: Integral counts between channels 301:4095 measured in KCl solutions

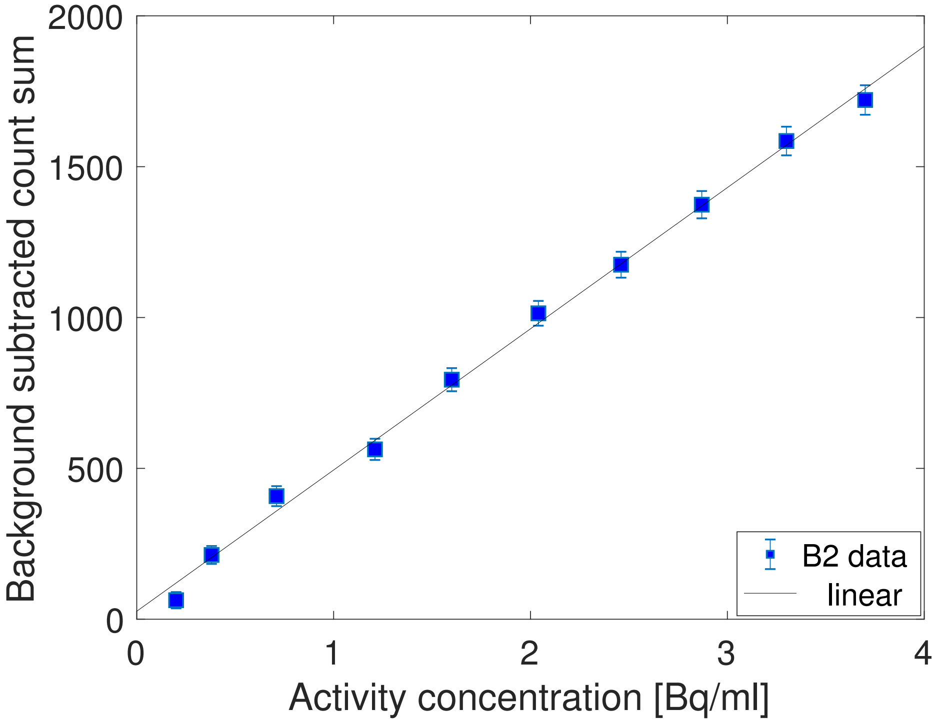

Figure 5.10: Potassium chloride solution calibration curve using fibre bundle B2

For each KCl solution, there is an observed linear increase in counts with respect to radionuclide concentration (Fig 5.10). An increase in count rate is observed even for concentrations as low as 0.2 Bq/ml, although at such low signal levels counting errors begin to become appreciable, 53% for the data point at 0.2 Bq/ml.

It has been shown the sensitivity of the device can be improved by increasing the number of fibres and the length of each fibre in contact with the solution, indicating the device could be further optimised to improve the signal-to-noise ratios and minimum detectable activity.

5.3.4 Alpha particle sensing of Polonium-210 in test solutions

For the purpose of these experiments, polonium-210 has a suitably long half life (138.4 days) and dissolves readily in dilute acids [81]. Upon emission of a 5.3 MeV alpha particle, ^{210}Po decays to a stable daughter ^{206}Pb, with only one out of every 100,000 alpha emissions resulting in a 803 keV gamma ray, which is considered a negligible component of the total activity.

A limited amount of Po^{210} was available, so a new bundle (A2), with a larger number of fibres for alpha particle sensing was created (Fig. 5.11). 1,500, 250 µm diameter BCF20 fibres were used, as opposed to 200 fibres in A1, to improve the chances of obtaining a meaningfully low detection limit. BCF20 fibres were used as there were insufficient BCF12 fibres left to make a bundle with a suitably large interaction volume.

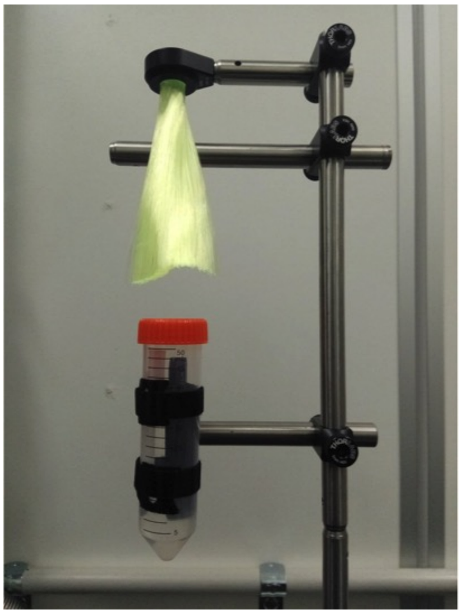

Figure 5.11: Fibre bundle A2 for beta particle detection.

A major challenge in creating a device for alpha particle detection is overcoming the lack of sensitive volume surrounding each fibre which is limited by the short range, R_α, of the alpha particle. For example, compare a 10 cm long fibre with 1 mm OD for beta particle detection, with a 250 µm OD fibre of the same length used for alpha particle detection (Figure 5.12). The 1 mm thick fibre is able to interact with beta particles emitted within a surrounding 8 mm radius for an active volume totaling 20.1 mL around the fibre. In contrast, an alpha particle can only interact with fluid 32.5 µm from the outside of the fibre because of the 7.5 µm cladding, which equates to a sensitive volume of only 0.0029 mL surrounding the fibre. This lack of sensitive volume needs to be overcome by using a large number of fibres. For a bundle containing 1500 fibres, with a 10 cm length to be immersed in solution, the total active sensing volume will be 4.4 ml, 7.8 times as large as the previous design used in Section 5.3.1.

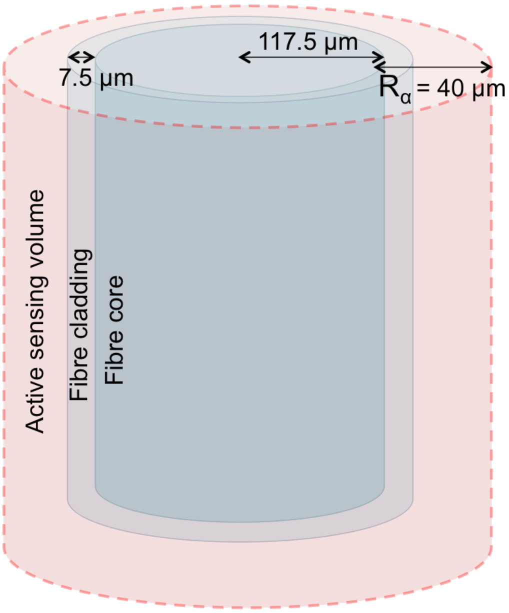

Figure 5.12: Diagram showing active sensing volume surrounding a cladded 250 µm OD fibre for alpha detection

Solution preparation

A concentrated solution of Po^{210} in 1 M HCl (pH 0) was used as a stock solution. To prepare appropriate dilutions down to 1 Bq/ml, the activity of the stock solution was first measured by placing a known volume of the solution between two zinc sulphide screens and the activity counted over 1000 s using a Daybreak alpha counter. The measured activity was 340 ± 10 Bq/ml. Solutions listed in Table 5.5 were prepared using this stock solution and diluting with 1 M HCl, with activities measured to confirm dilutions were performed correctly.

Solution no.	**A**$_C$[Bq/ml]
1	9.4 ± 0.3
2	4.6 ± 0.2
3	2.3 ± 0.2
4	1.1 ± 0.1

Table 5.5: Activity concentrations of ^{210}Po solutions used in experiment

Minimum detectable activity concentration

To determine the minimum detectable activity in a ^{210}Po test solution using the new alpha sensing bundle, the solutions listed in Table 5.5 were prepared. Measurements were taken by placing the fibre bundle in each solution, starting from the lowest activity and acquiring a pulse height spectrum. 100 s integration times were used, and background readings were taken prior to those in each solution in a blank 1 M HCl solution after rinsing the bundle in dilute acid followed by distilled water.

Following measurements in each polonium solution, there was an elevated background reading, especially noticeable in the high energy part of the spectrum. Figure 5.13 displays the pulse height spectra acquired in blank HCl solutions taken before measurements in solutions 1-4. Given the blank solutions should contain no significant traces of radioisotopes, the count numbers increase steadily with each new measurement. Care was taken to ensure the blank solutions used for background measurements contained no traces of ^{210}Po by (a) ensuring the bundle was rinsed each time in fresh aqueous HCl and distilled water, and (b) new plastic containers and HCl solutions were used each time a measurement was performed. In addition to the rising background signals, count numbers were steadily increasing over the course of a measurement in the higher activity polonium solutions 3 and 4, indicating the polonium may be adhering to and contaminating the fibres. A brief summary of the methods used to try remove contamination from the fibre bundle is given in Chapter 6. Although these methods proved unsuccessful, subtraction of the background signal from the measurement signal was sufficient for the purpose of these experiments and ensures contamination does not significantly affect measurements.

The gain settings were adjusted from the previous experiment with the beta sensing device, and a threshold set at channel 400 for event counting to remove low energy noise contributions. Five measurements were taken when collecting background data and for measurements in solutions 1 and 2. Due to the steadily rising count rate caused by polonium adhering to the fibres over the course of a measurement, only three data sets were taken in solutions 3 and 4. The mean and standard error of the mean ($\sigma/\sqrt{n}$) of the count sums are presented in Table 5.6.

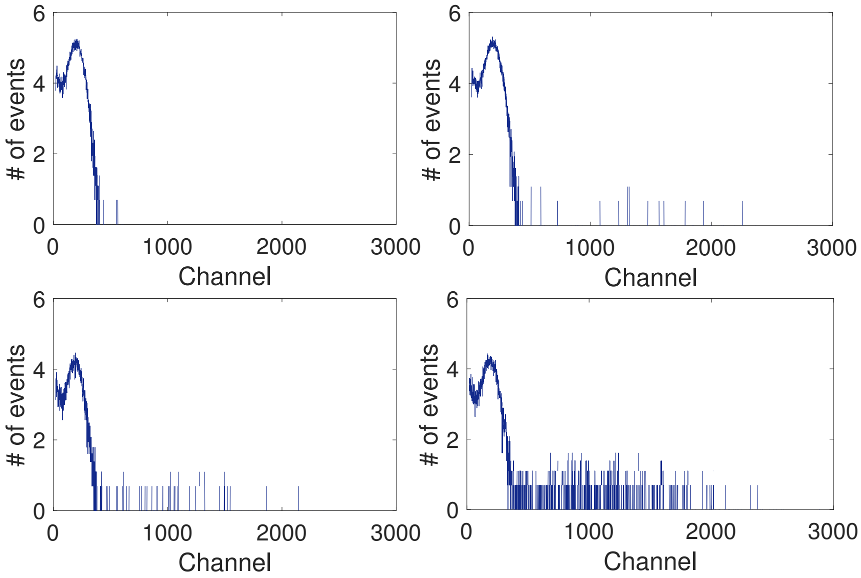

Figure 5.13: Background pulse height spectra taken before measurements in ^{210}Po solutions 1-4 (left to right)

A_C[Bq/ml]	Total counts	Bkg counts	Bkg subtracted counts
1.1 ± 0.1	411 ± 15	162 ± 5	249 ± 16
2.3 ± 0.2	745 ± 18	420 ± 15	325 ± 23
4.6 ± 0.2	1412 ± 33	685 ± 12	727 ± 35
9.4 ± 0.3	3045 ± 54	1600 ± 20	1445 ± 58

Table 5.6: Mean and standard errors of measured ^{210}Po solution and background counts measured from channels 401 to 4095.

There is an approximately linear increase in total counts with respect to activity concentration (Fig. 5.14), and signals above background noise are detected for activities as low as 1.1 Bq/ml, however more data points are required to better demonstrate a linear relationship. These measurements show low level detection of alpha emitters in solution with fibre bundles is possible, so further measurements were performed to improve the detection limit and focus on a smaller activity range.

Creating a new alpha sensor

To create another fibre bundle (A3), and improve upon previous results, more 250 µm diameter BCF12 fibre, a blue scintillator was acquired. Changes to the fibre bundle

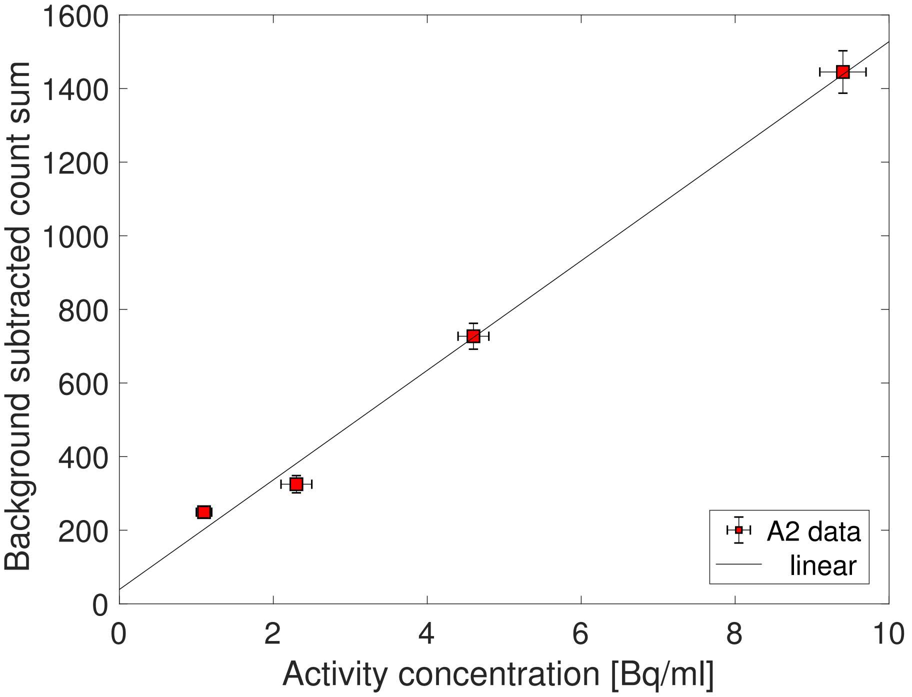

Figure 5.14: ^{210}Po calibration curve using fibre bundle A2

and experimental plan are:

- BCF12 (instead of BCF20 used for A2) was used. Use of a blue scintillator whose emissions are detected with higher QE using the PMT, in theory should produce a more sensitive device than the previous design.
- The number of fibres in the bundle was increased from 1500 to 1800, with the length unchanged. Increasing the number of fibres will increase the active sensing volume and should result in a sensitivity increase.
- Six new polonium dilutions were created with activity concentrations of 0.5, 1, 2, 3, 4 and 5 Bq/ml.
- In a further attempt to reduce any accumulating polonium contamination, 3 measurements were performed in each solution instead of 5 and care was taken to reduce the time the device was left in the solution.

Results are shown below, with count values presented as mean and standard error of 3 measurements.

A_C[Bq/ml]	Total counts	Bkg counts	Bkg subtracted counts
0.5 ± 0.01	238 ± 11	155 ± 9	83 ± 14
1 ± 0.02	338 ± 11	231 ± 5	107 ± 12
2 ± 0.04	563 ± 8	349 ± 9	215 ± 12
3 ± 0.05	897 ± 24	619 ± 12	278 ± 27
4 ± 0.07	1212 ± 12	861 ± 17	350 ± 21
5 ± 0.09	1790 ± 19	1337 ± 25	423 ± 31

Table 5.7: Mean and standard errors of measured ^{210}Po solution and background counts measured between channels 401:4095.

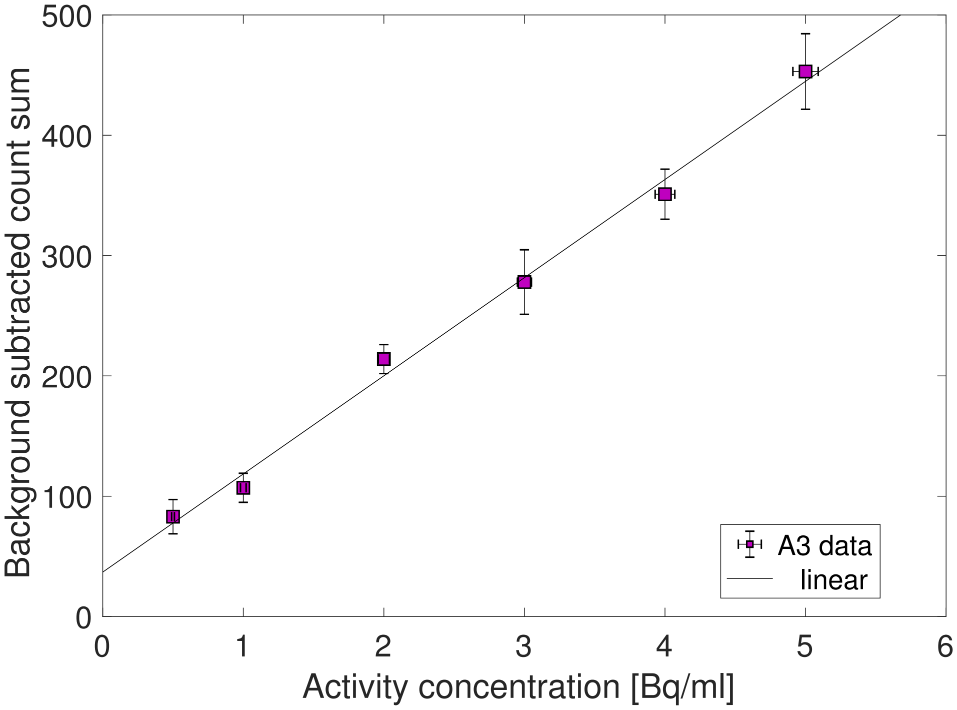

Figure 5.15: ^{210}Po calibration curve using fibre bundle A3

A comparison of the results from both fibre bundles is displayed in Figure 5.16. Despite the higher detection QE of the fibre emission, and the increase in fibre numbers in the second bundle compared to the first, lower count sums were observed for similar solution activities, and the efficiency is almost halved (The efficiency of each device is represented by the slope of the line of best fit). This could be due to a number of factors including differences in detector coupling, bundle end-face quality, and whether or not the end-face of the bundle had been polished down enough to expose all fibres through the epoxy. Furthermore, the line of fit for bundle 1 was taken over a larger activity range and uncertainties are high, hence a number of factors could be contributing to observed differences between the two bundles. Both fit lines do not pass through the point (0,0), which would correspond to zero measured counts when no radionuclides are present in solution. Background subtraction should account for detector noise and ≈ constant ambient sources, which indicates there may be some background noise sources unaccounted for in the measurements. These results do show a lower measured detection point of 0.5 Bq/ml from the previous bundle design and the linear relationship between detected counts and activity was improved.

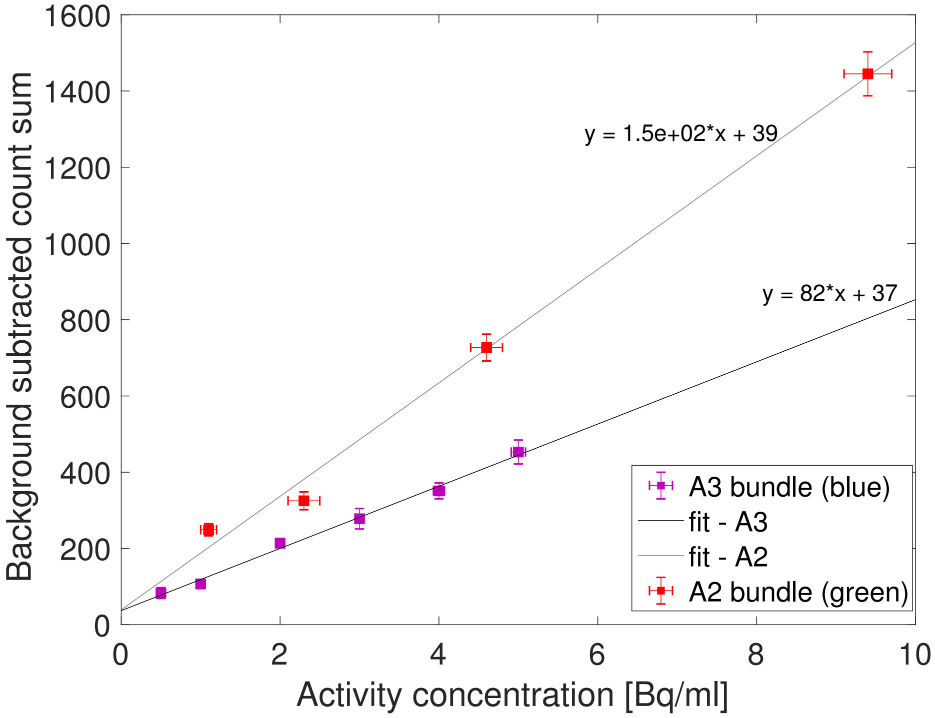

Figure 5.16: Comparison of alpha sensing bundle results

5.4 Summary

Previous chapters studied the optical properties and radiation response of a range of commercial and fabricated optical fibres for the purpose of alpha and beta particle detection. This chapter is the culmination of previous work to select the most appropriate fibre type as the basis for designing two types of radiation sensors, and the testing of their performance under environmental conditions analogous to those encountered during mineral processing. The devices were able to function effectively in elevated temperatures in an acidic liquid containing abrasive particles, and both devices well exceed the minimum detectable activity being targeted (1 Bq/ml per isotope of ^{238}U), showing that the use of scintillating optical fibres enables the construction of sensors capable of achieving the project goals.

Chapter 6

Operational considerations and prototype device testing

6.1 Introduction

This chapter addresses the testing of prototype fibre bundle sensors and focuses on the issue of sensor contamination which was encountered when calibrating devices in polonium containing solutions in Chapter 5. In Section 6.2, a number of techniques are investigated to both prevent ^{210}Po ions from adhering to fibre surfaces, and to remove them following adsorption. The accumulation behaviour of ^{210}Po on the surface of fibres and on the fibre bundle A2 from the preceding Chapter is briefly studied in Section 6.2.3, to investigate the feasibility of a semi-continuous operational mode of the sensor. Prototype devices incorporating improved designs are created and tested in mixed radionuclide solutions in Sections 6.3 and 6.4, and future device improvements are discussed.

6.2 Management of ^{210}Po contamination on fibre bundles

The ease with which polonium deposits onto polymer has proven problematic for establishing detection limits and calibrating the fibre sensors. To dissolve ^{210}Po for calibration of the fibre bundles, a dilute acid was required (in this case HCl was used, but ^{210}Po will also dissolve in sulphuric, nitric acid, etc.[81]). Once dissolved in a dilute acid, ^{210}Po can spontaneously plate onto a range of materials including polymers and glass, with deposition onto silver surfaces reported to occur especially readily [63, 31]. Full recoveries of polonium from dilute 1-2 M hydrochloric acid onto silver has been reported in as low as 60 minutes at temperatures between 85-90°C [32]. When designing experiments here, and attempting to remove Po^{210} ions from the fibre bundles, the affinity of polonium to silver and to a much lesser extent, glass, has been acknowledged. A brief summary of the preliminary decontamination methods used for the fibre bundles are presented below.

6.2.1 Contamination removal

Acid rinsing: Polonium adsorbs much less readily on plastic than glass so all dilutions were prepared and stored in plastic containers. As a first decontamination measure, fibre bundles were rinsed thoroughly in fresh 1M hydrochloric acid solutions, then distilled water. All rinsing solutions were contained in glass beakers with the hope any adsorbed polonium ions would plate to the glass walls once in solution, and so establish a very low equilibrium concentration of ^{210}Po in solution, which is conducive to dissolving further ^{210}Po off the fibres. Pulse height spectra were acquired using the fibre bundle in blank hydrochloric acid solutions before and after each decontamination attempt to determine if the procedure had any noticeable effect. Rinsing the fibre bundles with hydrochloric acid did not result in any changes to the background count numbers measured in the pulse height spectra. Fibre samples were also rinsed using 8 M hydrochloric and 1 M sulphuric acid solutions with no measurable change to contamination levels.

Silver plating: Given that polonium plates spontaneously onto silver in dilute acid, a piece of silver wool was placed in a 1 M hydrochloric acid rinsing solution to adsorb any ^{210}Po ions on the fibres or in the solution. The plating effectiveness, defined as the number of ions adsorbed per unit area of plating material, will increase with the surface area of the plating material, hence why silver wool was chosen over a solid piece of silver. Using the plating solution (1 M hydrochloric acid + silver wool), decontamination of the fibre bundle was attempted using the following methods:

1. The bundle was left in the plating solution and gently stirred using a magnetic stirrer for between 30 minutes to 48 hours.

2. The beaker containing the bundle and plating solution was placed in a warm ultrasonic bath to assist with dislodging any particles carrying adsorbed ^{210}Po from the optical fibres.

3. The beaker and plating solution was placed on a hotplate stirrer and heated to 45°C while gently stirring. Plating efficiency is optimised at temperatures between 85-90°C, however a lower heating temperature was chosen for two reasons: firstly, 85-90°C is too close to the transition temperature, T_g, of the polymer, and secondly, polonium begins to vaporise in air at 55°C. To reduce the risk of polonium becoming airborne and the optical fibres deforming, a solution temperature

of 45°C was used.

Unfortunately, no observable reduction of the level of adsorbed polonium ions on the fibre bundle was measured.

Aluminium chloride pre-treatment: This method was focused on preventing polonium ions from plating onto the optical fibres in the first place as opposed to removing them. The reasoning behind this method is that the Al^{3+} cations in solution will preferentially adsorb over Polonium cations to the negatively charged polymer surface and prevent any contamination occurring during measurements. A 1 M solution of aluminium chloride in distilled water was prepared, and the alpha sensing fibre bundle A2 was left to soak in the solution for 24 hours, before being placed in a polonium containing solution. This method also proved unsuccessful.

Decon 90 treatment: Decon 90 is a cleaning agent and radioactive decontaminant which contains anionic and non-ionic surface active agents, stabilisers, non-phosphate detergents, alkalis and sequestering agents. The alpha sensing fibre bundle A2 was sonicated in a ziplock bag containing water and Decon 90 liquid detergent for 60 minutes. This cleaning method resulted in a 19 x decrease in the contamination level of the contaminated fibre bundle, with count numbers in the measurement range of the pulse height spectrum decreasing from $\approx$ 3800 to 200 in a blank hydrochloric acid solution.

Treatment of the fibre bundle with diluted decon 90 detergent has been the only method tested which has been successfully able to produce a measurable decrease in the contamination level of the sensor. Lengthy sonication times were required to remove a significant amount of the particles carrying adsorbed polonium ions, so would only be useful for infrequently cleaning the bundles.

With this in mind, a range of fibre coatings have been tested to prevent the polonium ions adsorbing to the fibres to hopefully eliminate the requirement for decontamination treatments.

6.2.2 Fibre coatings for contamination prevention

Teflon is particularly resistant to contamination owing to its hydrophobic and oleophobic properties, and as such is often used for storing unsealed radionuclides in solutions and powders. Teflon solutions are suitable for coating materials like metals and glasses, however, the strong solvents required to dissolve teflon also dissolve polymers, making it unsuitable for coating polymer optical fibres. As an alternative, a range of hydrophobic and super-hydrophobic coatings which are compatible with polymer have been investigated to prevent polonium contamination. Water easily rolls or bounces off these hydrophobic substrates, carrying away most surface contaminants and providing a host of other benefits which may include corrosion and moisture resistance, self-cleanability and an increased substrate lifespan. A list of the coatings used and their general properties are shown in Table 6.1. The hydrophobicity of the coatings are specified in terms of their surface contact angle. To be classified as a hydrophobic surface, the contact angle must be greater than 90° or at least 150° for the case of superhydrophobic surfaces (see Figure 6.1).

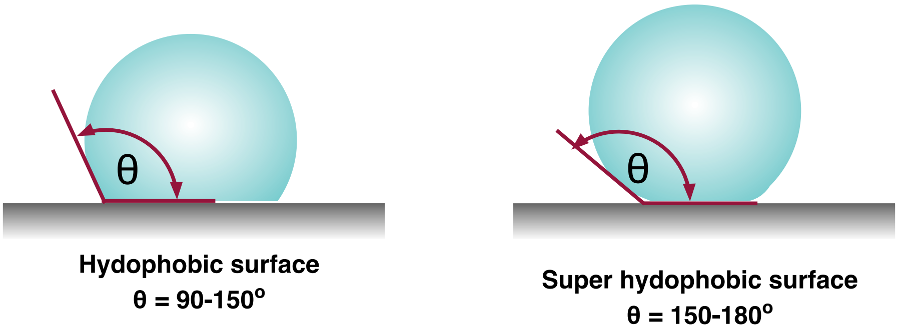

Figure 6.1: Surface contact angle and hydrophobicity relationship

Coating	Surface contact angle	Coating thickness	Temperature durability	Chemical resistance
ZR53[1]	105°	700-1000 nm	150°C	12>pH>1
MF2[1]	95°	200-300 nm	225°C	12>pH>1
SHBC[1]	171°	8-10 µm	175°C	Not specified
Textile shield[2]	> 150°	125 nm	Not specified	Not specified

Table 6.1: List of coatings trialled to prevent polonium accumulation on optical fibres
[1] Manufactured by Nasiol
[2] Manufactured by DryWired

To trial the effectiveness of the coatings, 3 cm lengths of fibres were coated by either using a:

- Spray application: The coating solution was sprayed onto the fibre with the included spray gun and left to cure for 48 hours. SHBC was the only coating solution that was recommended for application using a spray method (and came with an applicator), hence was the only material spray coated.
- Dip application: Fibre samples were dipped in the coating solutions then left to cure for 48 hours. This method was used with all coating solutions.
- Dip + buff application: The recommended application method for MF2 and ZR53

coatings was to apply the solution and gently buff the surface using a microfibre cloth. This was performed in addition to the dip only coating described above. Samples were left to cure for 48 hours.

Coated and uncoated fibres (1.5 mm diameter BCF12) were placed in polonium solutions then sandwiched between two ZnS screens and placed in an alpha counter. Polonium adhered to the fibre surface will decay via alpha particle emission and produce a scintillation pulse upon interaction with the ZnS which can be detected to quantify the amount of adsorbed ^{210}Po. Each fibre was immersed in a 1 M hydrochloric acid solution containing 20 Bq/ml of ^{210}Po for five minutes, rinsed with distilled water and placed in the alpha counter using a 20 minute integration time. Results are presented in Table 6.2

Coating	**Count number**
Uncoated	70 ± 8
SHBC - Sprayed	204 ± 14
SHBC - Dipped	155 ± 12
MF2 - Dipped	84 ± 9
MF2 - Dipped, buffed	67 ± 8
ZR53 - Dipped	77 ± 9
ZR53 - Dipped, buffed	67 ± 8
Textile Shield - Dipped	74 ± 8

Table 6.2: Measured ^{210}Po counts and counting errors for 3 cm long coated/uncoated fibre samples of 1.5 mm dia. BCF12.

None of the fibre coatings appear to produce a significant decrease in the amount of measured polonium adsorbed to the fibre surface. The superhydrophobic coating, SHBC, appears to cause a substantial increase in the amount of contamination, an effect potentially related to the breakdown of the polymer based coating in the acid causing an increase in surface area.

6.2.3 Accumulation rate of ^{210}Po on optical fibres

At this stage, a feasible solution to prevent the adsorption of ^{210}Po onto the optical fibre surface had not been realised. A potential approach to overcome the measurement effects caused by accumulation of contaminating radionuclides would be to automate the removal of the sensor at regular intervals from the measurement solutions to take background readings and subtract from the total measured signal. This approach would be feasible provided the contamination levels do not increase substantially over the course of a measurement. The uptake of ^{210}Po on the surface of a 1.5 mm thick optical fibre was monitored as a first approach towards understanding its accumulation behaviour on fibre surfaces. 3 cm long fibre samples were immersed in a 20 Bq/ml ^{210}Po solution for time intervals ranging from 10 s to 190 minutes. The polonium levels were measured as in Section 6.2.2, using the alpha counter with 20 minute integration times.

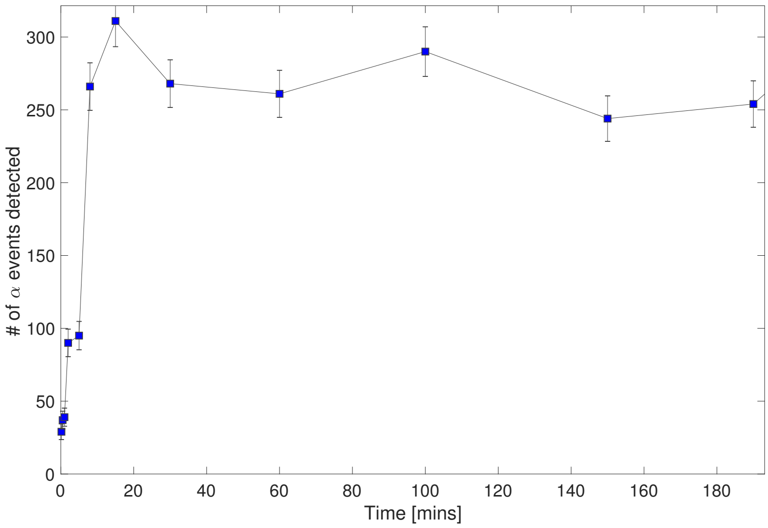

Figure 6.2: Detected alpha particle events from ^{210}Po on the surface of a 1.5 mm diameter BCF 12 fibre, plotted as a function of time.

Polonium adsorption on the fibre surface was evident after contact times as short as 10 s in the solution (see Figure 6.2). Accumulation levels of ^{210}Po were found to increase rapidly up until an immersion time of approximately 8 minutes, after which, the increase in contamination on the fibre surface appears to approach an asymptote (‘plateau‘).

Similar behaviour was observed when the A2 alpha sensing fibre bundle was immersed in a 10 Bq/ml ^{210}Po solution (Figure 6.3). The scintillation events produced within the fibres by the contaminating polonium ions were measured at regular intervals with a photomultiplier tube, and show an initial rapid increase before starting to plateau after an immersion time of approximately 20 minutes.

6.2.4 Summary of contamination management results

A number of decontamination measures have been investigated to remove particles carrying adsorbed ^{210}Po from the surface of polymer fibre bundles. A range of hydrophobic coatings were tested on optical fibres to prevent contamination with no improvement in the levels of contaminating ions detected. A 19 fold decrease in the contamination levels of the A2 fibre bundle was observed following a cleaning procedure where the

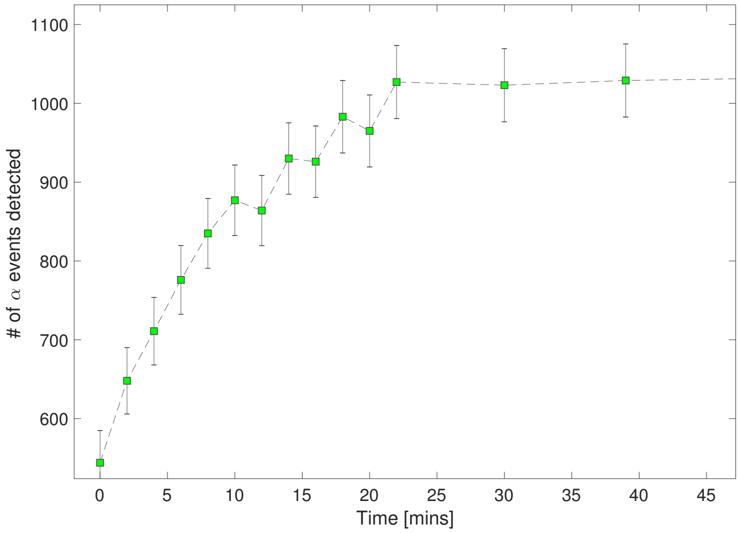

Figure 6.3: Detected alpha particle events from ^{210}Po using BCF20 fibre bundle, plotted as a function of time.

fibre bundle was placed in an ultrasonic bath with a Decon 90 solution for 60 minutes.

The uptake of ^{210}Po on the surface of the A2 alpha sensor was monitored by recording the number of scintillation events produced within the fibre by ^{210}Po when immersed in a solution containing 10 Bq/ml of the radionuclide. Contamination levels were observed to plateau after an immersion time of approximately 20 minutes.

6.3 Beta particle detection in mixed radionuclide solutions

Up until this point, efforts have been focused on radionuclide detection using solutions of either alpha or beta particle emitters. Both alpha and beta particle sensors have demonstrated detection limits below the targeted limit of 1 Bq/ml per isotope in the decay chain of ^{238}U, with improvements to signal-to-noise ratios achieved by refinements in the sensor design (see Chapter5). Although an effective method to prevent polonium adsorption on the fibre bundles has not been realised, the contamination levels have been shown to quickly plateau, which would allow the sensors to be operated in a semi-real-time mode by taking short, periodic background readings with the sensor removed from the measurement solution. In this section, the beta sensor design is further refined, and measurements in mixed radionuclide solutions are performed to demonstrate the potential of this technology to measure low level beta activity concentrations in real-world mineral processing liquids.

6.3.1 Sensor design improvements

With the exception of the alpha particle emitted by polonium-214 (E_α=7.83), all alphas in the ^{238}U decay chain have energies less than 6.11 MeV, and a maximum range in PMMA of around 43 µm. Previous beta particle sensors were constructed using 1 mm diameter BCF12 fibres with 30 µm thick outer claddings which are not thick enough to prevent most alpha particles in the decay chain from penetrating to fibre core and producing a signal, an undesirable effect if the beta particle signal is to be isolated. It was now intended to use test solutions of ^{238}U containing liquids, hence the following improvements to previous sensor designs have been implemented:

Fibre diameter

BCF12 fibres with outer diameter 1.5 mm and a cladding thickness of 45 µm have been used to stop alpha particles with energies less than 6.11 MeV reaching the core and and producing a signal in the fibres. Although the 7.8 MeV alpha particle from ^{214}Po is able to penetrate the fibre cladding and deposit energy in the core, this isotope represents a small fraction of the total decay products from ^{238}U. Given the comparatively limited range in solution of this alpha particle to the targeted beta particles, its detection efficiency will be so small we can confidently neglect its contribution to the total signal. A commercial fibre would need to be at least 2.2 mm in diameter to have a cladding sufficiently thick enough (66 µm - cladding thicknesses are specified as 3% of the fibre OD) to block the 7.8 MeV alpha particle emitted from ^{214}Po, at which point the interaction volume for gamma rays starts to become appreciable and is why a 1.5 mm diameter was seen as sufficient.

The 0.5 mm increase in fibre diameter from previous bundle designs (B1, B2, where 1 mm fibres were used) will result in a larger interaction volume for beta particles, allowing greater energy deposition, hence light production within the fibre core. The radiation response to ^{90}Sr/^{90}Y beta particles is $\approx 1.63 \pm 0.1$ times higher when using the 1.5 mm diameter fibres compared to the 1 mm fibres as shown in Figure 6.4.

Fibre cladding type

Optical fibres with a double cladding (instead of the single cladding layer on sensors B1 and B2) have been implemented in this sensor design. Instead of the two layers of material present in single clad fibres (PS core + PMMA cladding), the double clad fibre structure contains three layers of material, the polystyrene core, a PMMA inner cladding layer and an outer cladding layer made from a fluor-acrylic (Figure 6.5). The refractive index of the outer cladding (n=1.42) is lower than PMMA (n=1.45), which

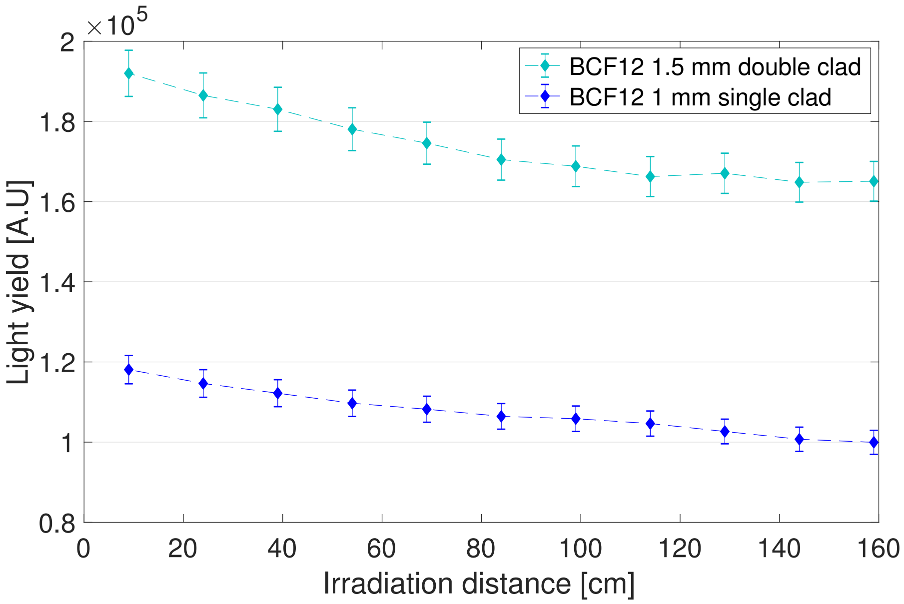

Figure 6.4: The light yield as a function of irradiation distance for 1 mm single cladded, and 1.5 mm double cladded BCF12 fibres in response to ^{90}Sr/^{90}Y beta particles

permits total internal reflection at a second boundary and causes an increase in the trapping efficiency, hence an increase in the number of guided photons.

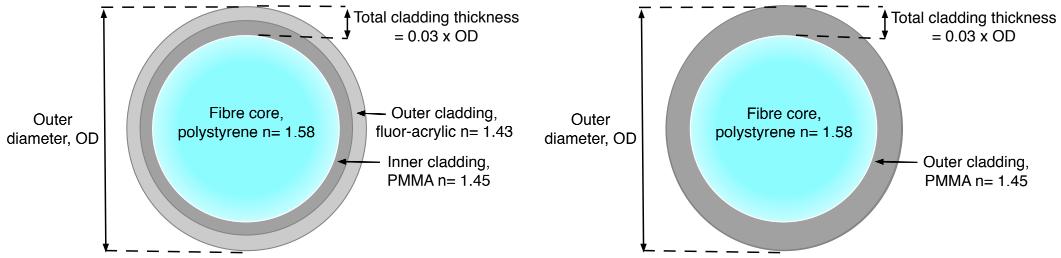

(a) (b)

Figure 6.5: Schematic illustrating the geometries of (a) a double clad optical fibre, and (b) a single clad optical fibre.

Use of a double clad fibre in the sensor design should result in increased signal levels, as for a given fibre length, more scintillation photons per radiation event are guided to the detection system compared to a single clad fibre. However, despite the larger diameter, and double cladded geometry, only a small decrease in loss is observed for the 1.5 mm fibre compared to the 1 mm variety (Figure 6.6).

Fibre spacing

The spacing between optical fibres in the array has been maintained at 5 mm, the same as with the B2 sensor design. If the spacing between fibres is too small, there is the potential for a single beta particle to trigger a signal in multiple fibres and give an overestimate for the solution activity (however, this can be accounted for by

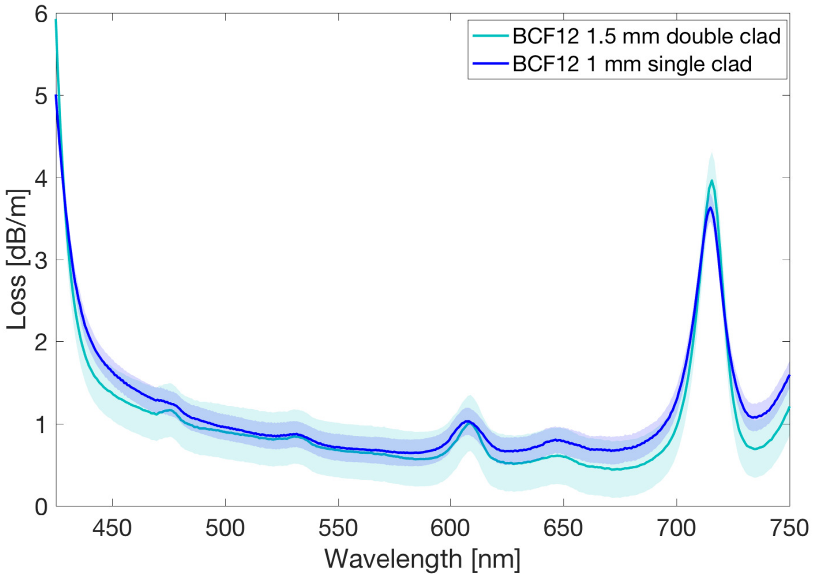

Figure 6.6: The loss of 1 mm single cladded, and 1.5 mm double cladded BCF12 fibres measured using the white light cutback technique.

calibrating the sensor). Conversely, if the fibre spacing is too large, then the sensor is under-sampling the signal contributions from the lower energy beta particles in the ^{238}U decay chain, so obviously a balance needs to be established.

There are six beta particles in the ^{238}U decay chain, with emission energies of 0.063, 0.27, 1.01, 1.16, 2.19 and 3.27 MeV, giving them a range of maximum penetration depths from 50 µm to 1.45 cm in water, for example. Ranges in mineral processing solutions would be similar or less depending on composition. This maximum penetration depth however, is only representative of a very small fraction of the beta particles emitted by a radionuclide, as they are emitted with a continuum of energies ranging from zero to a maximum. The average beta particle energy represents a much greater proportion of the electron energy yield from a radionuclide, and is given by approximately 1/3 of the maximum beta energy, as a rule of thumb. As such, the majority of beta particles in the decay chain of ^{238}U will have a range in water of approximately 5 mm, and the fibre spacing in the beta sensor has been chosen to reflect this.

Fibre numbers and lengths

Fibre lengths have been maintained at 10 cm, with 42 fibres in total used for this sensor. This is consistent with the B2 prototype device, as good signal-to-noise ratios were achieved with this configuration, and the effect of increasing fibre length and numbers on sensor performance have already been demonstrated. These parameters also ensure the sensor design remains compact and fits within the current experimental set-up.

6.3.2 Calibration in a potassium chloride test solution

To perform the beta particle calibration of the B3 fibre bundle, potassium chloride solutions were used as in Chapter 5.3.3, and the total number of events detected between channels 300 and 2049 using the pulse height spectra were used. Lead shielding was used to surround the experiment for this, and all subsequent measurements for reduction of background noise. All measurements were performed using 100 s integration times. The solution activity concentrations, $A_{C\beta}$, and count sums are shown in Table 6.3. The calibration curve was obtained using a linear least squares regression of the data, with the background subtracted count sum (C_S) related to the activity concentration of the solution via C_S=700×$A_{C\beta}$ + 49. Standard errors on the slope of the line, σ_m, and intercept, σ_b are 6.34 and 11.85 respectively.

$A_{C\beta}$ **[Bq/ml]**	**Bkg subtracted counts**
3.77	2667 ± 55
2.99	2141 ± 50
2.38	1741 ± 46
1.90	1417 ± 42
1.52	1114 ± 39
1.21	875 ± 36
0.96	744 ± 34
0.77	560 ± 31
0.61	485 ± 29
0.49	379 ± 28
0.25	221 ± 25

Table 6.3: Beta particle activity concentrations, $A_{C\beta}$, of potassium chloride solutions used for calibration of B3 beta sensor and corresponding background subtracted count numbers measured between channels 300 to 2049. Errors stated are counting errors.

Replacement of the 1 mm BCF fibres with the 1.5 mm variety in the fibre bundle has led to an increase in light yield by a factor of 1.5 (See Figure 6.7), consistent with the difference in measured light yield ratios between the two fibre types.

6.3.3 Calibration in a ^{210}Po test solution

Before the beta particle sensor can be used in mixed radionuclide solutions, two calibrations need to be established using seperate solutions containing alpha and beta particle emitters. The only alpha particle in the ^{238}U decay chain with enough energy

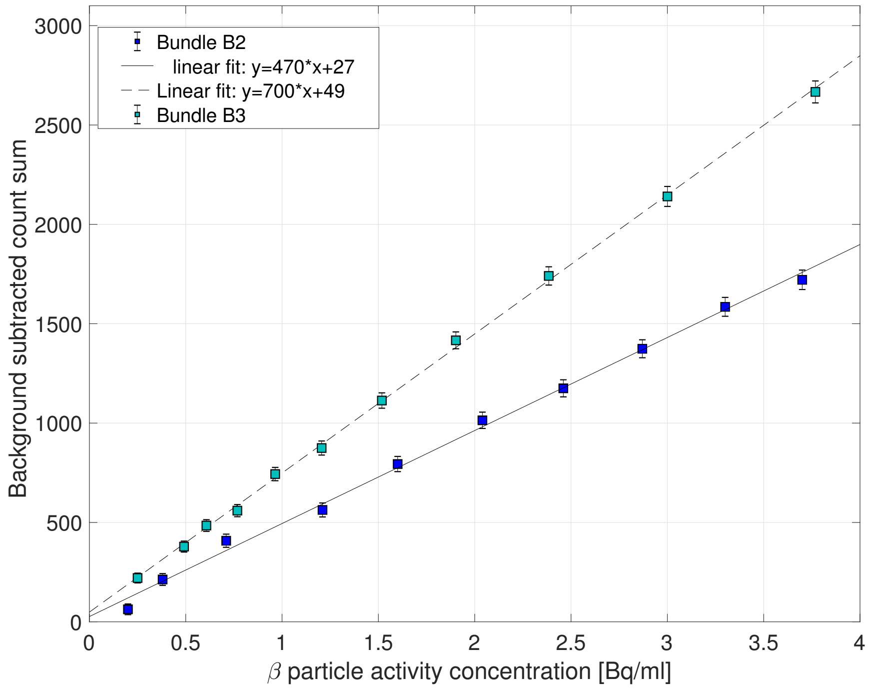

Figure 6.7: Calibration curves measured in potassium chloride solutions using new B3 fibre sensor (42 × 10 cm BCF12 1.5 mm double clad fibres) and B2 fibre sensor (42 × 10 cm BCF12 1 mm single clad fibres, see 5.3.3

to penetrate the fibre cladding is emitted by ^{214}Po, which has a lifetime of 164.3 µs, too short to establish an accurate calibration for the fibre bundle. Regardless, this isotope represents such a small fraction of the total decay products of ^{238}U, that failure to calibrate for its effects should not significantly affect the performance of the sensor.

The alpha particles emitted from ^{210}Po have an energy of 5.3 MeV, similar to the majority of alpha emissions in the ^{238}U chain. To determine if these alpha particles are able to produce a signal in the fibre within the 300 to 2049 channel measurement range of the pulse height spectrum, the fibre bundle was placed in a 10 Bq/ml solution of ^{210}Po. No signal above background noise was produced, which indicates the alpha particles are not able to penetrate the cladding and produce a signal in the measurement range, hence no alpha particle calibration of this fibre bundle is necessary.

6.3.4 Determination of beta particle activity in leach liquor

To perform a measurement in a mixed radionuclide solution using the beta particle sensor, B3, a sample of leach liquor (used to make the slurry in Chapter 5) was used. Gamma ray spectroscopy was used at an earlier date to determine the composition of the liquor, which was found to contain:

- **^{238}U**: 6.85 ± 0.3 Bq/ml
- **^{230}Th**: 6.52 ±0.4 Bq/ml
- **^{210}Pb**: 0.43 ±0.1 Bq/ml
- **^{226}Ra**: < 0.00035 Bq/ml

These numbers indicate most of the daughters down the decay chain from ^{230}Th have been removed (Refer to decay chain in Figure 1.1), and as such, 1 Bq/ml of ^{238}U should contain 3 alpha emissions (for a total alpha activity of 20.5 ± 0.9 Bq/ml based on ^{238}U activity), and 2 beta emissions (total beta activity 13.7 ± 0.6 Bq/ml).

The solubility limit of potassium chloride in water determines the upper limit of the beta particle calibration data for the fibre bundle at around 4 Bq/ml (Figure 6.7), and the linear fit was well matched to the data points which would allow extrapolation to higher solution activities if necessary. Given the goal of this research is to measure low radionuclide levels in solution, the leach liquor was diluted 1:3 using a 20% sulphuric acid solution to reduce the radionuclide concentration to a level such that beta activities should lie closer to the measured calibration range. Alpha ($A_{C\alpha}$) and beta ($A_{C\beta}$) activity concentrations in the diluted leach liquor should be reduced to 6.83 ± 0.3 Bq/ml and 4.5 ± 0.2 Bq/ml respectively.

The measurements will be affected by the height of liquid in contact along the fibre bundle, so care was taken to ensure the same volume of liquid was used for calibration, background (in blank H_2SO_4) and liquor measurements, with no changes made to the experimental setup. Consistent with the KCl measurements, the number of detected radiation events between channels 300 and 4095 were counted, and the average of three measurements taken (See Table 6.4).

Count sums	**Meas.1**	**Meas.2**	**Meas.3**	**Ave.**
Background	187	201	190	193 ± 14
Liquor	3364	3435	3329	3376 ± 58
Liquor - background				**3183** ± **60**

Table 6.4: Total count sums measured between channels 300 - 2059 using beta sensing bundle in blank sulphuric acid (background) and in diluted leach liquor. Errors shown are counting errors.

Using the calibration curve obtained previously (see Figure 6.7), a background subtracted count sum of 3183 ± 60 corresponds to an activity concentration of beta particles of $A_{C\beta}$= 4.48 ± 0.14 Bq/ml in the diluted leach liquor (Figure 6.8). This value is in agreement with that predicted (4.5 ± 0.2 Bq/ml) from the gamma spectroscopy analysis, and shows this sensor is able to effectively measure the beta component of total radionuclide activity in a solution of mixed radioisotopes.

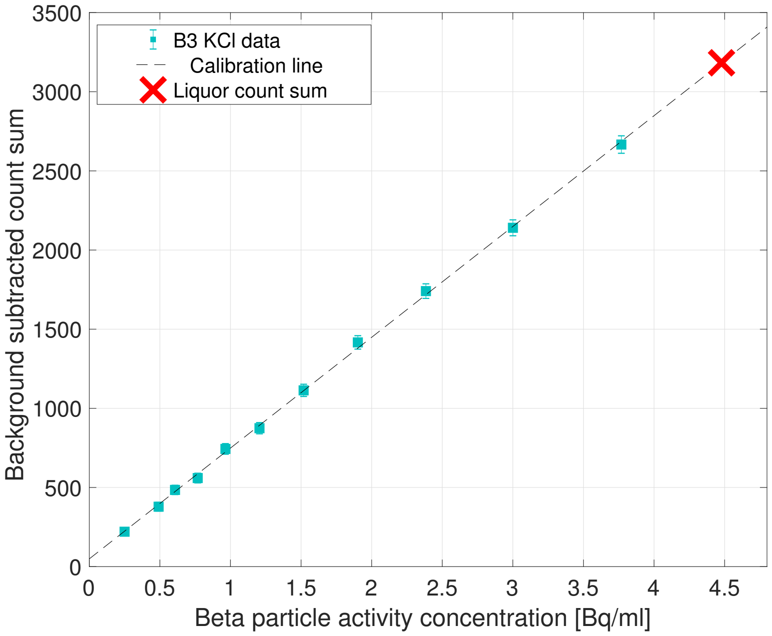

Figure 6.8: Calibration curve for beta sensor showing data point (marked 'X') corresponding to leach liquor measurement.

6.4 Alpha particle detection in mineral processing liquids

Improvements to alpha particle sensors A1 and A2 explored in Chapter 5 could be realised by using optical fibres with a smaller core diameter and thinner outer claddings to minimise attenuation in the cladding and thus maximise energy deposition in the fibre core, and improve the light yield. A method to reproducibly fabricate fibres with these thin-cladding geometries in-house has not yet been developed, hence fibre varieties are limited to those available commercially where the minimum outer diameter available is 250 µm, with a cladding thickness of 7.5 µm. Given these limitations, minimal changes have been implemented from previous alpha sensing bundles, and are discussed below.

6.4.1 Sensor design improvements

Fibre cladding type

250 µm diameter BCF12 fibres have been employed in this sensor design, however the fibres are double cladded, unlike the A1-A3 sensors which have a single cladding. The cladding thickness is 7.5 µm, and has the potential to improve the performance of the

sensor by improving the transmission loss and trapping efficiency of the fibres.

Unfortunately, this fibre did not meet the manufacturer listed specifications. In the first instance, the fibre cladding was measured to be 10 µm (instead of the specified value of 7.5 µm), which had the effect of significantly increasing attenuation in the cladding and therefore lowering the alpha particle detection efficiency. Replacement fibre was acquired, and since the cladding thickness was measured to be 6.5 µm, it was used to make a fibre bundle. It was later determined, upon poor performance of the sensor, that the fibre suffered extremely high transmission losses, ≈ 7.5 times larger than the equivalent single cladded fibre variety (See Figure 6.9 (a)).

The radiation response of the fibre was measured using ^{90}Sr/^{90}Y beta particles at varied irradiation points along the fibre length as was performed in Chapter 4.4, with a minimum achievable source-detector distance of 9 cm (experimental set-up would not permit a shorter irradiation distance). A comparison with the single clad 250 µm diameter BCF12 fibre is presented in Figure 6.9 (b). At short irradiation distances, the light yield of the double clad fibre appears to rapidly approach that measured using the single clad fibre, however the number of detected photons drops off rapidly with increasing irradiation distance. This observation indicates the scintillation efficiency of the double clad fibre is similar to that of the single clad variety, but the high transmission losses prevent the majority of photons produced from reaching the detector. The most likely explanation for this behaviour is that the concentration of the fluor molecules in the polymer is too high. It has been reported in the literature that high fluor concentrations lead to increased self-absorption of shorter wavelength components of the scintillation light, and consequently a red-shifting of the emission spectrum and increase in transmission loss [89]. In this case, the observed low light yields in the double clad BCF12 fibre would be caused by a combination of high transmission losses and a lower detection efficiency (Shifting of emission peak away from sensitive wavelength region of PMT), highlighting the requirement to balance optical quality and scintillation efficiency for efficient radiation detection.

Another alpha sensing bundle was not created, given it takes upwards of three months for the commercial fibres to be manufactured and shipped, with no guarantee on their quality. This was outside the timeframe for this project, and the results demonstrated using the prototype sensor in Section 6.4.5 are considered proof-of-concept for this approach to alpha sensing in liquids. Results for the bundle A4 are presented, as it was still capable of alpha particle detection, just with much lower efficiency than expected from the design improvements.

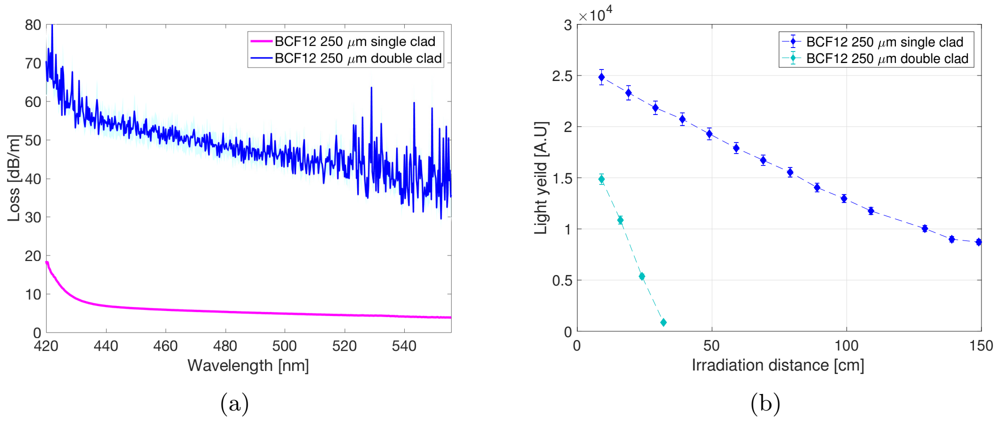

(a) (b)

Figure 6.9: (a) Transmission loss of 250 µm diameter BCF12 fibres with single and double claddings (b) Beta particle response of single and double clad 250 µm BCF12 fibres as a function of irradiation distance.

Fibre numbers and lengths

Both the fibre length, and total number of fibres have been increased to improve the active sensing volume of the fibre bundle A4. Fibre lengths have been changed from 10 cm used in A1 and A2 bundles, to 12 cm, with the total number of fibres increased to 2500 (1500 and 1800 fibres used previously) resulting in approximately a 70% increase in the active sensing volume. In theory, these improvements should result in a similar increase in alpha particle detection efficiency, however this expected sensitivity improvement was offset by the poor optical quality of the fibre.

6.4.2 Calibration Procedures

Unlike the sensor described in Section 6.3, which is essentially a pure beta particle detector, the signal produced from the alpha particle sensor will contain contributions from both alpha and beta particles when used in a mixed radionuclide solution. This sensor must be calibrated separately in both alpha and beta particle containing solutions, and using the activity information measured using the beta sensor, the alpha particle activity can be calculated using the method described below:

- **Step 1**: The alpha particle sensor is calibrated in a beta particle containing solution (KCl) to produce a relationship between the beta particle activity concentration of the solution, $\mathrm{A_{C\beta}}$, and the background subtracted count sum measured using the A4 alpha sensor in that solution (see Section 6.4.3) :

$$\mathrm{Sig_{A4,\beta}} = (\mathrm{m_1} \times \mathrm{A_{C\beta}}) + \mathrm{c_1}. \tag{6.1}$$

- **Step 2**: The alpha sensor is calibrated in an alpha particle containing solution (^{210}Po) so the alpha particle signal ($\mathrm{Sig}_{A4\alpha}$) produced in the bundle can be related to the alpha particle activity concentration, $A_{C\alpha}$ in the solution (see Section 6.4.4):

$$\mathrm{Sig}_{A4,\alpha} = (m_2 \times A_{C\alpha}) + c_2. \tag{6.2}$$

- **Step 3**: The alpha sensor is placed in a mixed radionuclide solution (i.e leach liquor) and the alpha particle activity is determined using:

$$\mathrm{Sig}_{A4,\alpha} = \mathrm{Sig}_{A4,(\alpha+\beta)} - \mathrm{Sig}_{A4,\beta} \tag{6.3}$$

  The alpha particle sensor is not capable of producing an isolated beta particle signal, $\mathrm{Sig}_{A4,\beta}$, in a mixed liquid so this information must be inferred using $A_{C\beta}$ which was measured using the beta particle sensor in the liquid. Once $A_{C\beta}$ is measured with B3, $\mathrm{Sig}_{A4,\beta}$ is calculated using the calibration equation for the alpha bundle in KCl in Equation 6.1 to yield the signal component due to beta particles ($\mathrm{Sig}_{A4,\beta}$).

- **Step 4:** The alpha particle signal ($\mathrm{Sig}_{A4,\alpha}$) is calculated using Equation 6.3, and the calibration data obtained using the ^{210}Po solutions are used to relate the alpha particle signal to the activity as in Equation 6.2.

Each step, and the associated calculations are explained in more detail in the sections that follow.

6.4.3 Calibration in a potassium chloride test solution

A calibration of the A4 fibre bundle in potassium chloride is performed using similar solution concentrations and beta particle activities to those shown in Table 6.3. The data points are less clearly linear than was observed with the B3 sensor, and this is hypothesised to be a result of solution retention in the fibre bundle after each measurement. Each solution was prepared by successively diluting a stock solution, hence any liquid held by the fibre bundle would be lost and affect the remaining solution concentrations. The solution retention was greater than was observed using the B3 bundle due to the larger surface area and smaller distance between the fibres in this case. Future calibrations will be improved by preparing each solution separately. The relationship between $A_{C\beta}$ and $\mathrm{Sig}_{A4,\beta}$ is given by:

$$\mathrm{Sig}_{A4,\beta} = 900 \times A_{C\beta} + 46 \tag{6.4}$$

Standard errors in the slope and intercept of the calibration line are σ_{m_1}=34.2 and σ_{c_1}=63.2.

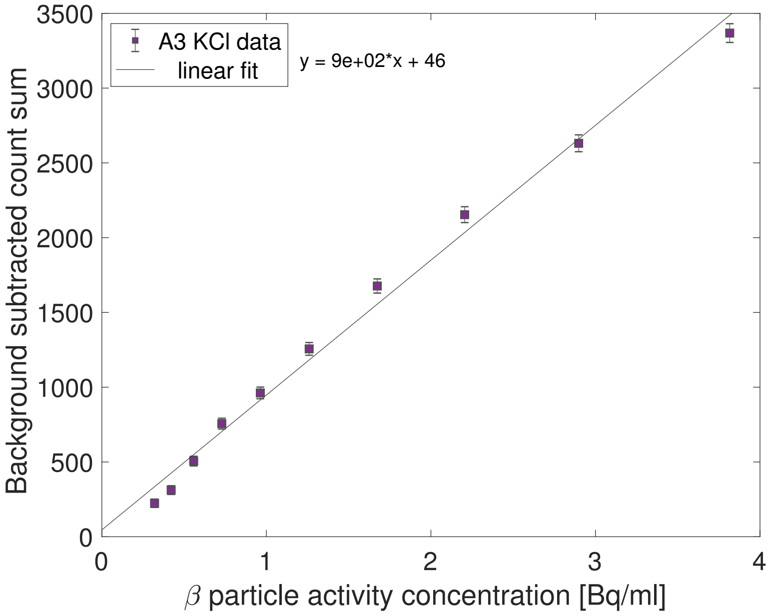

Figure 6.10: Beta particle calibration curve for alpha sensing bundle, A4, measured in potassium chloride solutions.

6.4.4 Calibration in ^{210}Po test solutions

^{210}Po solutions with activities between 0.1 Bq/ml to 5 Bq/ml were prepared in 1 M hydrochloric acid for calibration of the A4 sensor. Background measurements were taken with the bundle in a blank hydrochloric acid solution before each polonium measurement to account for contamination effects as was done in Section 5.3.4. No signal above background noise was detected in ^{210}Po solutions with 0.1 and 0.5 Bq/ml, and signal levels at higher solution activities were lower than what was observed with previous alpha sensors A1 and A2 (see. figure 6.11). This result is not unexpected given the high transmission loss of the fibres in this bundle.

The relationship between $A_{C\alpha}$ and $Sig_{A4,\alpha}$ is given by:

$$Sig_{A4,\alpha} = 68 \times A_{C\alpha} - 36 \tag{6.5}$$

Standard errors in the slope and intercept of the calibration line are σ_{m_2}=8.1 and σ_{c_2}=28.5.

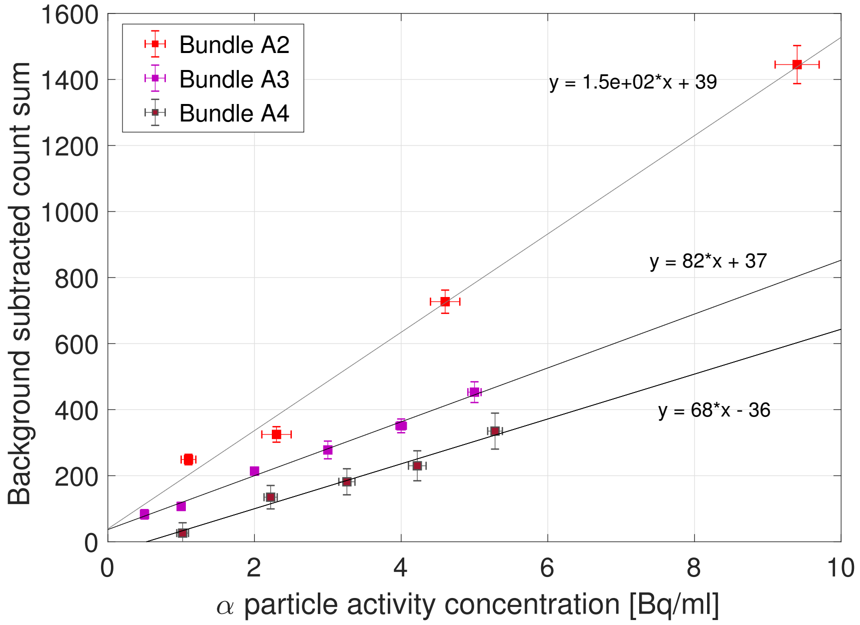

Figure 6.11: Alpha particle calibration curve for alpha sensing bundles measured in ^{210}Po solutions.

6.4.5 Determination of alpha particle activity in leach liquor

The alpha sensor (A4) was placed in a new sample of leach liquor which was diluted 1:3 in a 20% sulfuric acid solution as was used with the beta sensor in Section 6.3.4. A fresh dilution was used to ensure the radionuclide concentrations for each liquor sample measurement are as consistent as possible, given some radionuclides may have plated onto the beta sensor and depleted the solution activity, which would result in a falsely low measurement signal using the alpha sensor. Three measurements were taken using 100 s integration times, and the background was subtracted to give a mean signal of 3740 ± 67 counts. Hence $\mathrm{Sig}_{\mathrm{A4},(\alpha+\beta)}$ $\mathbf{= 3740 \pm 67}$ counts.

The beta particle activity measured with the beta sensor B3 ($\mathrm{A}_{\mathrm{C}\beta}$) was found to lie between 4.34 and 4.62 Bq/ml. Using Equation 6.4, the beta particle component of the signal $\mathrm{Sig}_{\mathrm{A4},\beta}$ is calculated to lie between 3674 and 4496 counts (background subtracted). Hence Sig_{β} **= 3674 to 4496** counts.

Using Equation 6.3, the bounds on the alpha particle signal are between -823 and 133 counts. The negative count number arises from uncertainties in the calibrations, and does not correspond to a physical solution activity, hence the alpha particle signal must lie between 0 and 133 counts. Using the polonium calibration fit for the A4 bundle (Equation 6.5), the alpha particle activity of the leach liquor should lie between 0 and 3.82 Bq/ml.

Based on the gamma spectrometry analysis of the leach liquor, the alpha particle activity is between 6.8 and 6.86 Bq/ml, which is approximately double the estimate from the fibre sensor, and outside the error bounds of what was measured. One possible explanation for this difference is that some of the alpha emitting radionuclides have plated onto the walls of the storage container after it was diluted, which would cause a decrease in the alpha activity. This speculation was testing by counting a sample of the diluted leach liquor in the alpha counter. It was shown to have a total alpha particle activity of 6 ± 0.1 Bq/ml still outside the bounds of what was measured with the sensor.

Based on the calibration curve in Figure 6.11, the difference in light yield between alpha particle solution activities of 3.8 and 5.9 Bq/ml (the measured activity in leach liquor and the lower bound solution measurement using the alpha counter) is only 137 counts. With an increase in alpha detection efficiency, the ability to discriminate between different solution activities, and hence accurately measure the alpha activity component of a mixed radionuclide solution will improve. Suggested design improvements will be discussed in Section 6.7.

6.5 Sensor reusability

The prototype sensors developed for this project are intended for long term, continuous use in mineral processing solutions. The latest iteration of the beta particle sensor appears capable of operating in this manner, however, polonium was found to accumulate on the surface of the alpha sensor which causes a steady increase in the background component of the signal. Left unaccounted for, this background signal would produce an overestimate in the alpha activity of a solution.

A proposed operational mode for this sensor would be a duty cycle in which is it periodically removed from the measurement solution to acquire background readings for subtraction from the total measurement signal. Once stabilised, the background levels appear to display little fluctuation over short timescales meaning any accumulation of polonium would be negligible over a duty cycle of minutes, allowing the background level to be subtracted and yield an accurate measurement of the radionuclide activity in solution. Depending on the radionuclide concentrations in the processing solutions, signal and background levels could even be measured in as little as 10 s to 100 s, allowing near-continuous operation of the sensor. The sensors could also be washed (Decon 90) on a less regular basis to remove any significant build up of radionuclides or debris.

To determine if the combined effect of cleaning the fibre bundle and elevated background levels affect the performance of the alpha sensor, the contaminated A4 bundle was partially cleaned with a Decon 90 solution. Following the cleaning procedure, the measured background counts decreased from 1416 to 591 (compared to 230 counts in the uncontaminated bundle).

The partially cleaned bundle was tested in potassium chloride solutions with activities 3.78 and 0.33 Bq/ml, and the measured signal compared to the data which was originally measured in solutions of approximately the same activity when the bundle was uncontaminated. KCl solutions were used for this measurement (as opposed to ^{210}Po solutions) due to the ease with which they could be prepared, to avoid any additional contamination effects affecting the measurements. Measured signals in both KCL solutions were within error of what was originally measured, as shown in Figure 6.12). If the fibre bundle were damaged during the cleaning procedure, or elevated background levels affected measurements, then the re-measured signals would be lower than anticipated. This result demonstrates that the cleaning procedure and sensor contamination do not affect its ability to measure radionuclide levels at very low (0.33 Bq/ml), or moderate (3.78 Bq/ml) activity levels.

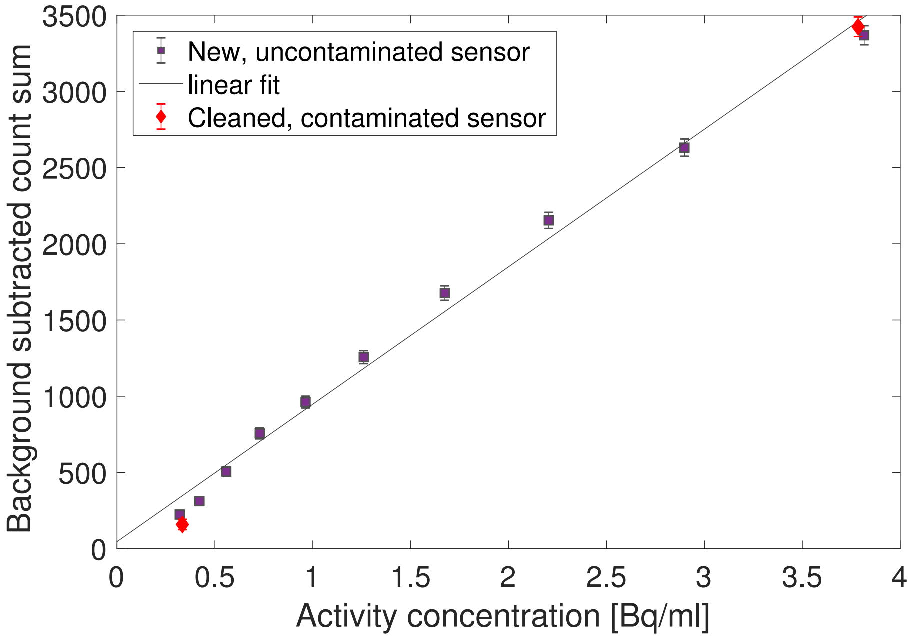

Figure 6.12: Calibration curve measured using uncontaminated A4 bundle in potassium chloride solutions shown, together with data points measured using the partially cleaned A4 bundle in solution activities of 0.33 and 3.78 Bq/ml.

6.6 Summary

Several methods have been explored to prevent adsorption of ^{210}Po onto the surface of the optical fibres, or to remove it after adsorption. Treatment of fibre bundles with Decon 90 detergent in an ultrasonic bath was shown to be the most effective treatment that was trialled for removing the majority of polonium, with no impact on sensor performance. Hydrophobic coatings were investigated for their ability to prevent polonium adsorption on fibre surfaces but gave no significant reduction in measured contamination levels. Although polonium adsorption on the fibre surface produces elevated background levels, background subtraction has shown to be an effective method to account for and remove this signal component.

The use of 1.5 mm diameter fibres with cladding thicknesses of 45 µm in the B3 beta particle sensor has resulted in a 50% signal increase from the previous sensor (B2). The cladding thickness was found to be sufficient for blocking any alpha particles from ^{210}Po, hence the majority of alpha particles in the ^{238}U decay chain are prevented from reaching the fibre core. Any gamma ray events are excluded from the measurement range, essentially making B3 a pure beta particle sensor. The sensor was tested in diluted leach liquor, with beta particle activity measured found to be in agreement with radionuclide content measured using gamma spectrometry.

Attempts to improve the signal-to-noise ratio of the A4 bundle from previous designs were made by increasing the fibre numbers and lengths in the bundle, and using double clad optical fibres. Despite these efforts, this sensor was shown to display the lowest detection efficiency of all alpha sensors, resulting from the high transmission loss of the optical fibres sourced from the manufacturer, an issue which remains ongoing. The A4 sensor was tested in leach liquor, and together with the beta particle activity measured using B3, the alpha activity was determined to lie between 0 and 3.82 Bq/ml, below the expected value of 6.83 ± 0.3 Bq/ml. Given the low signal levels (and correspondingly high counting errors) of the A4 bundle, accurate determination of the alpha particle activity in a mixed radionuclide solution has proven elusive, but the issues appear amenable to resolution in practice. Sourcing optical fibres with improved transmission loss and consistent quality would immediately greatly improve the alpha particle detection efficiency and hence improve measurement accuracy.

6.7 Future device improvements

Both prototype alpha and beta sensing fibre bundles function effectively under the required operating conditions and have sufficient sensitivity to detect radioisotopes at the 1 Bq/ml level in solution. The work presented in this thesis has shown the feasibility of these sensors in meeting the project goals of monitoring these low levels of alpha and beta particle activities in mineral processing solutions, in a near-continuous manner. However, there still remain a few ongoing issues which must be addressed before the sensors can be implemented as field-portable radiation monitoring instruments, as will be discussed in this section. It is concluded that the concept is proven by the work reported in this thesis.

Cladding thicknesses

To increase the amount of energy deposited in the fibre core by alpha particles, smaller cladding thicknesses are needed on the optical fibres. The minimum possible cladding thickness must first be determined, as a decrease in cladding thickness may degrade the transmission of the optical fibre and make it more susceptible to damage from abrasive slurry particles. The optimal cladding thickness will be a compromise between fibre transmission loss and alpha particle detection efficiency.

In-house fabrication using the IPAS fabrication facilities of cladded, scintillating polymer fibres has the potential to drastically improve sensor performance. Commercial fibres are limited in their outer diameter and cladding thicknesses, the most suitable variety available for alpha particle detection being the 250 µm diameter fibres with 7.5 µm cladding thickness. The quality of these commercial fibres were found to vary considerably in terms of geometrical dimensions and optical properties making them unsuitable for large scale production of field portable instruments. Fabrication of optical fibres in-house could be one way to address the quality control issue and time delays encountered using commercial fibres, and would enable the production of fibres with custom cladding thicknesses to improve alpha particle detection efficiencies.

Cladding thicknesses on the beta particle sensing fibres are sufficiently thick to stop the majority of alpha particles in the ^{238}U from reaching the fibre core, the only exception being the alpha particle emitted by ^{214}Po, and this is of negligible significance as this radionuclide represents only a small fraction of the total decay products and is unlikely to have a significant impact on measurements. Furthermore, its contribution can be removed by fabricating 1.5 mm optical fibres with cladding thicknesses of 70 µm in-house.

Sensor volume

The number of fibres incorporated within the sensors and their core diameters were found to have a dramatic impact on the device sensitivity. For the case of beta particles, sensitivity was shown to increase with the total volume of scintillator, which is achieved by using a large number of thicker fibres. Increasing the volume of active scintillating material has its drawbacks, as larger diameter fibres provide a greater interaction volume for gamma rays so can lead to increased background levels, while large volume sensors are limited in terms of geometry constraints and portability. The optimal detector would potentially be an array of 1.5 mm diameter fibres with dimensions (L × W × H) 10 × 10 × 20 cm, based on the results from the B3 sensor which demonstrated good signal-to-noise ratios in a volume a fraction of this size. However this remains to be determined, given the sensor has not been tested on-site.

The alpha particle sensitivity will increase with the surface area of scintillating material, however, unless the fibre core diameter is very small (≈ 40 µm) much of the scintillating material will be wasted as the alpha particles are not able to penetrate past a thin outside layer of the material. The use of smaller core optical fibres would allow a larger number of fibres to be used in a given volume, thus increasing the surface area of active material and hence the alpha particle detection efficiency. Smaller core fibres would also ensure less energy deposition in a single fibre by beta particles, which would improve the ability of this sensor to separate alpha and beta particle contributions to the total activity. In making the alpha sensing bundles, fibres were cut individually by hand which proved to be very time consuming, especially as the fibres needed to be handled with caution to prevent any damage which would degrade their optical quality. This process limited the size of the fibre bundles which were created, however a more automated procedure would allow the production of larger sensor arrays with more predictable performance in a shorter timescale.

6.7.1 Field portability

The experiments performed using the fibre bundles in this thesis were conducted in a homemade light-tight enclosure in a lab darkroom. The compact sensor design and portability of the detection system make the experimental set-up somewhat suitable for immediate real-world application, however further alterations and improvements are necessary. The sensor will need to be contained in a light-proof enclosure as any stray light in the system will affect the accuracy of measurements and possibly damage the detector. The use of a low loss, jacketed waveguide could be used to couple the sensor output to the detector which would allow the fibre bundles to be fully immersed in measurement solutions so signal levels are unaffected by changes in liquid levels. Such a configuration would also allow the photodetector to be removed from the immediate vicinity of the fibre bundle sensor and processing solutions and placed in a protected area.

The alpha sensor is intended to be operated semi-continuously, potentially on a duty cycle of seconds to minutes, and hence a simple, automated way to periodically remove the sensor from processing solutions at fixed time intervals is required. A simple cleaning procedure may be necessary on a regular basis to extend the sensor lifetime if particulate buildup on fibre surfaces begin to impede alpha particle detection. On-site cleaning may be a practical method to efficiently restore and decontaminate the sensors, one possibility would be to circulate cleaning solutions and rinses through the devices in a seperate enclosure. If field decontamination is not practical (or possible), the devices could be taken off site and cleaned in a more appropriate location, or replaced on a regular basis given the low costs associated with producing each sensor.

Some practical issues in relation to the sensor durability and reliability must also be considered. The performance of the optical fibres under an environment analogous to that encountered during mineral processing has been investigated in Chapter 5, however this was performed under controlled conditions within a laboratory. The ability of sensing devices to withstand chemically aggressive environments, abrasive damage, and its sensitivity to outdoor conditions can only be properly evaluated during field use, so a monitoring system to regularly check the sensor condition is required.

Chapter 7

Low energy X-ray response of plastic scintillators

7.1 Introduction

Experimental work presented up until this point has been concerned with the irradiation of plastic scintillators with alpha and beta radiation. Access to a low energy X-ray source at the Royal Adelaide Hospital was obtained in order to characterise a range of plastic scintillating fibres for medical dosimetry purposes. The aim of the work presented in this chapter is to characterise the energy dependent responses of a comprehensive range of plastic scintillators with different formulations and dimensions, between beam qualities of 30 to 150 $\mathrm{kV_p}$ with a range of filtrations. Applications of this work are relevant for dosimetry in low energy photon applications such as brachytherapy and radiology. This work also provides confirmation that the fibres are too insensitive to each ionising photon event to be suitable for the mining and mineral processing requirements.

7.2 Energy deposition

A brief description of photon interactions in matter were discussed in Chapter 1. A more detailed depiction of the physical processes occurring in plastic scintillators upon interaction with low energy photons is needed to understand the scintillator response.

Dose deposition within a plastic scintillator for the studied energy range results from the production of low energy secondary electrons via photoelectric absorption and Compton scattering. The electrons produced will be low energy and consequently have a high linear energy transfer (LET), as such they have been shown to produce a decrease in scintillation efficiency which is partially attributable to ionisation quenching. For dosimetric applications, the response of a plastic scintillator should be independent of the energy of the incident particle, a property which holds true for high energy electrons, however the decreased scintillation efficiency at lower energies means plastic scintillators suffer from an energy dependance which is noticeable at beam energies less than 100 $\mathrm{kV_p}$ [75]. The plastic scintillators response to charged particles can be understood using the Birks model [9] (Refer to Equations 2.1 and 2.2). For low energy electrons, the ionisation densities are large enough that quenching effects are non-negligible, and hence the fluorescent energy per unit path length is always less than that of a high energy electron by a factor of $\left[1+\left(\mathrm{kB}\frac{\mathrm{dE}}{\mathrm{dx}}\right)\right]$, resulting in a non linearity of the energy response, which will be shown shortly.

The radioluminescent signal produced upon irradiation of the fibre system consists of scintillation light emitted by the dopant within the plastic scintillator - the amount of which is proportional to the energy deposited for low LET radiations. There is also a stem signal, consisting of a Čerenkov and a fluorescent component. The Čerenkov light is produced when electrons exceed the speed of light in a material with refractive index, n, and thus have a threshold on the secondary electron energy, $\mathrm{E_k}$, such that

$$\mathrm{E_k} \geq \mathrm{m_e c^2}\left(\frac{\mathrm{n}}{\sqrt{\mathrm{n}^2-1}}-1\right) \tag{7.1}$$

Where $\mathrm{m_e}$ is the electron mass, and c is the speed of light in vacuum. A threshold secondary electron energy of $\mathrm{E_k}$=144 keV is required in polystyrene with refractive index n=1.6 to generate Čerenkov light, hence the primary photon energy must be larger than this value. The maximum energy used in this experiment is 61 keV so any Čerenkov contribution to the signal is assumed to be negligible. The second component of the stem light, the fluorescence, is produced by low energy photons of a few keV, and needs to be accounted for and subtracted from the total signal to minimise errors in the response of the dosimeter.

7.3 Scintillator varieties and sample preparation

A list of the scintillators used for this experiment and their relevant properties are shown in Table 7.1. ELJEN scintillators used in this study were all fabricated in-house from bulk polymer billets. Each scintillator was 3.1 mm long and optically coupled to a 13 cm long waveguide (BCF98 with a core diameter of 940 µm and a 30 µm thick PMMA outer cladding).

Scintillator samples were prepared by cutting a small section of fibre with a heated surgical blade and grinding down to a size of 3.1 mm using a home made holder and a 30 µm silicon carbide polishing film. Both ends of the scintillator were polished flat using a Krelltech REV2 automated fibre polisher with varied coarseness silica and alumina polishing films. Each sample was inspected under an optical microscope to ensure the surfaces and outer cladding (where applicable) were undamaged and intact to minimise coupling losses when connecting the scintillator to the light guide. Each scintillator tip was glued to the light guide using EJ-500 (ELJEN) optical cement, with all polished surfaces cleaned and inspected prior to coupling. The end of the scintillator not coupled to the light guide was blackened using a carbon based paint to minimise any back reflections of the scintillation light. A tip architecture was required to minimise the volume of scintillator exposed to the photon field, and ultimately reduce the count rate (hence pulse pile-up) of the photons detected which were produced within the scintillating element.

7.4 Experimental setup

X-ray generator

The photon response of the scintillators was evaluated using a superficial x-ray unit with peak voltages between 30 and 150 $\mathrm{kV_p}$ (Effective energies between 14 and 61 keV). X-rays were delivered using a 1.5 cm reference cone and a 180 cm focus-to-skin distance (FSD), with effective energies calculated based on half value layers (HVL). A list of the relevant beam qualities are shown in Table 7.2.

7.4.1 Experimental setup and data acquisition

Each scintillator was placed on a slab of solid plastic to provide backscatter (to replicate backscatter encountered when irradiating tissue), and oriented perpendicular to the X-ray beam. The output of the BCF98 fibre was coupled to a sheathed 2 m long silica multimode patch cable using a Thorlabs BFT1 bare fibre adaptor to transmit the scintillation signal to the detector which was located outside the treatment room. Both the patch cable and light guide were taped in place (Figure 7.1), and the positions

Scintillator	**Manufacturer**	**Core Diameter (µm)**	**Cladding thickness (µm)**	$\boldsymbol{\gamma}$	$\boldsymbol{\lambda}_{\text{peak}}$ **(nm)**
BCF 10	Saint-Gobain	940	30	8000	432
BCF 12	Saint-Gobain	940	30	8000	435
		1000	0		
		235	7.5		
BCF 20	Saint-Gobain	940	30	8000	492
		1000	0		
		235	7.5		
BCF 60	Saint-Gobain	940	30	7,100	530
		235	7.5		
BCF 98	Saint-Gobain	940	30	N/A	N/A
BCF 91a*	Saint-Gobain	940	30	N/A	494
BCF 92*	Saint-Gobain	940	30	N/A	492
EJ 204	ELJEN	1000	0	8,840	409
EJ 240	ELJEN	1000	0	5,355	435
EJ 260	ELJEN	1000	0	7,820	490
EJ 262	ELJEN	1000	0	7,395	481

Table 7.1: Scintillator properties. (*) Denotes wavelength shifting formulations, λ_{peak}=Wavelength corresponding to the scintillation emission maximum as specified by the manufacturer, γ=Scintillation efficiency, defined as the number of photons produced within the material per MeV of deposited energy by a minimum ionising particle, Values listed for ELJEN scintillators are taken as 85 % the value provided for PVT formulations. N/A = not applicable.

Peak Voltage (kV$_\text{p}$)	**HVL (mm Al)**	**Effective energy (keV)**
30	0.2	14
40	0.5	19
50	1.0	24
80	2.0	29
100	3	35
120	4.0	39
120	5.0	43
140	8	55
150	0.5 mm Cu	61

Table 7.2: Beam properties of SXR unit. HVL: Thickness of aluminium for which incident radiation intensity is reduced to half.

marked to ensure reproducibility of the setup during sample replacement. To estimate coupling uncertainties the lightguide was removed and re-coupled to the patch cable three times, irradiating at each beam quality for every re-connection. The reproducibility of measurements was assessed by taking three successive measurements for each 1 Gy delivered dose. Uncertainties, given as $\sigma/\sqrt{n}$ are applied to all data sets and range from between 0.8 to 1.7%, as indicated in the relevant graphs as error bars.

Light generated in the scintillator is transmitted to a photomultiplier tube (Electron Tubes Ltd, ET 9829B) outside the treatment room through the light guide and patch cable. The PMT is operated in analogue mode and connected to a charge sensitive pre-amplifier and multi-channel analyser (MCA). Total energy deposition is estimated using pulse height analysis to sum whole pulses within a specified region in the pulse height spectrum as in [51, 97]. All measurements were performed keeping high voltage, gain settings, and pulse shaping variables the same and the detector dead time was minimised by placing the scintillator 180 cm from the focus of the x-ray tube with pulse pile up rejection used in the measurement software. Dead times were kept below 15%, and measurements performed at each beam quality for 20 s.

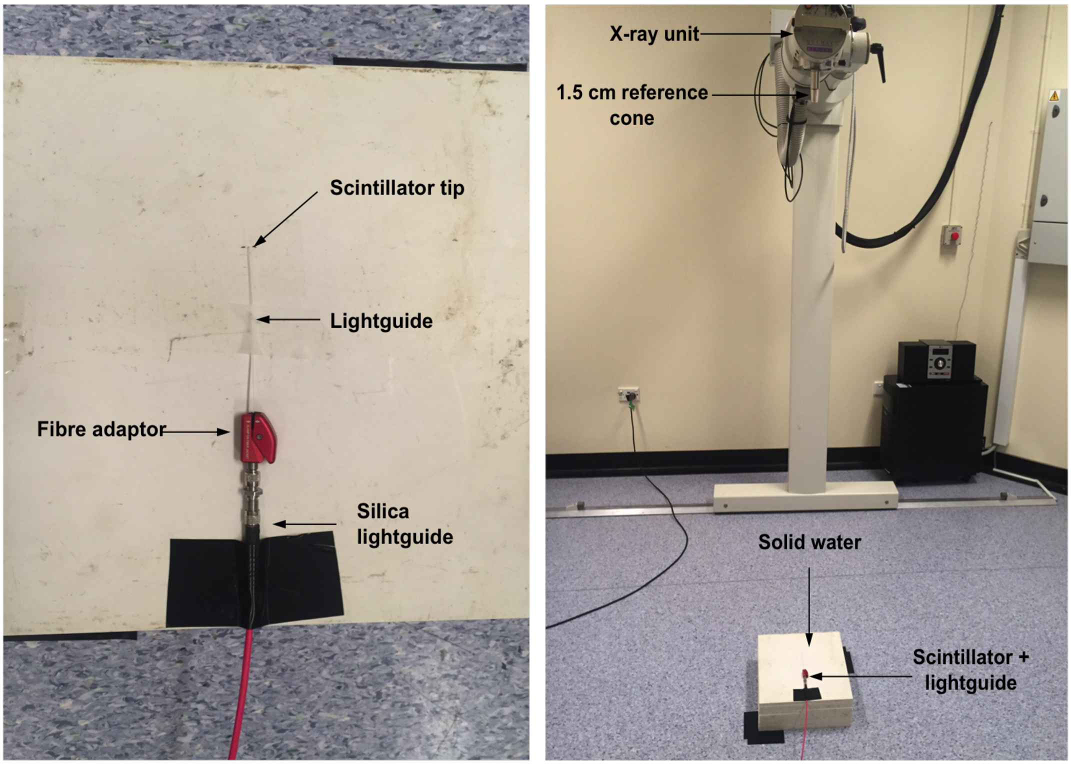

Figure 7.1: Plastic scintillator and light guide placement on plastic slab (left), scintillator set-up shown with SXR unit (right)

7.4.2 Results and discussion

An example of the pulse height spectrum is shown in Figure 7.2 using the 1 mm BCF12 scintillator with no outer cladding irradiated with 14 keV X-rays. The spectra in the region between channels 150 - 500 were used to estimate energy deposition for all subsequent analysis to account for potential count losses from pulse pile up and background noise in the low energy spectral region, and uncertainties due to decreased signal-to-noise ratios at high channel numbers. Absolute responses for each scintillator at a particular energy are calculated by integrating the total number of counts in the analysis region, and relative responses are calculated by normalising the absolute response at each energy to the absolute response at the 61 keV energy. The majority of detected X-ray events lie in the single electron peak region ($\approx$ channel 350) of the pulse height spectrum, which shows the X-rays deposit a very small fraction of their energy in the scintillator. In contrast, alpha and beta radiation produce much more signal in the higher energy region of the spectrum, which corresponds to a larger deposited energy (hence photon production) in the scintillator volume.

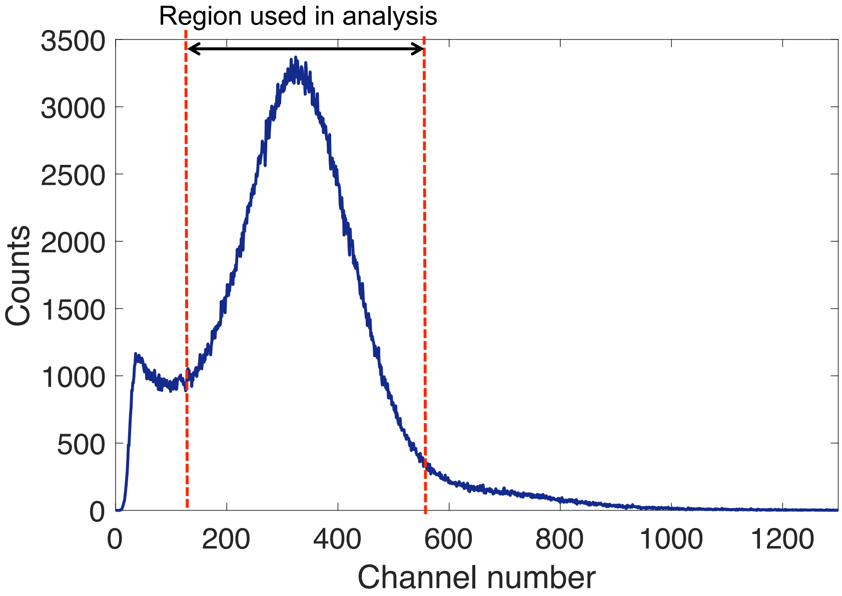

Figure 7.2: Pulse height spectrum for X-ray irradiation of 1 mm diameter BCF12 scintillator showing integrated region used to estimate energy deposition.

Stem effects

A number of techniques have been developed for removal of the stem (fluorescence + Čerenkov light, see Section 7.2) component the light produced within plastic scintillating fibres including chromatic removal [33], temporal discrimination [18], and the use of a dual, undoped reference fibre [4, 10]. For this work, spectrally resolving the scintillation and stem component is not a feasible approach as the fluorescence spectrum of polystyrene overlaps with the emission spectra of the majority of scintillators used here. This issue of spectral overlap between the two signal components is completely avoided with the dual fibre method, in addition this method is technically simple and effective so has been implemented here.

To measure the fluorescent component of the light produced within the fibres, a 13 cm length of BCF98 was prepared as in Section 7.3 without the scintillating tip attached, and the signal from the fibre measured for each beam quality. By subtracting the fluorescence component from the total signal, the scintillation component can be isolated. The fraction of stem light in the total signal depends on the beam quality and scintillator type and can account for anywhere between 10 - 65 % of the total light measured (Figure 7.3). The stem component for the wavelength shifting fibres, BCF91a and BCF92 accounts for up to half the total measured signal, as scintillation light yields were poor due to the lower efficiency with which wavelength shifting (ternary) formulations produce scintillation light under photon irradiation compared to binary scintillators. The signal-to-stem light ratio is even lower for the 250 µm scintillators due to the poor light yield resulting from the limited scintillator volume. In this case the stem component is as high as 65 % of the total signal, which could be improved by using a smaller diameter light guide. BCF98 was used as a lightguide as it was on-hand and had the same dimensions as the majority of scintillators used in this study, however use of a PMMA lightguide in place of polystyrene could also offer reduction in the stem component as it has a comparatively lower intrinsic fluorescence [72].

Relative response of scintillators

The scintillator response will depend on a variety of factors including the coupling efficiencies between the scintillator and light guide components, the light production efficiency, emission wavelength, positioning of the scintillator within the radiation beam etc. The responses presented are all normalised to the 61 keV point as this eliminates the need to measure and correct for these variables with each scintillator. The normalised response of the 14 scintillators with the stem component removed is shown in Figures 7.4 and 7.5. The response of the scintillators is lowest at 15 keV and increases steadily up until 45 keV before beginning to plateau after 55 keV. The relative response increases by approximately a factor of 4 between 15 to 61 keV, with a maximum variation of 11.6% between all scintillators studied. The reduction in sensitivity observed at low photon energies is believed to be a result of ionisation quenching. The low energy electrons which are produced by X-rays in the scintillator have higher ionisation densities than electrons of higher energies, and as a consequence there will be less fluorescent

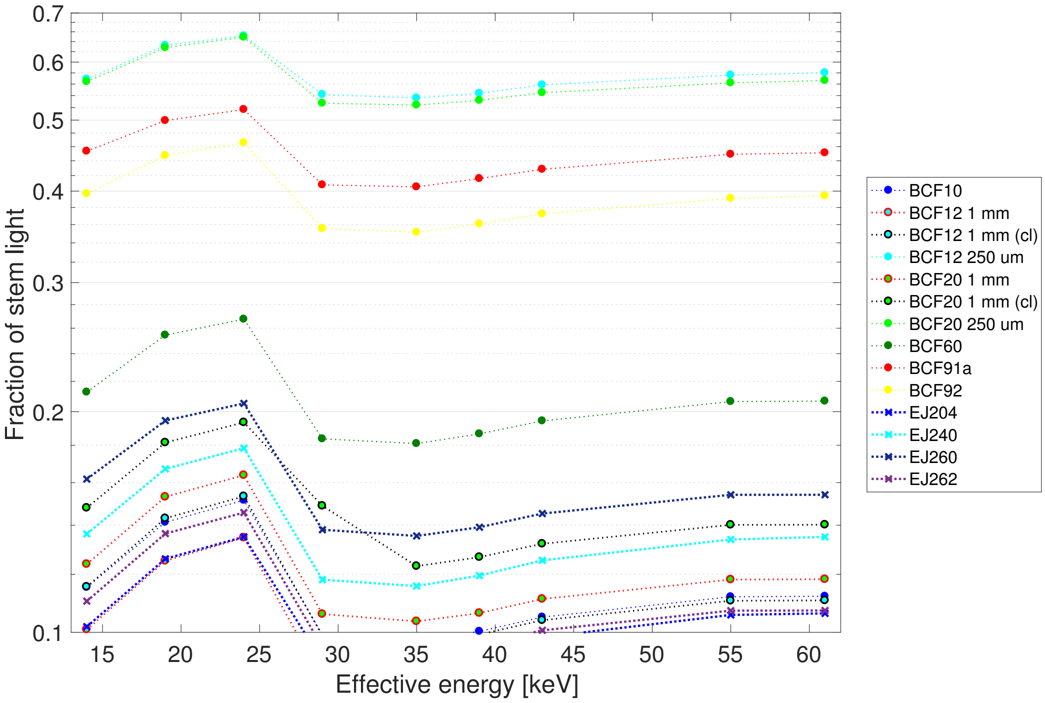

Figure 7.3: Fraction of measured stem light for each scintillator as a function of effective energy of the X-ray beam.

energy produced per unit track length (due to quenching effects, for reasons not fully understood) and a scintillation light yield which is not proportional to the deposited energy as is observed.

The percentage deviation from the mean response for each scintillator is shown in Figure 7.6. All 1 mm binary (1 fluor in base polymer) formulated Saint-Gobain scintillator varieties tested show similar responses at low energies with variations generally 5 % below average, and wavelength shifting formulations (2 fluors in base polymer), BCF91a and BCF92, in contrast, display higher than average responses (with the exception of the 14 keV point) up to 5.7 % above the mean value.

The similarity in response observed between cladded and uncladded varieties of the scintillators BCF12 and BCF 20 indicate the PMMA coating has little to no effect on the relative response of the scintillator, however a decrease in diameter lessens the relative sensitivity across most of the spectrum. ELJEN scintillators typically show little deviation from the mean response, similarly to the Saint-Gobain scintillators BCF10 and BCF60. Of the 14 studied scintillators, EJ204 displays the highest deviation from the mean response at lower energies, up to 8.3 % above average at 14 keV. Consequently, this scintillator has the lowest energy dependence.

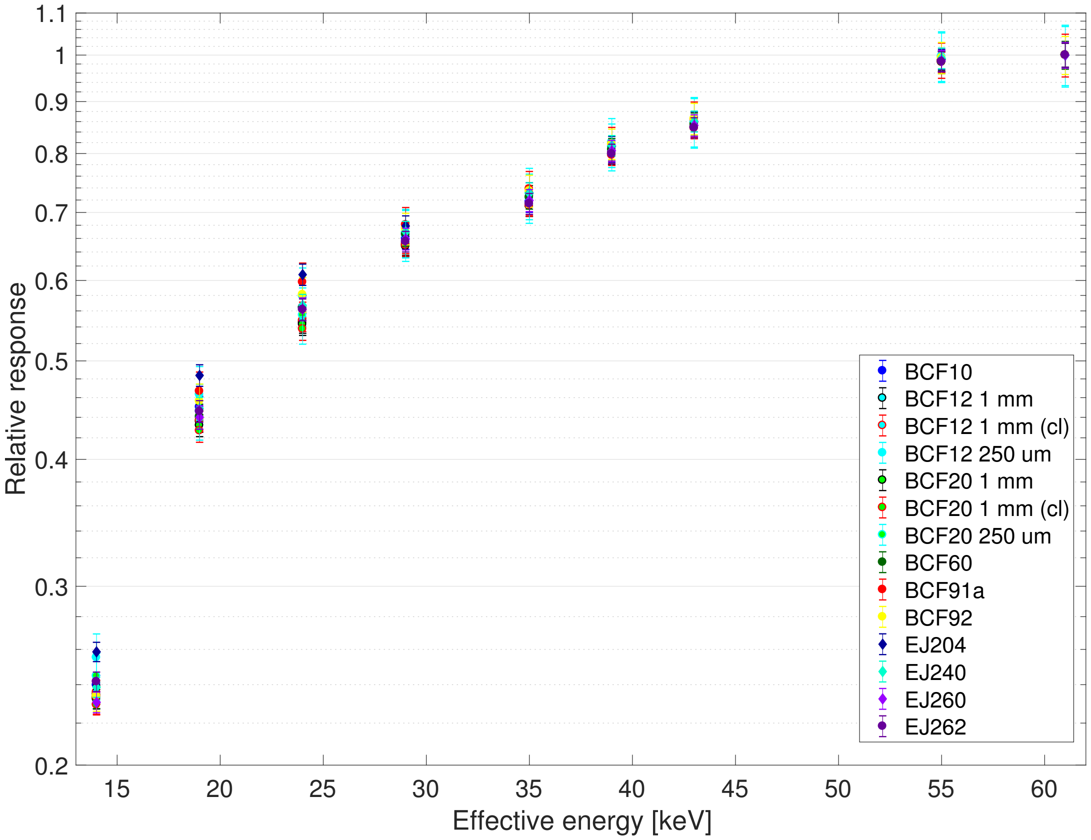

Figure 7.4: Relative response of all plastic scintillators

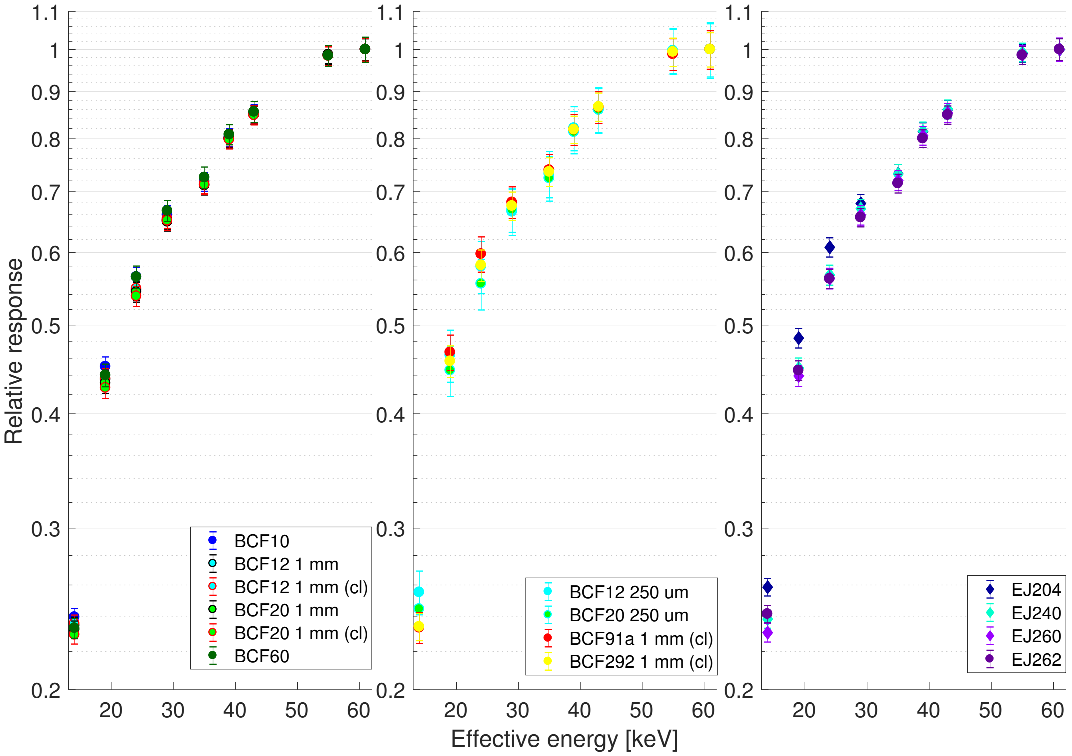

Figure 7.5: Relative response of plastic scintillators Left: St Gobain 1 mm OD scintillators (uncertainties ≤ 3.1 %)Middle: St Gobain wavelength shifters (uncertainties ≤ 4.9 %) and 250 µm OD scintillators (uncertainties ≤7 %) Right: ELJEN scintillators (uncertainties ≤ 2.9 %)

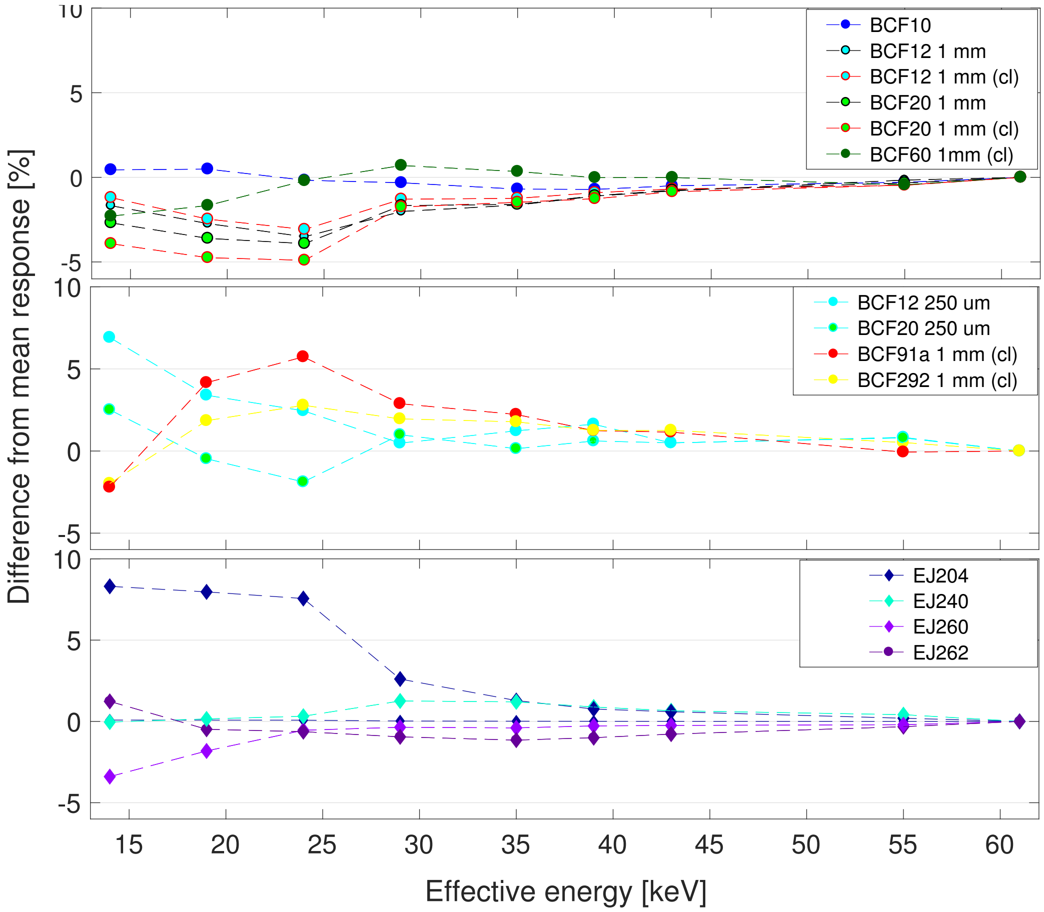

Figure 7.6: Differences from average scintillator responses for 1 mm OD St-Gobain scintillators (top), St.Gobain wavelength shifting fibres and 250 µm scintillating fibres (middle) ELJEN scintillators (bottom)

7.4.3 Conclusions

The energy dependent responses of 14 different commercial plastic scintillators have been measured using low energy x-rays in the 30 to 150 kV_p range with additional Al and Cu filtrations between 0.2 and 8 mm (Effective energies between 14 and 61 keV). The scintillators showed relative variations in response of 74 to 77 % between effective energies of 14 to 61 keV, with a maximum 11.6 % variation between all scintillators tested. The relative scintillator response was not affected by the presence of an outer cladding. A reduction in sensitivity was observed at most beam qualities for smaller diameter scintillators and wavelength shifting formulations, however the ratio of stem to signal light was considerably larger in these cases meaning uncertainties in the relative response were higher.

Generally, 1 mm binary formulated Saint-Gobain scintillators had a lower than average response across the energy range studied, with the exceptions of BCF10 and BCF60 whose sensitivities, like the ELJEN scintillators did not deviate significantly from mean values. Of all scintillators tested, the lowest energy dependance was observed for EJ204 with a maximum 8.3 % above average sensitivity at 14 keV, which would make this scintillator most suited for low energy photon dosimetry.

The scintillation pulse height spectra shows that there is minimal energy deposition by X-rays in the scintillator element, as the majority of detected events lie in the single electron peak region. This is the expected result given the low LET of X-rays and gamma rays in the scintillating plastic, and the small sensitive volume of the fibres. In the mineral processing applications, X-ray fluxes are very low, especially in comparison to noise events which also lie in the SEP region, and consequently it will not be possible to accurately distinguish any X-ray (and gamma ray) events from background noise. Hence these fibres are not optimal for X-ray or gamma ray detection for the mining and mineral processing applications considered in this thesis. In comparison, alpha and beta particles are able to deposit significantly more energy in the scintillator element, so a substantial component of the events produced by these radiation types will lie in the higher energy region of the pulse height spectra (away from most noise events) and are able to be effectively separated, even at low fluxes.

In contrast, the high dose rates (hence scintillator light yield) typical of medical X-ray units mean small noise fluctuations in the single electron peak region will not have a significant effect on measurements, hence these scintillators are well suited for medical and other high dose rate applications.

Chapter 8

Conclusion

The research documented throughout this thesis has explored the potential of optical fibres made from scintillating polymer for the development of radiation sensing devices in mineral processing and medical applications. The majority of this research has been focused on mineral processing applications, where plastic scintillating fibre bundles are intended for employment as dip sensors for the detection of alpha and beta radiation emitted by the various radionuclides of the uranium decay chain. The high sensitivity and fast response of plastic scintillators enable a fibre-based sensing platform capable of performing continuous, real-time sensing of low level radionuclides directly in mineral processing liquids, which is not possible with current methods.

The ability to perform direct, real-time sensing of radionuclides in mineral processing is critical for the improvement of current processing techniques, with the aim to efficiently and reliably extract high purity target metals like copper and gold for global export and trade.

The second application of this research relates to the use of plastic scintillating fibres in the medical field. Plastic scintillating fibres are well suited for in-vivo, low energy X-ray dosimetry owing to their small size, high sensitivity, tissue equivalence and real-time response. Research in this direction has been concerned with evaluating the response of a wide variety of scintillating fibres to keV X-rays for a more comprehensive study of their radiation response, and confirm they are not sensitive enough to ionising photons to be suitable for mining and mineral processing requirements.

In this research we conducted a comprehensive study on a large range of plastic scintillators to identify the optimal radiation sensitive polymers and to develop novel optical fibre-based radiation sensing devices. Plastic scintillators have been characterised in terms of their optical and material properties, and their response to a range of radiation types in order to select the scintillators most suited for detection of alpha and beta radiation under the proposed operating conditions.

Major progress has been made towards achievement of the ultimate goals of this project, most notably:

- Bulk plastic scintillators have been characterised in terms of their absorption and emission spectra, and key material properties relevant for optical fibre fabrication. The polystyrene based commercial bulk scintillator, EJ204, was selected for fibre fabrication based on its high light output, minimal fluorescence self-absorption, and emission peak lying close to the maximum sensitivity region of a bialkali photomultiplier tube.
- Bulk plastic scintillators have been successfully extruded into preforms and drawn into optical fibres. 160 µm diameter fibres were fabricated for the purpose of alpha particle detection, with refinements in drawing conditions producing an improvement in outer diameter stability from 12.5 % to 3.1% and transmission loss (from ≈ 30 dB/m to 13 dB/m at 450 nm). 1 mm diameter fibres were fabricated for beta particle detection, with measured losses and diameter stability comparable to commercially available scintillating fibres, demonstrating the in-house fibre drawing process can produce optical fibres of comparable quality.
- Commercially available optical fibres with outer claddings were found to display superior performance in terms of radiation sensitivity, optical properties and the ability to function under environmental conditions similar to those which will be encountered in mineral processing. 250 µm diameter blue scintillating BCF12 fibres were chosen for prototype device construction for alpha particle detection given they had the highest response to alpha particle response of all cladded fibre varieties. 1 mm cladded BCF12 fibres were chosen for device construction for beta particle detection for the same reason. Both prototype sensors exceed the minimum detectable activity being targeted (1 Bq/ml per isotope of ^{238}U which demonstrates that the use of scintillating polymer optical fibres enables the construction of sensors capable of achieving the project goals.
- Contamination of the polymer optical fibres by polonium-210 was found to produce elevated background levels in the alpha particle sensing devices. Polonium accumulation on the fibre sensor was found to stabilise, allowing the possibility of operating the sensor semi-continuously by periodic removal from measurement solutions to acquire and subtract background readings. The use of a decontaminant detergent, Decon 90, proved effective at removing the majority of contaminating polonium ions from the fibre bundle with no change in performance following the cleaning procedure.

- A final prototype beta sensor was created using 1.5 mm diameter, double cladded BCF12 fibres. The cladding thickness was shown to be effective at blocking 5.3 MeV alpha particles, hence the majority of alphas present in the ^{238}U decay series. The sensor was able to accurately measure the activity concentration of beta particles in a mixed radionuclide leach liquor, with measurement results in agreement with radionuclide concentrations obtained using gamma spectrometry.
- A final prototype alpha particle sensor was created using 250 µm diameter, double cladded BCF12 fibres. Design improvements from previous sensor iterations were implemented but were unable to be assessed due to the unexpectedly high transmission loss of the commercial fibres from which this prototype was constructed. The sensor was calibrated in terms of its response to alpha and beta particles and used in a leach liquor to estimate the alpha particle activity concentration, measuring between 0 and 3.82 Bq/ml of alpha emitters, outside the bounds predicted using gamma spectrometry (6.83 ± 0.3 Bq/ml). This result defines the direction for future work in improving fibre quality and sensor calibration. The ongoing quality control issues experienced with the commercial supplier which are associated with inconsistent optical quality and fibre dimensions provides motivation for further development in fabricating high-quality customised optical fibres in-house.
- The low energy X-ray response of a comprehensive range of scintillating fibres was investigated for medical dosimetry applications such as brachytherapy and radiology. The scintillator EJ204 was shown to have the lowest energy dependance of all scintillators tested, making this material most suited for low energy X-ray dosimetry. The optical fibres were shown to have a much lower sensitivity to keV X-rays compared to alpha and beta particles, making them unsuitable for X-ray and gamma ray detection in the low flux environment of mining and mineral processing application considered in this thesis.

The two optical fibre-based sensors which have been developed here have demonstrated the feasibility of detecting alpha and beta emitting radionuclides in mineral processing liquids at levels below the targeted 1 Bq/ml per isotope of ^{238}U. The detection method which has been employed offers many advantages over existing techniques, as the sensors are able to be placed directly in processing liquids which enables direct, near real-time measurements and eliminates the need for lengthy off-site analysis.

Appendices

Appendix A

Alpha and beta particle ranges and stopping powers

A.1 Alpha particle ranges and stopping powers

A.1.1 Polystyrene

$\rho_{\mathrm{PS}} = 1.03\ \mathrm{g/cm^3}$

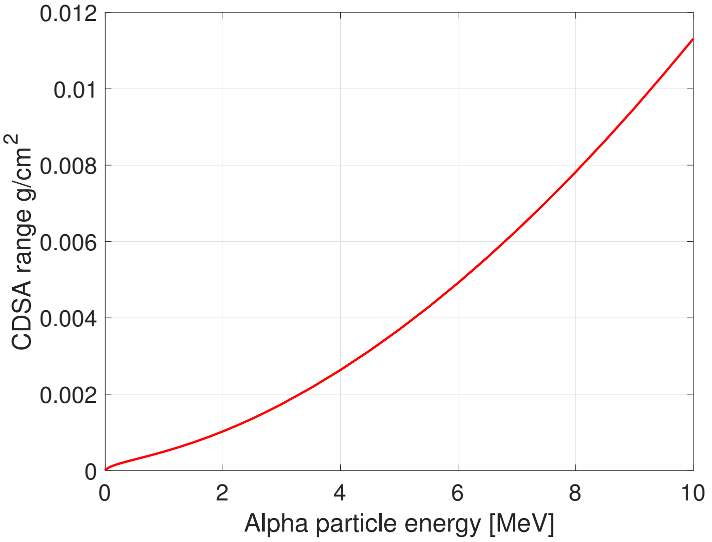

Figure A.1: CSDA range for alpha particles in polystyrene

Kinetic Energy **[MeV]**	**Total Stp. Pow.** **[MeV cm^2/g]**	**CSDA Range** **[g/cm^2]**
1.00E+00	2.27E+03	4.97E-04
1.50E+00	1.90E+03	7.39E-04
2.00E+00	1.61E+03	1.03E-03
2.50E+00	1.40E+03	1.36E-03
3.00E+00	1.24E+03	1.74E-03
3.50E+00	1.12E+03	2.17E-03
4.00E+00	1.02E+03	2.63E-03
4.50E+00	9.42E+02	3.14E-03
5.00E+00	8.75E+02	3.70E-03
5.50E+00	8.18E+02	4.29E-03
6.00E+00	7.69E+02	4.92E-03
6.50E+00	7.26E+02	5.59E-03
7.00E+00	6.88E+02	6.29E-03
7.50E+00	6.55E+02	7.04E-03
8.00E+00	6.24E+02	7.82E-03
8.50E+00	5.97E+02	8.64E-03
9.00E+00	5.72E+02	9.50E-03
9.50E+00	5.50E+02	1.04E-02
1.00E+01	5.29E+02	1.13E-02

Table A.1: Alpha particle stopping powers, and CSDA ranges for energies 1-10 MeV in polystyrene

A.1.2 PMMA

ρ_{PMMA}=1.18 g/cm^3

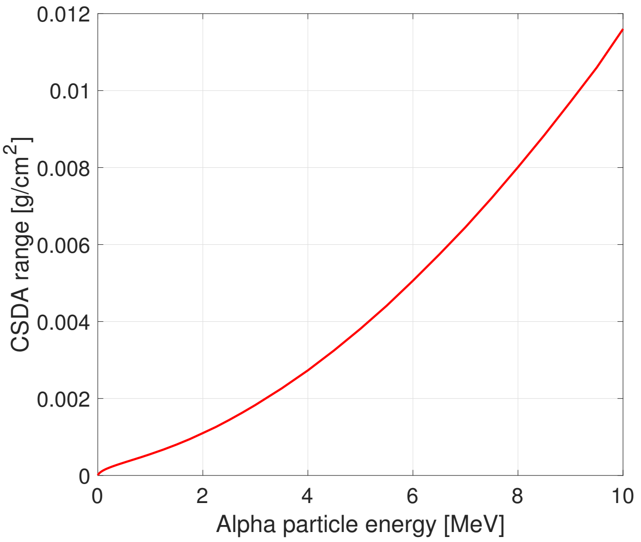

Figure A.2: CSDA range for alpha particles in PMMA

Kinetic Energy [MeV]	**Total Stp. Pow. [MeV cm^2/g]**	**CSDA Range [g/cm^2]**
1.00E+00	2.18E+03	5.53E-04
1.50E+00	1.85E+03	8.02E-04
2.00E+00	1.58E+03	1.10E-03
2.50E+00	1.37E+03	1.44E-03
3.00E+00	1.22E+03	1.83E-03
3.50E+00	1.10E+03	2.26E-03
4.00E+00	1.00E+03	2.73E-03
4.50E+00	9.26E+02	3.25E-03
5.00E+00	8.61E+02	3.81E-03
5.50E+00	8.05E+02	4.41E-03
6.00E+00	7.57E+02	5.06E-03
6.50E+00	7.15E+02	5.74E-03
7.00E+00	6.77E+02	6.45E-03
7.50E+00	6.44E+02	7.21E-03
8.00E+00	6.15E+02	8.01E-03
8.50E+00	5.88E+02	8.84E-03
9.00E+00	5.64E+02	9.71E-03
9.50E+00	5.41E+02	1.06E-02
1.00E+01	5.21E+02	1.16E-02

Table A.2: Alpha particle stopping powers, and CSDA ranges for energies 1-10 MeV in PMMA

A.1.3 Air, dry (near sea level)

$\rho_{\text{air}} = 1.225 \times 10^{-3}$ g/cm^3

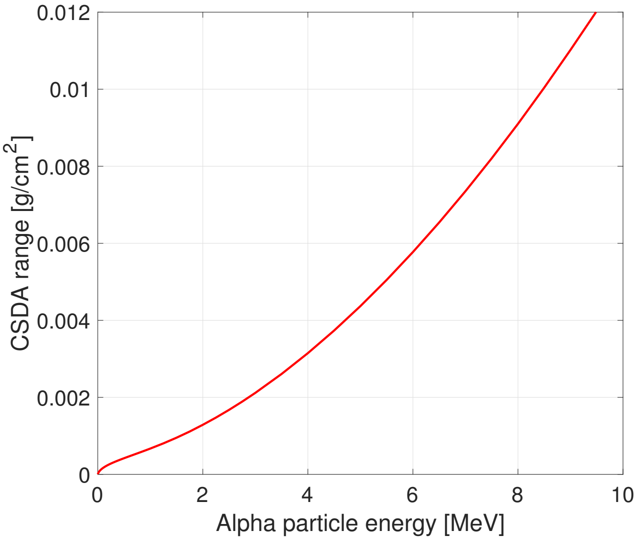

Figure A.3: CSDA range for alpha particles in air

Kinetic Energy [MeV]	**Total Stp. Pow.** [MeV cm^2/g]	**CSDA Range** [g/cm^2]
1.00E+00	1.92E+03	6.70E-04
1.50E+00	1.63E+03	9.52E-04
2.00E+00	1.38E+03	1.29E-03
2.50E+00	1.21E+03	1.68E-03
3.00E+00	1.07E+03	2.12E-03
3.50E+00	9.69E+02	2.61E-03
4.00E+00	8.87E+02	3.15E-03
4.50E+00	8.19E+02	3.73E-03
5.00E+00	7.61E+02	4.37E-03
5.50E+00	7.12E+02	5.05E-03
6.00E+00	6.70E+02	5.77E-03
6.50E+00	6.33E+02	6.54E-03
7.00E+00	6.01E+02	7.35E-03
7.50E+00	5.72E+02	8.21E-03
8.00E+00	5.46E+02	9.10E-03
8.50E+00	5.22E+02	1.00E-02
9.00E+00	5.01E+02	1.10E-02
9.50E+00	4.82E+02	1.20E-02
1.00E+01	4.64E+02	1.31E-02

Table A.3: Alpha particle stopping powers, and CSDA ranges for energies 1-10 MeV in air

A.1.4 Water

$\rho_{\mathrm{water}} = 1\ \mathrm{g/cm^3}$

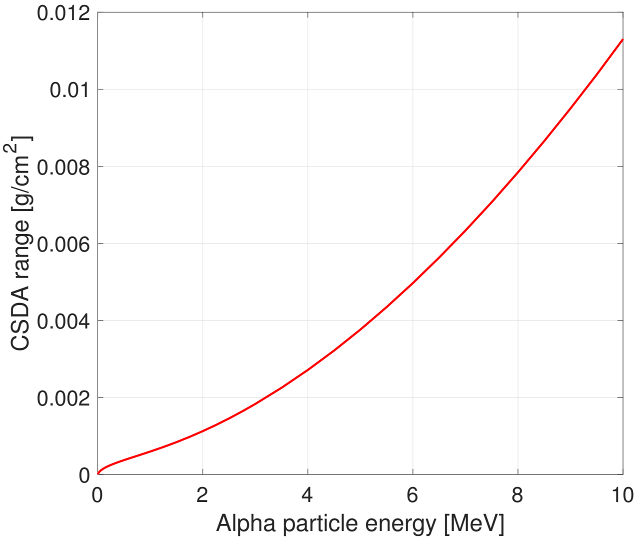

Figure A.4: CSDA range for alpha particles in water

Kinetic Energy [MeV]	**Total Stp. Pow. [MeV cm^2/g]**	**CSDA Range [g/cm^2]**
1.00E+00	2.19E+03	5.93E-04
1.50E+00	1.90E+03	8.37E-04
2.00E+00	1.63E+03	1.12E-03
2.50E+00	1.42E+03	1.45E-03
3.00E+00	1.26E+03	1.83E-03
3.50E+00	1.13E+03	2.25E-03
4.00E+00	1.04E+03	2.71E-03
4.50E+00	9.54E+02	3.22E-03
5.00E+00	8.86E+02	3.76E-03
5.50E+00	8.28E+02	4.34E-03
6.00E+00	7.78E+02	4.97E-03
6.50E+00	7.34E+02	5.63E-03
7.00E+00	6.95E+02	6.33E-03
7.50E+00	6.61E+02	7.07E-03
8.00E+00	6.31E+02	7.84E-03
8.50E+00	6.03E+02	8.65E-03
9.00E+00	5.78E+02	9.50E-03
9.50E+00	5.55E+02	1.04E-02
1.00E+01	5.34E+02	1.13E-02

Table A.4: Alpha particle stopping powers, and CSDA ranges for energies 1-10 MeV in water

A.2 Beta particle ranges and stopping powers

A.2.1 Polystyrene

$\rho_{\mathrm{PS}} = 1.03\ \mathrm{g/cm^3}$

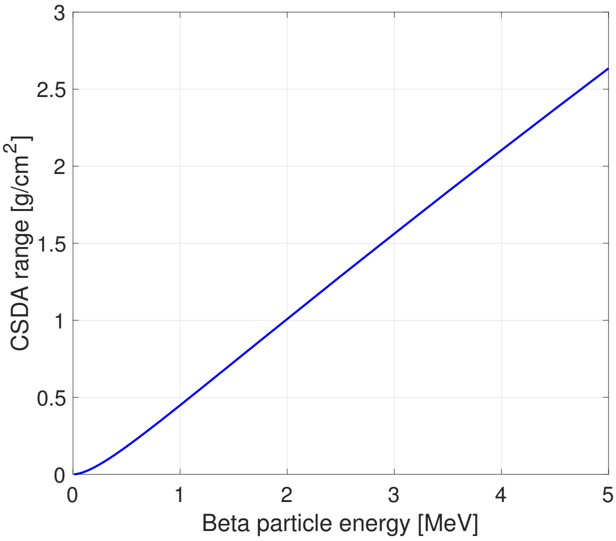

Figure A.5: CSDA range for beta particles in polystyrene

Kinetic Energy [MeV]	**Total Stp. Pow. [MeV cm^2/g]**	**CSDA Range [g/cm^2]**
1.00E-01	4.04E+00	1.46E-02
2.00E-01	2.74E+00	4.58E-02
3.50E-01	2.19E+00	1.08E-01
4.00E-01	2.11E+00	1.32E-01
4.50E-01	2.04E+00	1.56E-01
5.00E-01	1.99E+00	1.81E-01
5.50E-01	1.95E+00	2.06E-01
6.00E-01	1.92E+00	2.32E-01
7.00E-01	1.87E+00	2.85E-01
8.00E-01	1.84E+00	3.39E-01
9.00E-01	1.82E+00	3.93E-01
1.00E+00	1.80E+00	4.48E-01
1.25E+00	1.79E+00	5.88E-01
1.50E+00	1.78E+00	7.28E-01
1.75E+00	1.78E+00	8.68E-01
2.00E+00	1.79E+00	1.01E+00
2.50E+00	1.81E+00	1.29E+00
3.00E+00	1.83E+00	1.56E+00
3.50E+00	1.85E+00	1.84E+00
4.00E+00	1.87E+00	2.10E+00
4.50E+00	1.88E+00	2.37E+00
5.00E+00	1.90E+00	2.64E+00

Table A.5: Beta particle stopping powers, and CSDA ranges for energies .1-5 MeV in polystyrene

A.2.2 PMMA

ρ_{PMMA}=1.18 g/cm^3

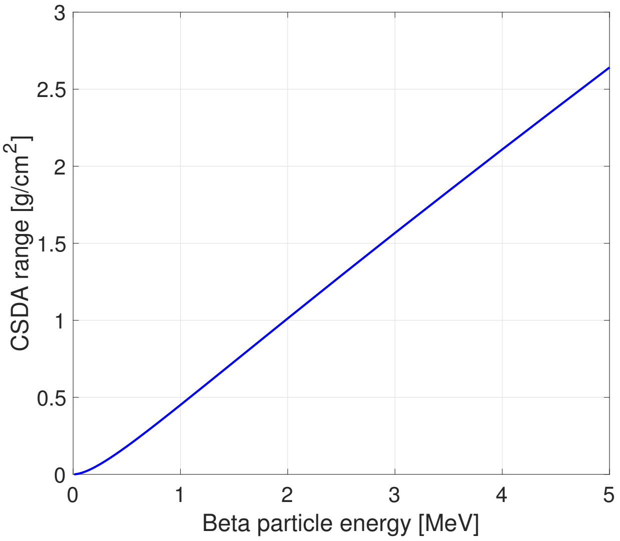

Figure A.6: CSDA range for beta particles in PMMA

Kinetic Energy [MeV]	Total Stp. Pow. [MeV cm^2/g]	CSDA Range [g/cm^2]
1.000E-01	4.010E+00	1.470E-02
1.500E-01	3.155E+00	2.894E-02
2.000E-01	2.723E+00	4.610E-02
2.500E-01	2.465E+00	6.547E-02
3.000E-01	2.297E+00	8.653E-02
3.500E-01	2.180E+00	1.089E-01
4.000E-01	2.096E+00	1.323E-01
4.500E-01	2.032E+00	1.566E-01
5.000E-01	1.981E+00	1.815E-01
5.500E-01	1.942E+00	2.070E-01
6.000E-01	1.910E+00	2.330E-01
7.000E-01	1.864E+00	2.860E-01
8.000E-01	1.834E+00	3.401E-01
9.000E-01	1.813E+00	3.950E-01
1.000E+00	1.799E+00	4.504E-01
1.250E+00	1.781E+00	5.902E-01
1.500E+00	1.776E+00	7.308E-01
1.750E+00	1.779E+00	8.715E-01
2.000E+00	1.785E+00	1.012E+00
2.500E+00	1.802E+00	1.291E+00
3.000E+00	1.822E+00	1.567E+00
3.500E+00	1.842E+00	1.839E+00
4.000E+00	1.862E+00	2.109E+00
4.500E+00	1.882E+00	2.376E+00
5.000E+00	1.901E+00	2.641E+00

Table A.6: Beta particle stopping powers, and CSDA ranges for energies .1-5 MeV in PMMA

A.2.3 Air, dry (near sea level)

$\rho_{\text{air}} = 1.225 \times 10^{-3}$ g/cm^3

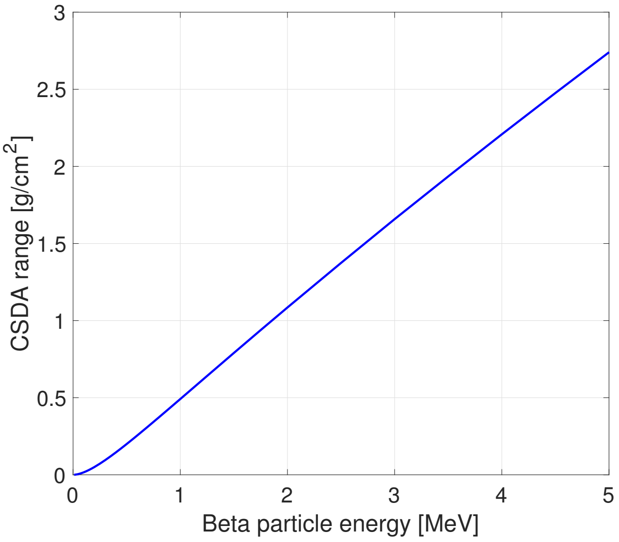

Figure A.7: CSDA range for beta particles in air

Kinetic Energy [MeV]	**Total Stp. Pow. [MeV cm^2/g]**	**CSDA Range [g/cm^2]**
1.00E-01	3.64E+00	1.62E-02
1.50E-01	2.87E+00	3.19E-02
2.00E-01	2.47E+00	5.08E-02
2.50E-01	2.24E+00	7.21E-02
3.00E-01	2.09E+00	9.53E-02
3.50E-01	1.98E+00	1.20E-01
4.00E-01	1.91E+00	1.46E-01
4.50E-01	1.85E+00	1.72E-01
5.00E-01	1.81E+00	2.00E-01
5.50E-01	1.78E+00	2.27E-01
6.00E-01	1.75E+00	2.56E-01
7.00E-01	1.72E+00	3.14E-01
8.00E-01	1.69E+00	3.72E-01
9.00E-01	1.68E+00	4.32E-01
1.00E+00	1.67E+00	4.91E-01
1.25E+00	1.67E+00	6.41E-01
1.50E+00	1.68E+00	7.90E-01
1.75E+00	1.69E+00	9.38E-01
2.00E+00	1.71E+00	1.09E+00
2.50E+00	1.75E+00	1.37E+00
3.00E+00	1.78E+00	1.66E+00
3.50E+00	1.82E+00	1.94E+00
4.00E+00	1.85E+00	2.21E+00
4.50E+00	1.88E+00	2.48E+00
5.00E+00	1.91E+00	2.74E+00

Table A.7: Beta particle stopping powers, and CSDA ranges for energies .1-5 MeV in air

A.2.4 Water

$\rho_{\text{water}} = 1 \text{ g/cm}^3$

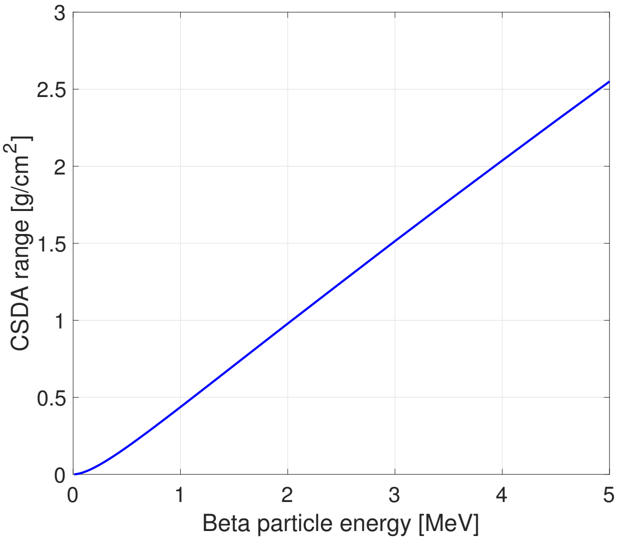

Figure A.8: CSDA range for beta particles in water

Kinetic Energy [MeV]	**Total Stp. Pow. [MeV cm^2/g]**	**CSDA Range [g/cm^2]**
1.00E-01	4.12E+00	1.43E-02
1.50E-01	3.24E+00	2.82E-02
2.00E-01	2.80E+00	4.49E-02
2.50E-01	2.53E+00	6.37E-02
3.00E-01	2.36E+00	8.42E-02
3.50E-01	2.24E+00	1.06E-01
4.00E-01	2.15E+00	1.29E-01
4.50E-01	2.09E+00	1.52E-01
5.00E-01	2.04E+00	1.77E-01
5.50E-01	2.00E+00	2.01E-01
6.00E-01	1.97E+00	2.27E-01
7.00E-01	1.93E+00	2.78E-01
8.00E-01	1.90E+00	3.30E-01
9.00E-01	1.88E+00	3.83E-01
1.00E+00	1.86E+00	4.37E-01
1.25E+00	1.85E+00	5.72E-01
1.50E+00	1.84E+00	7.08E-01
1.75E+00	1.84E+00	8.43E-01
2.00E+00	1.85E+00	9.79E-01
2.50E+00	1.87E+00	1.25E+00
3.00E+00	1.89E+00	1.51E+00
3.50E+00	1.91E+00	1.78E+00
4.00E+00	1.93E+00	2.04E+00
4.50E+00	1.95E+00	2.30E+00
5.00E+00	1.97E+00	2.55E+00

Table A.8: Beta particle stopping powers, and CSDA ranges for energies .1-5 MeV in water

Appendix B

List of fibre bundles

B.0.5 Beta particle sensing fibre bundles

A list of the beta particle sensing bundles which were created for this project, and their relevant properties are shown in Table B.1

Name	**Material**	**OD (µm)**	**Cladding thickness (µm)**	**Single (S) or double (D) clad**	**N**	**L (cm)**
B1	BCF12	1000	30	s	20	15
B2	BCF12	1000	30	s	42	20
B3	BCF12	1500	45	d	42	20

Table B.1: List of prototype beta sensors and corresponding physical properties.
OD = fibre outer diameter.
N = number of fibres in bundle.
L = Total fibre length.

B.0.6 Alpha particle sensing fibre bundles

A list of the alpha particle sensing bundles which were created for this project, and their relevant properties are shown in Table B.2

Name	**Material**	**OD (µm)**	**Cladding thickness (µm)**	**Single (S) or double (D) clad**	**N**	**L (cm)**
A1	BCF12	250	7.5	s	200	15
A2	BCF20	250	7.5	s	1500	10
A3	BCF12	250	7.5	s	1800	10
A4	BCF12	250	7.5	d	2500	12

Table B.2: List of prototype beta sensors and corresponding physical properties.
OD = fibre outer diameter.
N = number of fibres in bundle.
L = Total fibre length.

Bibliography

[1] O. Abdi, K.C. Wong, T. Hassan, K.J. Peters, and M.J. Kowalsky. Cleaving of solid single mode polymer optical fiber for strain sensor applications. *Optics Communications*, 282(5):856 – 861, 2009.

[2] M. Alam, J. Abramczyk, J. Farroni, U. Manyam, and D. Guertin. Passive and active optical fibers for space and terrestrial applications. *Proceedings of SPIE–the international society for optical engineering.*, 6308, 2006.

[3] K. Awazu, H. Kawazoe, and M. Yamane. Simultaneous generation of optical absorption bands at 5.14 and 0.452 ev in 9 sio2: Geo2 glasses heated under a H2 atmosphere. *Journal of Applied Physics*, 68(6):2713–2718, 1990.

[4] A S Beddar, T R Mackie, and F H Attix. Water-equivalent plastic scintillation detectors for high-energy beam dosimetry: I. physical characteristics and theoretical considerations. *Physics in Medicine & Biology*, 37(10):1883, 1992.

[5] A.S. Beddar. Plastic scintillation dosimetry and its application to radiotherapy. *Radiation Measurements*, 41(Supplement 1):S124 – S133, 2006. The 2nd Summer School on Solid State Dosimetry: Concepts and Trends in Medical Dosimetry.

[6] M. Benabdesselam, F. Mady, S. Girard, Y. Mebrouk, J.B. Duchez, M. Gaillardin, and P. Paillet. Performance of ge-doped optical fiber as a thermoluminescent dosimeter. *IEEE Transactions on Nuclear Science*, 60(6):4251–4256, 2013.

[7] Thomas Berger. Radiation dosimetry onboard the international space station ISS. *Zeitschrift für Medizinische Physik*, 18(4):265 – 275, 2008.

[8] R. Berthet, Y. Chalamet, M. Taha, and A. Zerroukhi. Optical fibers by reactive extrusion of butyl methacrylate. *Macromolecular materials and engineering*, 291(6):720–731, 2006.

[9] J.B Birks. *The Theory and Practice of Scintillation Counting.* Pergamon Press, 1964.

[10] Jonathan Boivin, Sam Beddar, Chris Bonde, Daniel Schmidt, Wesley Culberson, Maxime Guillemette, and Luc Beaulieu. A systematic characterization of the low-energy photon response of plastic scintillation detectors. *Physics in Medicine and Biology*, 61(15):5569, 2016.

[11] L.M. Bollinger, G.E. Thomas, and R.J. Ginther. Neutron detection with glass scintillators. *Nuclear Instruments and Methods*, 17(1):97 – 116, 1962.

[12] Alexander I. Bolozdynya. *Emission detectors.* World Scientific, 2010.

[13] Kenneth E. Bower, Yuri A. Barbanel, Yuri G. Shreter, and George W. Bohnert. *Polymers, Phosphors, and Voltaics for Radioisotope Microbatteries.* CRC Press, 2002.

[14] D.A. Bradley, R.P. Hugtenburg, A. Nisbet, A.T. Abdul Rahman, F. Issa, N. Mohd Noor, and A. Alalawi. Review of doped silica glass optical fibre: Their tl properties and potential applications in radiation therapy dosimetry. *Applied Radiation and Isotopes*, 71(SUPPL.):2–11, 2012.

[15] J Canning, E Buckley, N Groothoff, B Luther-Davies, and J Zagari. Uv laser cleaving of air–polymer structured fibre. *Optics Communications*, 202(1):139 – 143, 2002.

[16] M. Caria, P. Macciotta, and S. Serci. On the detection of low energy γ-rays with plastic scintillators. *Nuclear Instruments and Methods in Physics Research*, 188(2):473 – 474, 1981.

[17] J. H. Chan and P. B. Price. Composition and energy spectra of heavy nuclei of unknown origin detected on skylab. *Phys. Rev. Lett.*, 35:539–542, Aug 1975.

[18] Mark Clift, Peter Johnston, and David Webb. A temporal method of avoiding the cerenkov radiation generated in organic scintillator dosimeters by pulsed mega-voltage electron and photon beams. *Physics in medicine and biology*, 47:1421–33, 05 2002.

[19] B.M. Coursey, W.B. Mann, A. Grau Malonda, E. Garcia-Toraño, J.M. Los Arcos, J.A.B. Gibson, and D. Reher. Standardization of carbon-14 by $4\pi\beta$ liquid scintillation efficiency tracing with hydrogen-3. *International Journal of Radiation Applications and Instrumentation. Part A. Applied Radiation and Isotopes*, 37(5):403 – 408, 1986.

[20] C. D'Ambrosio, T. Gys, H. Leutz, and D. Puertolas. Particle tracking with scintillating fibers. *IEEE Transactions on Nuclear Science*, 43(3):2115–2127, Jun 1996.

[21] A. Dimitriadis, I. Silvestre Patallo, I. Billas, S. Duane, A. Nisbet, and C.H. Clark. Characterisation of a plastic scintillation detector to be used in a multicentre stereotactic radiosurgery dosimetry audit. *Radiation Physics and Chemistry*, 140(Supplement C):373 – 378, 2017. 2nd International Conference on Dosimetry and its Applications (ICDA-2) University of Surrey, Guildford, United Kingdom, 3-8 July 2016.

[22] Carl W. Dirk, Albert Peralez, Sarah Kopecky, Elder de la Rosa-Cruz, Victor M. Castano, and M. Rogelio Rodriguez. Luminescence characterization of rhodamine-b-doped plastic optical fibers using the side induced fluorescence method. *Proc. SPIE 4106, Linear, Nonlinear, and Power-Limiting Organics*, 2000.

[23] H. Ebendorff-Heidepriem, T.M Monro, and M.A. van Eijkelenborg M.C.J. Large. Extruded high-na microstructured polymer optical fibre. *Optics communications*, 273(1):133–137, 2007.

[24] Heike Ebendorff-Heidepriem and Tanya M. Monro. Extrusion of complex preforms for microstructured optical fibers. *Opt. Express*, 15(23):15086–15092, Nov 2007.

[25] Heike Ebendorff-Heidepriem and Tanya M. Monro. Extrusion of complex preforms for microstructured optical fibers. *Opt. Express*, 15(23):15086–15092, Nov 2007.

[26] J. M. Edmund, C. E. Andersen, C. J. Marckmann, M. C. Aznar, M. S. Akselrod, and L. Bøtter-Jensen. Cw-osl measurement protocols using optical fibre al2 o3:c dosemeters. *Radiation protection dosimetry*, 119(1-4):368–374, 2006.

[27] G. Espinosa and J.S. Bogard. Optically stimulated luminescence response of commercial sio2 optical fiber. *Journal of radioanalytical and nuclear chemistry.*, 277(1):125–129, 2008.

[28] A. Fernandez Fernandez, B. Brichard, S. O'Keeffe, C. Fitzpatrick, E. Lewis, J.-R. Vaille, L. Dusseau, D.A. Jackson, F. Ravotti, M. Glaser, and H. El-Rabii. Real-time fibre optic radiation dosimeters for nuclear environment monitoring around thermonuclear reactors. *Fusion Engineering and Design*, 83(1):50 – 59, 2008.

[29] A.F. Fernandez, B. Brichard, F. Berghmans, and M. Decréton. Dose-rate dependencies in gamma-irradiated fiber bragg grating filters. *IEEE transactions on nuclear science*, 6:2874–2878, 2002.

[30] Alberto Fernandez Fernandez, Gaspar Rego, A Gusarov, Benoit Brichard, José Santos, Henrique Salgado, and Francis Berghmans. Evaluation of long-period fiber grating temperature sensors in nuclear environments. *Proceedings of SPIE - The International Society for Optical Engineering*, 5502, 06 2004.

[31] P.E. Figgins. *THE RADIOCHEMISTRY OF POLONIUM.* Subcommittee on Radiochemistry, National Academy of Sciences-National Research Council, Jan 1961.

[32] W.W. Flynn. The determination of low levels of polonium-210 in environmental materials. *Analytica Chimica Acta*, 43(Supplement C):221 – 227, 1968.

[33] jean-marc Fontbonne, G Iltis, G Ban, A Battala, J.C. Vernhes, J Tillier, N Bellaize, C Le Brun, B Tamain, K Mercier, and J.C. Motin. Scintillating fiber dosimeter for radiation therapy accelerator. *Nuclear Science, IEEE Transactions on*, 49:2223 – 2227, 11 2002.

[34] K.L. Gale, D.R. Boreham, S. Maves, and D.P. Morrison. Developments in biological dosimetry for the nuclear industry. In *CNS proceedings of the 16. annual conference, volume I and II*, volume 2, page 8pp, 1995.

[35] R. Gaza and S.W.S. McKeever. A real-time, high-resolution optical fibre dosemeter based on optically stimulated luminescence (osl) of kbr:eu, for potential use during the radiotherapy of cancer. *Radiation protection dosimetry*, 120(1-4):14–19, 2006.

[36] K Geetha, M Rajesh, V P N Nampoori, C P G Vallabhan, and P Radhakrishnan. Loss characterization in rhodamine 6g doped polymer film waveguide by side illumination fluorescence. *Journal of Optics A: Pure and Applied Optics*, 6(4), 2004.

[37] David L. Griscom. Optical properties and structure of defects in silica glass. *Nippon Seramikkusu Kyokai Gakujutsu Ronbunshi/Journal of the Ceramic Society of Japan*, 99(1154):923–942, 1991.

[38] R.K. Gupta. *Polymer and Composite Rheology.* Marcel Dekker Inc., 2000.

[39] M.S. Hamlat, S. Djeffal, and H. Kadi. Assessment of radiation exposures from naturally occurring radioactive materials in the oil and gas industry. *Applied Radiation and Isotopes*, 55(1):141–146, 2001.

[40] S. Hashim, D.A. Bradley, M.I. Saripan, A.T. Ramli, and H. Wagiran. The thermoluminescence response of doped sio2 optical fibres subjected to fast neutrons. *Applied Radiation and Isotopes*, 68(4):700 – 703, 2010. The 7th International Topical Meeting on Industrial Radiation and Radio isotope Measurement Application(IRRMA-7).

[41] J. Hect. *Understanding Fiber Optics.* Pearson Prentice Hall, New Jersey, USA, 2006.

[42] H. Henschel, M. Körfer, J. Kuhnhenn, U. Weinand, and F. Wulf. Fibre optic radiation sensor systems for particle accelerators. *Nuclear Instruments and Methods in Physics Research Section A: Accelerators, Spectrometers, Detectors and Associated Equipment*, 526(3):537 – 550, 2004.

[43] M.R. Hoerner, E.J. Stepusin, D.E. Hyer, and D.E. Hintenlang. Characterizing energy dependence and count rate performance of a dual scintillator fiber-optic detector for computed tomography. *Medical physics.*, 42(3):1268–1279, 2015.

[44] C. Hurlbut. Personal communication, February 13 2015.

[45] C. Hurlbut. Personal communication, Spetember 17 2015.

[46] C. Hurlbut. Personal communication, March 27 2016.

[47] I.R. Husdi. Sensing characteristics of plastic optical fibres measured by optical time-domain reflectometry. *Measurement science & technology*, 15(8):1553–1559, 2004.

[48] A.L Huston, B.L Justus, P.L Falkenstein, R.W Miller, H Ning, and R Altemus. Remote optical fiber dosimetry. *Nuclear Instruments and Methods in Physics Research Section B: Beam Interactions with Materials and Atoms*, 184(1):55 – 67, 2001. Advanced Topics in Solid State Dosimetry.

[49] A. Ikhlef and M. Skowronek. Application of a plastic scintillating fiber array for low-energy x-ray imaging. *Applied optics*, 37(34):8081–8084, 1998.

[50] M Ishii, K Harada, Y Hirose, N Senguttuvan, M Kobayashi, I Yamaga, H Ueno, K Miwa, F Shiji, F Yiting, M Nikl, and X.Q Feng. Development of bso (bi4si3o12) crystal for radiation detector. *Optical Materials*, 19(1):201 – 212, 2002. Photonic Materials for the 21st Century. Proceedings of the 2nd International Symposium on Laser, Scintillator and Nonlinear Optical Materials.

[51] M Ishikawa, G Bengua, K L Sutherland, J Hiratsuka, N Katoh, S Shimizu, H Aoyama, K Fujita, R Yamazaki, K Horita, and H Shirato. A feasibility study of novel plastic scintillation dosimetry with pulse-counting mode. *Physics in Medicine and Biology*, 54(7):2079, 2009.

[52] Kyoung-Won Jang, Dong-Hyun Cho, Sun-Cheol Jeong, Jae-Hun Jun, Bong-Soo Lee, Sin Kim, Hyo-Sung Cho, Sung-Yong Park, and Dong-Ho Shin. Measurements and characterizations of cerenkov light in fiber-optic radiation sensor irradiated by high energy electron beam. *Journal of Sensor Science and Technology*, 15:186–191, 01 2006.

[53] Kyoung Won Jang, Takahiro Yagi, Cheol Ho Pyeon, Wook Jae Yoo, Sang Hun Shin, Tsuyoshi Misawa, and Bongsoo Lee. Feasibility of fiber-optic radiation sensor using cerenkov effect for detecting thermal neutrons. *Opt. Express*, 21(12):14573–14582, Jun 2013.

[54] Kyoung Won Jang, Wook Jae Yoo, Sang Hun Shin, Dongho Shin, and Bongsoo Lee. Fiber-optic cerenkov radiation sensor for proton therapy dosimetry. *Opt. Express*, 20(13):13907–13914, Jun 2012.

[55] C.A.G. Kalnins, H. Ebendorff-Heidepriem, N.A. Spooner, and T.M. Monro. Luminescent properties of fluoride phosphate glass for radiation dosimetry. *Optical materials express.*, 3(7):960–967, 2013.

[56] I. Kamiji and K. Nakagiri. Upgrade of in-beam charged particle detector for the koto experiment. *Journal of Physics: Conference Series*, 800(1), 2017.

[57] Faiz. M. Khan. *The physics of radiation therapy.* Lippincott Williams & Wilkins, 2003.

[58] Glenn F Knoll. *Radiation detection and measurement*, volume 4. New York, NY : Wiley, 2010. - 830 p., 2010.

[59] Katerina Krebber, Henning Henschel, and Udo Weinand. Fibre bragg gratings as high dose radiation sensors? *Measurement Science and Technology*, 17(5):1095, 2006.

[60] NIST Physical Measurement Laboratory, 2018.

[61] NIST Physical Measurement Laboratory, 2018.

[62] S.H. Law, J.D. Harvey, R.J. Kruhlak, M. Song, E. Wu, G.W. Barton, M.A. van Eijkelenborg, and M.C.J. Large. Cleaving of microstructured polymer optical fibres. *Optics Communications*, 258(2):193 – 202, 2006.

[63] Hyun Mi Lee, Gi Hoon Hong, Mark Baskaran, Suk Hyun Kim, and Young ILL Kim. Evaluation of plating conditions for the recovery of 210po on a ag planchet. *Applied Radiation and Isotopes*, 90:170 – 176, 2014.

[64] François Lessard, Louis Archambault, Mathieu Plamondon, Philippe Després, François Therriault-Proulx, Sam Beddar, and Luc Beaulieu. Validating plastic scintillation detectors for photon dosimetry in the radiologic energy range. *Medical physics.*, 39(9):5308–5316, 2012.

[65] Robert R. J. Maier, William N. MacPherson, James S. Barton, Julian D. C. Jones, Scott McCulloch, Alberto Fernandez-Fernandez, Lin Zhang, and Xianfeng Chen. Fiber bragg gratings of type i in smf-28 and b/ge fibre and type iia b/ge fibre under

gamma radiation up to 0.54 mgy. *Proc. SPIE 5855, 17th International Conference on Optical Fibre Sensors*, 2005.

[66] C.J. Marckmann, C.E. Andersen, M.C. Aznar, and L. Bøtter-Jensen. Optical fibre dosemeter systems for clinical applications based on radioluminescence and optically stimulated luminescence from al2o3:c. *Radiation protection dosimetry*, 120(1-4):28–32, 2006.

[67] D. McCarthy, S. O'Keeffe, E. Lewis, D. Sporea, A. Sporea, I. Tiseanu, P. Woulfe, and J. Cronin. Optical fibre radiation dosimeter for radiotherapy applications. In *2012 IEEE Sensors*, pages 1–4, Oct 2012.

[68] E. Miller and J. P. Rothstein. Control of the sharkskin instability in the extrusion of polymer melts using induced temperature gradients. *Rheologica acta*, 44(2):160–173, 2004.

[69] F. Moradi, N.M. Ung, G.A. Mahdiraji, M.U. Khandaker, A. Entezam, M.H. See, N.A. Taib, Y.M. Amin, and D.A. Bradley. Angular dependence of optical fibre thermoluminescent dosimeters irradiated using kilo- and megavoltage x-rays. *Radiation Physics and Chemistry*, 135(Supplement C):4 – 10, 2017.

[70] H. Nakamura, Y. Shirakawa, S. Takahashi, and H. Shimizu. Evidence of deep-blue photon emission at high efficiency by common plastic. *EPL (Europhysics Letters)*, 95(2):22001, 2011.

[71] C. Nodine. Personal communication, July 28 2016.

[72] R Nowotny. Radioluminescence of some optical fibres. *Physics in Medicine and Biology*, 52(4):N67, 2007.

[73] Paul C. Painter and Michael M. Coleman. *Essentials of Polymer Science and Engineering*. DEStech Publications, Inc., 2009.

[74] F Pauss. The electromagnetic calorimeter technical design report cern. Technical report, LHCC, 1977.

[75] Luis Peralta and Florbela Rêgo. Response of plastic scintillators to low-energy photons. *Physics in Medicine and Biology*, 59(16):4621, 2014.

[76] J.C. Polf, E.G. Yukihara, M.S. Akselrod, and S.W.S. McKeever. Real-time luminescence from al2o3 fiber dosimeters. *Radiation Measurements*, 38(2):227 – 240, 2004.

[77] L. Ren, Y. Zhang, Y. Wang, X. Li, Y. Zhao, and L. Wang. Fabrication and characteristics of rhodamine-doped micro-structured polymer optical fabrication

and characteristics of rhodamine-doped micro-structured polymer optical fibres. *Proceedings of the international plastic optical fibres conference*, 14, 2005.

[78] R. C. Ruchti. The use of scintillating fibers for charged-particle tracking. *Annual Review of Nuclear and Particle Science*, 46(1):281–319, 1996.

[79] F. Rüdiger, G. Schmidt, K. Wille, M. Körfer, and W. Göttmann. Beam loss position monitoring with optical fibres at delta. *EPAC 2008 - Contributions to the Proceedings*, pages 1032–1034, 2008.

[80] J. M. Ryan, J. R. Macri, M. L. McConell, R. A. Messner, W. Li, H. H. Cutlip, Q. Zheng, C. M. Castaneda, and J. L. Romero. A scintillating plastic fiber tracking detector for neutron and proton imaging and spectroscopy. In *1999 IEEE Nuclear Science Symposium. Conference Record. 1999 Nuclear Science Symposium and Medical Imaging Conference (Cat. No.99CH37019)*, volume 1, pages 483–488 vol.1, 1999.

[81] Max Schmidt. Book review: The chemistry of selenium, tellurium and polonium. by k. w. bagnall. *Angewandte Chemie International Edition in English*, 6(12):1090–1090, 1967.

[82] S.V. Shatalin, V.N. Treschikov, and A.J. Rogers. Interferometric optical time-domain reflectometry for distributed optical fiber sensing. *Proceedings of SPIE–the international society for optical engineering.*, 3479:181–191, 1998.

[83] Montgomery T. Shaw and William J. MacKnigh. *Introduction to Polymer Viscoelasticity.* John Wiley and sons, 2005.

[84] D. Solatie, P. Carbol, E. Hrnecek, T. Jaakkola, and M. Betti. Sample preparation methods for the determination of plutonium and strontium in environmental samples by low level liquid scintillation counting and α-spectrometry. *Radiochimica Acta*, 90(8):447–454, 2002.

[85] T. Suzuki, Y. Fujii, K. Hara, T. Ishizaki, F. Kajino, N. Kanaya, J. Kanzaki, K. Kawagoe, S. Kim, T. Matsui, A. Miyajima, A. Nakagawa, S. Nakazawa, M. Nozaki, T. Ota, K. Sendai, Y. Sugimoto, Y. Sugimoto, H. Takayama, H. Takeda, T. Takeshita, S. Tanaka, A. Tanaka, T. Toeda, and Y. Yamada. Systematic measurement of energy resolution and e/π ratio of a lead/plastic-scintillator sampling calorimeter. *Nuclear Instruments and Methods in Physics Research, Section A: Accelerators, Spectrometers, Detectors and Associated Equipment*, 432(1):48–65, 1999.

[86] S.B. Thacker, D.F. Stroup, G. Parrish, and H.A. Anderson. Surveillance in environmental public health: Issues, systems, and sources. *American Journal of Public*

Health, 86(5):633–638, 1996.

[87] L Thinova, C Karasinski, J Tous, and T Trojek. Investigation of thin yap and yag scintillator characteristics for alpha radiation spectrometry. *Journal of Physics: Conference Series*, 41(1):573, 2006.

[88] L. Thinova, A. Kunka, P. Maly, F. de Notaristefani, K. Blazek, T. Trojeka, and L. Moucka. Measurement of radon daughters in water and in air using the detection unit "yapmare" with a yap:ce scintillation detector. *International Congress Series*, 1276:383–384, 2005.

[89] M. P. Tornai, E. J. Hoffman, L. R. MacDonald, and C. S. Levin. Characterization of fluor concentration and geometry in organic scintillators for in situ beta imaging. *IEEE Transactions on Nuclear Science*, 43(6):3342–3347, Dec 1996.

[90] unknown, Aug 2017.

[91] unknown, Feb 2018.

[92] Carel W.E van Eijk. Inorganic scintillators in medical imaging detectors. *Nuclear Instruments and Methods in Physics Research Section A: Accelerators, Spectrometers, Detectors and Associated Equipment*, 509(1):17 – 25, 2003. Proceedings of the 4th Internatonal Workshop on Radiation Imaging Detectors.

[93] C.W.E van Eijk, A Bessière, and P Dorenbos. Inorganic thermal-neutron scintillators. *Nuclear Instruments and Methods in Physics Research Section A: Accelerators, Spectrometers, Detectors and Associated Equipment*, 529(1):260 – 267, 2004. Proceedings of the Joint Meeting of the International Conference on Neutron Optics (NOP2004) and the Third International Workshop on Position-Sensitive Neutron Detectors (PSND2004).

[94] M. Wurm, F. von Feilitzsch, M. Göger-Neff, K. A. Hochmuth, T. Marrodán Undagoitia, L. Oberauer, and W. Potzel. Detection potential for the diffuse supernova neutrino background in the large liquid-scintillator detector lena. *Phys. Rev. D*, 75:023007, Jan 2007.

[95] Michael Wurm, John F. Beacom, Leonid B. Bezrukov, Daniel Bick, Johannes Blümer, Sandhya Choubey, Christian Ciemniak, Davide D'Angelo, Basudeb Dasgupta, Alexander Derbin, Amol Dighe, Grigorij Domogatsky, Steve Dye, Sergey Eliseev, Timo Enqvist, Alexey Erykalov, Franz von Feilitzsch, Gianni Fiorentini, Tobias Fischer, Marianne Göger-Neff, Peter Grabmayr, Caren Hagner, Dominikus Hellgartner, Johannes Hissa, Shunsaku Horiuchi, Hans-Thomas Janka, Claude Jaupart, Josef Jochum, Tuomo Kalliokoski, Alexei Kayunov, Pasi Kusiniemi, Tobias Lachenmaier, Ionel Lazanu, John G. Learned, Timo Lewke, Paolo

Lombardi, Sebastian Lorenz, Bayarto Lubsandorzhiev, Livia Ludhova, Kai Loo, Jukka Maalampi, Fabio Mantovani, Michela Marafini, Jelena Maricic, Teresa Marrodán Undagoitia, William F. McDonough, Lino Miramonti, Alessandro Mirizzi, Quirin Meindl, Olga Mena, Randolph Möllenberg, Valentina Muratova, Rolf Nahnhauer, Dmitry Nesterenko, Yuri N. Novikov, Guido Nuijten, Lothar Oberauer, Sandip Pakvasa, Sergio Palomares-Ruiz, Marco Pallavicini, Silvia Pascoli, Thomas Patzak, Juha Peltoniemi, Walter Potzel, Tomi Räihä, Georg G. Raffelt, Gioacchino Ranucci, Soebur Razzaque, Kari Rummukainen, Juho Sarkamo, Valerij Sinev, Christian Spiering, Achim Stahl, Felicitas Thorne, Marc Tippmann, Alessandra Tonazzo, Wladyslaw H. Trzaska, John D. Vergados, Christopher Wiebusch, and Jürgen Winter. The next-generation liquid-scintillator neutrino observatory {LENA}. *Astroparticle Physics*, 35(11):685 – 732, 2012.

[96] W. J. Yoo, S. H. Shin, K.-T. Han, D. Jeon, S. Hong, S. G. Kim, H. I. Sim, K. W. Jang, S. Cho, B. G. Park, , and B. Lee. Feasibility study on development of cerenkov fiber-optic dosimeter for radiotherapy application. *... Annual international conference of the IEEE engineering in medicine and biology society.*, pages 485–487, 2013.

[97] H Yücel, Ş Çubukçu, E Uyar, and Y Engin. Determination of the energy dependence of the bc-408 plastic scintillation detector in medium energy x-ray beams. *Physics in Medicine and Biology*, 59(22):6749, 2014.

[98] Y. Zhang. Casting preforms for microstructured polymer optical fibre fabrication. *Optics express*, 14(12):5541–5547, 2006.

[99] C. Zorn, S. Majewski, R. Wojcik, C. Hurlbut, and W. Moser. Preliminary study of radiation damage in liquid scintillators. *IEEE Transactions on Nuclear Science*, 37(2):487–491, Apr 1990.